Origin of the Stellar Discs at the Galactic Centre of the Milky Way

Christian Alig

München 2013

Origin of the Stellar Discs at the Galactic Centre of the Milky Way

Christian Alig

Dissertation
an der Fakultät für Physik
der Ludwig–Maximilians–Universität
München

vorgelegt von
Christian Alig
aus Regensburg

München, den 2.12.2013

Erstgutachter: Prof. Dr. Andreas Burkert

Zweitgutachter: PD Dr. Frank Eisenhauer

Tag der mündlichen Prüfung: 3.2.2014

Zusammenfassung

Im Zentrum der Milchstraße existiert ein massereiches Objekt mit etwa 4 Millionen mal der Masse der Sonne. Beobachtungen dieses Objekts sind bereits gut genug so dass viele alternative Erklärungen außer einem schwarzen Loch ausgeschlossen werden können. Nahe dem schwarzen Loch kann man komplexe Gas und Sternstrukturen beobachten. Unser Hauptinteresse gilt den zwei entgegengesetzt rotierenden Scheiben von Sternen in etwa einem halben parsec Entfernung vom schwarzen Loch.

Der Ursprung dieser Sternscheiben ist schwer erklärbar mit dem Standardmodell der Sternentstehung welches die Entstehung von Sternen in isolierten Gaswolken die unter dem Einfluss von Gravitation kollabieren annimmt. Nahe dem schwarzen Loch würden Gezeitenkräfte jede Gaswolke zerreißen und so den Kollaps der Wolke verhindern. Die Annahme dass die Sterne in größerer Entfernung entstanden sind und dann nach innen gewandert sind ist problematisch aufgrund des geringen Alters der Sterne von etwa 6 Millionen Jahren. Die Lösung dieses auch "Paradox of Youth" genannten Problems war die Hauptaufgabe dieser Arbeit.

Bisherige Arbeiten die sich mit dem "Paradox of Youth" beschäftigt haben bevorzugen ein Modell in dem die Sternscheiben immer noch von einer Gaswolke stammen, wobei die Entstehung der Scheiben aber in einem Prozess von zwei Schritten abläuft. Zuerst wird die Wolke eingefangen und von dem schwarzen Loch zerrissen. Dadurch bildet sich eine Gasscheibe um das schwarze Loch. Die Masse dieser Scheibe nimmt immer weiter zu, bis sie gravitativ instabil wird und sich Sterne bilden können.

Wir verwenden numerische Simulationen um den Einfall und Einfang einer Gaswolke, sowie die Anschließende Sternentstehung um das schwarze Loch zu simulieren. Inspiriert von dem analytischen Modell von Wardle & Yusef-Zadeh (2008) simulieren wir eine Wolke die das schwarze Loch während dem Einfall teilweise überlappt. Dadurch rotieren unterschiedliche Teile der Wolke mit entgegengesetztem Drehimpuls um das schwarze Loch. Das führt zu einer sehr effizienten Umverteilung des Drehimpulses am Kollisionspunkt. In unserem ersten Paper in Kapital 3 zeigen wir wie dieses Modell mit Hilfe von hochaufgelösten Simulationen die Bildung einer kompakten Akkretionsscheibe erklären kann. Im Vergleich zu vorigen Modellen, welche auch Wolken voraussetzen die sich auf fast radialen Orbits bewegen aber an dem schwarzen Loch in einigem Abstand vorbeifliegen, können sogar stark nicht gebundene Wolke eingefangen werden wenn Teile der Wolke das schwarze Loch überlappen.

Im ersten Paper haben wir uns Hauptsächlich auf die Entstehung der kompakten Akkretionsscheiben konzentriert. In Kapitel 4 untersuchen wir Sternentstehung in den simulierten Scheiben und versuchen die Ergebnisse mit Beobachtungen zu vergleichen. Die Beobachteten Sternscheiben zeigen ein charakteristisches Merkmal das benutzt werden kann um Entstehungsmodelle zu testen. Sterne die in einer kollabierenden Gaswolke entstehen zeigen eine

typische Massenverteilung. Es gibt viele Sterne mit einer niedrigen Masse wie die Sonne und einige Sterne mit hohen Massen. Die Sternscheiben zeigen allerdings nur Sterne mit hohen Massen. Diese Tatsache kann man benutzen um die Gültigkeit eines Entstehungsmodells zu testen. Die Simulationsergebnisse deuten darauf hin das nur sehr massereiche Sterne entstehen. Allerdings führen numerische Probleme beim auflösen der sehr dünnen Scheiben dazu das wir diesen Ergebnissen nicht trauen können.

Die Masse und die Ausdehnung der aus den Simulationen stammenden kompakten Akkretionsscheiben sind vergleichbar mit den Beobachteten Sternscheiben. Allerdings gibt es einige Nachteile des Wolkeneinfang Modells. Erstens muss die Wolke fast radial auf das schwarze Loch zufallen. Zweitens, wenn wir eine zweite Stellare Scheibe erzeugen wollen brauchen wir eine zweite Wolke mit dem gleichen fast radialen Orbit die kurz nach der ersten Wolke einfällt, um das ähnliche Alter aller Sterne zu erklären. Um eine entgegengesetzt rotierende Scheibe zu erzeugen bräuchte die zweite Wolke schließlich noch einen entgegengesetzten Drehimpuls.

Test-Simulationen mit dem Ziel den Ursprung einer massereichen Wolke die fast radial auf das schwarze Loch zufällt zu erklären haben zu einem neuen Entstehungsmodell geführt, welches die Entstehung zweier Entgegengesetzt rotierender Scheiben mit einer einzigen Kollision erklären kann. Im zweiten Paper in Kapitel 5 präsentieren wir dieses neue Entstehungsmodell, in welchem wir die Kollision einer einzelnen Wolke mit einem Ring aus Gas in einigen parsec Entfernung von dem schwarzen Loch annehmen. Beobachtungen zeigen das ein ähnliches Ereignis gerade im Galaktischen Zentrum passieren könnte wo eine Gaswolke mit der Beobachteten zirkumnuklearen Gasscheibe kollidiert. In unseren Simulationen bilden sich durch die Kollision mehrere Streams aus. Diese Streams erreichen das schwarze Loch zu unterschiedlichen Zeiten und bilden dabei massive Akkretionsscheiben. Die Mischung aus Wolken und Gasring Materie bestimmt den Drehsinn dieser Scheiben.

Ein weiterer Aspekt der Physik des Galaktischen Zentrums an dem wir gearbeitet haben, welcher aber nicht direkt mit dem Hauptfokus dieser Arbeit verbunden ist, sind Simulationen der kleinen Gaswolke G2 auf ihrem Weg zu SgrA*. Ähnlich wie in unseren vorigen Simulationen betrachten wir wieder den Einfall einer Gaswolke auf das zentrale schwarze Loch, diesmal aber auf einer viel kleineren Skala. Da die Wolke den kleinsten Abstand zum schwarzen Loch Anfang 2014 erreichen wird ist gerade ein guter Zeitpunkt für diese Simulationen. Die Entwicklung der Wolke hängt stark von den Eigenschaften der Umgebung von SgrA* ab. Deswegen hilft der Vergleich von Simulationen der Entwicklung der Wolke mit Unterschiedlichen Parametern für die Umgebung zu der Beobachteten Entwicklung der Wolke um ein besseres Verständniss der Umgebung von SgrA* zu bekommen. Der extreme Dichte und Temperaturkontrast der Umgebung von SgrA* im Vergleich zu G2 führt allerdings zu Problemen mit der Standardimplementierung der numerischen Methode die wir für unsere Simulationen benutzen. Anhand der G2 Simulationen diskutieren wir diese Probleme in Kapitel 6. In Kapitel 7 zeigen wir Simulation von G2 aus unserer Gruppe die eine andere numerische Methode benutzen bei der keine Probleme auftreten.

Summary

At the centre of the Milky Way lies a massive object of around 4 million times the mass of our sun. Observations of this object are already good enough so that many alternative explanations besides a supermassive black hole can already be ruled out. Around the black hole one can observe complex gaseous and stellar structures. Our main interest focuses on the two inclined, counter-rotating discs of stars at around half a parsec distance from the black hole.

The formation of those discs is difficult to explain with the help of the standard model of star formation in which stars form in an isolated gaseous cloud that is able to collapse under the influence of gravity. Close to the black hole, tidal forces would tear the cloud apart, preventing collapse of the cloud. The assumption that those stars formed further away from the black hole and then migrated inwards is problematic due to the common young age of the stars of around 6 Myrs. Solving this so called "Paradox of Youth" was the main goal of this thesis.

Previous work which has already been conducted on the "Paradox of Youth" favoured a model in which the discs of stars still originate from a gaseous cloud, however this formation happens in a two step process. First the cloud gets captured and torn apart by the black hole, leading to the formation of a gaseous disc around the black hole. This disc then grows in mass and at some point becomes gravitationally unstable so that stars can form inside the disc.

Using numerical hydrodynamics simulations, we study the infall and capture of a gaseous cloud and the subsequent star formation around a supermassive black hole. Inspired by the analytical model of Wardle & Yusef-Zadeh (2008) the infalling cloud overlaps the black hole in parts during the infall, so that different parts of the cloud rotate with opposite angular momentum around the black hole. This leads to a very efficient redistribution of angular momentum at the collision point of the two streams of gas rotating around the black hole. In our first paper in chapter 3 we present how this model is able to explain the formation of a compact accretion disc around the black hole using high resolution simulations. Compared to previous models, which assume clouds which are also on nearly radial orbits towards the black hole but which pass the black hole at some distance, even highly unbound clouds can be captured when parts of the cloud overlap the black hole.

In the first paper we mainly concentrated on the progenitor accretion disc formation. In chapter 4 we study the fragmentation behaviour of the simulated discs and try to compare the results to observations. Observations of the stellar discs show a distinguished feature that can be used to test formation models. Normally stars which formed in a gaseous cloud show a typical distribution of masses. There are many stars which have a low mass like our sun and there are only a few stars with high masses. However the observed discs

show only stars at high masses, a fact that can be used to check the validity of a formation model. The simulation results seem to indicate that only high mass stars are forming, however numerical problems with resolving the razor-thin accretion discs prevent us from being able to trust those results.

So far the resulting simulated accretion discs are comparable to observations of the stellar discs in size and mass. However there are several drawbacks of the black hole cloud-capture model. First the infalling cloud needs to be on an extremely radial orbit towards the black hole. Second, if we want to create a second stellar disc we would need a second cloud with a similar nearly radial orbit falling in shortly after the first cloud to explain the similar age of all the stars. And finally to create a counter-rotating disc, the second cloud would also need opposite angular momentum.

Test simulations to understand the origin of a massive cloud with a nearly radial orbit lead us to a new formation model which can explain the formation of two counter-rotating accretion discs using a single collision event. In the second paper in chapter 5 we present simulations of this new formation model in which we assume the collision of a single cloud with a circum-nuclear ring of gas at parsec scale distance from the black hole. Observations indicate that a similar event might be happening again right now with a cloud crashing into the observed circum-nuclear disc. Our simulations show that several streams form during the collision event. Those streams arrive at the black hole at different times and form compact accretion discs. The mixture of cloud and circum-nuclear ring material determines the direction of rotation.

Another aspect of the physics of the Galactic Centre which we worked on, but which is not directly connected to the main focus of this work are simulations of the small gaseous cloud G2 on its way towards SgrA*. The situation is similar to our previous work in the sense that we have again a gaseous cloud which is falling towards the central black hole, however this happens on a much smaller scale. The simulations are also timely since G2 will pass the supermassive black hole at the beginning of 2014. The cloud will be a sensitive probe of the close environment of SgrA*. Thus comparisons of simulations with different parameters for the environment to the observed evolution of the cloud will help to get a better understanding of the vicinity of the central black hole. The extreme contrast in density and temperature between the cloud and the environment however puts great stress on the numerical method used for our simulations. Using the G2 simulations we discuss the problems the standard implementation of the numerical method encounters in chapter 6. In chapter 7 we present simulations of G2 which we have conducted using a different numerical technique which does not encounter those problems.

Contents

Introduction

1.1 The Galactic Centre of the Milky Way

We start with an historical and observational overview of the Milky Way Galactic Centre. During the course of the introduction we also gather the problems and questions we will address and try to answer in this thesis.

1.1.1 Discovery of the Galactic Centre

Following the old paradigm of putting humanity at a special place in the universe, it was first thought that if the earth was not the centre of the solar system, at least the solar system was the centre of the Milky Way Galaxy. It was in 1914 when Harlow Shapley, using the 60-inch reflecting telescope at Mount Wilson Observatory in California started a survey of globular clusters. Using Cepheid variable stars in the closest globular clusters and applying the luminosity-period relationship of Cepheids he determined their relative distances (Russell & Shapley, 1914). To derive absolute distances the actual distance to at least one Cepheid had to be measured, which was done in 1915 using parallax methods (Shapley, 1918).

Shapley analysed the obtained distribution of globular clusters in space and found its centre to be located within the Sagittarius constellation at a distance of roughly 50,000 light years or around 17 kpc from earth. Shapley then claimed this point would be the centre of the whole Galaxy, which turned out to be correct (Shapley, 1918). The measured distance however was not correct. This places the Sun at a distance of around two third of the radius of the Galaxy away from the Milky Way Galactic Centre, destroying again our view of a special position for humanity within the universe. The paradigm was resurrected with the claim that at least the Milky Way must be placed at the centre of the universe (which also turned out to be the wrong point of view).

In 1918 the role of absorption due to the concentration of gas and dust close to the galactic plane was not yet fully understood. Because of this effect the distance Shapley measured was overestimated. Taking absorption into account, the actual distance from the Galactic Centre was reduced from 17 kpc to around 9 kpc in the 1930s (Reid, 1993).

In 1927 Jan Oort found a similar result for the centre of our Galaxy by studying the motion of stars close to the Sun. He noticed that the stars are differentially rotating, with stars closer to the centre of the galaxy travelling faster compared to stars at a larger distance from the centre. The centre of the rotation then determines the centre of the Galaxy. Jan Oort found a distance of 19,000 light years or around 7 kpc (Oort, 1927b,a). Modern measurements (Gillessen et al., 2009b) determine the distance towards the Galactic Centre to be 8.33 ± 0.35 kpc.

Now that it was known that we are not placed at the centre of our galaxy, there was a strong interest in actually observing this special place within our galaxy. However direct observations of the Galactic Centre are very difficult for optical astronomy since the line-of-sight is obscured by gas and dust which is impenetrable by visible light. It took until the invention of radio astronomy by Karl Jansky in the 1930s that is was possible to directly observe the central part of the galaxy.

Jansky's 1932 data (20.5 MHz) already showed a strong concentration of galactic background emission originating from the direction of the Galactic Centre (Jansky, 1933). Still technology had to advance until in 1951 Piddington and Minnett conducted a high frequency observation (1210 and 3000 MHz) and found what they called a "new, remarkable and powerful discrete source", the so called "Sagittarius-Scorpius" source (Piddington & Minnett, 1951). This is commonly credited as the discovery of the core of the Milky Way Galaxy. In a 1954 report on a 250 MHz all sky image made by Kraus and Ko, the source was called SgrA for the first time, a name that was already commonly adapted in 1958 (Kraus et al., 1954). General acceptance that SgrA marks the core of the Milky Way took until 1960 when finally Oort and Rougoor conclude in a series of papers on the position of the Galactic Centre that it is almost certain that SgrA is situated at the centre of the galaxy.

The astonishing success of radio astronomy in the 1950s and 1960s, leading to new discoveries that were not possible before, including the observation of the centre of the galaxy lead to the rise of observational techniques outside the traditional visible wavelength regime. Especially the birth of modern infrared and X-Ray astronomy provided to be extremely useful for observations of the Galactic Centre. Whereas visible light, ultraviolet light and soft X-rays from the Galactic Centre are obscured, radio, infrared light, gamma rays and hard X-rays are detectable on earth.
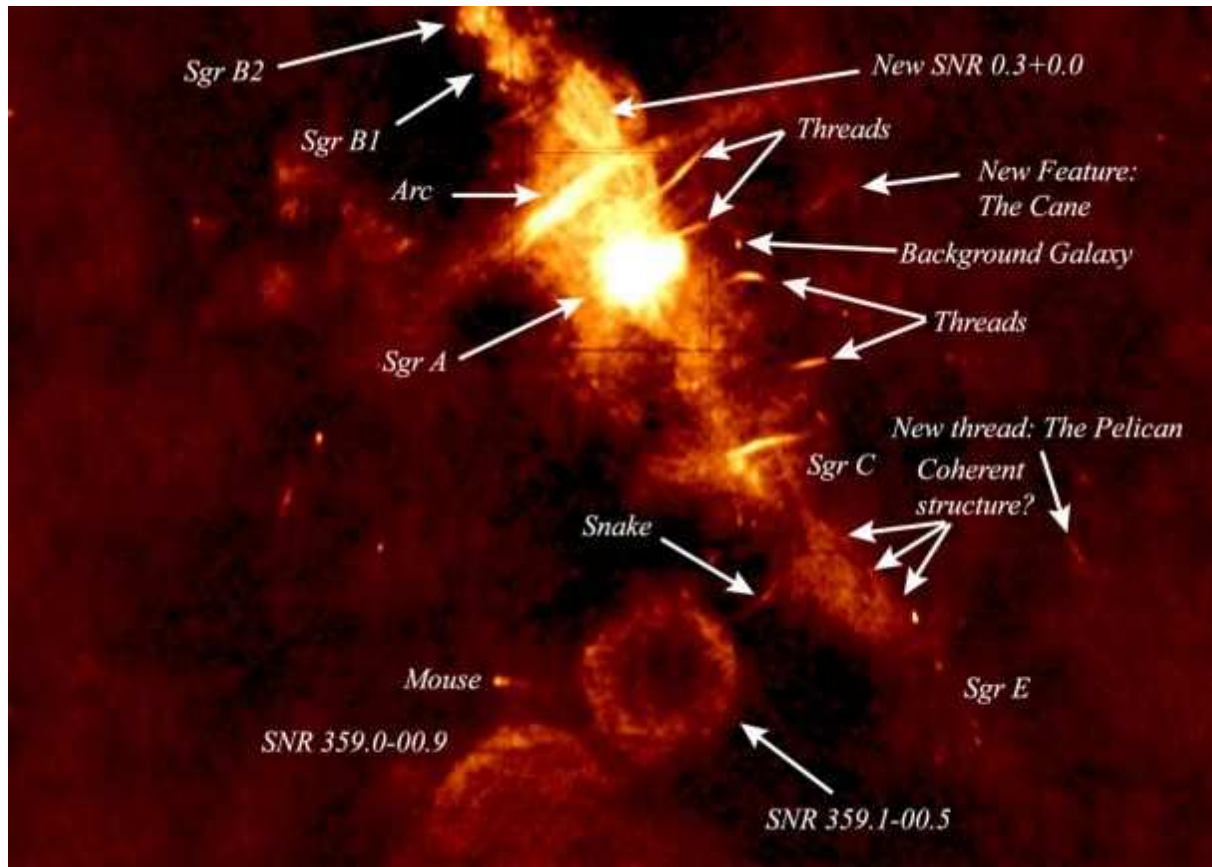
Figure 1.1: Radio data (90 cm) of the Galactic Centre taken by the National Radio Astronomy Observatory's Very Large Array. The Sagittarius region is shown, with the bright SgrA source at the centre. The diameter of SgrA is roughly 75 pc. All the bright features are labelled by capital letters. The abbreviation SNR refers to a supernova remnant. Credit: N. E. Kassim, D. S. Briggs, T. J. W. Lazio, T. N. LaRosa, J. Imamura (NRL/RSD).

Figure 1.1 shows an image of the Galactic Centre at radio-wavelengths (90 cm) obtained with the National Radio Astronomy Observatory's Very Large Array (LaRosa et al., 2000). All the bright features are labelled by capital letters with SgrA being the central and brightest feature. Supernova remnants are labelled SNR and are clearly distinguishable as spherical features. The diameter of the SgrA source is roughly 75 pc in this image. The galactic plane runs diagonally through the image. There are many distinguished features like threads, arcs and filaments visible which are still not completely understood. These features have been detected first in 1984 by Yusef-Zadeh et al. (1984b,a) using the VLA. They were first attributed to bad data, but additional data confirmed their existence. One interpretation is that the filaments and threads are magnetic features, providing clues about the Galactic Centre magnetic field morphology.
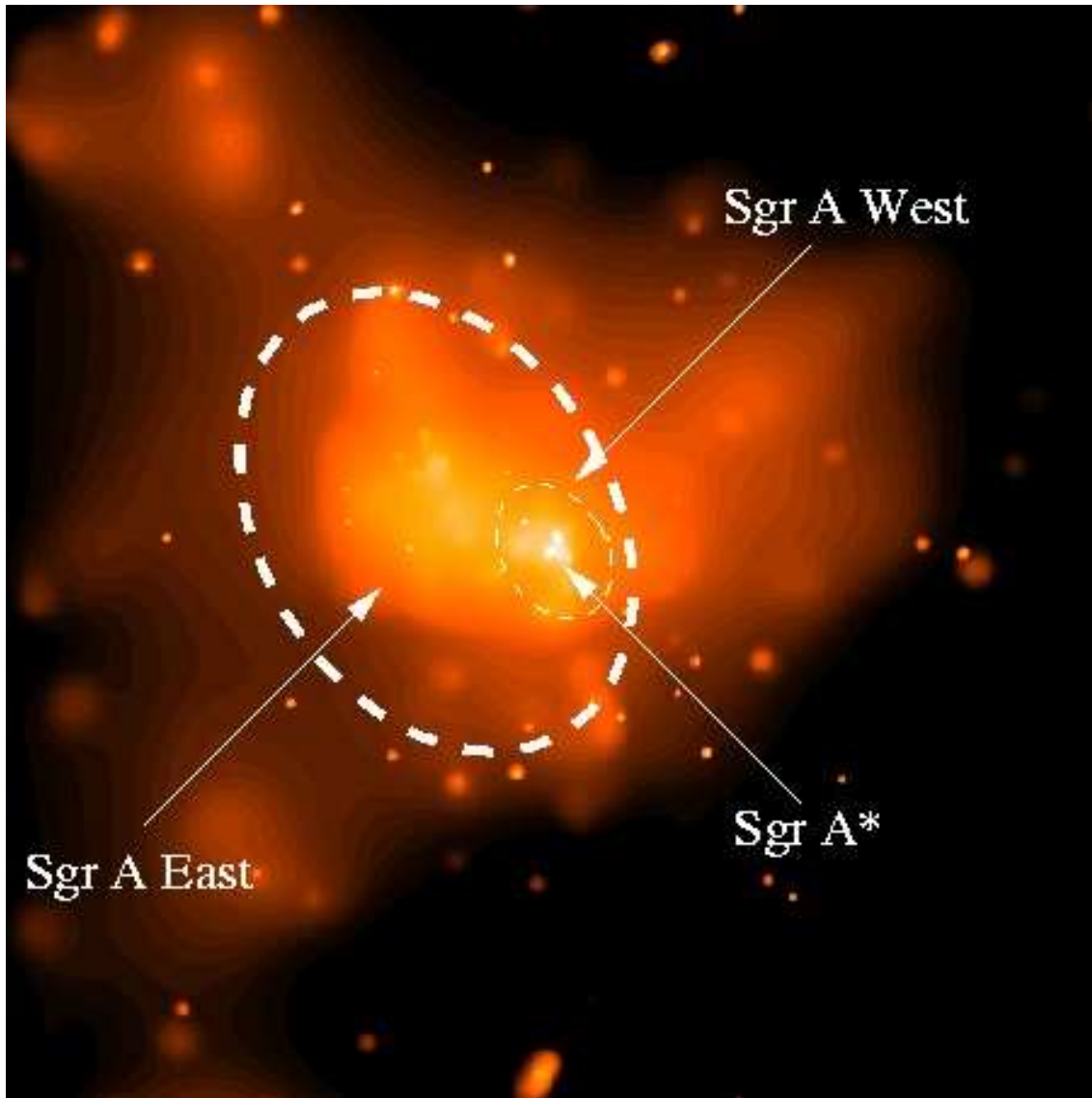
Figure 1.2: This X-ray image shows that the source SgrA itself can be divided into further parts. The most interesting part is the small bright sub-source called SgrA* inside the SgrA West region. Credit: NASA/Penn State/Garmire (2001), data taken with the Chandra X-ray Observatory in the 0.1 - 10 keV regime by the Advanced CCD Imaging Spectrometer (ACIS).

Switching to X-ray, Figure 1.2 shows an image taken in X-rays by the Chandra satellite (Garmire, 2001). The resolved SgrA source now reveals a bright, small sub-source called SgrA* inside the SgrA West region.
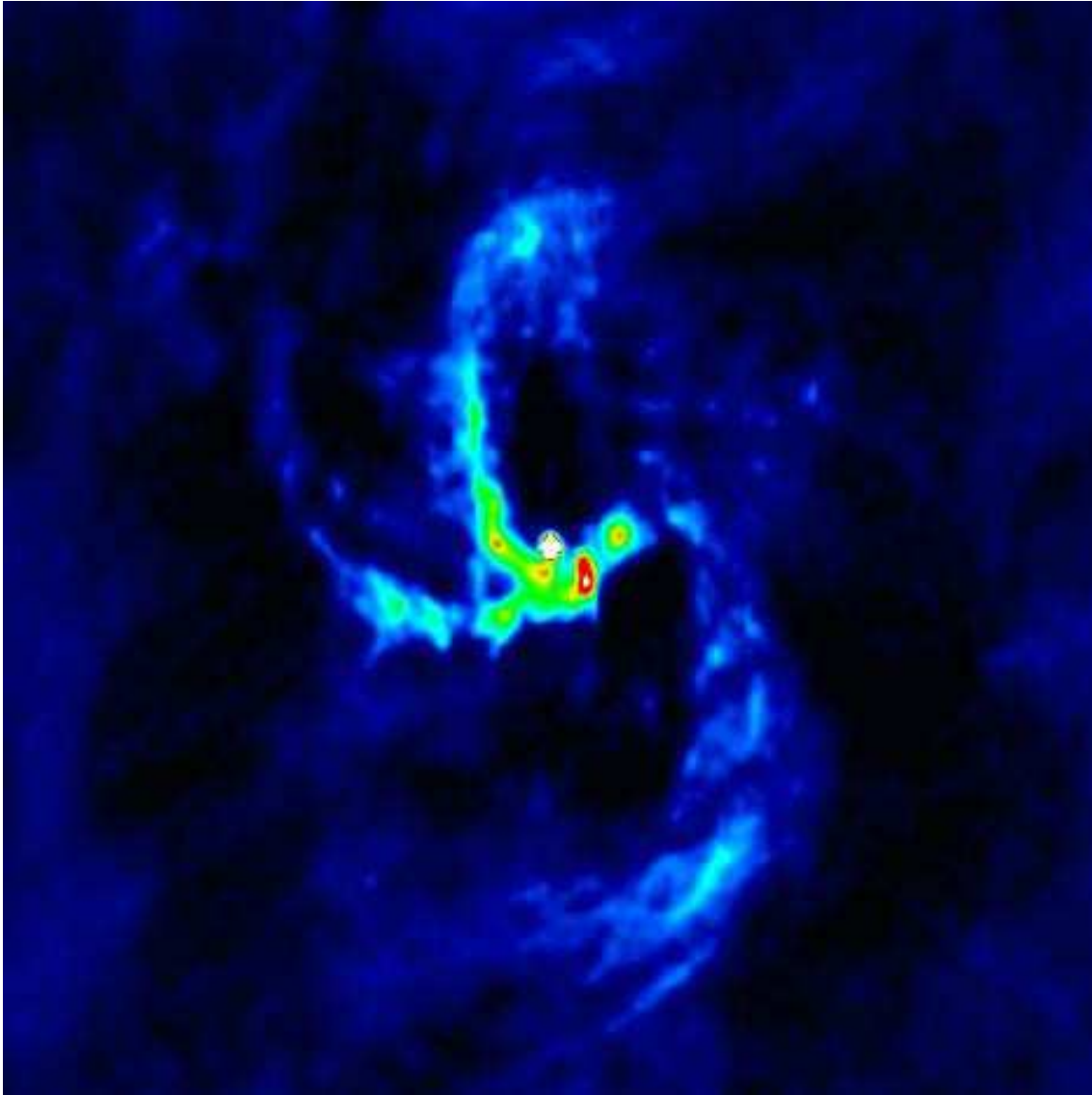
Figure 1.3: Resolving the SgrA West region (the central few parsec of the galaxy) in radio (3.6 cm) shows a spiral like structure of gas which seems to be rotating around the point like source SgrA*. The box size is roughly 2 pc. Credit: Roberts et al. NRAO / AUI / NSF. Radio data taken at the Very Large Array.

Going back to radio, Figure 1.3 resolves the SgrA West region, revealing a spiral like structure of gas around the still point like source SgrA*. The source SgrA* was first discovered in 1974 at the NRAO's Green Bank Interferometer in West Virginia. In 1983 Lo and Claussen created a detailed image of the region that for the first time clearly separated SgrA* from any other structure in the central region (Lo & Claussen, 1983). The source SgrA* remains point like until today (2013). Even the most powerful telescopes so far are

not able to resolve any sub-structure of the object.

The origin of the radio source SgrA* was not known for quite some time. However, as telescopes became more powerful, infrared imaging and spectroscopy was able to follow the orbits of individual stars at the Galactic Centre. In 2002, Schödel et al. (2002) at the MPE (Max Planck Institut für extraterrestrische Physik) reported about their 10 year observation of the star S2 which orbits SgrA* with a period of 15.2 years and a pericentre distance to SgrA* of only 17 light hours. Analysing the Keplerian orbit leads to a mass of around 2.9×10^6 M$_\odot$ within the central 17 light hours. This already strongly constrained the number of possible models for SgrA*.

Finally in 2009 the MPE group reported a summary of their 16 years of observations of stellar orbits around SgrA* (Gillessen et al., 2009b) and the group leader R. Genzel concluded that the central mass concentration, which was now found to be more than 4×10^6 M$_\odot$ must be a black hole beyond any reasonable doubt.

Lynden-Bell and Rees already suggested in 1971 that the Milky Way could contain a super-massive black hole (Lynden-Bell & Rees, 1971), however the proof took nearly 40 years. Today it is assumed that almost every galaxy contains a central super-massive black hole. The radio source SgrA* itself is believed to originate from close to the black hole, either inside an accretion disc around the black hole or from a jet.

Commonly the inner 500 pc around SgrA* are defined as the central region of the galaxy (Morris & Serabyn, 1996). We will now look in more detail at the individual components of the Galactic Centre region, starting first with a summary of how material from the outskirts of the galaxy is transported into the central region.

1.1.2 The Milky Way's Bar and Transport of Material into the Galactic Centre
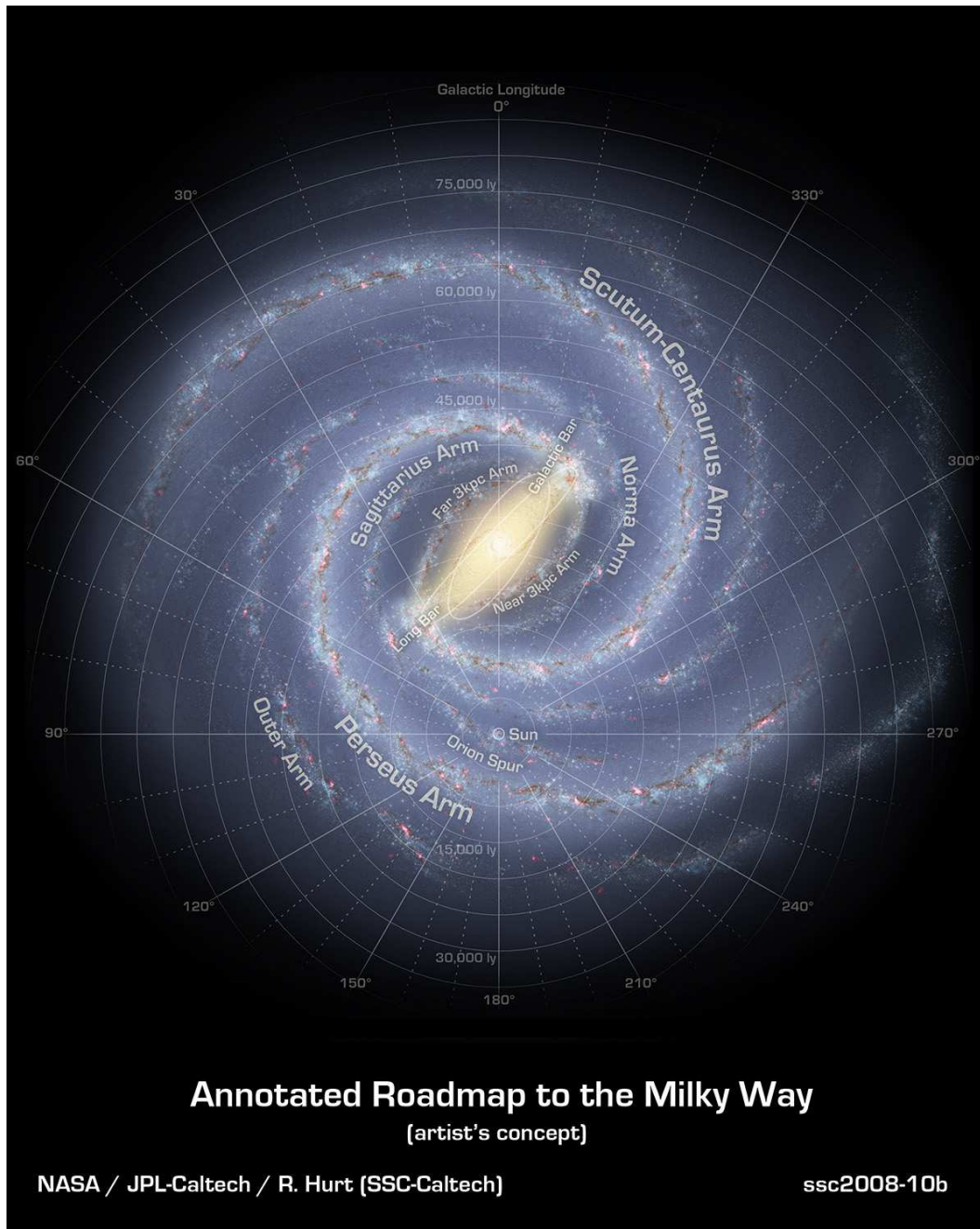
Figure 1.4: Artist's concept of the Milky Way, centred on our Sun. The spiral arms are visible together with the prominent bar at the centre. Credit: NASA/JPL-Caltech/R. Hurt (SSC-Caltech).

There is strong evidence for a bar in the Milky Way extending out to the co-rotation radius (the radius at which the stars rotate at the same speed as the spiral arms) at around 2.4 kpc (Morris & Serabyn, 1996). The bar contains a total mass of roughly 2×10^{10} $M_{\odot}$. The existence of a bar strongly determines the dynamics of the gas near the Galactic Centre, with the possible bar induced inflow of material into the central region being the most interesting effect. Figure 1.4 shows an artist's concept of the Milky Way, with the prominent bar clearly visible at the central region.

A strong bar leads to deviations from circular orbits and to strong shocks. At a radius of around 200 pc a transition from the outer mixed atomic/molecular layer of gas towards a mostly molecular high density layer occurs. This so called central molecular zone (CMZ) consists mainly of two components. An outer dense tilted ring, the so called 180 pc molecular ring and an inner molecular disc which lies within the galactic plane. Studying the velocity field of the 180 pc molecular ring provides evidence about the shape of the central gravitational potential.

Gas moving inside a bar potential tends to settle into closed and elongated orbits due to the dissipation of energy resulting from collisions. The special orbits at radii between the co-rotation radius and the inner Lindblad resonance (resonance of the orbital frequency of individual stars with the large scale (e.g. spiral) structure frequency) are called X_1 orbits. They are basically oval orbits with major axis along the bar. At the innermost edge the X_1 orbits become self crossing, leading again to dissipation of energy and further inward migration. The gas settles in a closed oval orbit deeper within the potential, the so called X_2 orbits. This time the major axis is oriented perpendicular with respect to the bar and the outermost edge of the X_2 orbits touch the innermost orbits of X_1. Thus, gas migrating inwards from X_1 crashes into X_2 shocking the material.

Figure 1.5 which we adapted from Morris & Serabyn (1996) shows a illustration of the shape and orientation of the X_1 and X_2 orbits, as well as the 180 pc molecular ring. The X_2 orbits major axes are always perpendicular to the more extended X_1 orbits major axes.
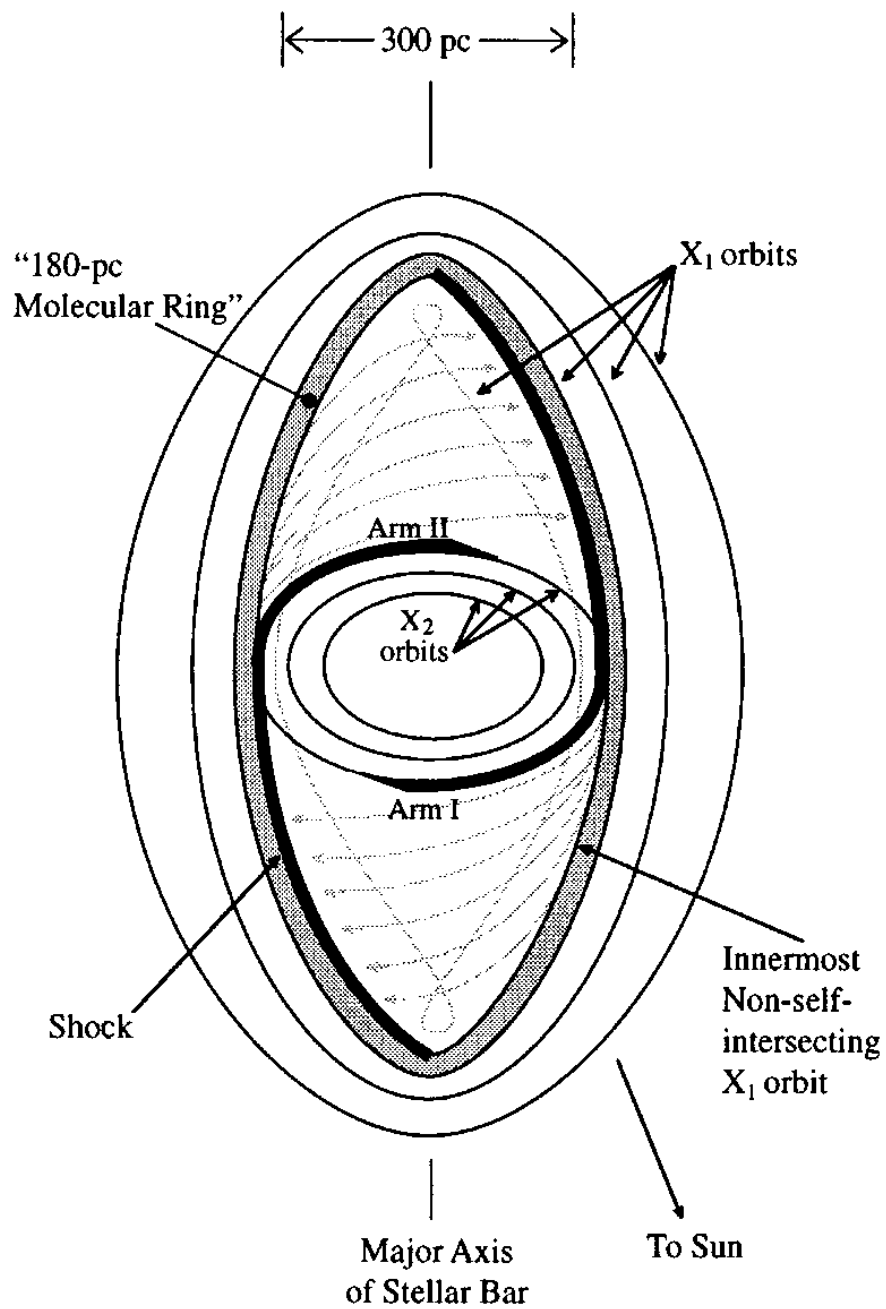
Figure 1.5: Schematic of the shape of the X_1 and X_2 orbits in the Milky Way. Adapted from Morris & Serabyn (1996).

The 180 pc molecular ring is thought to consist of the innermost X_1 orbits (Binney et al., 1991). Shocks at the inner edge of the ring convert the gas into molecular form (the shocked

high density gas can cool efficiently). Enclosed inside the molecular ring is a population of molecular clouds which is believed to be distributed on the X_2 orbits. All the material on the X_2 orbits is estimated to contain around 85 to 90 percent of the total molecular mass within the Galactic Centre region, thus the X_2 orbits seem to be more stable compared to X_1. Still, gravitational torques due to the faster rotation of clouds on X_2 compared to the bar lead to the loss of angular momentum. Additional effects leading to inward migration are movement within the strong magnetic field (see section 1.1.11) inside the central 100 pc, tidal friction from the bulge stars and the viscous evolution in a differentially rotating disc. This way, large clouds can reach the core region within a timescale of around 100 Myrs.

Assuming that gas inside the innermost X_1 orbit moves inwards on a timescale roughly equal to one orbital period and taking into account the total gas inside X_1 one can estimate the rate of inflow of material into the central region to be around 0.1 to 1 $M_\odot/yr$, depending on the uncertainty in the mass contained in X_1. The gas migrating inwards can either form stars (the dominant process), lead to a galactic wind or move towards the inner 10 pc, contributing to the circum-nuclear disc. The circum-nuclear disc is a thick and clumpy ring of gas of roughly 10^4 to 10^5 $M_\odot$ rotating around SgrA* within the galactic plane which we will present in more detail in section 1.1.5.

The conditions for star formation in the central region differ a lot from the outside region. The strong tidal field sets a lower limit of 10^7 cm^{-3} $\times$ $(\frac{1.6 \text{ pc}}{r})^{1.8}$ on cloud density (Morris & Serabyn, 1996), with r the distance from the galactic core, below which tidal forces are stronger than the self-gravity of a cloud. Also pressure, temperature, magnetic field strength and velocity dispersion are much higher compared to the outer parts of the galaxy. Only very dense clouds can thus collapse. It is reasonable to assume that many of the star formation events in the central region are actually triggered. Collisions of clouds, supernova events or even outflow from the core may tip over marginally stable clouds and initiate star formation. Metallicity in the central region can be up to two times solar. The changed conditions for star formation within the Galactic Centre might be reflected within the stellar IMF, leaning towards more heavy stars and a higher cutoff in low mass stars.

The effect of stellar winds on the Galactic Centre environment has only been reliably demonstrated for the very central star cluster extending roughly 10 pc around SgrA*. Here it is believed that the inner 1.5 pc cavity of the circum-nuclear disc has been evacuated by winds originating from the star cluster. This also implies that the inflow onto SgrA* might be completely due to those winds.

1.1.3   Clouds and Star Formation in the Galactic Centre region

Commonly the Galactic Centre region is defined to be the innermost 500 pc of the Milky Way. Molecular clouds in the Galactic Centre region tend to be different ("more extreme") compared to their counterparts in the outer regions of the galactic disc. Güsten & Philipp (2004) compiled an observational comparison of the common properties of both cloud populations. Table 1.1 shows a side by side comparison of the properties of the gas layer outside of and inside the Galactic Centre, which we adapted from Güsten & Philipp (2004). Table 1.2 shows the same comparison for the cloud population.

	Central 500 pc	Galactic Disc
Masses and Densities		
Stars $[M_\star]$	$10^{9.8} M_\odot$	$--$
Gas, atomic	$10^{6.4} M_\odot$	$\sim 10^{9} M_\odot$
... molecular	$10^{7.9} M_\odot$	$\sim 10^{9} M_\odot$
Molecular Gas fraction $M_g/M_\star$	~ 0.01	$\sim 0.05 - 0.10$
Fract. abundance $[\mathrm{HI}]/[\mathrm{H_2}]$	~ 0.05	~ 2
Gas density	100 cm^{-3}	$1 - 2$ cm^{-3}
Gas surface density	$\geq 100 M_\odot \mathrm{pc}^{-2}$	$\sim 5 M_\odot \mathrm{pc}^{-2}$
Star Formation Rate		
Rate Φ	$0.3 - 0.6 M_\odot \mathrm{yr}^{-1}$	$\sim 5.5 M_\odot \mathrm{yr}^{-1}$
Efficiency Φ/M_g	$5 \cdot 10^{-9} \mathrm{yr}^{-1}$	$10^{-9} - 10^{-8} \mathrm{yr}^{-1}$

Table 1.1:   Comparison of the properties of the Galactic Centre gas layer to the gas layer outside the Galactic Centre, adapted from Güsten & Philipp (2004).

	Center Clouds	**Disc Clouds**
Cloud Characteristics		
Mass spectrum: dN/dM $\propto$ M$^{-\gamma}$	$\gamma \sim$1.6 ($\geq$10^4 $M_\odot$)	1.6 - 1.7
Vel. dispersion [km/s]	15 $-$ 30	$\leq$ 5
Vel.dispersion-Size: $\triangle$V [km/s]	12$\cdot$R$^{0.5}$	2$\cdot$R$^{0.5}$
Mean Gas Density [cm^{-3}]	$\sim$10$^{4.0}$	$\sim$ 10$^{2.5}$
Temperatures [K]: Gas	bulk: 50 $-$ 70	$\sim$ 15
	wide range of coex. hot phases	
: Dust	21 $\pm$2	
Magnetic Field [mG]	order mG	$\leq$ 0.1
Isotopic Abundances		
[^{12}C]/[^{13}C]	$\sim$ 25	$\sim$ 75
[^{16}O]/[^{18}O]	$\sim$ 200	$\sim$ 400
[^{14}N]/[^{15}N]	$\sim$ 1000	$\sim$ 400

Table 1.2: Comparison of the properties of Galactic Centre clouds to the cloud population outside the Galactic Centre, adapted from Güsten & Philipp (2004).

Inside the Galactic Centre there is a large amount (around 10^8 M$_\odot$) of mostly molecular gas. The distribution of gas is asymmetric and densities peak towards the Sgr B2 complex (See Figure 1.1). Also the gas is mostly concentrated in cloud complexes which can be as large as 50-70 pc.

A comparison to normal clouds in the galactic disc shows that the Galactic Centre clouds are denser, warmer, more massive and more turbulent. Due to tidal friction inside the steep gravitational potential in the central region it is likely that only those extreme clouds survive long enough in the central region to be observed, leading to the different cloud populations.

Studies using density tracers like CS, H$_2$, CO and HC$_3$ show that the average cloud density is around 10^4 cm^{-3}. On the other hand excitation studies show a higher density of 10^5 cm^{-3} for the clouds which are embedded in a lower density medium of around $10^{3.7}$ cm^{-3}.

A more detailed study of the Galactic Centre clouds has been conducted by Miyazaki & Tsuboi (2000). Using the tracers CS(1-0) and CO(1-0), the authors mapped each individual cloud in the Galactic Centre region, leading to a table of 159 clouds. Using their data they find a mass spectrum for the clouds that can be described by a power law
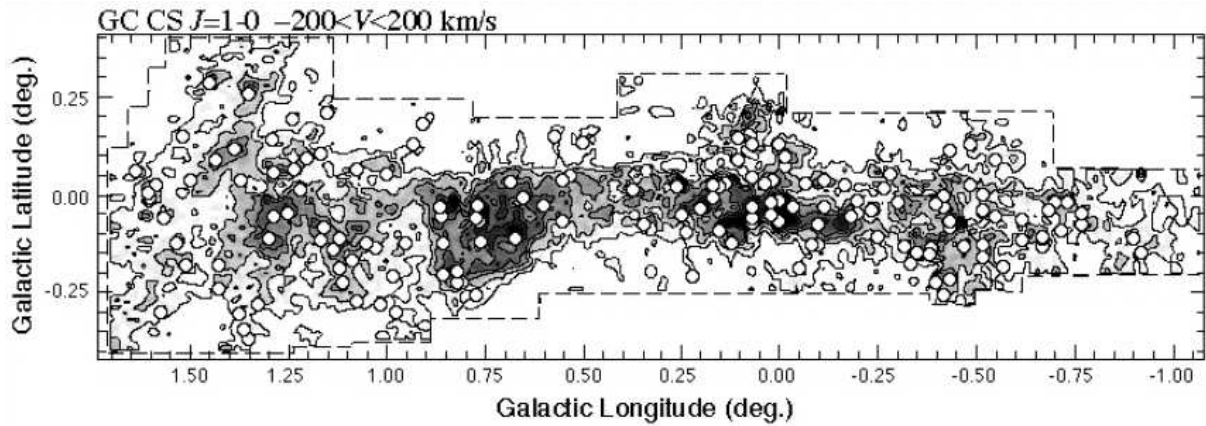
Figure 1.6: Distribution of the identified 159 Galactic Centre molecular clouds (open circles) overlaid on the CS(1-0) integrated intensity map in the velocity range of $V_{LSR} = \pm$ 200 km/s. Contour intervals and the lowest contour level are both 35.7 K km/s. The plot has been adapted from Miyazaki & Tsuboi (2000).

$$\frac{dN}{dM} \propto M^{-1.59\pm0.07}$$

with M $\gtrsim 10^4$ M$_\odot$. The size spectrum also follows a power law that can be described by

$$\frac{dN}{dR} \propto R^{-3.97\pm0.36}$$

with R $\gtrsim$ 3.3 pc (the resolution limit). The identified clumps are shown in Figure 1.6.

Although the conditions in the Galactic Centre region could suggest a higher star formation rate, the rate is only around 10% of the outer regions. Effects that suppress star formation could be the large turbulence in the Galactic Centre clouds and the strong tidal forces.

A more recent study finds evidence for current star formation events even within the very inner parts of the Galactic Centre. Figure 1.7 shows an ALMA image of the inner 6 pc region around SgrA*. In red, regions of Si-O (5-4) line emission are marked which indicate regions of star formation. One has to be cautious though since clump-clump collisions are an alternative source for the Si-O emission. Yusef-Zadeh et al. (2013) argue however that the number of sources detected is too large to be accounted for by collisions only.
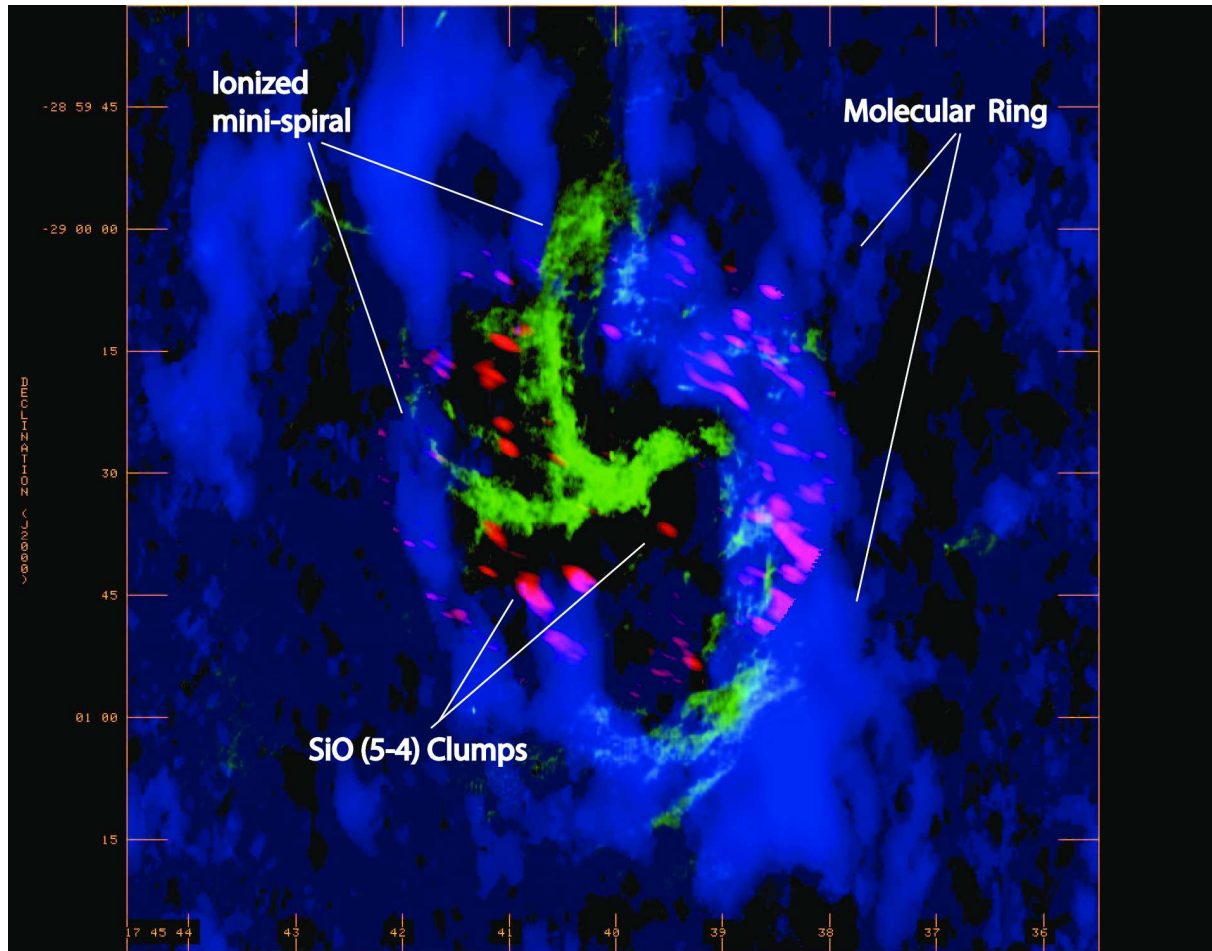
Figure 1.7:   The inner 6 pc around SgrA* recorded by ALMA (Atacama Large Millimeter/submillimeter Array), adapted from Yusef-Zadeh et al. (2013). The red areas represent Si-O (5-4) line emission and indicate regions of star formation.

1.1.4   Nuclear Star Cluster

The Galactic Centre contains a number of star clusters which are the densest found in the whole galaxy (Buchholz et al., 2009; Schödel et al., 2008). In particular the star cluster around the central black hole SgrA* exceeds the density of every other cluster (Genzel et al., 2010). Figure 1.8 shows the central 7×7 pc region around the black hole, with the nuclear cluster inside the white box.
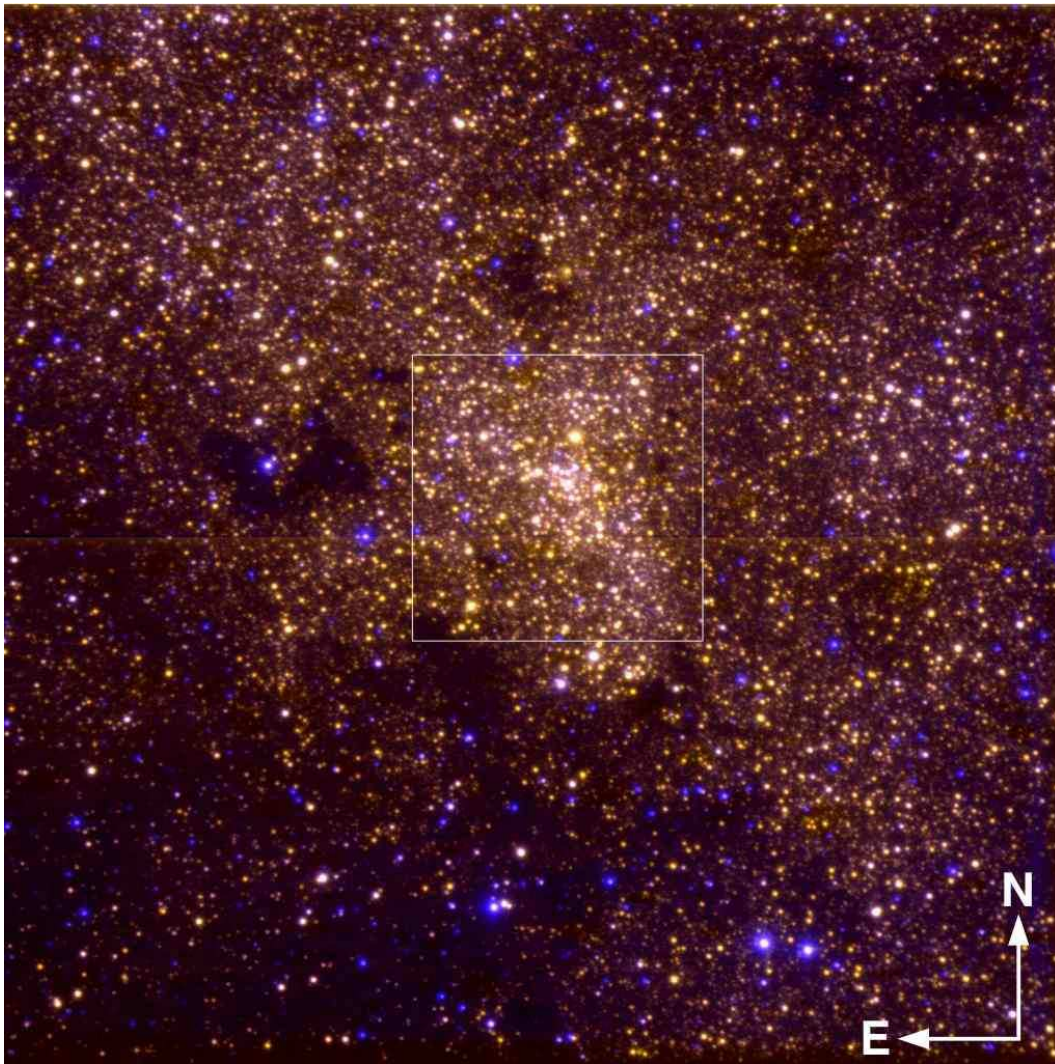
Figure 1.8:   Large scale view of the Galactic Centre, composed from ISAAC (Infrared Spectrometer And Array Camera, ESO) observations at 2.09 μm and J-band data. The image size is roughly 7×7 pc. The blue sources are foreground stars. The data shown in Figure 1.9 is taken from the box marked around the centre of the current Figure. Adapted from Schödel et al. (2007).
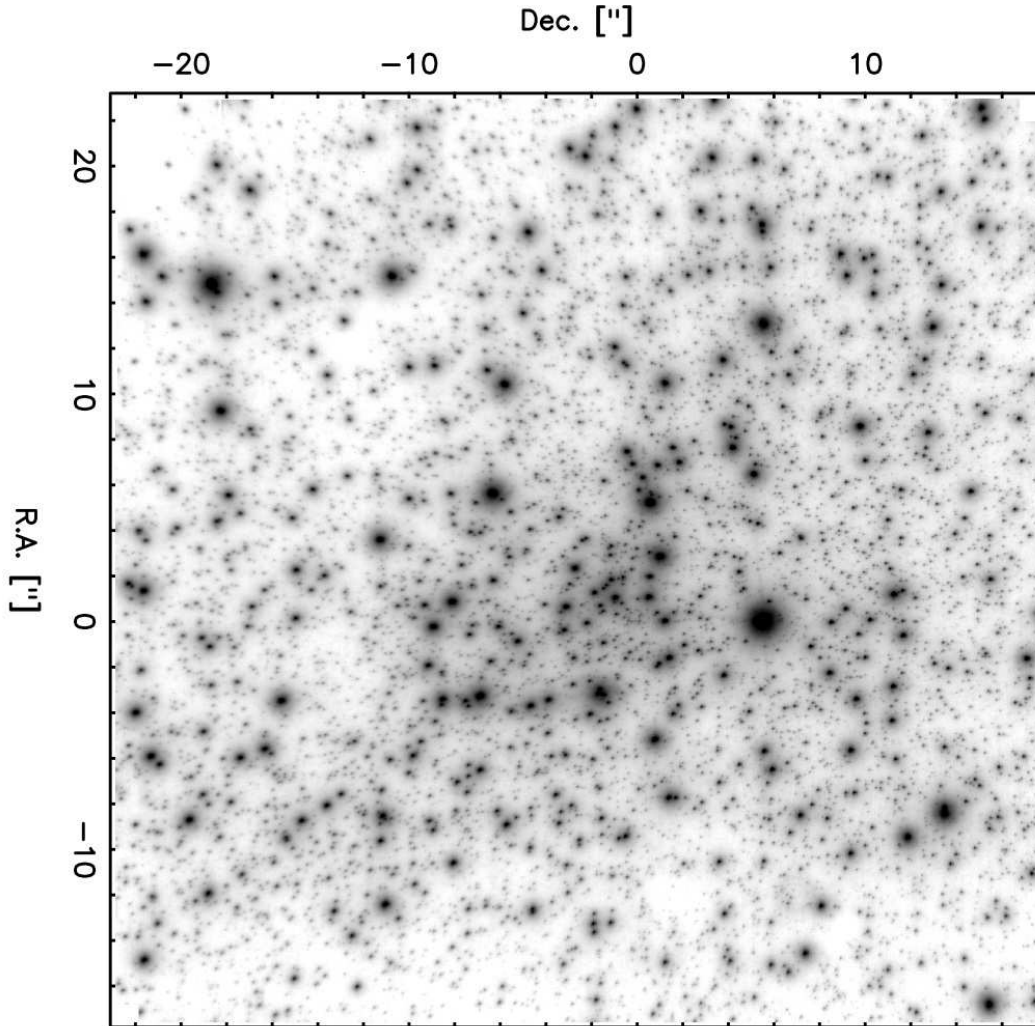
Figure 1.9: Mosaic of the cluster stars, taken at the ESO VLT using adaptive optics and the near infrared camera CONICA. Adapted from Schödel et al. (2007).

The distribution of stars can be described by a broken power law (Genzel et al., 2003):

$$\rho_\star(R) = 1.2 \times 10^6 \left(\frac{R}{0.4pc} \right)^{-\alpha} M_\odot \ \mathrm{pc}^{-3} \tag{1.1}$$

with $\alpha = 2.0$ for R $\geq$ 0.4 pc and $\alpha = 1.4$ for R $<$ 0.4 pc.

Observations indicate that the cluster is not completely homogeneous, there are density clumps detected at projected distances of 1.5 pc and 3.5 pc from SgrA* (Schödel et al., 2007). The stellar population can be well described by assuming a collection of old and metal rich stars, together with a contribution from young, early and late-type stars at the

bright end.

However there is a strong break in the stellar population within the very central parsec around SgrA*. Here the population shows a featureless luminosity function. This suggests that old and low mass stars are lacking and that the central population consists mostly of bright, early type stars which are strongly bound to the black hole.

1.1.5   Circum-nuclear Disc

19.7 µm

19.7 µm

1 pc a_1

1 pc a_2

31.5 µm

31.5 µm

1 pc b_1

1 pc b_2

37.1 µm

37.1 µm

1 pc c_1

1 pc c_2
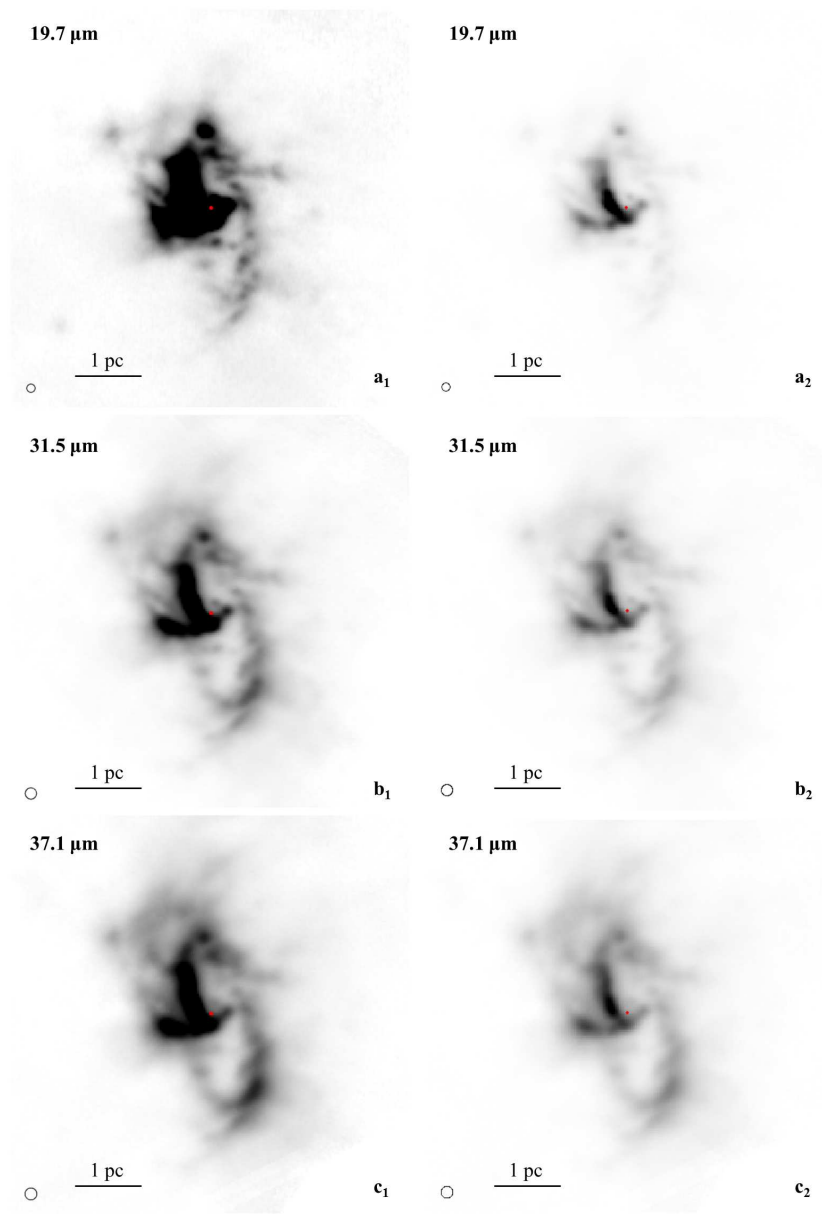
Figure 1.10:   The inner 6 pc around the black hole (marked as a red dot) taken at the wavelength shown in the top left of every subplot. The ringlike structure of the circum-nuclear disc together with the minispiral inside the central cavity of the circum-nuclear disc are visible. On the left side the images have been stretched linearly to show emission from the ring, on the right side the images have been stretched linearly to show emission from the mini-spiral. The data has been taken with the Faint Object Infrared Camera using SOFIA. The plot has been adapted from Lau et al. (2013).

Embedded into the nuclear stellar cluster and surrounding SgrA*, a large number of gas and dust clouds can be found. The kinematics and distribution of those clouds show that they are mostly contained within a very clumpy, thick and torus like structure, the so called circum-nuclear disc. The circum-nuclear disc extends from roughly 7 pc (there is still a debate if there is a real outer edge (Vollmer & Duschl, 2001)) down to 1.5 pc distance from SgrA*.

Figure 1.10 shows a recent observation by SOFIA (Stratospheric Observatory for Infrared Astronomy) of the central 6 pc region around the black hole. Inside the central evacuated region of the circum-nuclear disc the mini spiral is visible, which we will present in more detail in the next section.

The sharp inner ionised boundary at 1.5 pc is affected by the ionising radiation from the young stars within the central parsec region. The small volume filling factor of the circum-nuclear disc with clumps allows ionising radiation to travel far beyond the boundary layer. The possible large interclump velocity dispersion in the inner region implies frequent shocks and clump collisions within the circum-nuclear disc. Models hint towards circular orbits as a good first order approximation for the observed kinematics (Morris & Serabyn, 1996).

Temperature maps reveal a decreasing radial temperature gradient. The ring temperature at the inner edge is found to be around 85 K (Lau et al., 2013). The interclump medium density is found to be $\sim 10^4$ cm^{-3}, the clump density and diameter at the inner edge of the circum-nuclear disc is found to be 5 - 9 $\times 10^4$ cm^{-3} and ~ 0.15 pc. The fact that those clumps should only be able to survive half an orbit (due to tidal friction) provides an interesting problem. In the course of this thesis we had to create a computer-model of the circum-nuclear disc which encounters exactly this problem. Since there is no solution so far of how to stabilise those clumps the circum-nuclear disc was modelled as a constant density disc as a first approach.

Face on View   **Observed View**

Molecular disk
(unobserved)

Sgr A*

Emitting dust
region (CNR)

a   b
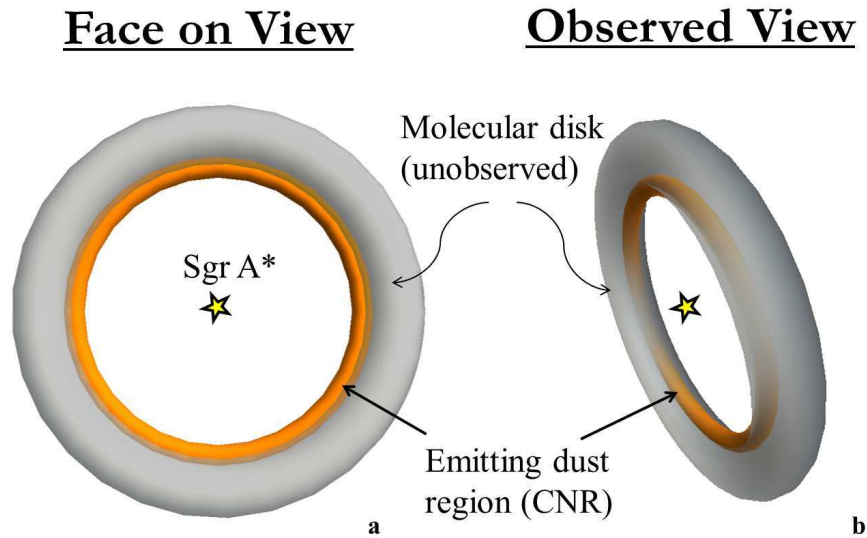
Figure 1.11: Orientation of the circum-nuclear disc within the plane of sky, adapted from
Lau et al. (2013). From earth the circum-nuclear disc is seen almost edge-on.

Figure 1.11 shows the orientation of the circum-nuclear disc within the plane of sky. The
disc is seen almost edge-on from earth. To understand how the remaining components of
the Galactic Centre region at even smaller distances from the black hole are oriented we
adapted Figure 1.12 from Paumard et al. (2006). Those components will be described in
more detail in the next sections.

In Figure 1.12 the orientation of all planar structures below 6 pc at the Galactic Centre is
shown. The black face-on circle represents the plane of sky. The black edge-on circle shows
the galactic plane together with the direction of rotation represented by the white arrow.
The stellar discs are shown in blue (clockwise disc) and red (counter-clockwise disc). The
circum-nuclear disc is marked with magenta. The two stellar discs and the circum-nuclear
disc are almost perpendicular to each other. The mini spiral northern arm is marked in
green and the mini spiral bar is marked in cyan.
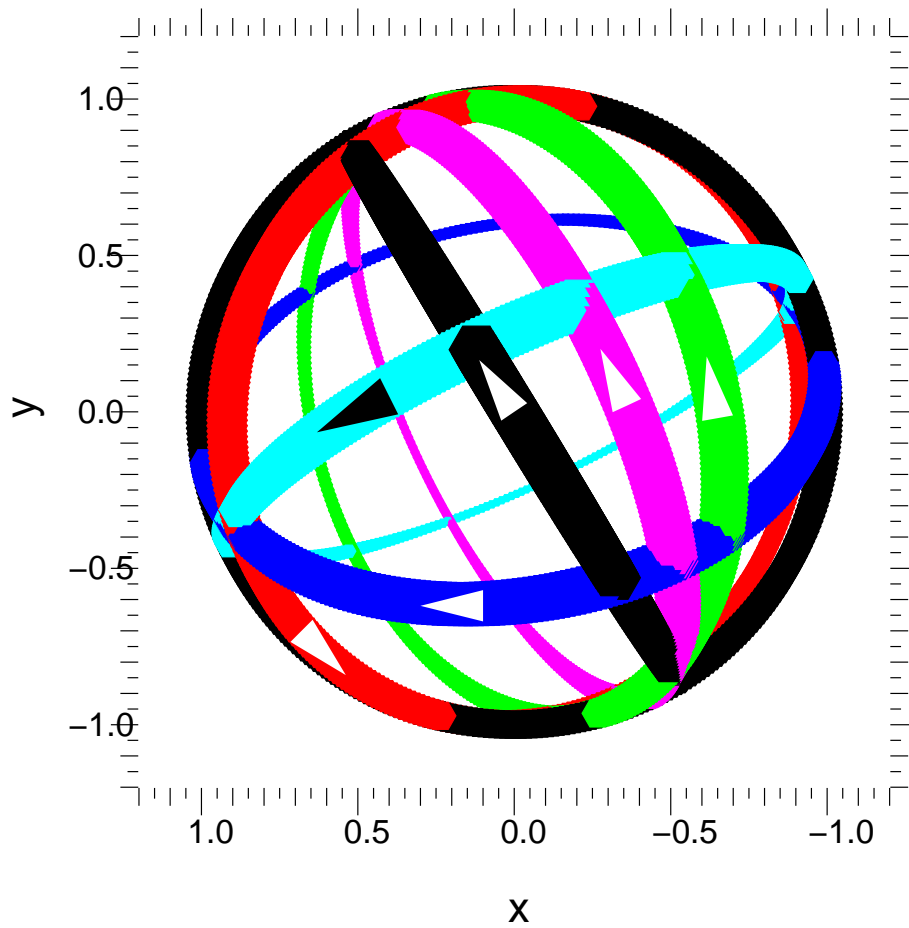
Figure 1.12: Orientation of individual planar components at the Galactic Centre in the plane of sky, adapted from Paumard et al. (2006). The black face-on circle represents the plane of sky. The black edge-on circle represent the galactic plane. Arrows always indicate the direction of rotation. The clockwise stellar disc is shown in blue and the counter-clockwise disc in red. The Northern Arm of the mini spiral is marked as green and the bar of the mini spiral as cyan. The circum-nuclear disc is marked in magenta.

1.1.6   Mini Spiral
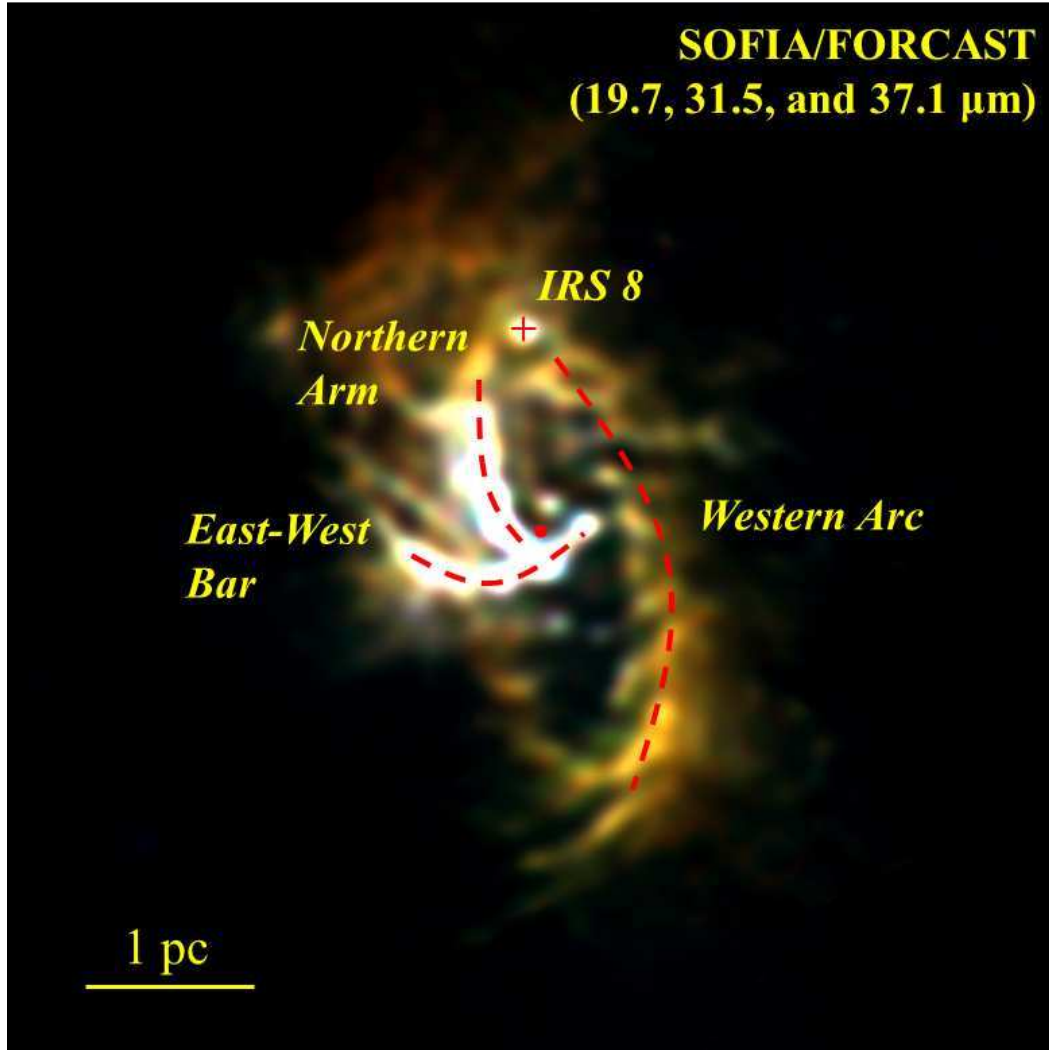
Figure 1.13:   SOFIA image of the mini-spiral, inside the circum-nuclear disc cavity taken with the FORCAST (Faint Object Infrared Camera) camera, adapted from Lau et al. (2013). The image is a combination of blue, red and green for the three wavelengths shown at the upper right. SgrA* is marked as red dot, the source IRS 8 as a red cross. The very prominent spiral arms are marked with a red dotted line.

The so called mini-spiral is a system of three ionised streams of gas within the central 3 pc around SgrA*. The arms are commonly called the Northern Arm, the Eastern Arm/Bar and the Western Arc as shown in Figure 1.13. Also visible in Figure 1.13 is a source called IRS 8 (the only source within the circum-nuclear disc) which could be a young and (possibly very) massive star (Geballe et al., 2006).
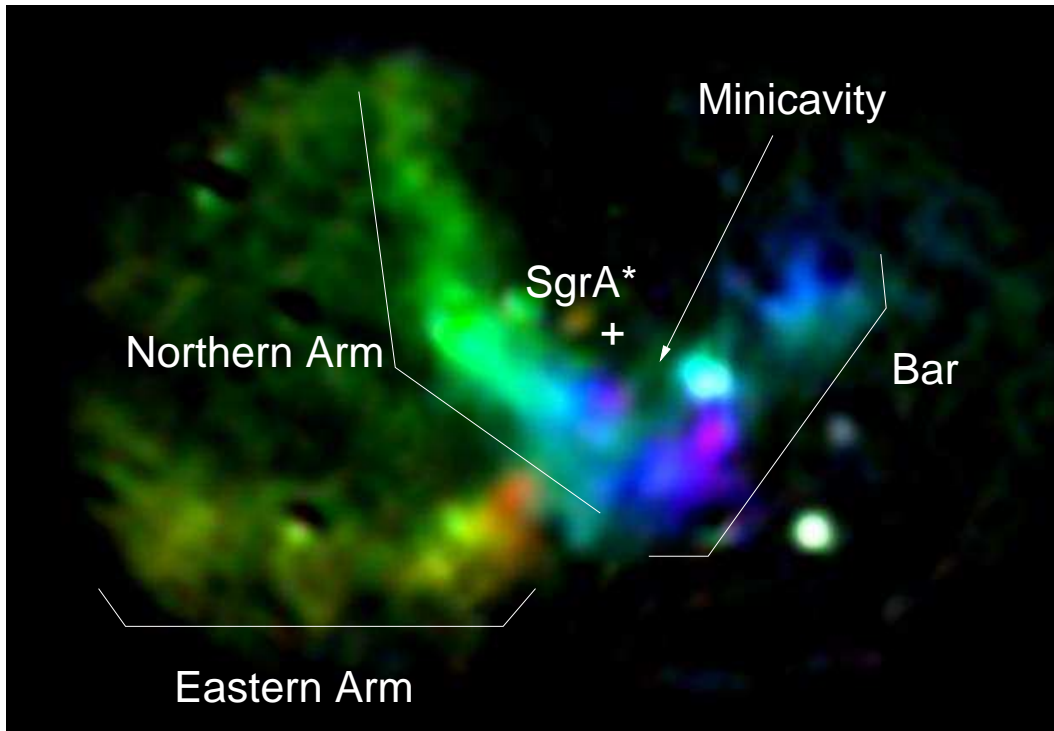
Figure 1.14: Box of the inner 2 pc region of the mini-spiral using BEAR (an imaging Fourier Transform Spectrometer) at the Canada-France-Hawaii Telescope in Brγ, between -350 (purple) and +350 km/s (red), adapted from Paumard et al. (2004). The Minicavity next to SgrA* becomes visible.

Close to SgrA* a small cavity inside the mini-spiral can be found, seen in Figure 1.14. Yusef-Zadeh et al. (2012) argue that this might be the result of a weak jet originating from SgrA*. The total mass within the mini-spiral is a matter of debate and ranges from roughly 10^2 to 10^3 M$_\odot$.
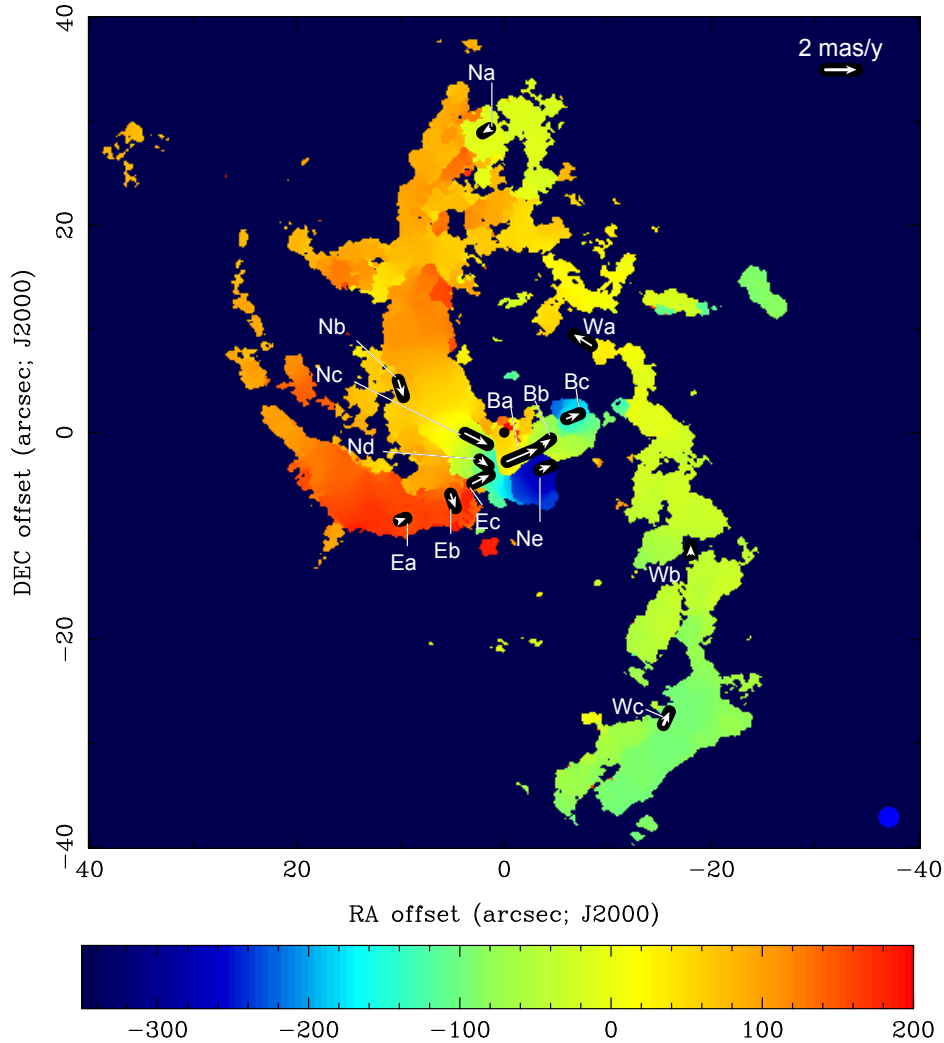
Figure 1.15:   3D velocity field of the mini-spiral in a 3 pc box obtained from VLA data, adapted from Zhao et al. (2009). The colour map shows radial velocity in km/s, whereas vectors show the mean transverse velocity of different radio components. The annotations mark the different points at which transverse velocity was measured (see Figure 18 in Zhao et al. (2009) for details). The black dot marks the position of SgrA*.

The complex velocity structure of the mini-spiral has been observed by Zhao et al. (2009). They reconstructed a 3D velocity field shown in Figure 1.15. Radial velocity is colour coded and vectors represent the mean transverse velocity component of a number of radio components within the mini-spiral. This velocity field can be modelled well using three Keplerian elliptical orbits (one for each stream). The resulting orbits suggest that the northern and eastern arm are colliding within the bar region. There are also hints from those observations that the northern arm reveals a helical structure, which suggests that

MHD (Magnetohydrodynamics) might play a role in the formation of the mini-spiral. As we will see in the second paper, similar morphologies like the mini-spiral can also be obtained within our model for the build-up of the young stellar discs.

1.1.7 Galactic Centre Stellar Discs
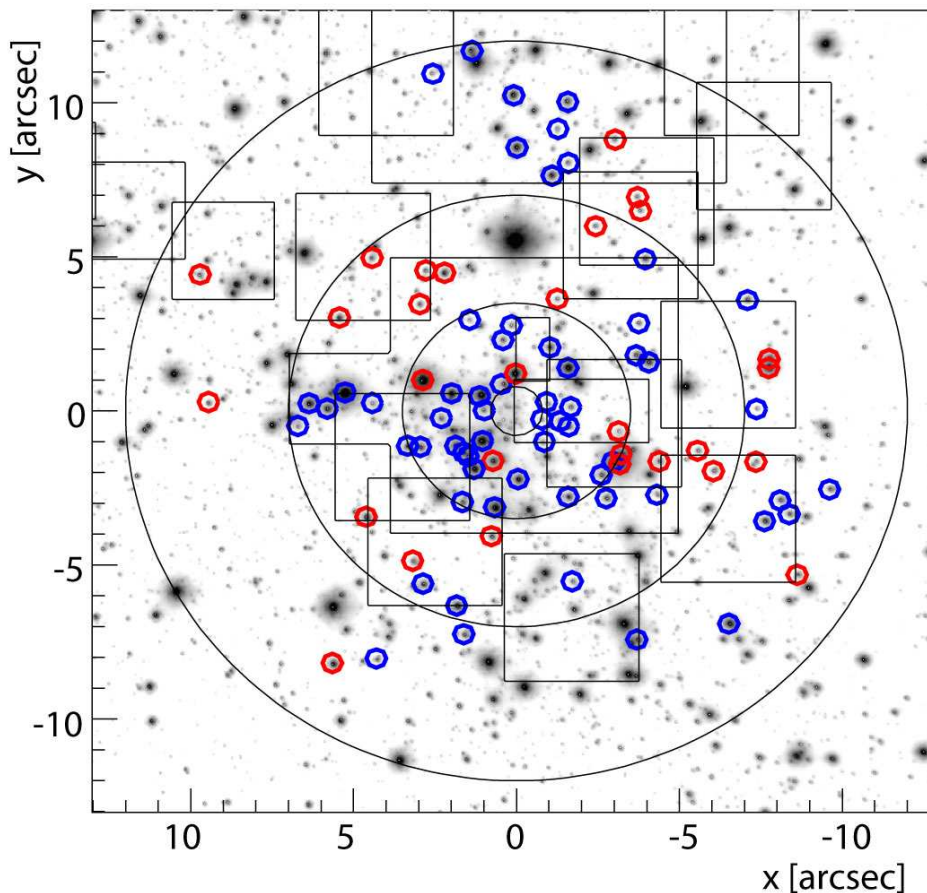
Figure 1.16: A sample of 90 Wolf-Rayet and O stars within the central 0.5 pc observed with SINFONI at the ESO/VLT, adapted from Bartko et al. (2009). Clockwise rotating stars (61) are marked in blue, counter-clockwise rotating stars (29) are marked in red.

The existence of twelve young massive O and Wolf-Rayet stars orbiting the Milky Way central black hole SgrA* was first reported in Krabbe et al. (1991). The number of O and Wolf-Rayet stars has increased over time with advances in observational techniques (especially SINFONI on the ESO VLT) and there are currently around 177 known stars (Bartko et al., 2010). The stars are found at distances of around 0.05 to 0.5 pc from SgrA* and their common age is around 6 ± 2 Myrs (Paumard et al., 2006).

Most of the stars are rotating within a well defined, clockwise rotating disc. But there is also evidence for a number of stars rotating counter-clockwise inside a second disc which
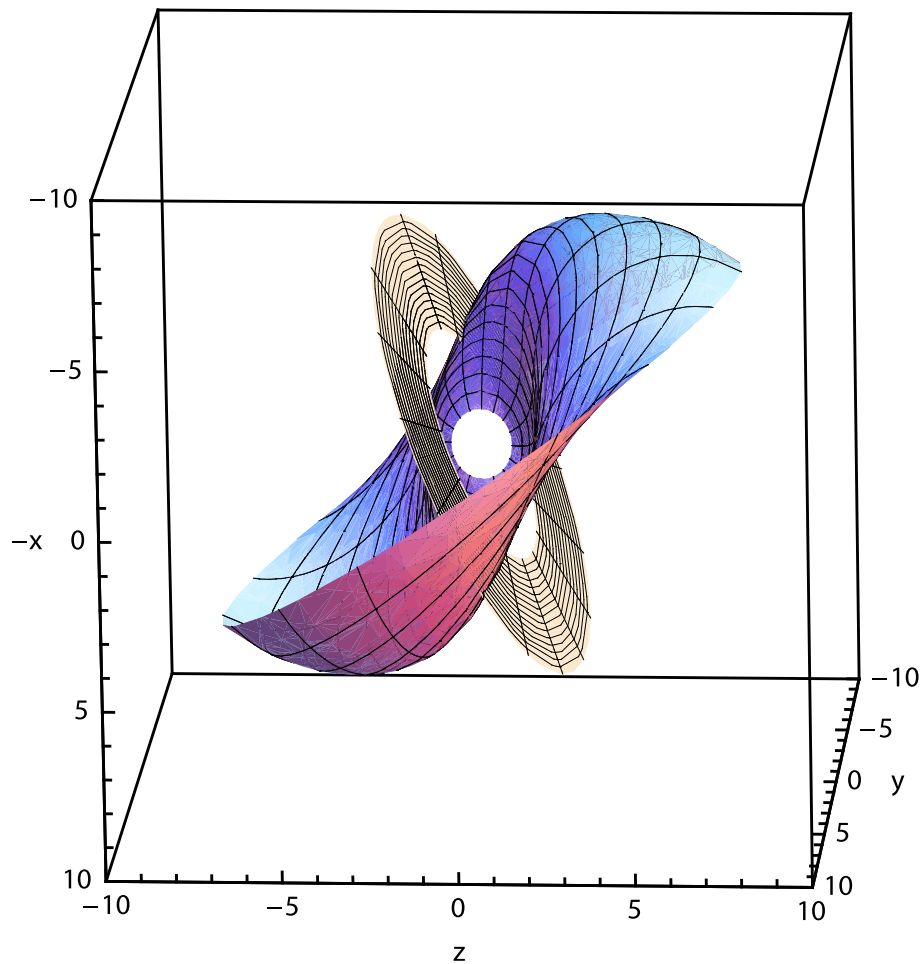
Figure 1.17: 3D representation of the fitted stellar orbits for the warped clockwise disc and the flat counter-clockwise disc. Adapted from Bartko et al. (2009).

is strongly inclined with respect to the first disc (Genzel et al., 2003; Ghez et al., 2005). Figure 1.16 shows an observational sample of 90 of those stars, divided into clockwise rotating stars (blue) and counter-clockwise rotating stars (red).

The statistical significance of the second, counter-clockwise rotating disc is questioned in Lu et al. (2009) using a sample of 6 counter-clockwise rotating stars and additional lower quality data from Paumard et al. (2006).

In Bartko et al. (2009) the authors improved the observational data of Paumard et al. (2006) (reducing the uncertainties in proper motion by a factor of four) and increased the sample of counter-clockwise stars to 29. They find (using simulations) that there is a slight chance of 2% for an isotropic distribution, confirming a disc-like distribution of the counter-clockwise stars at a confidence level beyond 98%.

They conclude that the significance of the counter-clockwise system is about as large as can be reasonably expected on the basis of the small numbers of stars contained in it, as well as its observed azimuthal and broader angular distribution of stars.

Figure 1.17 shows the best fit disc of Bartko et al. (2009) using the stellar orbits of the clockwise disc, which turns out to be moderately warped and the flat counter-clockwise disc (fitted by using the innermost 16 counter-clockwise stars).

The IMF of the disc stars is shown to be extremely top-heavy (Bartko et al., 2010), however a more recent study (Lu et al., 2013) finds that the IMF is not as extreme as in Bartko et al. (2010) but still top-heavy compared to a standard Salpeter-slope.

Figure 1.18 shows the number of stars plotted against K-band luminosity for three different radial bins. The red triangles (scaled by a factor of 0.05) show the radial bin below 0.05 pc from SgrA* and thus represent the S-stars. The blue circles show the radial bin between 0.05 and 0.5 pc and thus represent the stellar discs. Finally the black stars show the radial bin at distances larger then 0.5 pc and represent field stars. The distinct distribution of the stellar discs can be fitted well with a top heavy IMF (assuming an age of 6 Myrs) power law:

$$\frac{dN}{dm} \propto m^{-0.45 \pm 0.3}$$

The similar distributions of field and S-stars can be both fitted with a power law

$$\frac{dN}{dm} \propto m^{-2.15 \pm 0.3}$$

which is consistent with a standard Salpeter IMF. The surface density of stars in the clockwise disc can be best fit by a power law:

$$\Sigma(R) \propto R^{-1.5 \pm 0.2}$$

The mean eccentricity of the clockwise system is measured to be around 0.34 ± 0.06 (Bartko et al., 2009) and the combined mass of both discs is 1.5×10^6 M$_\odot$. Since the stars inside those discs are all very similar in type and age, it is generally assumed that they all formed at the same time in a single, short time event around 6 Myrs ago.

The young age of the disc stars and also the S-stars (placed even closer to SgrA*) which we will discuss in the next section, presents a puzzle. Close (~ 1 pc radius) to the black hole tidal forces are very strong, ripping apart even dense molecular clouds without problems. Thus one would expect that if you find stars close to the black hole, they must have formed further away and then migrated close to SgrA* by some mechanism since standard (molecular cloud collapse) star formation does not work. This however leads to problems since the migration process will have to be very quick due to the age of the stars (such a
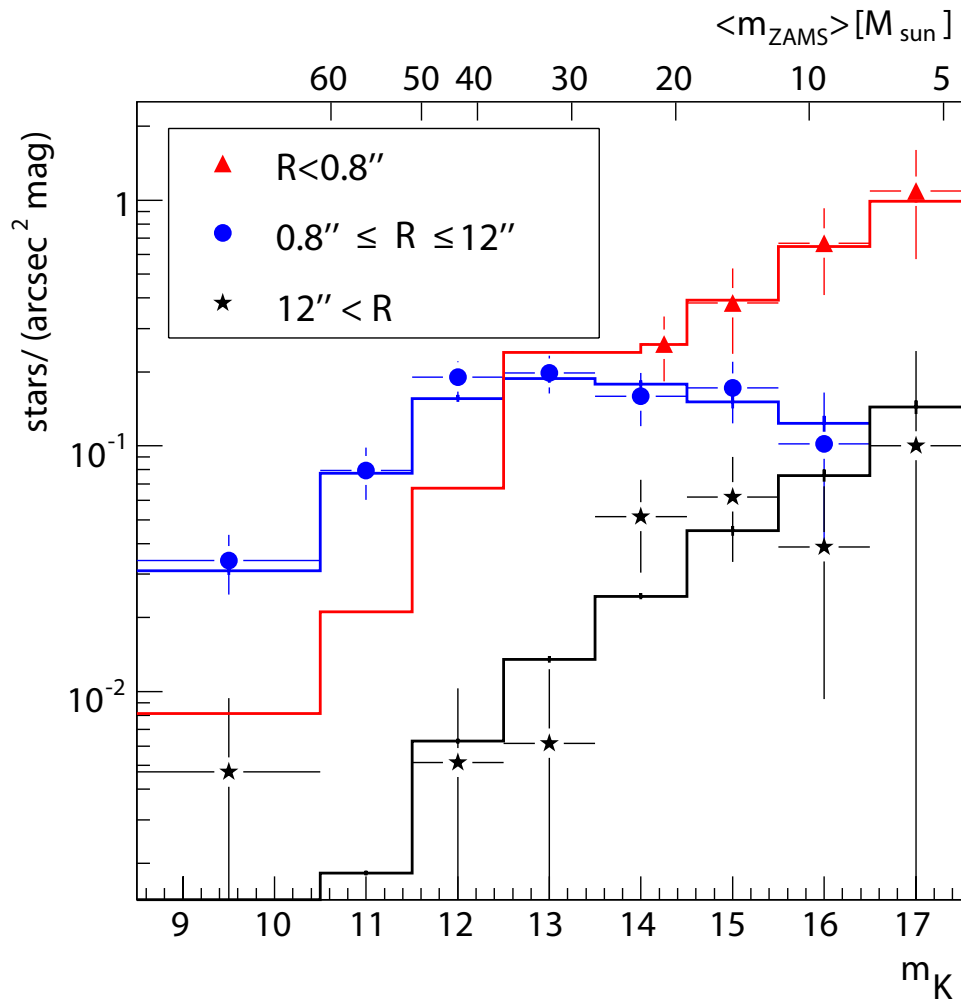
Figure 1.18:   Number of stars against K-band luminosity, adapted from Bartko et al. (2010). The red triangles represent the S-stars at distances below 0.05 pc from SgrA* (scaled by a factor of 0.05), the blue circles represent the stellar discs at 0.05 pc to 0.5 pc distance from SgrA* and the black stars represent field stars at distances larger than 0.5 pc. The S-star and the field star population show a very similar distribution, whereas the stellar discs show a very distinct distribution which can be fit by a top-heavy IMF.

migration model will be discussed in section 1.2.1).

The question is then how these young stars formed, this problem is also known as 'The Paradox of Youth'. One of the main goals of this work is to address this paradox. The results will be presented in the first two papers. Also the important task to understand the unique top-heavy IMF of the disc stars was one of the goals of this work.

1.1.8   S-Stars
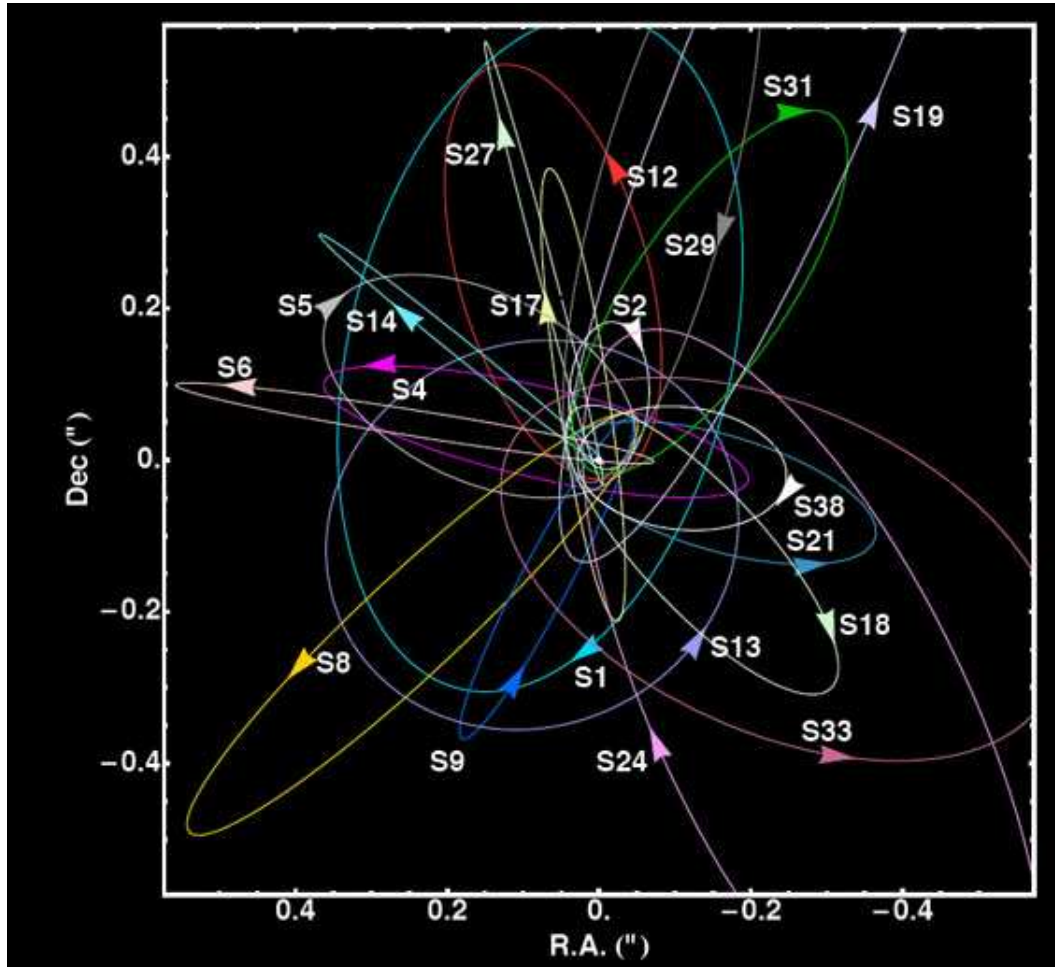
Figure 1.19:   Orbits of the S-stars within the central 0.05 pc around SgrA*. The small orbit of the famous S2 star which was used to constrain the mass of SgrA* can be seen. Until the discovery of a new S-star in 2012, S2 had the smallest orbital period of all S-stars with only ∼ 15.5 years (Schödel et al., 2002). Credit: Gillessen et al. (2009a).

Inside the inner edge of the stellar discs observations show one more cluster of young stars, which are mainly B-type stars. These so called S-stars reside in a spherical cluster and are the closest stars next to the black hole. Eccentricities are rather large for the S-stars (Schödel et al., 2003). They provide an excellent laboratory for studying SgrA*, as already pointed out in the introduction.

Figure 1.19 shows the orbits of a number of S-stars, especially the famous S2 star which was used to constrain the mass of SgrA* and which has the smallest pericentre distance (17

light hours) of all S-stars and had the shortest orbital period of only ~ 15.5 years (Schödel et al., 2002) until the discovery of a new S-star in 2012.

In 2012 the S-star called S0-102 was found (Meyer et al., 2012) with an even smaller orbital period of ~ 11.5 years. Explaining the origin of the S-stars provides a similar puzzle like the origin of the stellar discs. One idea is that the S-stars originate from the inner edge of the stellar discs and that relativistic (Lense-Thirring) precession (combined with scattering by an intermediate mass black hole) tilted the orbits into the observed spherical distribution. There is a number of other formation scenarios (Perets et al., 2009; Löckmann et al., 2008, 2009; Genzel et al., 2003), but so far there seems to be no strong consensus as to which model is favoured.

1.1.9 G2 Cloud

The recent detection of a small gas cloud called G2 (Gillessen et al., 2012) which is on an almost radial orbit towards the central black hole has sparked a lot of research interest. The long term evolution of G2 will depend critically on the properties of the accretion zone of SgrA*, thus providing an excellent probe to study the immediate environment of SgrA* (Burkert et al., 2012). Figure 1.20(c) shows G2 approaching SgrA* (marked as white cross) over the last years.
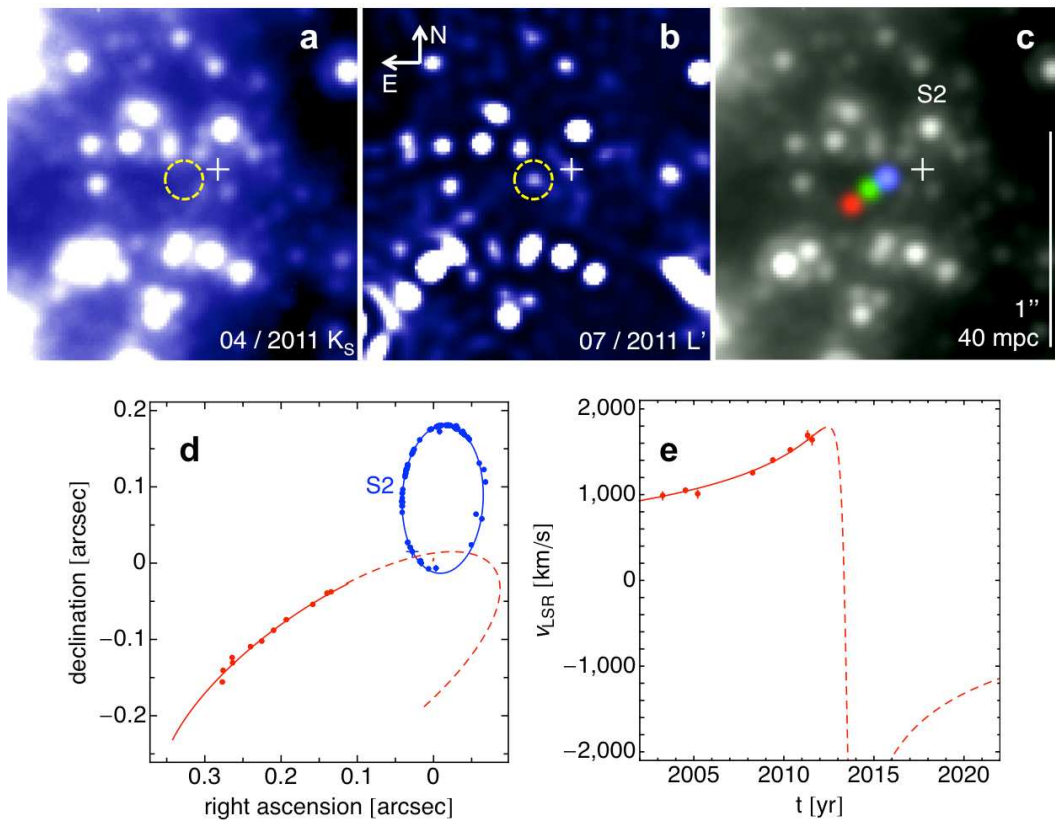
Figure 1.20:   VLT images of G2, adapted from Gillessen et al. (2012). The object is visible in L'-band (b) but not in K_S-band (a) which indicates that it is not a star, but a dusty cloud at a temperature around 550K. Panel (c) shows data from 2004.5 (red), 2008.3 (green) and 2011.3 (blue) overlaid onto a K_S-band image from 2011, showing that the cloud is moving towards SgrA* (marked as white cross). The fitted orbit is shown in panels (d) and (e).

The cloud's mass is only around 3 earth masses and it already starts stretching around the pericentre of the orbit, which is ~ 20 light hours away from the black hole according to the newest observational data of Gillessen et al. (2013b).

A number of simulations have been performed (Anninos et al., 2012; Schartmann et al., 2012) trying to predict the future evolution of G2 and trying to validate the compact source scenario (Ballone et al., 2013) which states that G2 actually is only the hull of a small compact object. Models for the origin of G2 have been proposed in a number of papers (Murray-Clay & Loeb, 2012; Schartmann et al., 2012; Scoville & Burkert, 2013). We later present simulations of the evolution of G2 we performed in the course of this thesis. However due to restrictions with the standard formulation of the SPH simulation technique we use, a number of problems arise which we discuss in detail.

Using a grid based code, which is better suited for the extreme density contrasts one has to deal with when modelling the Galactic Centre environment and the G2 cloud, we performed similar simulations together with improved models for G2 using the PLUTO code. The resulting paper is present as the third paper of this thesis.

1.1.10   Central Black Hole SgrA*

In 1969 Lynden-Bell (1969) proposed that the centres of most galaxies could harbour a supermassive black hole. Given enough resolution one could test if the orbits of objects close to the nucleus are dominated by a mass concentration that can not be explained other than being a black hole. Obviously this test is hard for very distant galaxies. The most promising candidate for such a test hence is the nucleus of our Milky-Way, although the direct view towards the central region is obscured by dust.

VLBI observations of the NGC 4258 nucleus from Miyoshi et al. (1995) gave the first evidence that there is a central mass concentration that can not be explained with alternative models like clusters of neutron stars or white dwarfs.

As already pointed out in 1.1.1, the object which drives the source SgrA* at the centre of the Milky Way Galaxy is now known to be a black hole beyond any reasonable doubt after 16 years of observations of the S-star S2 close to SgrA*.

The current mass estimate is $4.31 \pm 0.06 \times 10^6$ M$_\odot$ (Gillessen et al., 2009b). Determining the black hole spin proves to be rather hard and the results are plagued with large uncertainties (Broderick et al., 2009, 2011; Aschenbach, 2006; Török, 2005).

However the general consensus seems to be that the black hole spins quite rapidly with a spin parameter a > 0.9. Also the spin axis orientation is quite uncertain, here newer observations of a possible jet outflow from SgrA* could lead to a more direct measurement of the black hole spin axis (Yusef-Zadeh et al., 2012).

For a long time there have been speculations that a number of intermediate mass black holes could orbit the supermassive black hole. In Maillard et al. (2004) the authors show some proof that a system of 7 stars close to the supermassive black hole is orbiting a common, unseen central object, which itself orbits the supermassive black hole. This at least hints towards the existence of such an intermediate mass black hole.

The GRAVITY instrument (Eisenhauer et al., 2008, 2011) planned by a collaboration lead by F. Eisenhauer at MPE has the goal to empirically test if SgrA* really is a black hole. It will combine all four 8 metre telescopes at the VLTI and reach a 10μas astrometric precession, which will allow to measure orbital motions more accurately than ever before.

Direct imaging of the event horizon of SgrA* is currently only possible through means of computer simulations. Using Ray-Tracing techniques within the Kerr metric of a rotating black hole one can produce images of how observations of the black hole accretion disc would look like. The "shadow" of the black hole (due to light bending backwards into the black hole and never reaching the outside world) is visible as a central dark area in the resulting Ray-Tracing images.

Figure 1.21 shows the resulting Ray-Tracing image for a rotating black hole, adapted from Müller & Camenzind (2004). Shown is the redshift factor g for the emitted light of a Kerr black hole accretion disc. A factor of g > 1.0 corresponds to blueshift, a factor of g < 1.0 to redshift. The shadow of the black hole can be seen at the centre.
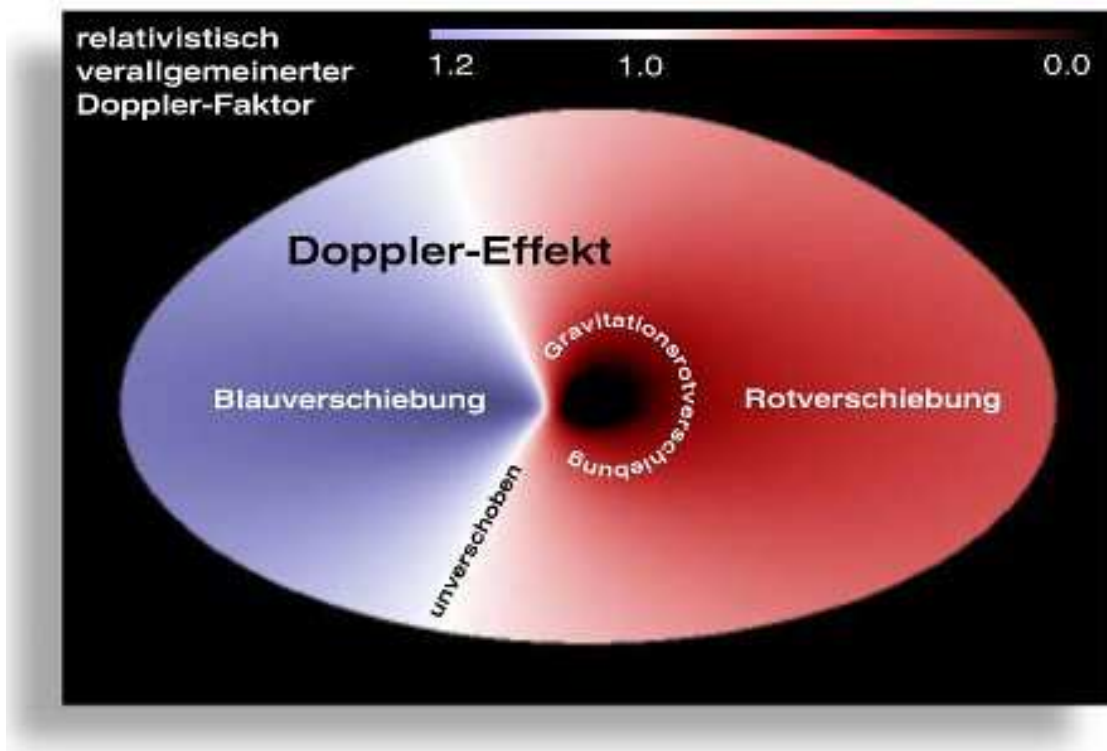
Figure 1.21:   Redshift factor g for the light emitted from the Kerr black hole accretion disc. A factor of g > 1.0 means the light is blueshifted, a factor of g < 1.0 means the light is redshifted. Adapted from Müller & Camenzind (2004).

1.1.11   Magnetic Fields in the Galactic Centre

In general, magnetic fields play an important role in the physics of the ISM. They help to stabilise the ISM against gravity and also influence the dynamical behaviour of the ISM. The MRI (magneto-rotational instability) helps to drive the transport of matter and angular momentum in a black hole accretion disc.

In the optical, the polarisation of light from stars by dust grains in the line of sight can be measured. Because of the elongated structure of dust grains they can align perpendicular to the magnetic field lines. Due to the obscuration of the Galactic Centre the fact that the dust grains also emit polarised infrared emission can be used to measure the magnetic field within the Galactic Centre. Other methods to measure the magnetic field include measurements of the Zeeman splitting of radio spectral lines and synchrotron emission due to the movement of cosmic-ray electrons within magnetic field lines.

The polarisation vector is normally perpendicular to the field orientation. However the polarisation vector can be rotated on the path to the observer by Faraday rotation. This requires a magnetised plasma in the line of sight. The degree of rotation is determined by several factors, including the strength of the magnetic field along the line of sight. If the field points towards the observer, the polarisation vector is rotating counter-clockwise, if the field points away from the observer the polarisation vector rotates clockwise. Combining the polarisation measurements together with the line of sight measurements obtained from Faraday rotation yields the 3D structure of the magnetic field.

On large scales the total magnetic field strength can be measured relatively accurately using the intensity of the total synchrotron emission and assuming equipartition between magnetic fields and cosmic rays. Typical values for the magnetic field strength of spiral galaxies would be 5×10^{-6} to 5×10^{-5} G (Widrow, 2002). The Milky way mean field strength is around 6×10^{-6} G near the sun and increases to 20-40 $\times 10^{-6}$ G near the Galactic Centre. The manifestation of the magnetic field within the Galactic Centre region is demonstrated by Non-thermal Filaments (NTFs) within the IMF, which are unique to the Galactic Centre. Examples of those structures can be seen in Figure 1.1
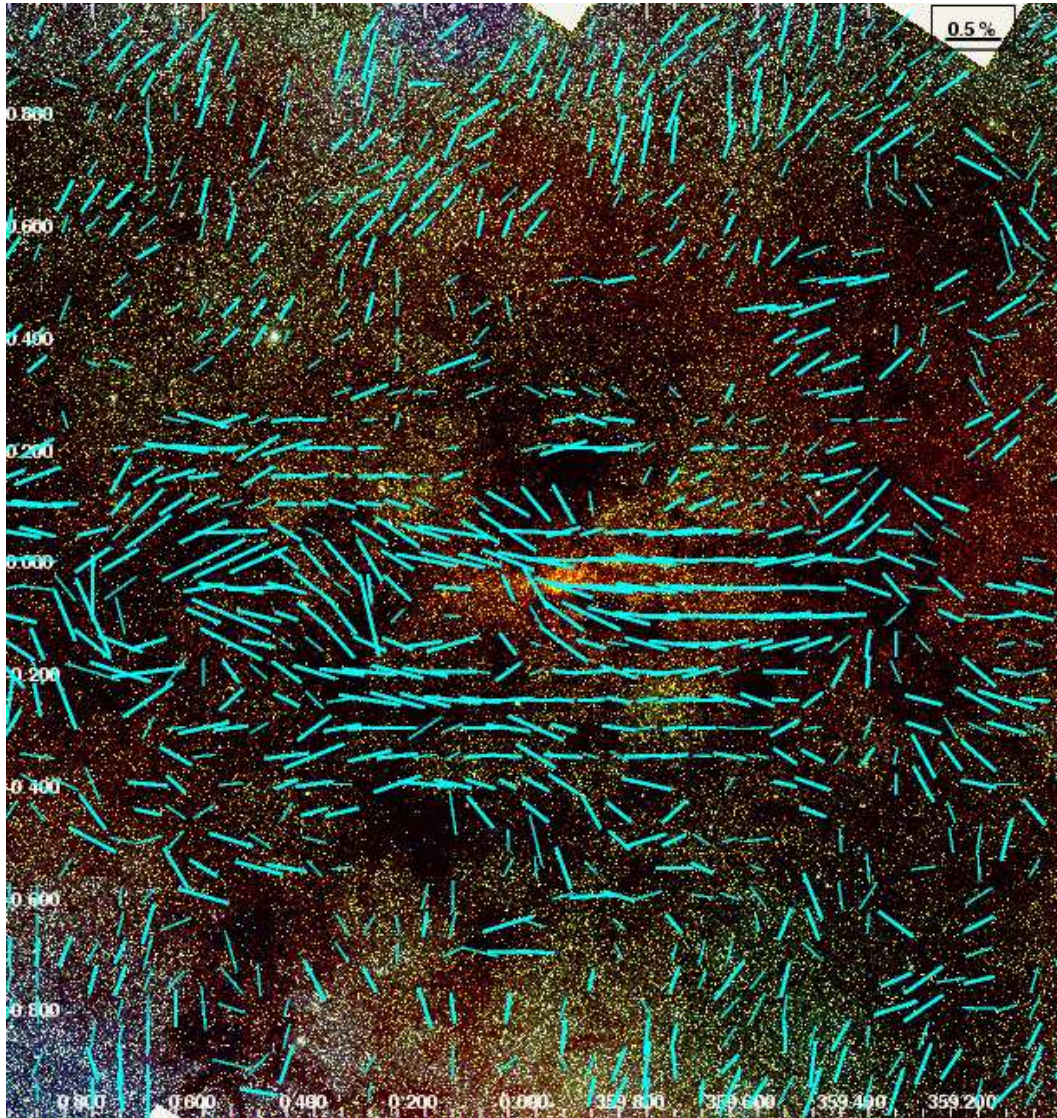
Figure 1.22:   Mosaic of the ~ 300 pc Galactic Centre region taken with the IRSF telescopes NIR camera SIRIUS, adapted from Nishiyama et al. (2010). Overlaid on the J (blue), H (green) and K_S (red) band image are the K_S band polarisation vectors, with length indicating the degree of polarisation.

Figure 1.22 shows the magnetic field distribution within the central ~ 300 pc around SgrA*, taken from Nishiyama et al. (2010). The yellow blob at the middle of the picture is the nuclear starcluster (see section 1.1.4). The field configuration depends on the distance from the Galactic plane (y-axis) and seems to be homogeneous along Galactic longitude (x-axis), thus indicating a toroidal field configuration for the central part of the field.

The magnetic field strength within 27 individual clouds of the Milky Way has been mea-

sured by Crutcher (1999). It can rise up to several 100×10^{-6} G. The results show that magnetic pressure plays an important role in many clouds and that it can even dominate over thermal pressure in many cases.

1.2   Origin of the Galactic Centre Stellar Discs

In this section we will summarise the work already done on the "Paradox of Youth". We present different models that try to explain the formation of the young stellar discs at the Galactic Centre and briefly summarise our own models which will be fully presented in the first two papers of this thesis.

1.2.1   Stellar Cluster Model

The first theoretical approach to explain the formation of a small (sub-parsec) disc of stars close to the Galactic Centre black hole comes from Gerhard (2001). Because of the strong tidal field in the Galactic Centre region the author assumes that in-situ formation of these stars is problematic. In his model a massive and young star cluster spirals into the Galactic Centre, looses most of its mass on the way and then forms a disc of stars around the black hole.

Examples for nearby clusters are the Arches and the Quintuplet cluster which are at a distance of about 30 pc from the Galactic Centre. The orbit of such a heavy cluster evolves due to dynamical friction with field stars, given a dense enough stellar system (Tremaine et al., 1975). Calculations show that at a cluster mass of 10^6 M$_\odot$ and an initial distance of 30 pc, the cluster can spiral into the centre within the lifetime of most of its massive stars ($\sim$ 3 Myr). For a smaller initial distance of 10 pc, the cluster mass can be reduced to around 10^5 M$_\odot$. Since the outer parts of the cluster are stripped, only the core survives and forms the stellar disc around the black hole. The required core density to explain the observed stellar disc is very high with $\rho_{\mathrm{core}} = 2 \times 10^7 \; \frac{\mathrm{M}_\odot}{\mathrm{pc}^3}$.

Simulations carried out by Kim & Morris (2003) and McMillan & Portegies Zwart (2003) to study the estimates of Gerhard (2001) show that only extreme parameters lead to the formation of a system similar to the observed disc. The cluster has to be very massive ($> 10^6$ M$_\odot$) and only a low number of core stars ends up inside the final disc. Also the system needs extreme fine-tuning to end up in the desired configuration. For a smaller cluster mass ($\sim 10^5$ M$_\odot$) the number of stars ending up inside the disc can be higher, but the required core density is unrealistic.

1.2.2 Accretion Disc Origin

An alternative explanation for the origin of the stellar disc around the Milky Way black hole quickly gained popularity and now seems to be widely accepted as the origin of the disc stars. In Levin & Beloborodov (2003) the authors suggest a compact, self-gravitating accretion disc as the origin of the disc stars.

From the orbits of the 13 known stars back in 2003, a sample of 10 clockwise rotating stars is shown to move within a common plane. The disc is found to be rather thin, with a half-opening angle that does not exceed 10°. The proposed origin of such a disc could be a dense gaseous accretion disc formed by an infalling molecular cloud which is tidally disrupted and captured by the black hole. Since there is no accretion disc observed at the Galactic Centre currently, the disc itself must have been accreted by the black hole and/or destroyed by the star formation event and thus is no longer visible.

The accretion disc model offers a number of properties that are compatible with observations of the disc stars. The properties of the clockwise-disc presented in 1.1.7 (eccentric, top-heavy IMF) can be reproduced quite well with simulations of fragmenting accretion discs (Nayakshin & Cuadra, 2005; Alexander et al., 2008).

The authors of Alexander et al. (2008) showed that in an eccentric accretion disc, the formation of low mass clumps can be suppressed due to tidal disruption during pericentre passage. Also an eccentric accretion disc can be heated during pericentre passage of the gas, leading to a large Jeans length and thus higher mass clumps. The suppression of low-mass clumps leads to a top-heavy IMF in the formed stars.

The accretion disc origin scenario has been first tested by Nayakshin & Cuadra (2005) and the authors conclude that the origin from a self-gravitating accretion disc is very likely. The minimum required mass for such an accretion disc to explain observations is estimated to be around 10^4 M$_\odot$. Precession due to self-gravity sets an upper limit of 10^5 M$_\odot$ on the total mass of the stellar system.

1.2.3   Forming the Progenitor Accretion Disc

The next step was to explain the origin of the compact, self-gravitating accretion disc itself. Since the disc stars are all almost the same age (6 ± 2 Myrs) a quick one time deposit of a large amount of gas was favoured. This would require a molecular cloud of several 10^4 to 10^5 M$_\odot$ to fall into the central region.

This model has been simulated by several groups (Bonnell & Rice, 2008; Alig et al., 2011; Mapelli et al., 2012; Lucas et al., 2013) and it has been concluded that a cloud of around 10^5 M$_\odot$ is able to produce a compact self-gravitating accretion disc which can produce a top-heavy clump mass function.

However the cloud model requires some extreme parameters for the cloud which are very unlikely. The cloud needs to be on an extremely eccentric, almost radial orbit towards the black hole. Since there is no large ($> 10^5$ M$_\odot$) reservoir of gas in the inner few parsec, the cloud must originate from further out.

The cloud infall model also has the problem that it can only explain the formation of a single disc. Two counter-rotating gaseous accretion discs sharing the same volume can not co-exists without destroying each other (Nixon et al., 2012). To explain the formation of a second disc one would require a second cloud falling in after a short time with opposite angular momentum but the very same unrealistic infall parameters as the first cloud, which makes the whole scenario very unlikely. This argument has also been made in Lu et al. (2009) to strengthen the position that only the existence of a single stellar disc would be preferable since no second star formation event would then be required.

One way to deflect a cloud into the central region and to reduce its angular momentum would be to assume the collision of two clouds further away from the central parsec region. This has been tested in Hobbs & Nayakshin (2009) and the authors show that this leads to two streams of gas, forming an inner compact accretion disc together with an outer counter-rotating ring of gas. This already shows that since some mechanism is required to deflect a cloud and reduce its angular momentum we would rather expect streams of gas falling into the central region as opposed to a single compact cloud.

1.2.4   Single Cloud infall
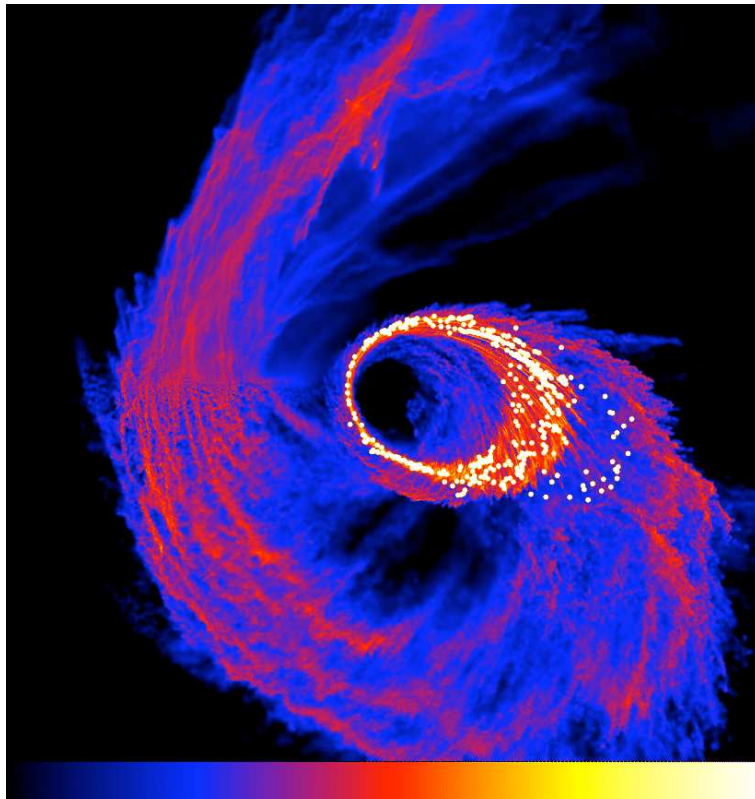
Figure 1.23:   Stellar disc forming during the infall of a 10^4 M$_\odot$ cloud onto a 10^6 M$_\odot$ black hole, adapted from Bonnell & Rice (2008). Shown is a region of 0.5 pc around the black hole, colour encodes surface density ranging from 0.1 g/cm^2 to 1000 g/cm^2 (logarithmic). The stars have major axes between 0.11 and 0.19 pc.

The first simulations to explain the origin of the massive accretion disc that produced the stellar discs have been performed by Bonnell & Rice (2008) using smoothed particles hydrodynamics. The model assumes the collision of a 10^4 M$_\odot$ cloud with a 10^6 M$_\odot$ black hole and the collision of a 10^5 M$_\odot$ cloud with a 3×10^6 M$_\odot$ black hole. The clouds are initially placed at a distance of 3 pc from the black hole and have impact parameters of 0.1 pc. Initial temperature was set to 100 K, mimicking the UV background heating due to the cluster stars.

Dense fragments (many particles) are replaced by a single massive so-called sink particle, which is still able to accrete gas, to speed up the simulation. The resulting disc from the 10^4 M$_\odot$ cloud can be seen in Figure 1.23. The logarithmic surface density in a region of 0.5 pc around the black hole is shown. Stars are quickly forming inside a small disc.
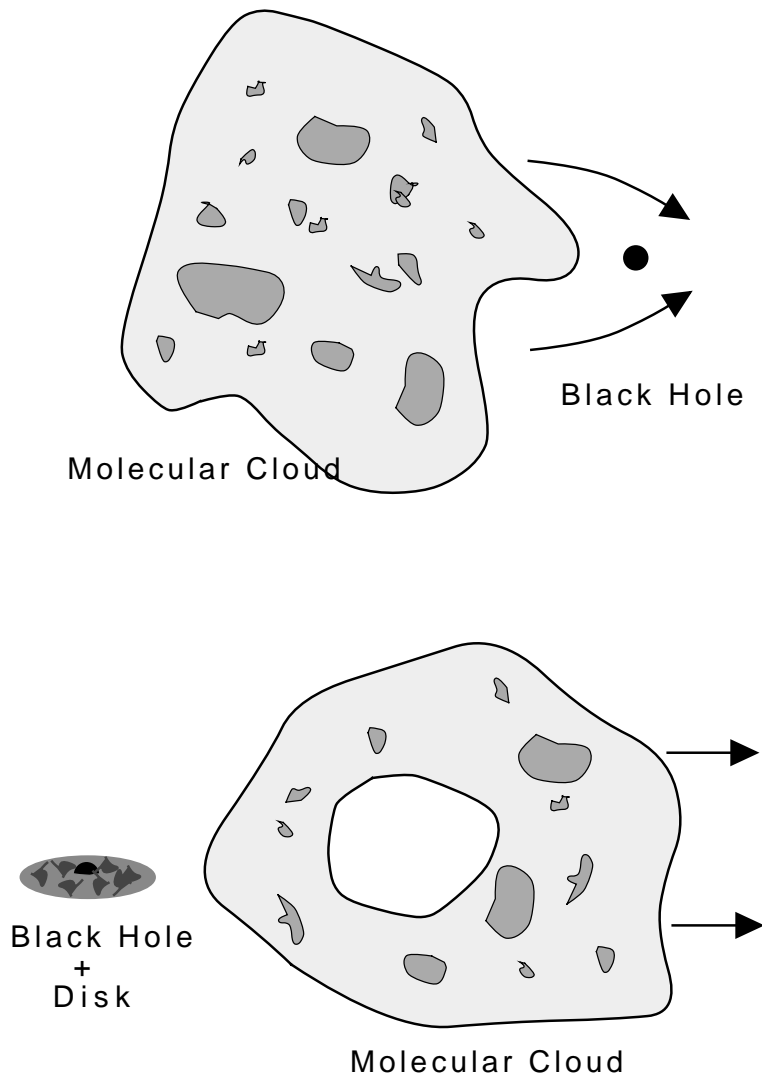
Figure 1.24:   Direct collision of a cloud with a black hole, adapted from Wardle & Yusef-Zadeh (2008). After the redistribution of angular momentum a compact accretion disc is left around the black hole.

Both initial cloud masses lead to the creation of several hundred stars. The IMF in the case of the 10^4 $M_\odot$ cloud shows a normal Salpeter slope. However the 10^5 $M_\odot$ cloud produces two distinct populations of stars, with one of them showing a top-heavy distribution.

Another scenario which has been proposed is the direct collision of a single cloud with the black hole (Wardle & Yusef-Zadeh, 2008). In this scenario parts of the cloud overlap the black hole. This leads to two streams of gas around the black hole, which have opposite angular momentum. Downstream, at the collision point, angular momentum can be redistributed very efficiently so that the gas can settle into a closed orbit around the black hole. This scenario has the advantage that the cloud does not have to be on a bound, closed orbit around the black hole from the beginning. Figure 1.24 illustrates the idea of this scenario, which we adapted from Wardle & Yusef-Zadeh (2008). Our simulations of this scenario are presented in the first paper of this thesis.

A similar study to Bonnell & Rice (2008) has been performed by Mapelli et al. (2012). The authors also simulate two initial cloud masses of 4.3×10^4 $M_\odot$ and 1.3×10^5 $M_\odot$ falling onto a 3.5×10^6 $M_\odot$ black hole. The study compares isothermal and adiabatic simulations with radiative cooling. They confirm that a rather high mass cloud of 10^5 $M_\odot$ is needed to reproduce a top-heavy IMF. They also find from the isothermal simulations that a local gas temperature > 100 K is necessary to produce a top-heavy IMF.

All these scenarios are still plagued by the problem that they can only explain the formation of a single disc. Very recently this problem has been addressed by Lucas et al. (2013). The authors still assume the infall of a single cloud, which again needs to be on a nearly radial path towards the black hole. The 2×10^4 $M_\odot$ cloud is prolate and oriented perpendicular to the orbital plane. The spread of angular momentum during the infall leads to the creation of two misaligned discs, one disc at 0.3 pc and another disc at 0.5 pc distance from the black hole. Again, the IMF can be shown to be top-heavy. Figure 1.25 shows the resulting two stellar discs created by the misaligned streamers.
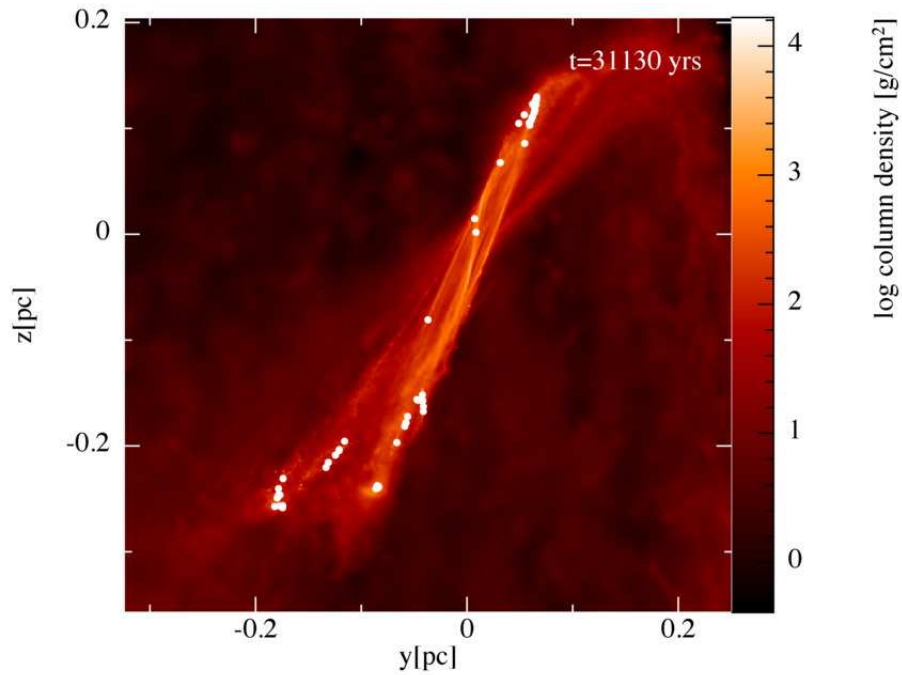
Figure 1.25:   Surface density for a simulation showing two populations of stars (white dots) separated by 17 degrees due to misaligned streamers, adapted from Lucas et al. (2013).

Still those simulations need a cloud on a nearly radial orbit and lead to the creation of two nested discs, which are rotating in the same direction. The observed stellar discs however are intersecting, which is not possible to create with two gaseous discs existing at the same time. Also the direction of rotation for both discs has to be the same whereas observations show that the stellar discs are rotating opposite to each other.

1.2.5 Cloud-Cloud Collisions
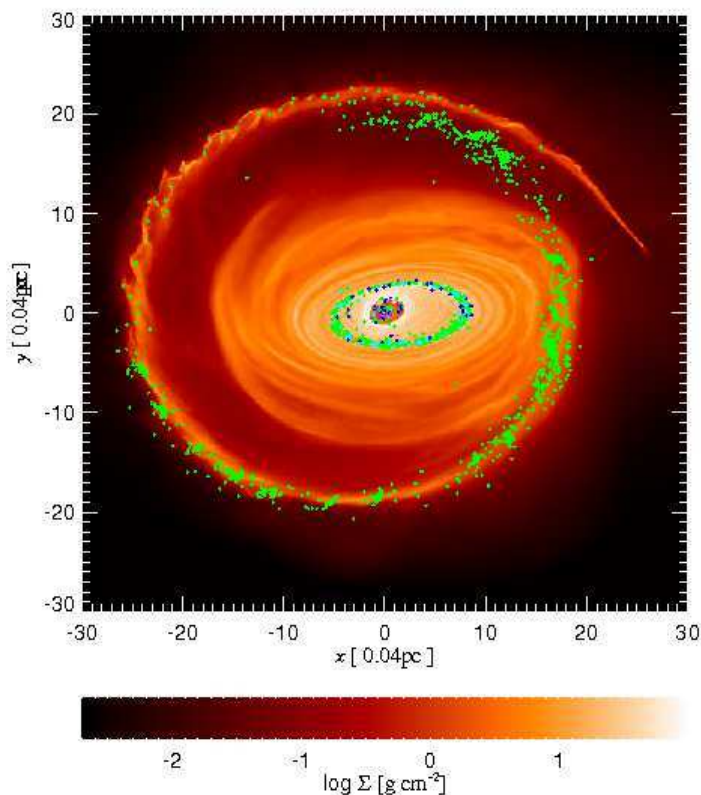
Figure 1.26: Surface density of a simulation of the off-centre collision of two molecular clouds. Green dots stand for stars with masses 1-10 $M_{\odot}$, blue dots for stars with masses 10-150 $M_{\odot}$. Adapted from Hobbs & Nayakshin (2009). Clearly visible is the formation of an inner small stellar disc surrounded by a larger stellar ring.

The approach taken by Hobbs & Nayakshin (2009) assumes the collision of two clouds further away from the Galactic Centre. In this case there is no need for a radially infalling cloud and the infalling streams are able to create counter-rotating streams of gas around the black hole. Still those streams exist at the same time and thus are not able to explain the origin of intersecting discs. The clouds in the model are assumed to have masses of 3.4×10^4 $M_{\odot}$ and 2.6×10^4 $M_{\odot}$, with radii of 0.2 and 0.172 pc. The collision is off-centre.

Regions that are not affected by the direct collison tend to cool and settle into orbits corresponding to the initial cloud orbit, occasionally colliding with parts of the disc that formed from gas that took part in the direct collision. Figure 1.26 shows the surface density for a simulation creating two rings of stars from a collision of two clouds. The green dots represent stars with masses 1-10 $M_{\odot}$, the blue dots represent stars with masses 10-150 $M_{\odot}$.

1.2.6   Circum-nuclear Disc Origin

In our new formation model, we assume the collision of a cloud with a ring of gas similar to
the circum-nuclear disc. Since the ring is destroyed in this process, the currently observed
circum-nuclear disc can form afterwards. Observations indicate that such a collision also
happens right now at the Galactic Centre (Montero-Castaño et al., 2009) with the current
circum-nuclear disc, providing proof that this is a likely and probably periodic event. Figure
1.27 shows evidence for the so called 20 km/s cloud close to the circum-nuclear disc mixing
with material of the circum-nuclear disc at the point indicated by the white cross on the
lower left.
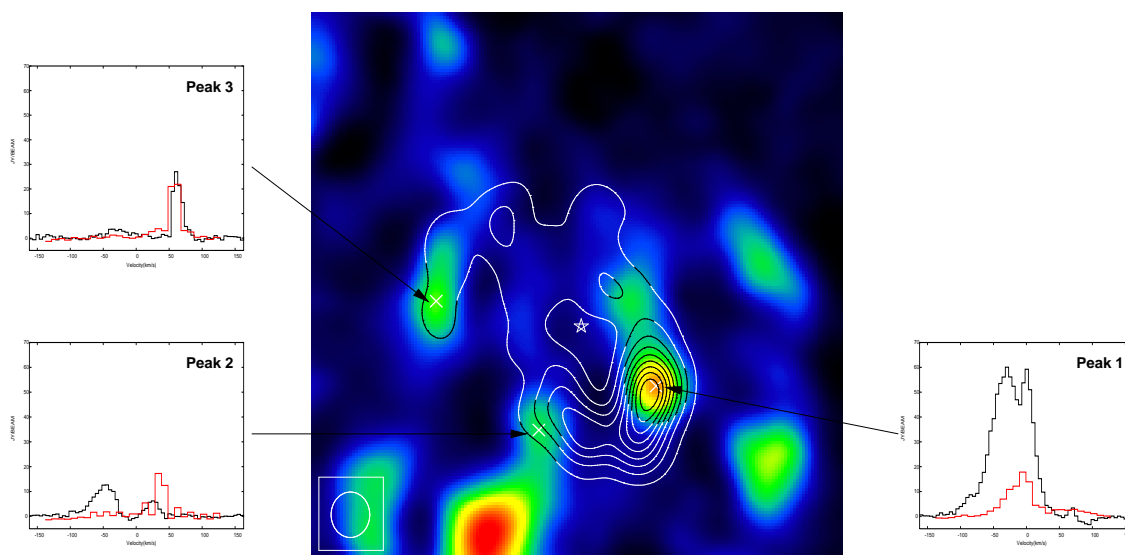
Figure 1.27:   Data from the SMA (Submillimeter Array) showing HCN(4-3) integrated
intensity in contours and NH₃ (3,3) integrated intensity in false colour-scale, adapted from
Montero-Castaño et al. (2009) and McGary et al. (2001). The spectra show HCN(4-3)
(black) and NH₃ (3,3) (red, scaled up by a factor of 50). Peak 2 shows evidence for the
20 km/s molecular cloud interacting with -50 km/s material from the circum-nuclear disc.
Cold, high density material, traced by HCN(4-3) shows the common rotation of the circum-
nuclear disc. However, in contrast to peak 1 and 3, the warm lower density material traced
by NH₃ (3,3) in peak 2 shows an opposite velocity peak at 20 km/s compared to -50 km/s
of the cold and dense material. This suggests that material at this position is warmed up
by the 20 km/s cloud.

The original idea of the cloud circum-nuclear disc collision model was to explain the origin
of a heavy clump on a nearly radial orbit towards the black hole. Test simulations set up
to destabilise parts of the circum-nuclear disc however showed that not a single isolated

clump of material was send towards the black hole but rather streams of material.

The collision of a cloud with opposite angular momentum direction compared to the circum-nuclear disc leads to multiple streams of gas flowing towards the central parsec. The timing of those streams leads to the creation of multiple discs at different times which are rotating clockwise or counter-clockwise depending on the mixture of material from the cloud and circum-nuclear disc. Using a simple, probable assumption, this model can explain the formation of two counter-rotating accretion discs which could be the progenitors of the observed stellar discs. We will present this scenario in detail in the second paper of this thesis.

A compelling feature of all the formation scenarios so far is the deposit of a large amount of gas onto the black hole. Taking into account the age of the disc stars of 6 Myrs and the time it takes to form the stars and the disc we would expect a large accretion event around 10 Myrs ago. This coincides well with the age of the Milky Way X-Ray Lobes, also called the "Fermi-Bubbles" (Su et al., 2010; Carretti et al., 2013), which are believed to originate from a recent accretion event.

Chapter 2

Theory

In this chapter we develop the theoretical background necessary to understand the simulation techniques and results.

2.1 Gravity

2.1.1 Point Masses

According to Newtons law of gravitation point masses attract each other with a force that is inversely proportional to the squared point mass distance and directly proportional to the product of the masses. The law can be written as:

$$\vec{F_{ij}} = G \frac{m_i m_j}{|\vec{r_{ij}}|^2} \hat{r_{ij}} \tag{2.1}$$

with $\vec{F_{ij}}$ the force exerted on particle i from particle j, m_i and m_j the two masses, $\vec{r_{ij}}$ the vector pointing from particle i towards particle j, $\hat{r_{ij}} = \frac{\vec{r_{ij}}}{|\vec{r_{ij}}|}$ and G the gravitational constant. The latest 2012 value for G from the Particle Data Group (Beringer et al., 2012) is given by:

$$G = (6.6738 \pm 0.0008) \times 10^{-11} \frac{m^3}{kg\ s^2}$$

Of all constants of nature, the gravitational constant has the largest uncertainty in measurement due to the weakness of the force and the resulting difficulty of isolating the measurement against external influences.

Given a number of point masses, the resulting force on a single point mass can be calculated by summing over the contribution to force (2.1) from all other point masses. The force exerted on particle i can then be calculated by:

$$\vec{F}_i = \sum_{j \neq i} \vec{F}_{ij} \tag{2.2}$$

Using a computer code that approximates an arbitrary density distribution by a number of point masses, the gravitational forces can be calculated using equation (2.2) for a small number of particles. However for a large number of particles equation (2.2) quickly becomes extremely expensive to calculate. In section 2.4.3 we will introduce a method that is better suited for calculating the forces between a large number of gravitationally interacting particles on a computer.

2.1.2 Point Mass in a Central Force

A central force is a conservative field. Conservative fields can always be expressed as the gradient of a scalar potential:

$$\vec{F} = -\vec{\nabla}V$$

with V the scalar potential. Total energy is conserved in a conservative field. Assuming a particle moves within a central force in the xy-plane, the angular momentum vector will be aligned along the z-axis. Let the absolute value of angular momentum be called L_0, the particle mass m and the vector connecting the particle with the central point $\vec{r}$. Then energy conservation can be written as:

$$E = \frac{1}{2}m|\dot{\vec{r}}|^2 + U \tag{2.3}$$

with $U = V + \frac{L_0^2}{2mr^2}$ the effective potential and $\dot{\vec{r}}$ the time derivative of $\vec{r}$. The effective potential is a combination of the contribution to the potential from the conservative field and the potential from the centrifugal force. The form of the effective potential determines the orbits the particle can have. A local minimum of U opens the possibility of closed orbits.

We now assume a special potential, the gravitational potential of a point mass:

$$V = -\frac{GmM}{r}$$

with m the mass of a test particle within the field of the heavy particle M (M ≫ m). Using energy conservation (2.3) one can solve for $\dot{\vec{r}}$ and integrate. This leads to the orbital equation:

$$\boxed{r = \frac{p}{1 + \epsilon \, cos(\phi)}} \tag{2.4}$$

with substitutions $p = \frac{L_0^2}{Gm^2M}$ and $\epsilon = \sqrt{1 + \frac{2EL_0^2}{G^2m^3M^2}}$. Within the plane of motion of the test particle, equation (2.4) gives the distance from the central mass M in dependence of the angle ϕ. The type of orbit is given by the total energy E:

Circle	$E = \frac{-GmM}{2p}$ (U_{min})
Ellipsis	$\frac{-GmM}{2p} < E < 0$
Parabola	$E = 0$
Hyperbola	$E > 0$

A closed elliptical orbit has the semi-major axis a:

$$a = -\frac{GmM}{2E}$$

The semi-minor axis b can be calculated from the relation $\frac{b}{a} = \sqrt{1 - \epsilon^2}$. The value ϵ is also called numerical eccentricity. Its value is zero for a circle, between zero and one for an ellipsis, equal to one for a parabola and larger than one for a hyperbola. The point of closest distance of the test particle to the central mass on the elliptical orbit is called the pericentre, the farthest point the apocentre.

2.1.3 Spherical Mass Shell

The Gauss theorem from vector calculus:

$$\int_V (\vec{\nabla} \cdot \vec{A}) dV = \int_S (\vec{A} \cdot \hat{n}) dS \tag{2.5}$$

states that the volume integral over the divergence of a (continuously differentiable) vector field $\vec{A}$ is equal to the surface integral (over the boundary of the volume V) over the fields flux through the surface. The unit-vector $\hat{n}$ represents the outwards (away from the volume) pointing surface normal. In terms of a fluid, if we want to know how much of a fluid flows out of (or into) a certain region, the left side of equation (2.5) sums up all fluid sources and sinks within the whole volume. The right side of equation (2.5) sums up the total amount of fluid that flows into and out of the surface of the volume, giving the net flow into or out of the volume.

From equation (2.1) we know that the law of gravity has the form $\vec{F} = m\vec{g}$ with $\vec{g}(\vec{r}) = -\frac{GM}{|\vec{r}|^2}\hat{r}$ the gravitational field of the point mass M. For an arbitrary density distribution $\rho(\vec{r})$ the gravitational field can be calculated by summing over the contributions to the mass from every point in space:

$$\vec{g}(\vec{r}) = -G \int \rho(\vec{s}) \frac{\vec{r} - \vec{s}}{|\vec{r} - \vec{s}|^3} d^3 s$$

Applying the divergence operator on both sides and using the fact that $\vec{\nabla} \cdot \left(\frac{\vec{x}}{|\vec{x}|^3} \right) = 4\pi\delta(\vec{x})$ with the Dirac delta function $\delta(\vec{x})$, one can rewrite:

$$\boxed{\vec{\nabla} \cdot \vec{g}(\vec{r}) = -4\pi G \rho(\vec{r})} \tag{2.6}$$

Equation (2.6) is called Gauss's law of gravity. To obtain the integral form of (2.6) one can simple rewrite (2.6) as volume integral on both sides and use (2.5) to arrive at the integral form of Gauss's law of gravity:

$$\int_S (\vec{g} \cdot \hat{n}) dS = -4\pi GM \tag{2.7}$$

A direct consequence that can be seen especially good from Gauss's law of gravity in form (2.7) is that for a spherically symmetric mass distribution $\vec{g} = \vec{g}(|\vec{r}|)$ the mass distribution can be treated as if it was concentrated within a single point of mass M (the enclosed mass). Another consequence is that any test particle which is placed inside the radius of the mass distribution only feels a force that is exerted by the mass enclosed by radii smaller than the radius at which the particle is placed.

The gravitational field is conservative, thus we can express it in terms of the gradient of a scalar field ϕ:

$$\vec{g} = -\vec{\nabla}\phi \tag{2.8}$$

Substituting (2.8) for $\vec{g}$ in (2.6) gives:

$$\boxed{\vec{\nabla}^2\phi = 4\pi G\rho(\vec{r})} \tag{2.9}$$

which is called Poisson's equation for gravity.

2.1.4   Black Holes

Equating gravitational potential energy and kinetic energy one can calculate the minimum velocity needed for a test particle to leave the gravitational influence of a massive object with mass M. No further acceleration is needed to escape the massive objects influence if this so called escape velocity is reached at the distance r from the massive objects centre. The escape velocity is given by

$$v = \sqrt{\frac{2GM}{r}} \tag{2.10}$$

Now the question arises what happens if the escape velocity was so large that even the velocity of light, which no object can exceed, was not fast enough to escape the massive object. A massive object with a large enough mass concentrated within a small enough volume of space such that the escape velocity above the surface exceeds the velocity of light is a black hole. Contrary to popular belief the total mass of a black hole does not have to be high, even particles inside an accelerator could in principle get so close that enough mass was inside a small radius to form a black hole (Alig et al., 2006). The resulting black hole would not be a large world eating object like commonly depicted in movies, the total mass would still only correspond to the combined mass of the initial particles.

Setting the velocity in equation (2.10) equal to the velocity of light c and solving for r we get the Schwarzschild radius

$$r_s = \frac{2GM}{c^2} \tag{2.11}$$

If all the mass M of an object is concentrated within a radius smaller than the Schwarzschild radius, the object will be a black hole. For earth this radius is only ~ 10 mm. For a non-rotating black hole, the Schwarzschild radius is also equal to the so called event horizon, the boundary below which events can no longer in any way influence events outside the boundary. Due to the fact that not even light can escape from a black hole, one would imagine that black holes are perfectly black. However, according to J. Bekenstein and S. Hawking taking quantum mechanical effects into account (electron/positron pair creation close to the event horizon) black holes can evaporate, with the rate of evaporation (the "temperature" of the black hole) inversely proportional to the black hole mass.

Thus a low mass black hole could actually be quite "bright". This process takes energy from the black hole, leading to its evaporation. However massive black holes at masses larger than the mass of the sun evaporate so slowly that even the absorption of new mass from the cosmic microwave background is enough to replenish the mass lost from evaporation and even grow in mass.

Due to the extreme nature of black holes, the classical mechanics approach in dealing with the properties of black holes quickly breaks down and the effects predicted by general

relativity have to be taken into account. The fact that a black hole basically "shields" all information beyond the event horizon from the outside world is formulated in the no-hair theorem. It states that all black hole solutions obtained in general relativity can be characterised by three external and observable properties of the black hole. Those properties are mass, angular momentum and electric charge of the black hole. All other information about the matter which formed the black hole is lost behind the event horizon.

For a rotating black hole the event horizon is no longer spherical but rather a spheroid. A rotating black hole is characterised by the spin-parameter a:

$$a = \frac{Jc}{GM^2}$$

with black hole angular momentum J and mass M. The spin-parameter is equal to 0 for a non-rotating black hole and equal to 1 for a maximally rotating (maximally allowed by general relativity) black hole. A prediction of general relativity is that a rotating massive object actually distorts the space-time metric, thus altering the orbits of test particles within its sphere of influence. This effect is called frame-dragging or Lense-Thirring effect. The orbits of particles close to a rotating black hole can be described using the Kerr-metric, a vacuum solution of the Einstein field equations of general relativity for rotating black holes.

Restricting ourselves to the equatorial plane of the black hole, one can derive from the Kerr-metric the angular speed Ω at which the frame-dragging effect would force space time to rotate (Tartaglia, 2000):

$$\Omega = \frac{r_s \alpha c}{r^3 + \alpha^2 r + r_s \alpha^2} \tag{2.12}$$

with $\alpha = \frac{J}{Mc}$ and r_s the Schwarzschild radius. Applied to the Galactic Centre black hole SgrA* this would result in 0.023 full rotations every Myr, at a distance of 25000 r_s or 0.01 pc from SgrA*. This assumes that SgrA* spins nearly maximally with a = 0.99, a lower spin would even lower the number of rotations. In our simulations the very inner boundary is set to 0.01 pc and the maximum time that anything happens close to the inner boundary is around 1 Myr. Considering that this distance represents the innermost border close to which physics is not resolved well anyways and that most of the interesting physics happens at distances > 0.1 pc (with 2.3×10^{-5} full rotations every Myr) we can safely ignore the effect of frame dragging as a first approximation using our non-relativistic simulation code.

2.1.5 Timescales in the Galactic Centre

The seminal paper of Kocsis & Tremaine (2011) gives an excellent overview of timescales due to gravity within the Galactic Centre.
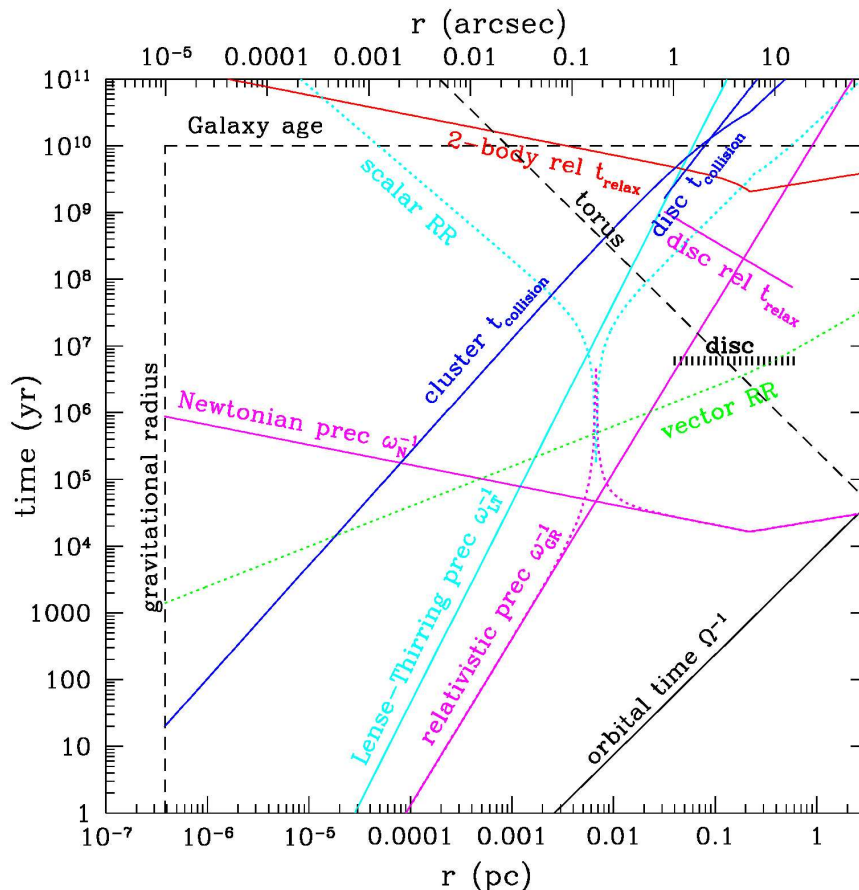
Figure 2.1: Timescales in the Galactic Centre, adapted from Kocsis & Tremaine (2011). The plots are from the following equations. Orbital time on the lower right in black, equation (2.13). Relativistic precession in magenta, equation (2.14). Newtonian precession in magenta, equation (2.15). The magenta dots represent the sum of equation (2.14) and (2.15). Solid cyan (Lense-Thirring precession) equation (2.12). Dashed black, the precession time due to the circum-nuclear disc/torus, equation (2.16). We are not interested in the relaxation times here. The Galactic Centre stellar discs extend and age is marked in the plot in order to see which timescales are important in influencing the evolution of the discs. The left boundary marks the gravitational radius (Schwarzschild radius) of SgrA* and the upper boundary the age of the Milky Way Galaxy.

For simplicity the timescales have all been calculated assuming a SgrA* mass of $M = 4 \times 10^6 \ M_\odot$ and a distance of 8 kpc from the Galactic Centre. The orbital frequency of a star

with semi-major axis a is given by:

$$\Omega^{-1} = \left(\frac{a^3}{GM}\right)^{1/2} = 236\text{yr} \left(\frac{a}{0.1 \text{ pc}}\right)^{3/2} \tag{2.13}$$

The relativistic apsidal precession timescale (also seen in the famous Mercury precession, that can only be explained by general relativity) is given by

$$\omega_{\text{GR}}^{-1} = \frac{c^2 a^{5/2}(1 - e^2)}{3(GM)^{3/2}} = 4.11 \times 10^7 yr \ (1 - e^2) \left(\frac{a}{0.1 \text{ pc}}\right)^{5/2} \tag{2.14}$$

with eccentricity e. The plot of equation (2.14) in Figure 2.1 assumes nearly circular orbits ($e \approx 0$).

In section 2.1.4 we already presented the frame-dragging/Lense-Thirring timescale due to a rotating mass, dragging space-time itself with it.
The Newtonian precession timescale is given by:

$$|\omega_{\text{N}}|^{-1} = \begin{cases} 2.1 \times 10^4\text{yr} \ (\text{r}/0.1\text{pc})^{-0.3}, & \text{if r} < 0.22 \text{ pc} \\ 1.3 \times 10^4\text{yr} \ (\text{r}/0.1\text{pc})^{0.25}, & \text{if r} > 0.22 \text{ pc} \end{cases} \tag{2.15}$$

This precession is caused by the gravitational field of a spherical stellar cluster. Equation (2.15) was adapted to the Galactic Centre nuclear star-cluster values presented in section 1.1.4 in the introduction.

Also an external perturber influences the stellar discs. The precession timescale due to the influence of the circum-nuclear disc (assuming that all the mass is concentrated within a ring at a given distance) is given by:

$$t_p \simeq 8.5 \times 10^6\text{yr}\frac{10^6\text{M}_\odot}{\text{M}_\text{p}} \left(\frac{\text{r}_\text{p}}{1.5 \text{ pc}}\right)^3 \left(\frac{0.1 \text{ pc}}{\text{r}}\right)^{3/2} \frac{0.5}{\cos \text{I}}. \tag{2.16}$$

with I the relative inclination between the circum-nuclear disc and the stellar discs, M_p the circum-nuclear disc (perturber) mass and r_p the radius of the ring at which all of the mass of the perturber is placed.

Another perturbing process, which we do not present here, could be an internal perturber (inside the inner region of the stellar discs) like an intermediate mass black hole. The scenario of an external perturber has been tested by many groups (Hunter & Toomre, 1969; Nelson & Tremaine, 1996; Ulubay-Siddiki et al., 2009; Nayakshin, 2005; Löckmann et al., 2009; Löckmann & Baumgardt, 2009). They find that an external perturber can warp the stellar discs significantly if the inclination angle I is not too large. However we know from observations (see section 1.1.5) that the circum-nuclear disc is almost perpendicular to both stellar discs. This could hint towards a scenario in which at least the clockwise stellar disc was initially aligned with the circum-nuclear disc and later on changed its inclination.

From Figure 2.1 we see that relativistic effects play nearly no role, however the influence of the nuclear star cluster and the circum-nuclear disc can not be neglected and have to be included when studying the formation of the stellar discs.

2.1.6 Tidal Forces

A small, extended object passing close to a massive object experiences higher forces on the side facing the massive object compared to the side pointing away from the massive object. If the internal gravitational force of the small object is not strong enough to hold against this gradient in external force, the small object starts to break apart and shear within the gravitational field of the massive object.

The radius at which this happens is called the Roche Limit. A fluid like object like a molecular cloud should have a much larger Roche Limit compared to a massive object like a moon. The Roche Limit can be calculated by equating the force of the small object itself onto a small part facing the massive object with the force the massive object exerts on that small part. This gives a Roche Limit of (Roche, 1849):

$$r_{\text{Roche,solid}} = 1.44R \left(\frac{\rho_M}{\rho_m} \right)^{\frac{1}{3}} \tag{2.17}$$

with R the radius of the massive object and ρ_M, ρ_m the mean densities of the massive object and the small object. Equation (2.17) assumes a solid test-object. For a fluid like object the calculation becomes more complicated (the shape can change) and the solution can not be written down in an analytically closed form. An approximation (Rappaport et al., 2013) is given by:

$$r_{\text{Roche,fluid}} \approx 2.44R \left(\frac{\rho_M}{\rho_m} \right)^{\frac{1}{3}} \tag{2.18}$$

with the same labelling as in equation (2.17). As expected, the Roche Limit is larger for a fluid like object with the same density as a solid body. Using $V = \frac{4}{3}\pi r^3$ and $\rho = \frac{m}{V}$ we can rewrite (2.18) as:

$$r_{\text{Roche,fluid}} \approx 2.44r \left(\frac{M}{m} \right)^{\frac{1}{3}}$$

with r the radius of the small object, M the massive objects mass and m the small objects mass. Inserting typical values for SgrA* as the massive object and a molecular cloud as the small object (M = 4×10^6 M$_\odot$, m = 10^4 M$_\odot$, r = 4 pc) gives a Roche Limit of around 72 pc.

2.2 Hydrodynamics

2.2.1 Boltzmann and Vlasov Equations

Our main goal and interest in this section is to calculate properties of a fluid like velocity, density, pressure and temperature as function of position and time. One can take on two points of view in following the evolution of a fluid. An Eulerian reference frame stays fixed in space and describes the flow of the fluid in and out of the fixed space. A Lagrangian reference frame moves with the fluid. Depending on the problem one is trying to solve, either view can be more useful. Astrophysical fluid simulation codes that employ the Eulerian reference frame are grid codes like FLASH, Pluto, RAMSES and Athena. Codes that employ the Lagrangian reference frame are SPH (smoothed particle hydrodynamics) codes like Gadget, VINE and Seren.

We start with a derivation of the Boltzmann and Vlasov equations and define a distribution function f($\vec{x}$,$\vec{v}$,t) such that

$$f(\vec{x}, \vec{v}, t) \ d^3x \ d^3v = dN \tag{2.19}$$

gives the number of particles within the volume element d^3x around $\vec{x}$ and with velocity inside the velocity cube d^3v around $\vec{v}$ at the time t. The distribution is normalised such that integrating gives the total number of particles N of the system.

$$\int_{space} \int_{velocity} f(\vec{x}, \vec{x}, t) \ d^3x \ d^3v = N$$

We assume that all the particles in the system have the same mass m. The principle statement is that the change of f with time is only due to three influences. First, an external force can lead to a change in f. Second, diffusion (random movement) of the particles can lead to a change in f. Finally collisions between particles can lead to a change in f. In equation form:

$$\frac{\partial f}{\partial t} = \frac{\partial f}{\partial t}_{force} + \frac{\partial f}{\partial t}_{diffusion} + \frac{\partial f}{\partial t}_{collision}$$

We want an equation which describes exactly this behaviour. For that we first ignore collisions and only look at changes due to an external force and diffusion. An external force acting on the particles during a time interval of dt changes their positions and velocities, which we now call $\vec{x_2}$ and $\vec{v_2}$. The relation to the old values is:

$$\vec{x_2} = \vec{x} + \vec{v}dt$$

and

$$\vec{v_2} = \vec{v} + \vec{a}dt$$

with $\vec{a}$ the acceleration due to the external force. The new phase space volume (position and velocity) is related to the old one by:

$$d^3x_2 \; d^3v_2 = J(\vec{x_2}, \vec{v_2}/\vec{x}, \vec{v})d^3x \; d^3v$$

with J the transformation Jacobian. To first order in dt the Jacobian is equal to unity, so that in first order one can write:

$$d^3x_2 \; d^3v_2 = d^3x \; d^3v \tag{2.20}$$

Due to the absence of collisions and the conservation of mass, all the particles from the original volume must end up within the new phase space element. Using equation (2.19) for the number of particles inside both phase spaces and equating them using (2.20) gives:

$$f(\vec{x} + \vec{v}dt, \vec{v} + \vec{a}dt, t_0 + dt) = f(\vec{x}, \vec{v}, t)$$

which simply states that in the absence of collisions, the distribution function is invariant against changes in time due to an external force. Expanding to first order in dt gives:

$$\boxed{\frac{\partial f}{\partial t} + \sum_{i=1..3} \left(v_i \frac{\partial f}{\partial x_i} + a_i \frac{\partial f}{\partial v_i} \right) = 0} \tag{2.21}$$

This equation is also known as collisionless Boltzmann equation or Vlasov's equation. Taking into account collisions between particles can force particles to end up within different phase space volumes than before. This leads to the addition of another term on the right hand side of the Vlasov equation, that symbolises the net rate at which particles end up in the current phase space element.

$$\boxed{\frac{\partial f}{\partial t} + \sum_{i=1..3} \left(v_i \frac{\partial f}{\partial x_i} + a_i \frac{\partial f}{\partial v_i} \right) = \frac{df}{dt}_{collision}} \tag{2.22}$$

This is the so called Boltzmann equation. It describes the statistical behaviour of a thermodynamical system. The 6 dimensional Boltzmann equation is normally hard to handle and provides a lot more information than is necessary to know. Thus commonly the momenta of the Boltzmann equation are taken resulting in the equations of motion of hydrodynamics. The density of a fluid at the point $\vec{x}$ at the time t is obtained from the distribution function by integration:

$$\rho(\vec{x}, t) = \int m f(\vec{x}, \vec{v}, t)d^3v$$

The zeroth moment of the Boltzmann equation is obtained by multiplying with m and integrating over d^3v which results in the continuity equation:

$$\boxed{\frac{\partial \rho}{\partial t} + \vec{\nabla} \cdot (\rho \vec{u}) = 0} \tag{2.23}$$

with $\vec{u}$ the mean fluid velocity at $\vec{x}$. The continuity equation states the conservation of mass. In mathematical terms the zeroth moment corresponds to the mean of a distribution.

The first moment of the Boltzmann equation is obtained by multiplying with $m\vec{v}$ and again integrating over d^3v. This results in the momentum equation (in component form):

$$\frac{\partial}{\partial t}(\rho u_j) + \sum_i \frac{\partial}{\partial x_i}(\rho u_i u_j + P\delta_{ij} - \pi_{ij}) = \rho a_j \tag{2.24}$$

with P the pressure, π_{ij} the viscous stress tensor and δ_{ij} the Kronecker-Delta. The momentum equation describes local momentum conservation with acceleration due to an external force, pressure gradients or viscous forces.

Finally, the second moment of the Boltzmann equation can be obtained by multiplying with mv^2 and integration. The obtained equation is called the energy-equation:

$$\frac{\partial \epsilon}{\partial t} + \vec{u} \cdot \vec{\nabla}\epsilon = -\frac{P}{\rho}\vec{\nabla} \cdot \vec{u} - \frac{1}{\rho}\vec{\nabla} \cdot \vec{F} + \frac{1}{\rho}\Psi \tag{2.25}$$

with ϵ the specific internal energy, $\vec{F}$ the conduction heat flux and Ψ the viscous dissipation rate. Changes in internal energy are due to PdV work, conduction and viscous heating. One can also add external heat sources and sinks as additional terms to this equation.

The set of equations (2.23), (2.24) and (2.25) forms the so called Navier-Stokes equations. Diffusive effects like heat conduction and viscosity are often small compared to the other dynamical effects and thus can be neglected. Neglecting those terms in the Navier-Stokes equations gives the Euler-equations of hydrodynamics. Together with an equation of state, the Euler-equations describe the dynamics of a perfect fluid, which is the goal we wanted to reach.

The simulation code we are going to work with in this thesis numerically implements the Euler-equations. However there are situations in Astronomy in which the diffusive effects can not be neglected. This is normally "repaired" by introducing artificial sources of diffusion which are then added to or subtracted from the calculated quantities. Shocks, viscously evolving accretion discs or a multiphase medium are examples in which those terms can not be neglected. As we will see when we present simulations of the G2 cloud neglecting any one of the diffuse terms can lead to a complete breakdown of a simulation. In the following we will derive the Euler continuity and momentum equations using a more intuitive approach.

2.2.2 Continuity Equation

Following Greiner & Stock (1991) we first we look at a certain volume V inside an ideal, streaming fluid. The mass M inside that volume is then given by integrating the fluid density ρ over the volume:

$$M = \int_V \rho dV$$

Now let $d\vec{A}$ be a surface element of the volume with $|d\vec{A}| = dA$ the size of the area. The orientation of $d\vec{A}$ is such that it is parallel to the normal of the surface pointing away from the volume.

The mass that flows through the surface element during the time dt is then given by

$$\rho\vec{v} \cdot d\vec{A}dt \tag{2.26}$$

If mass flows out of the volume (parallel to the surface normal) (2.26) becomes positive. When mass flows into the volume (anti-parallel to the surface normal) (2.26) becomes negative. Thus the total change in mass over time can be calculated by integrating

$$dM_1 = dt \int \rho\vec{v} \cdot d\vec{A} \tag{2.27}$$

But mass can also change due to a change in density with time inside the volume. So we also have

$$dM_2 = -dt \int \frac{\partial \rho}{\partial t} dV \tag{2.28}$$

When mass is conserved, the two terms (2.27) and (2.28) must be equal so that we can write:

$$\int_A \rho\vec{v} \cdot d\vec{A} = -\int_V \frac{\partial \rho}{\partial t} dV \tag{2.29}$$

Using the divergence theorem (2.5) we can turn the surface integral on the left side of (2.29) into a volume integral:

$$\int_A \rho\vec{v} \cdot d\vec{A} = \int_V \vec{\nabla} \cdot (\rho\vec{v}) dV \tag{2.30}$$

Inserting (2.30) into (2.29) we get

$$\int_V \left(\frac{\partial \rho}{\partial t} + \vec{\nabla} \cdot (\rho\vec{v}) \right) dV = 0 \tag{2.31}$$

This equation is true for all volumes. If we go to an infinitesimal volume, the variables ρ and $\vec{v}$ take on the local values at the place of the volume. So, the vanishing relation (2.31) is equal to the statement

$$\boxed{\frac{\partial \rho}{\partial t} + \vec{\nabla} \cdot (\rho \vec{v}) = 0} \tag{2.32}$$

which is the continuity equation. The term $\vec{j} = \rho \vec{v}$ is called current density vector. Its direction points into the direction of motion of the fluid and its absolute value gives the amount of fluid per unit time that flows through a unit area perpendicular to $\vec{j}$.

2.2.3   Momentum Equation

Again we look at a volume V inside an ideal, streaming fluid. Analogously to point particles where the movement is governed by the forces acting on the particles, a fluids movement is also governed by the acting forces. We assume a force $\Delta \vec{F}$ acting on the fluid inside the volume V. We can express the force as a force density

$$\Delta \vec{F} = \int_{\Delta V} \rho \vec{f} dV$$

In the case of the earth gravitational field we would have $\vec{f} = \vec{g}$.

Now the fluid inside the volume V also acts on the surrounding with a pressure, leading to a force given by

$$\Delta \vec{F}_p = - \int_A p d\vec{A}$$

with p the pressure and the surface integral taken over the surface of the volume V. Summing up the forces, after using (2.5) to turn the surface integral into a volume integral, gives

$$\int \rho \frac{d\vec{v}}{dt} dV = \int \left(\rho \vec{f} - \vec{\nabla} p \right) dV \tag{2.33}$$

Again this is true for all volumes and if we go to an infinitesimal volume, the acceleration $\frac{d\vec{v}}{dt}$ will have a uniform local value inside the volume. So we can replace (2.33) with the local statement:

$$\rho \frac{d\vec{v}}{dt} = \rho \vec{f} - \vec{\nabla} p$$

Using the general relation $\frac{dX}{dt} = \frac{\partial X}{\partial t} + (\vec{v} \cdot \vec{\nabla}) X$ for a scalar field component shifted in time $X(\vec{r} + \vec{v} dt, t + dt)$ to substitute $\frac{d\vec{v}}{dt}$, we can rewrite as

$$\boxed{\rho \left(\frac{\partial \vec{v}}{\partial t} + (\vec{v} \cdot \vec{\nabla}) \vec{v} \right) = \rho \vec{f} - \vec{\nabla} p} \tag{2.34}$$

This is the Euler momentum equation.

2.2.4   Turbulence

First, we rewrite the momentum Navier-Stokes equation (2.24) in terms of dimensionless variables with $\vec{v}' = \vec{v}/V_0$, $\vec{x}' = \vec{x}/L_0$, $P' = P/(\rho_0 V_0^2)$, $t' = t/(L_0/V_0)$, $\rho' = \rho/\rho_0$ and $\vec{\nabla}' = L_0\nabla$. L_0, V_0 and ρ_0 represent a characteristic length, volume and density of the observed flow. Also assuming an incompressible fluid ($\vec{\nabla} \cdot \vec{u} = 0$) the equation is:

$$\frac{D\vec{v}'}{Dt'} = -\frac{\vec{\nabla}'P'}{\rho'} + \frac{\nu}{L_0V_0}\vec{\nabla}'^2\vec{v}' \tag{2.35}$$

with the kinematic viscosity ν. In this form the equation does not depend on any input besides a single number $\frac{\nu}{L_0V_0}$ which completely determines the type of flow. The inverse of this number is called the Reynolds number:

$$Re = \frac{L_0V_0}{\nu} \tag{2.36}$$

The Reynolds number determines if a flow is "laminar" or "turbulent". The Euler equations are always in the limit of $Re \to \infty$, which means that viscosity is unimportant and one approaches an ideal gas. A Reynolds number of ~ 1 means that the system is completely dominated by viscosity. As the Reynolds number inside a flow e.g. around a cylinder increases, the onset of "turbulence" can be seen. At $Re < 0.1$ the flow is completely symmetric around the cylinder. At $Re > 10$ eddies (swirls) start to form behind the cylinder, whilst the overall flow still is symmetric. At $Re > 100$ eddies form all over the place behind the cylinder and the symmetry of the flow is broken.

There is no real definition for "turbulence". The breaking of the symmetry of a flow and the appearance of chaos are associated with turbulence, thus turbulence is a statistical phenomenon. In the sub-sonic case a turbulent flow can often be treated as incompressible.

In 1941 Kolmogorov formed a theory about turbulence, based on three hypotheses. First, for high Reynolds numbers all symmetries of the Navier-Stokes equations are restored in a statistical sense at distances far away from the boundaries. Second, for high Reynolds numbers the flow is self-similar on all scales. Third, the turbulent flow has a finite, non-vanishing rate of dissipation per unit mass.

For the largest eddies in a high Reynolds number flow, viscosity is not important. However, the eddies are unstable and transfer their energy to smaller eddies. This continues until the Reynolds number for the observed scale reaches order unity. For those eddies viscosity is important and the kinetic energy will be dissipated. This transfer of energy to smaller scales gives rise to the energy cascade of turbulence.

The hypotheses of Kolmogorov resulted in a phenomenological law, describing the form of the energy cascade if we inject energy at a certain scale:

$$E(k, \epsilon) = C k^{-\frac{5}{3}} \epsilon^{\frac{2}{3}}$$

with ϵ the energy injection rate per unit mass and $k = \frac{1}{L_0}$. The highest energies will be found at the injection scale and the energy drops with the famous $-\frac{5}{3}$ slope down to the dissipation scale. The constant C is universal, but has to be determined by experiment, which gives a value of $C \approx 1.5$.

2.2.5 Thin Accretion Disc

We now investigate the dynamics of a thin accretion disc around a central object of mass M, following the work of Lin & Pringle (1987). The matter is assumed to move in circles with Keplerian angular velocity

$$\Omega = \left(\frac{GM}{R^3}\right)^{\frac{1}{2}} \tag{2.37}$$

and thus circular velocity $v_\phi = R\Omega$.

The central object accretes gas from the disc, hence the circular motion is overlayed by a small radial component v_R which can be a function of radius R and time t. We now want to derive an equation for the surface density $\Sigma = \Sigma(R, t)$ of the accretion disc. For this we use the equations for the conservation of mass and angular momentum. A segment of the disc, positioned between R and R + Δ R has the mass $2\pi R\Delta R\Sigma$ and angular momentum $2\pi R\Delta R\Sigma R^2\Omega$.

We can calculate the rate of change of these quantities due to the in and outflow of neighbouring disc segments. For the mass we get

$$\frac{\partial}{\partial t}(2\pi R\Delta R\Sigma) = v_R(R, t)2\pi R\Sigma(R, t) - v_R(R + \Delta R, t)2\pi (R + \Delta R)\Sigma(R + \Delta R, t) \tag{2.38}$$

For small ΔR we can rewrite (2.38):

$$R\frac{\partial \Sigma}{\partial t} + \frac{\partial}{\partial R}(R\Sigma v_R) = 0 \tag{2.39}$$

The conservation of angular momentum can be done analogously, only this time we get an additional term on the right side

$$R\frac{\partial}{\partial t}(\Sigma R^2\Omega) + \frac{\partial}{\partial R}(\Sigma v_R R^3\Omega) = \lambda \tag{2.40}$$

Here λ encodes the effect of the viscous torques due to the neighbouring disc segments. If we have an outer disc segment acting on a neighbouring inner one then we find

$$\lambda = \frac{1}{2\pi}\frac{\partial G}{\partial R} \tag{2.41}$$

with G(R,t) = $2\pi\nu\Sigma R^3\Omega'$ and the prime mark denoting the radial derivative.

Combining (2.40) and (2.41) we get

$$\frac{\partial}{\partial t}(\Sigma R^2\Omega) + R^{-1}\frac{\partial}{\partial R}(\Sigma R^3 v_R\Omega) = R^{-1}\frac{\partial}{\partial R}(\nu\Sigma R^3\Omega') \tag{2.42}$$

Combining the mass equation (2.39) and the angular momentum equation (2.42) we can eliminate v_R to get

$$\frac{\partial \Sigma}{\partial t} = R^{-1} \frac{\partial}{\partial R} \left[[(R^2 \Omega)']^{-1} \frac{\partial}{\partial R} [\nu \Sigma R^3 (-\Omega')] \right]$$

We now insert Ω using (2.37):

$$\boxed{\frac{\partial \Sigma}{\partial t} = 3R^{-1} \frac{\partial}{\partial R} \left(R^{\frac{1}{2}} \frac{\partial}{\partial R} [\nu \Sigma R^{\frac{1}{2}}] \right)} \tag{2.43}$$

Equation 2.43 represents the basic equation for the time evolution of the surface density of a thin Keplerian accretion disc. If the initial configuration is ring like, it spreads over time, transferring angular momentum from the inner to the outer parts.

Assuming a hydrostatic equilibrium for the disc (z-component of the Euler momentum equation for $\vec{v} = 0$ and the z-component from the central objects force), we can find the vertical disc thickness H:

$$\frac{1}{\rho} \frac{\partial P}{\partial z} = \frac{\partial}{\partial z} \left[\frac{GM}{(R^2 + z^2)^{\frac{1}{2}}} \right] \tag{2.44}$$

Taking the derivative on the right side and replacing $R^2 + z^2$ with R^2 in the denominator using the assumption of a thin disc ($R \gg z$), we can replace the right side with $\frac{-GMz}{R^3}$.

Assuming a typical scale height of H in z direction, the term $\frac{\partial P}{\partial z}$ on the left side of (2.44) can be replaced with $\frac{P}{H}$ (now implying that $R \gg H$). With $P \sim \rho c_s^2$ (adiabatic equation of state, c_s^2 the sound speed) we can solve (2.44) for H:

$$H \approx c_s \left(\frac{R}{GM} \right)^{\frac{1}{2}} R$$

The requirement that $H \ll R$ is fulfilled if:

$$c_s \ll \left(\frac{GM}{R} \right)^{\frac{1}{2}}$$

which states that for the disc to be thin, the local sound speed must be smaller than the rotational speed (the Kepler velocity must be supersonic).

2.2.6   Accretion

The radial transport of material within an accretion disc due to the viscous dissipation of energy leads to material falling onto the central object, which we will assume to be a black hole in our case. In contrast to Bondi-Hoyle accretion, which assumes spherical infall onto the central object, the infall from an accretion disc will be mostly constrained to within the plane of the disc. For the sake of simplicity we will restrict ourselves to spherical symmetric accretion in the following.

Accretion onto a massive object provides an energy source by the release of gravitational potential energy. This energy release can be described in terms of a luminosity, which leads to a outward directed radiation pressure acting against the inflow of material. This results in a self regulating process. With a high accretion rate, the outward radiation pressure will become high, suppressing the accretion of material. The low accretion rate in turn will lead to a lower outward radiation pressure, so that the accretion rate can rise again. Assuming a steady accretion flow and spherical symmetric accretion, the luminosity at which the outward pressure and the accretion rate are in equilibrium is called Eddington-Luminosity, given by:

$$L_{edd} = 4\pi G M m_p c / \sigma_T \tag{2.45}$$

with m_p the proton mass and σ_T the Thompson cross-section. The Eddington luminosity is derived assuming low-energy elastic scattering of photons of the outward radiation flow on the inflowing electrons of the ionised accretion flow (Thompson scattering). Protons inside the accretion flow will be dragged along by the electrons due to the Coulomb force. If accretion occurs only on a fraction f of the sphere but still only depends on the distance from the central object, the Eddington luminosity is given by $f \cdot L_{edd}$.

We now assume that the central object accretes matter at a rate $\dot{M}$ and that a fraction ϵ of the rest mass energy is radiated away. Then the luminosity can be written as:

$$L = \epsilon \dot{M} c^2 \tag{2.46}$$

However, we know that luminosity can not exceed the Eddington luminosity. Setting the luminosity (2.46) equal to the Eddington luminosity (2.45), we can solve for the limiting accretion rate:

$$\boxed{\dot{M}_{edd} = \frac{4\pi G M m_p}{\epsilon\ c\ \sigma_T}}$$

This is the so called Eddington accretion rate, the maximum allowed rate of accretion of material. A typical value of ϵ (which is also called accretion efficiency) for accretion onto a black hole would be around 0.1 (10 percent). The Eddington rate is not a strict global limit. Objects can accrete at rates higher than the Eddington rate, for example if the accretion disc is geometrically thick and optically thin (which allows black holes in the early

Universe to grow very fast) or if the outward radiation is extremely collimated towards a direction different from the infall of material.

The sphere of influence of a black hole, also called the accretion radius, can be calculated by simply equating the escape velocity (2.10) at the distance r from the black hole to the local sound speed. If the escape velocity is larger than the local sound speed, gas can no longer escape the influence of the black hole and will start falling towards it. The accretion radius is given by:

$$r_{acc} = \frac{2GM}{c_s^2}$$

2.2.7   Gravitational Disc Instabilities

Following the lecture of Weinberg (2003) we consider a plane parallel flow problem (no y or z dependence). In this case the continuity, momentum and gravity (Poisson) equations are given by:

$$\frac{\partial \rho}{\partial t} + u\frac{\partial \rho}{\partial x} + \rho\frac{\partial u}{\partial x} = 0$$

$$\frac{\partial u}{\partial t} + u\frac{\partial u}{\partial x} = -\frac{1}{\rho}\frac{\partial P}{\partial x} + g$$

$$\frac{\partial g}{\partial x} = -4\pi G\rho$$

We assume a uniform and static medium, such that $u = 0$, $P = P_0$, $\rho = \rho_0$. Now we introduce small perturbations, u_1, P_1, ρ_1, g_1 with $\rho = \rho_0 + \rho_1$, $P = P_0 + P_1$, $u = u_1$ and $g = g_1$. The last equation assumes $g_0 = 0$, which would require $\rho = 0$ from the gravity equation. Since we only approximate to lowest order we can ignore this problem (the so called "Jeans swindle").

After substitution into the equations, keeping only terms that are first order in the perturbations we get:

$$\frac{\partial \rho_1}{\partial t} + \rho_0\frac{\partial u_1}{\partial x} = 0$$

$$\frac{\partial u_1}{\partial t} = -\frac{1}{\rho_0}\frac{\partial P_1}{\partial x} + g_1$$

$$\frac{\partial g_1}{\partial x} = -4\pi G\rho_1$$

With $P = P(\rho)$ and multiplying by ρ_0 the momentum equation can be rewritten as:

$$\rho_0\frac{\partial u_1}{\partial t} + \frac{dP}{d\rho}\Big|_0\frac{\partial \rho_1}{\partial x} = g_1\rho_0$$

Taking the time derivative of the continuity equation and the spatial derivative of the momentum equation gives:

$$\frac{\partial^2 \rho_1}{\partial t^2} + \rho_0\frac{\partial}{\partial t}\left(\frac{\partial u_1}{\partial x}\right) = 0$$

$$\rho_0\frac{\partial}{\partial x}\left(\frac{\partial u_1}{\partial t}\right) + \frac{dP}{d\rho}\Big|_0\frac{\partial^2 \rho_1}{\partial x^2} = \frac{\partial g_1}{\partial x}\rho_0$$

Substituting the gravity equation for $\frac{\partial g_1}{\partial x}$ on the right side of the second equation and subtracting the second equation from the first, gives the equation:

$$\frac{\partial^2 \rho_1}{\partial t^2} - \frac{dP}{d\rho}\Big|_0 \frac{\partial^2 \rho_1}{\partial x^2} = 4\pi G \rho_0 \rho_1 \tag{2.47}$$

In the case of negligible self-gravity, the right side of equation (2.47) is zero. Then (2.47) is simply a wave equation for a wave propagating at sound speed $c_s^2 = \frac{dP}{d\rho}\big|_0$. Perturbations thus propagate like waves.

Taking the case of non-negligible self-gravity in equation (2.47), we consider a special form for the perturbation:

$$\rho_1 = exp[i(\omega t - kx)] \tag{2.48}$$

From Fourier analysis we know that the superposition of such perturbations can form any periodic function. In linear perturbation theory the different modes do not interact to first order, so we can solve for the general representation above and later add up modes by inserting specific values. Inserting the second derivatives of (2.48), which are $\frac{\partial^2 \rho_1}{\partial t^2} = -\omega^2 \rho_1$ and $\frac{\partial^2 \rho_1}{\partial x^2} = -k^2 \rho_1$ into equation (2.47) gives:

$$\omega^2 = k^2 c_s^2 - 4\pi G \rho_0 \tag{2.49}$$

Defining $k_J = \frac{\sqrt{4\pi G \rho_0}}{c_s}$, we find for $k > k_J$ that ω is real which implies oscillating sound waves that propagate without growing. For $k < k_J$, ω is imaginary and long wavelength perturbations grow exponentially due to self-gravity. For $k \ll k_J$ the growth timescale is approximately the free fall time $(G\rho_0)^{\frac{1}{2}}$.

The so called Jeans length is defined by $\lambda_J = \frac{2\pi}{k_J}$. Perturbations are gravitationally unstable if a sound wave can not cross within a free fall time. Equation (2.49) can be rewritten in terms of the surface density of a gaseous disc. A useful quantity is then represented by the Toomre Q parameter, which determines the threshold between the gravitationally stable and unstable regime. The parameter is defined as:

$$Q = \frac{\kappa c_s}{\pi G \Sigma}$$

with Σ the disc surface density and κ the epicyclic frequency (rate of oscillation of a radially displaced fluid element). A Toomre parameter of $Q < 1$ means the region is gravitationally unstable, whereas a $Q > 1$ means the region is stable.

2.2.8 Shocks and Hydrodynamical Instabilities

In general a shock is a pressure driven compressive disturbance in a flow, which produces irreversible change in the fluid state due to the increase of entropy. Assuming certain conditions in the unshocked flow, namely a density ρ_1 and a temperature T_1, it is possible to relate those quantities to the post-shock state ρ_2 and T_2. The derivation of those "jump conditions" uses again the momentum and energy fluid equations.

The results are the so called Rankine-Hugoniot jump conditions (for a plane-parallel shock):

$$\rho_1 u_s = \rho_2(u_s - u_2)$$

$$\rho_1 u_s u_2 = \rho_2 u_2(u_s - u_2)$$

$$\rho_2 u_2 = \rho_1 u_s(\frac{1}{2}u_2^2 + e_2 - e_1)$$

with u_s the shock wave speed, u_2 the fluid velocity inside the shock and e_1, e_2 the specific internal energy of the fluid before and after the shock.

The strength of a shock is characterised by the ratio of the speed of sound of the pre-shock flow u_1 to the shock wave speed:

$$M = \frac{u_1}{u_s}$$

This number is called the Mach Number. A shock is supersonic if $M > 1$ and strong if $M \gg 1$.

Hydrodynamic stability is an important part of fluid mechanics. The onset of instabilities rapidly changes the flow and can lead to the development of turbulence. We restrict ourselves to two well known types of instabilities, the Kelvin-Helmholtz instability and the Rayleigh-Taylor instability.

The Rayleigh-Taylor instability occurs when a dense fluid is placed "above" (in the sense of the direction of a external force) lower density fluid, leading to acceleration of one fluid into the other. Figure 2.2 shows a density plot from a simulation of the Rayleigh-Taylor instability. The characteristic mushroom like feature is well developed, together with eddies at the edges.
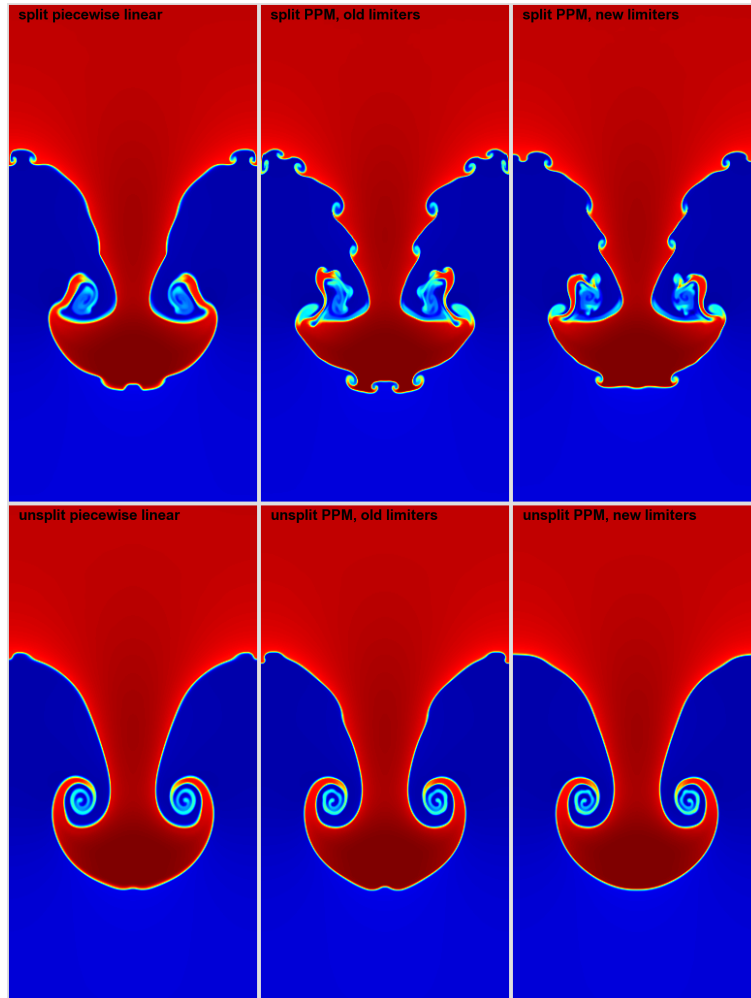
Figure 2.2: Density plot of a simulation of the Rayleigh-Taylor instability using different modes of operation of the simulation-code. Adapted from Almgren et al. (2010).

The Kelvin-Helmholtz instability can occur due to a velocity shear within a single (continuous) fluid or at the interface of two fluids with different velocities. Perturbations at the interface start to grow and form eddies that start mixing the two phases. Figure 2.3 shows a density plot from a simulation of the Kelvin-Helmholtz instability. The characteristic eddies at the interface between the low density fluid part and the high density fluid part are clearly visible.
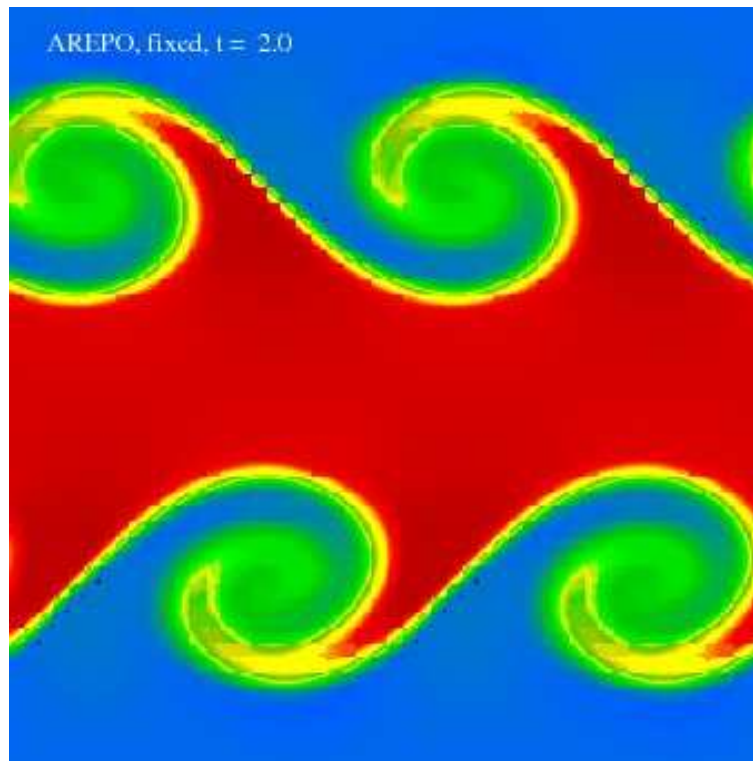
Figure 2.3: Density plot of a simulation of the Kelvin-Helmholtz instability, adapted from Springel (2010).

An analytic analysis of those instabilities, again using the equations of motion of hydrodynamics and applying perturbation theory yields several facts. For the Kelvin-Helmholtz instability, the growth rate of the perturbation is proportional to the component of the wave number in the direction of the flow. This implies that the smallest wavelength perturbations (with largest wave number) grow fastest. The growth rate reduces to zero perpendicular to the direction of the flow. And finally the perturbations diminish exponentially away from the fluid interface. In the case of the Rayleigh-Taylor instability it can be shown that the growth of perturbations at the fluid interface is exponential and that the smallest wavelength also grows the fastest.

2.3   Smoothed Particle Hydrodynamics

In order to solve the equations of motion of hydrodynamics to follow the evolution of a given fluid system we have to rely on computers in most cases, since analytic solutions are only available for a number of idealised systems. However a simulation always means that certain simplifications have to be made. One can not represent every single particle within a fluid due to memory restraints. Also a finite time difference in the time evolution has to be used. There are many considerations and constraints one has to take care of when doing simulations in order not to produce garbage results.

Smoothed Particle Hydrodynamics (SPH) is a particle based (Lagrangian) method to numerically solve the equations of motion of hydrodynamics. The original approach to SPH can be found in the papers of Gingold & Monaghan (1977); Monaghan & Gingold (1977) and Lucy (1977). Here we follow the approach of Price (2012) to derive the equations of motion from first principles.

2.3.1   Calculating Density

In SPH the density at position $\mathbf{r}$ is calculated using a weighted summation over the neighbouring particles:

$$\rho(\mathbf{r}) = \sum_{i=1}^{N_{neigh}} m_i W(\mathbf{r} - \mathbf{r}_i, h) \tag{2.50}$$

Here, h is a scale parameter that determines the fall-off rate of the weight function W. The weight function W is also called the smoothing kernel and the scale parameter h is called the smoothing length. One can make some reasonable requirements for the smoothing kernel. First the weighting of the kernel should be positive and decrease with distance. The kernel also should have smooth derivatives. Second the kernel should be symmetric with respect to $(\mathbf{r} - \mathbf{r}_i)$. And third, the central part of the kernel should be flat so that the density estimate is not too strongly influenced by a small change in position of close particles.

The standard choice for simulations is a Gaussian shaped kernel that is truncated at a finite radius. This has the advantage that the sum (2.50) must not be taken over all the particles inside the domain, which greatly increases the calculation speed for a large number of particles.

A popular choice in SPH codes are B-spline functions which approximate the Gaussian. The lowest order B-spline which is useful for SPH (derivable at least two times) is the cubic spline:

$$W(q,h) = \frac{\sigma}{h^{\mathrm{d}}} \begin{cases} \frac{1}{4}(2-q)^3 - (1-q)^3, & 0 \le q < 1 \\ \frac{1}{4}(2-q)^3, & 1 \le q < 2 \\ 0. & q \ge 2 \end{cases} \qquad (2.51)$$

with q = $|\mathbf{r} - \mathbf{r}'|$. The variable d stands for the number of dimensions and σ is a normalisation constant given by $\sigma = \left[\frac{2}{3}, \frac{10}{7\pi}, \frac{1}{\pi}\right]$ for [1,2,3] dimensions. The kernel is truncated at 2h, particles beyond that distance no longer contribute to the density sum.

One choice for the smoothing length h can be that the mass inside the smoothing sphere is constant. In a high-density region (a large number of particles, which we all assume to have equal mass) the smoothing length automatically should be small so that the mass inside the smoothing sphere stays constant. In a low-density region the smoothing length needs to increase to engulf enough particles so that the mass inside the smoothing sphere is the same constant as in the high-density region. Thus SPH is inherently adaptive and can automatically treat high density regions with a better accuracy.

An obvious choice for the mass inside the smoothing sphere is normally a multiple of the mass of a single SPH particle. Depending on the kernel the choice for this number of neighbours is different. In the case of the cubic spline in three dimensions around 60 neighbours are normally used. If the number of neighbours is too small there can be increased noise and inaccurate wave propagation speeds (Børve et al., 2004). In case the number of neighbours is too high the particle pairing instability can occur (Price, 2012). Higher order B-splines need a larger number of neighbours and increase the accuracy of the density estimate. However this leads to increased computational cost.

2.3.2   Equations of Motion

The fully conservative SPH algorithm can be derived from first principles by using only the density estimate (2.50). Dissipative terms can be inserted later by hand. To derive the equations of motion we start with the Lagrangian $L = T - V$ with T the kinetic and V the potential (here thermal) energy. A single point particle has $T = \frac{1}{2}m_i v_i^2$ and $V = m_i u_i$. Here m_i is the particle mass, v_i the particle velocity and u_i the internal energy per unit mass. In general the internal energy is a function of density ρ and entropy s, $u_i = u_i(\rho_i, s_i)$. For a system of particles the Lagrangian can then be written as:

$$L = \sum_i m_i \left(\frac{1}{2}v_i^2 - u_i \right) \tag{2.52}$$

Using the Euler-Lagrange equations

$$\frac{d}{dt}\left(\frac{\partial L}{\partial \mathbf{v}} \right) - \frac{\partial L}{\partial \mathbf{r}} = 0. \tag{2.53}$$

we can derive the equations of motions from the Lagrangian (2.52). The derivatives are:

$$\frac{\partial L}{\partial \mathbf{v}_i} = m_i \mathbf{v}_i$$

$$\frac{\partial L}{\partial \mathbf{r}_i} = -\sum_j m_j \left. \frac{\partial u_j}{\partial \rho_j} \right|_s \frac{\partial \rho_j}{\partial \mathbf{r}_i} \tag{2.54}$$

We assume here that the entropy is constant, thus only the dependence of u on ρ is important in the derivative. From the first law of thermodynamics we know that

$$dU = TdS - PdV \tag{2.55}$$

where $\delta Q \equiv TdS$ is the heat added to the system per unit volume and $\delta W \equiv PdV$ is the work done by expansion and compression of the fluid. The volume is not computed directly in SPH, but instead one can use the volume estimate given by $V = m/\rho$ resulting in change in volume given by $dV = -m/\rho^2 d\rho$. Switching to quantities per unit mass instead per unit volume (i.e., du instead of dU) equation (2.55) can be rewritten:

$$du = Tds + \frac{P}{\rho^2}d\rho$$

With constant entropy, the term Tds vanishes and the change in thermal energy is:

$$\left. \frac{\partial u}{\partial \rho} \right|_s = \frac{P}{\rho^2}. \tag{2.56}$$

The term $\frac{\partial u_j}{\partial \rho_j}$ in (2.54) can be rewritten using the first law of thermodynamics in this form. To rewrite the term $\frac{\partial \rho_j}{\partial \mathbf{r}_i}$ we use the total derivative of the SPH density estimate (2.50). Assuming that the smoothing length is a function of density we get:

$$\frac{\partial \rho_j}{\partial \mathbf{r}_i} = \frac{1}{\Omega_j} \sum_k m_k \frac{\partial W_{jk}(h_j)}{\partial \mathbf{r}_i} \left(\delta_{ji} - \delta_{ki} \right) \tag{2.57}$$

with Ω defined as

$$\Omega_i \equiv \left[1 - \frac{\partial h_i}{\partial \rho_i} \sum_j m_j \frac{\partial W_{ij}(h_i)}{\partial h_j} \right] \tag{2.58}$$

and W_{ij} the kernel (2.51) evaluated for particle i and j. For a constant smoothing length Ω becomes equal to 1. Now we can insert (2.56) and (2.57) into (2.54) to get

$$\boxed{\frac{d\mathbf{v}_i}{dt} = - \sum_j m_j \left[\frac{P_i}{\Omega_i \rho_i^2} \frac{\partial W_{ij}(h_i)}{\partial \mathbf{r}_i} + \frac{P_j}{\Omega_j \rho_j^2} \frac{\partial W_{ij}(h_j)}{\partial \mathbf{r}_i} \right]} \tag{2.59}$$

Rewriting the equation for specific internal energy (2.56) yields

$$\frac{du_i}{dt} = \frac{P_i}{\rho_i^2} \frac{d\rho_i}{dt} \tag{2.60}$$

Again we use the SPH density estimate (2.50) and substitute for ρ:

$$\boxed{\frac{du_i}{dt} = \frac{P_i}{\Omega_i \rho_i^2} \sum_j m_j (\mathbf{v}_i - \mathbf{v}_j) \cdot \nabla_i W_{ij}(h_i)} \tag{2.61}$$

2.3.3 Artificial Dissipation

Equations (2.50), (2.59) and (2.61) form the full set of equations necessary for conservative SPH. We can now add dissipative terms to the equations of motion to introduce for example viscous effects. A commonly used form for artificial viscosity is given by Monaghan (1992):

$$\left(\frac{d\mathbf{v}}{dt}\right)_{diss} = -\sum_j m_j \frac{-\alpha \bar{c}_{s,ij}\mu_{ij} + \beta \mu_{ij}^2}{\bar{\rho}_{ij}} \hat{\mathbf{r}}_{ij} F_{ij}; \qquad \mu_{ij} = \frac{h\mathbf{v}_{ij}\cdot\mathbf{r}_{ij}}{\mathbf{r}_{ij} + \epsilon \bar{h}_{ij}^2}$$

with barred quantities denoting the average i.e. $\bar{\rho}_{ij} = (\rho_i + \rho_j)/2$, c_s the sound speed, α and β dimensionless (strength) parameters and $\epsilon \sim 0.01$ a small parameter to prevent divergences. Typical values for α and β are $\alpha = 1$ and $\beta = 2$. For shock-capturing viscosity only acts when particles are approaching, which requires $\mathbf{v}_{ij}\cdot\mathbf{r}_{ij} < 0$, otherwise μ_{ij} is set to zero. Advanced viscosity formulations use an adaptive viscosity strength α instead of a fixed value to reduce viscosity within a smooth flow and apply sufficient viscosity at discontinuities.

The Euler equations were derived from the Navier-Stokes equations by neglecting the dissipative effects of viscosity and thermal conduction. Thus we can add another dissipative term which also introduces diffusion in the thermal energy:

$$\left(\frac{du}{dt}\right)_{diss} = -\sum_j \frac{m_j}{\bar{\rho}_{ij}}\left[\frac{1}{2}\alpha v_{sig}(\mathbf{v}_{ij}\cdot\hat{\mathbf{r}}_{ij})^2 + \alpha_u v_{sig}^u(u_i - u_j)\right]\bar{F}_{ij} \qquad (2.62)$$

with α the artificial viscosity strength parameter, α_u the thermal conduction strength parameter and $\bar{F}_{ij} = \hat{\mathbf{r}}_{ij}\cdot\overline{\nabla_i W_{ij}}$. The signal velocity v_{sig} is given by:

$$v_{sig} = \begin{cases} \frac{1}{2}[c_{s,i} + c_{s,j} - \beta\mathbf{v}_{ij}\cdot\hat{\mathbf{r}}_{ij}]; & \mathbf{v}_{ij}\cdot\hat{\mathbf{r}}_{ij} \leq 0; \\ 0; & \mathbf{v}_{ij}\cdot\hat{\mathbf{r}}_{ij} > 0. \end{cases} \qquad (2.63)$$

and the thermal signal velocity in the commonly used form $v_{sig}^u = \sqrt{|P_i - P_j|/\bar{\rho}_{ij}}$. The signal velocities correspond to the maximum (averaged) signal speed between a pair of particles. The left part of the sum in brackets in (2.62) represents the change in thermal energy due to the dissipation of kinetic energy by viscosity. The right part of the sum in brackets represents the diffusion of thermal energy due to the conduction of heat.

SPH simulations of the Kelvin-Helmholtz instability for example need the artificial conductivity term (2.62) to be enabled, otherwise surface tension effects will prevent the formation of eddies at the fluid interface. We will discuss this effect in more detail when we present SPH simulations of the G2 cloud in chapter 6.

2.3.4   Timestep

The concept of a signal velocity (2.63) provides an intuitive way to define a hydrodynamical timestep size. This requires defining the signal velocity such that it reduces to the sum of the sound speeds instead of zero in the non-approaching case. Information between particles is exchanged with the signal velocity. Thus if a signal has travelled far enough to affect other particles, we have to do a force update. A natural scale for the sphere of influence in SPH is the smoothing length h. A simple choice for the timestep of particle i is then given by:

$$\Delta t_i = C_{courant} \frac{2h_i}{\max_j(v_{sig,j})}$$

with the maximum of all signal velocities with respect to i in the denominator. The so called Courant-Factor $C_{courant}$ depends on the solver used to integrate the equations of motion. A value of $C_{courant} < 1$ is used to ensure convergence (Courant-Friedrichs-Lewy Condition). In our simulations we use a value of $C_{courant} = 0.65$.

In practice a number of different timesteps will be calculated for different physics parts, like radiative cooling, gravity calculations and so forth. The minimum of all those timesteps will then be chosen for the evaluation of the particle in question.

2.4   Numerics

2.4.1   Integrating the Equations of Motion

After deriving the equations of motion for SPH (2.50), (2.59) and (2.61), we need a scheme to integrate those equations so that we can follow the time evolution of the system. The partial differential equations of motion can be transformed into a set of ordinary differential equations (ODEs), with a wide range of possible solving methods from mathematics. The solvers can be as accurate as one wants them to be, but a higher accuracy always brings increased computational cost. Thus a trade-off has to be made between accuracy and a reasonable time the integration can take.

ODEs of higher order can always be transferred into a system of first order ODEs, so that we always end up with a coupled system of n first order ODEs with the general form:

$$\frac{dy_i}{dt} = f_i(t, y_1, y_2, ..., y_n)$$

with i = 1..n. In our case the boundary conditions are always given as initial conditions y_i^0 at the starting time t_0. We then want to find y_i^k at time t_k.

The first naive approach one could take is assuming a fixed timestep Δt and just advance all quantities by this timestep. For a single first order ODE this would look like:

$$y^{k+1} = y^k + \Delta t f(t_k, y^k)$$

This method is called Euler forward and a Taylor expansion shows that the leading error term is of the order Δt^2 thus the method is called first order accurate in Δt. The method assumes a simple linear interpolation from time-point to time-point, using the slope at the old point in time as estimate for the linear interpolation to the next point.

For this method to be accurate, the slope should not change much between the current and the next point in time. If we choose the timestep Δt to be smaller and smaller this condition will be better and better fulfilled (given a smooth enough function to approximate). For large timesteps however the assumption that the slope at the current point in time is a good estimate to reach the next point in time on the curve to approximate will completely break down at some point.

The Euler method can be modified and improved. This is done by taking the derivative at the current point and also the next point in time into account. This results in a so called predictor-corrector scheme. First a prediction for y^{k+1} is made using the Euler forward method. This predicted value is then used to calculate the slope at t_{k+1}. Finally y^{k+1} is calculated again (corrected) using the average of the slope at the current point in time t_k and the one calculated for t_{k+1}. The predictor step is:

$$y_{pred}^{k+1} = y^k + \Delta t f(t_k, y^k)$$

Using y_{pred}^{k+1} we get $f_{pred}(t_{k+1}, y_{pred}^{k+1})$. The corrector step is:

$$y^{k+1} = y^k + \Delta t \frac{f + f_{pred}}{2}$$

This method is second order accurate, thus reducing the timestep by a factor of 10 reduces the error by a factor of 100.

The so called Runge-Kutta method evaluates the slope at midpoints between timesteps. For example second order Runge-Kutta does Euler forward towards the middle $\Delta t/2$ of the timestep. Then, using the slope estimated at the midpoint, a full Euler forward step is taken. As the name suggests, second order Runge-Kutta is also second order accurate. Higher order Runge-Kutta divides the timestep into even more sub-steps.

Another class of solvers is designed to control the error of the result. The goal is to have adaptive accuracy, so that the integration can be refined until the error is below a given threshold. An example would be the Fehlberg method, which refines the timestep until the wanted accuracy is reached.

Another important example for a solver is the Leapfrog algorithm, which we will be mainly using in this thesis. The position update is given by:

$$\vec{r}(t + \Delta t) = \vec{r}(t) + \Delta t \vec{v}(t + \Delta t/2)$$

and the velocity update is given by:

$$\vec{v}(t + \Delta t/2) = \vec{v}(t - \Delta t/2) + \vec{a}(t)\Delta t$$

The positions are evaluated at full timesteps and the velocities ("leaping" over the positions) at half-timestep. A great advantage of the Leapfrog is that it is reversible in time. It also conserves energy especially well, which is called a symplectic integrator, thus providing long term integration stability for example in orbital dynamics.

2.4.2   A Small SPH Implementation

To get a better understanding of the SPH algorithm we implemented a small SPH toy code during the course of this thesis. The code uses the conservative SPH formulation from equations (2.50), (2.59) and (2.61). Numerical integration is performed via the leapfrog integrator presented in section 2.4.1. An adaptive hydro smoothing length is used, as well as the standard artificial viscosity prescription from section 2.3.3. The code is weakly parallised using OpenMP and can be used for 1D, 2D and 3D simulations. The nearest neighbour search is also only weakly optimised, giving a slightly better result compared to a direct search over all particles.

In Figure 2.4 we present the result of a standard Sod-Shocktube test conducted with our code in 1D. The red lines show the expectation from the analytic solution, the black dots represent simulation values.
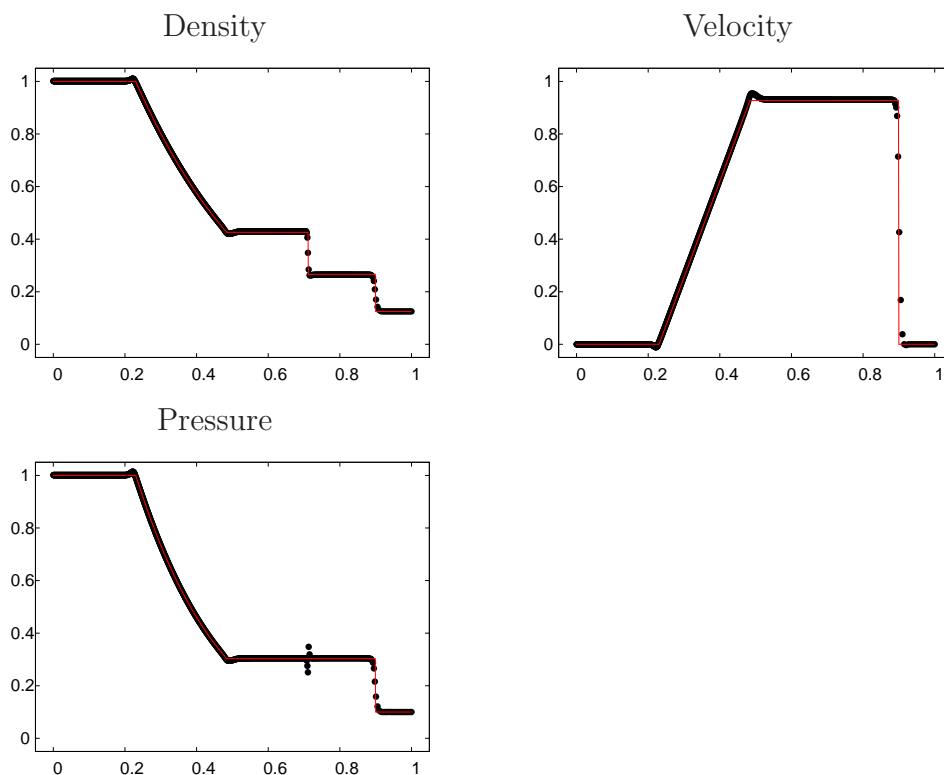
Figure 2.4:   Results of a Sod-Shocktube test conducted with our toy-SPH code. The analytical expectation is shown in red, the values from the simulation as black dots.

Due to the simple nature of the code, it is ideally suited for quick tests involving changes in the SPH formalism. For normal simulations, involving a large number of particles we employed the workhorse code Gadget (Version 2 and 3) written by V. Springel (Springel, 2005). Gadget will be introduced in more detail in the first paper.

2.4.3 Gravity Tree

Calculating forces for a large number of gravitationally interacting particles can become quite costly because the force of every particle towards every other particle has to be calculated. One approach to circumvent this problem is to handle a group of particles like a single particle with the combined mass of all the particles, concentrated at the particle groups centre of mass. This approach is valid if we want to calculate the force onto a test-particle far from this group. Then the force of the single combined mass point onto the test-particle gives an approximately correct estimate for the sum of the individual particle forces from the group.

An algorithm which implements this approach is the so called "Barnes-Hut" algorithm. If we imagine a 2 dimensional distribution of point masses, the algorithm starts with subdividing the square containing all the particles into four sub-squares. Every sub-square is divided into four sub-squares again, until at some point a sub-square only contains a single particle.

If we want to calculate the force exerted onto a given test-particle, we start with the largest sub-squares and calculate for each one the distance r towards the centre of mass from the test-particle. If we call the side length of the sub-square d, we obtain the ratio:

$$\theta = \frac{d}{r}$$

The ratio θ determines the quality of our approximation. Normally a fixed value $\theta_0 < 1$ is set at the beginning and the approximation is accepted if $\theta \leq \theta_0$. If the criterion is not satisfied for a given sub-square, we have to go into the sub-squares of the sub-square and test the criterion again (until we hit a sub-square containing only a single particle). If the criterion is satisfied, the approximation is accepted and we treat all particles within the corresponding sub-square as a single mass point, concentrated at the centre of mass.

For $\theta_0 = 0$ we never satisfy the criterion which corresponds to the full summation over all particles. Larger values of θ_0 correspond to an increasing error in the approximation. The choice of θ_0 reflects a trade-off between increased computation speed and accuracy. In Figure 2.5 an example for a Barnes-Hut tree can be seen, obtained from a code we wrote to calculate the gravitational potential for individual simulation snapshots.
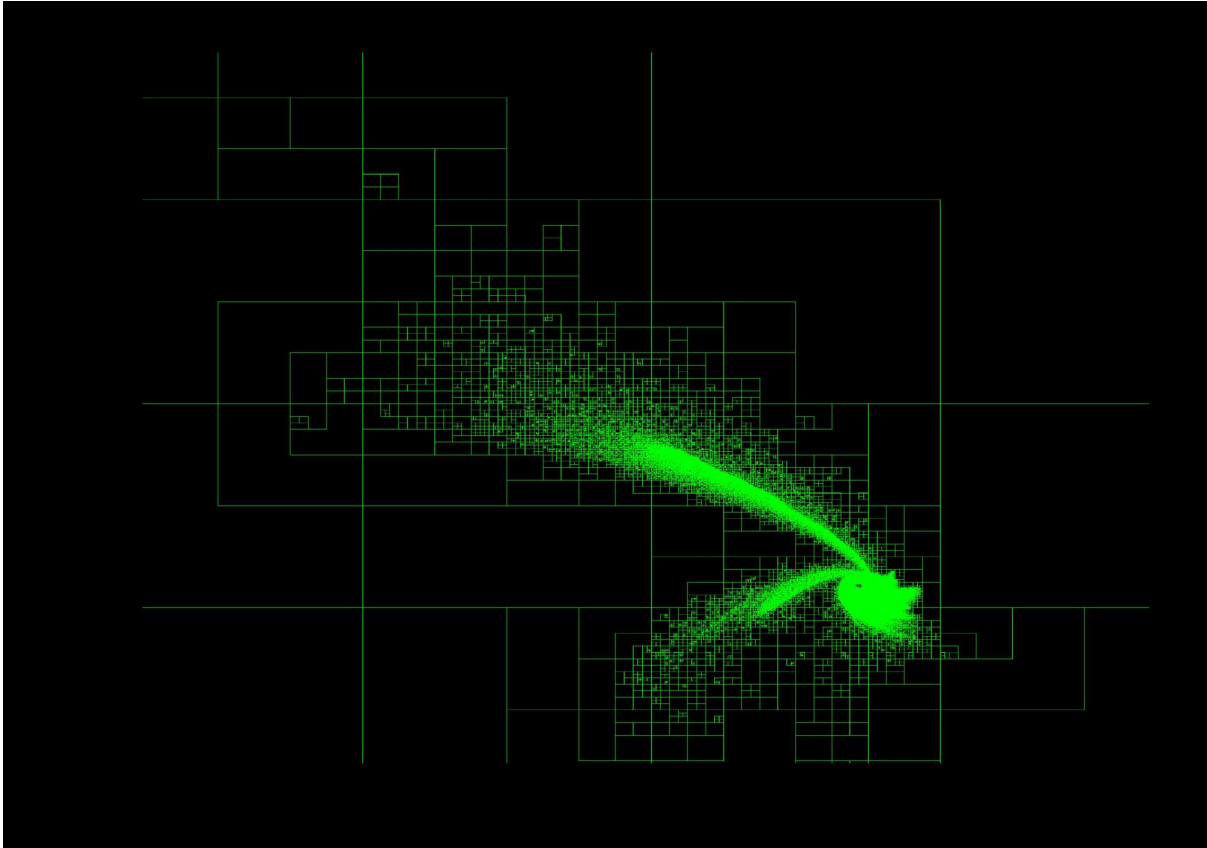
Figure 2.5:   Example of a Barnes-Hut tree using input data from one of our simulations.

Another method to calculate gravitational forces more efficiently is the so called particle-particle-mesh method. Here the density distribution of the particles is mapped onto a grid. Using Fourier-transformation the potential energy at each grid point can be determined very efficiently. For close interactions the mesh is ignored and the direct particle-particle forces are calculated. For far interactions the grid is used.

2.4.4   Resolution Constraints

We start by considering the impact of the smoothing length on simulations. We assume a fixed gravitational smoothing length ϵ and an adaptive hydro-smoothing length h, with a minimum allowed value h_0. At distances smaller than ϵ or h_0, gravitational and hydro forces are strongly suppressed, thus it would be desirable if those distances are never reached. However processes like a gravitational collapse lead to ever-collapsing regions, which will reach the minimum values in any case.

In Bate & Burkert (1997) the authors examine how the choice of ϵ and h_0 influences the result of simulations. The results show that if the values are chosen such that $\epsilon > h_0$, then in a collapsing region gravity will be suppressed before the hydro forces are suppressed. Since the thermal pressure support can dominate, the region can no longer collapse thus artificially stabilising a potentially still gravitationally unstable region.

In the case of $\epsilon < h_0$ the hydro-forces are suppressed before the gravitational forces. In this case a potentially thermal pressure supported region can no longer withstand the gravitational forces and starts to collapse, thus artificially enhancing collapse. The best choice in this case would be $\epsilon = h_0$ so that hydro and gravitational forces are being suppressed at the same scale.

Using an adaptive smoothing length at first gives no spatial resolution limit, since we can choose the minimum values always as small as we want. However normally in SPH the smoothing length h is chosen such that a fixed number of SPH particles lies within h. This corresponds to a fixed mass within the adaptive smoothing length region. A consequence of this fact is that SPH has a mass limited resolution. For a given mass, SPH has to use a certain h, which could be too large if one would be interested in a region small compared to h. To make sure that a region of a certain density is still resolved with a small enough h so that the physics inside is handled correctly and not smoothed out, the authors of Bate & Burkert (1997) developed a formula for the critical density in simulations of gravitationally unstable regions:

$$\rho_{crit} \approx \left(\frac{3}{4\pi}\right)\left(\frac{5R_g T}{2G\mu}\right)^3 \left(\frac{N_{tot}}{2N_{neigh}M_{tot}}\right)^2 \tag{2.64}$$

with R_g the gas constant, T the temperature, μ the mean molecular weight, N_{neigh} the number of particles within the smoothing kernel, N_{tot} the total number of particles and M_{tot} the total mass. The simulation results can no longer be trusted if the local density exceeds ρ_{crit}.

Another important study on numerical simulation requirements has been conducted by Nelson (2006). As a result, three requirements for SPH simulations of gaseous, fragmenting discs are given. The first requirement reproduces the result of Bate & Burkert (1997). The second requirement is that particle based codes with self-gravity should also use an adaptive gravitational smoothing length instead of a fixed length. Test simulations have

shown that even if the critical density criterion is fulfilled, a bad choice for the fixed grav-itational smoothing length can artificially enhance or prevent fragmentation.

The third requirement is that 3D SPH simulations should resolve the vertical disc structure with at least $\sim 4h$ per scale height in both directions from the disc mid plane. Test simulations show that a failure to fulfil this criterion can lead to an underestimation of the disc mid plane density of up to 30-50 percent, which is quite substantial. The resulting underestimation of the gas pressure can again lead to artificially enhanced fragmentation.

2.4.5 Radiative Cooling

Adiabatic and isothermal test-simulations have shown that a large range of densities (10^{-22} $\frac{\text{g}}{\text{cm}^3}$ - 10^{-10} $\frac{\text{g}}{\text{cm}^3}$) and temperatures (50 K up to several 100.000 K) are possible during the course of a simulation which implements the Galactic Centre scenario we are interested in.

In order to carefully account for the thermodynamics of disc formation, we implemented the cooling formalism of Stamatellos et al. (2007) into Gadget. It approximates cooling processes for optically thin, as well as optically thick regions by applying an approximative radiative transfer mechanism using the diffusion approximation. We assume metal abundances that are solar, following observations of Davies et al. (2009).

The basic equation determining the cooling rate is given by:

$$\frac{du}{dt} = \frac{4\,\sigma_{\text{SB}}\,(T_0^4 - T^4)}{\bar{\Sigma}^2\,\bar{\kappa}_{\text{R}}(\rho, T)\,+\,\kappa_{\text{P}}^{-1}(\rho, T)} \tag{2.65}$$

with T_0 the background radiation temperature, T and ρ the particle temperature and density, $\bar{\Sigma}$ the pseudo-mean surface density, $\bar{\kappa}_{\text{R}}$ the pseudo-mean opacity and κ_{P} the Planck-mean opacity.

To model the environment around an SPH particle the method assumes that each SPH particle is embedded into a pseudo cloud with a central density ρ_{c} and a scale radius R_0. The method uses the particle density, temperature and gravitational potential to calculate a pseudo-mean surface density and pseudo-opacity for this cloud. If the pseudo cloud has a high pseudo-mean surface density $\bar{\Sigma}$ and a high pseudo-mean opacity $\bar{\kappa}_{\text{R}}$ the cooling radiation is assumed to be trapped inside the environment and the cooling rate (2.65) is decreased.

The density profile of the pseudo cloud is assumed to be a solution of the Lane-Emden equation

$$\frac{1}{\xi^2}\frac{d}{d\xi}(\xi^2\frac{d\theta}{d\xi}) + \theta^n = 0 \tag{2.66}$$

Solutions of the dimensionless Lane-Emden equation describe the structure of a self-gravitating sphere of fluid, obeying a polytropic equation of state P = K $\rho^{1+\frac{1}{n}}$. Here P is the pressure, K a proportionality constant, ρ the density and n the polytropic index.

Now suppose the SPH particle sits at radius ξ within the pseudo cloud with $0 \leq \xi \leq \xi_{\text{B}}$ and ξ_{B} the radius of the pseudo cloud. The dimensionless radius ξ relates to the real Radius via $R = R_0\xi$. We choose ρ_{c} and R_0 such that it reproduces the actual density and gravitational potential of the particle at its radius $R_0\xi$ inside the cloud.

To get the surface density at the particle radius inside the pseudo cloud, we integrate over density times differential radial element from the particle radius up to the cloud surface.

$$\Sigma(\xi) = \int_{\xi'=\xi}^{\xi'=\xi_{\mathrm{B}}} \rho_c \, \theta^n(\xi') \, R_0 d\xi' \tag{2.67}$$

Now define a pseudo-mean surface-density by using the average of $\Sigma(\xi)$ over all possible radii ξ:

$$\bar{\Sigma} = \left[-\xi_B^2 \frac{d\theta}{d\xi}(\xi_B) \right]^{-1} \int_{\xi=0}^{\xi=\xi_B} \Sigma(\xi) \ \ \theta^n(\xi) \, \xi^2 d\xi \tag{2.68}$$

The trick here is that since we do not know the actual position of the SPH particle within the pseudo cloud, we just average over all possible positions. The first term in (2.68) represents the dimensionless mass of the polytrope, so the average is mass weighted. Figure 2.6 shows a sketch of the pseudo-cloud model.
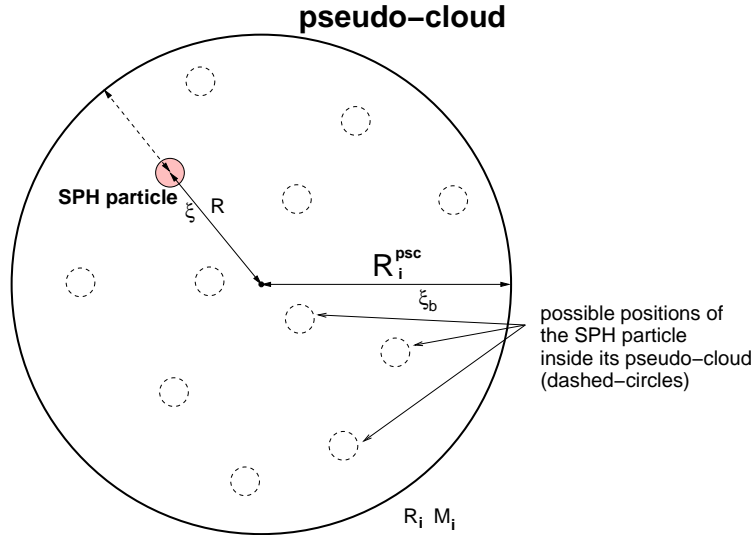
Figure 2.6: A sketch depicting the position of the SPH particle within the pseudo cloud at radius ξ, adapted from Stamatellos et al. (2007)
.

The Planck-mean opacity is implemented using the simple parametrisation by Bell & Lin (1994):

$$\kappa_P(\rho, T) = \kappa_0 \rho^a T^b \tag{2.69}$$

with κ_0, a and b parameters that depend on the dominant physical process contributing to the opacity in different temperature and density regimes. Table 2.1 gives an overview of

the used values and Figure 2.7 shows the density and temperature regimes for the different processes.

Dominant process	κ_0	a	b
Ice grains	2×10^{-4}	0	2
Evaporation of ice grains	2×10^{16}	0	-7
Metal grains	0.1	0	$\frac{1}{2}$
Evaporation of metal grains	2×10^{81}	1	-24
Molecules	10^{-8}	$\frac{2}{3}$	3
H- scattering	10^{-36}	$\frac{1}{3}$	10
Bound-free and free-free	1.5×10^{20}	1	$\frac{-5}{2}$
Electron scattering	0.348	0	0

Table 2.1: Table of processes that contribute to opacity, adapted from Bell & Lin (1994).
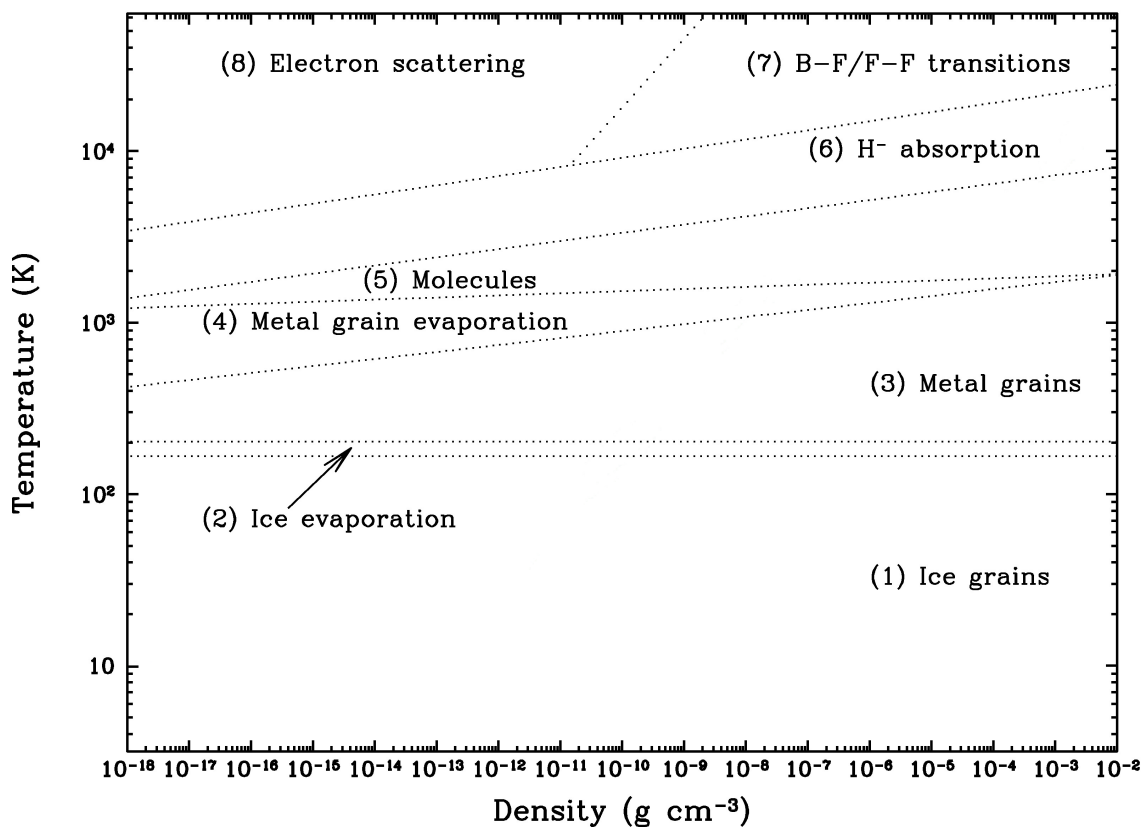
Figure 2.7: Temperature and density range in which the processes from Table 2.1 are valid, adapted from Stamatellos et al. (2007).

In the same way as before (just replace Σ in (2.67) by κ) one can calculate the radial optical depth τ and from that a pseudo-mean optical depth $\bar{\tau}$.

Define a pseudo-mean opacity by using $\bar{\kappa} = \frac{\bar{\tau}}{\bar{\Sigma}}$ to get:

$$\bar{\kappa} = \left[-\zeta_n \, \xi_{\mathrm{B}}^2 \, \frac{d\theta}{d\xi}(\xi_{\mathrm{B}}) \right]^{-1} \int_{\xi=0}^{\xi=\xi_B} \int_{\xi'=\xi}^{\xi'=\xi_B} \times$$

$$\kappa_R \left(\rho \left[\frac{\theta(\xi')}{\theta(\xi)} \right]^n, T \left[\frac{\theta(\xi')}{\theta(\xi)} \right] \right) \left[\frac{\theta^{n+2}(\xi')}{\phi(\xi)} \right]^{1/2} d\xi' \xi^2 d\xi$$

We can now act as if radiation has to pass through surrounding material with an optical depth $\bar{\tau} = \bar{\kappa}\bar{\Sigma}$ and calculate how much of this radiation gets absorbed.

The pseudo-mean opacity $\bar{\kappa}$ can be pre-calculated for a range of values suited for the simulation, thus reducing the computational demands of the cooling routine. The pseudo-mean surface density $\bar{\Sigma}$ depends on the gravitational potential of the particle, so it can not be pre-calculated, but it can be integrated analytically so that no numerical integration during the simulation is necessary.

Figure 2.8 shows our pre-calculated values for the Planck-mean opacity and the pseudo-mean opacity for the range of temperatures and densities suited for our simulations.

Assuming a mixture of (X = 0.7) 70% hydrogen, (Y = 0.3) 30% helium (metals are negligible although their contribution to opacity is large) the specific internal energy is a composition of:

$$u = u_{H_2} + u_H + u_{He} + u_{H_2 diss} + u_{H_{ion}} + u_{He_{ion}} + u_{He_{ion}^+} \tag{2.70}$$
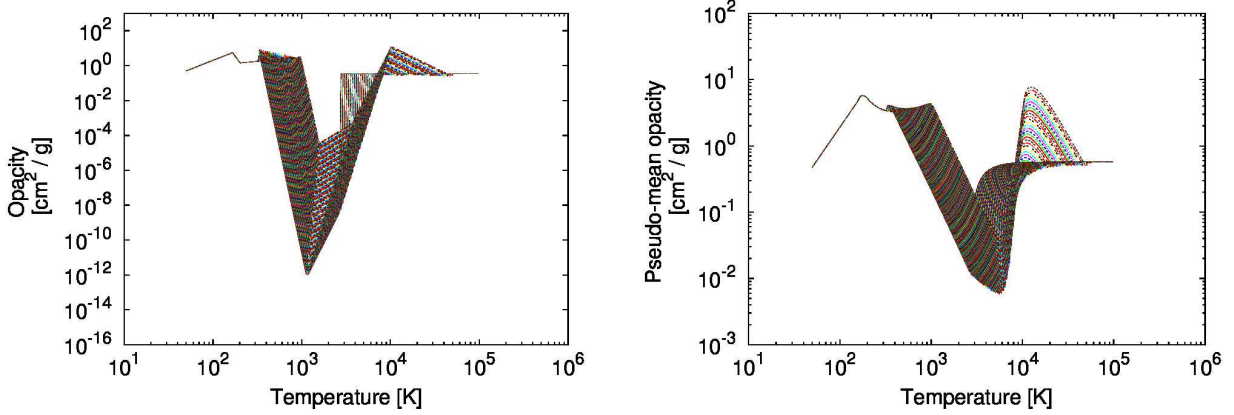
Figure 2.8:   Our pre-calculated values for the Planck-mean opacity and the pseudo-mean opacity. Different curves represent different density values, from 10^{-22} cm^{-3} (bottom) to 10^{-9} cm^{-3} (top).

The abundances of the individual components are calculated using the Saha-equation:

$$\frac{n_{i+1}\, n_e}{n_i} = \frac{2}{\Lambda^3}\frac{g_{i+1}}{g_i} exp\left(\frac{-\epsilon_{i+1} + \epsilon_i}{kT}\right) \tag{2.71}$$

with n$_i$ the particle density, i the ionisation degree, n$_e$ the electron density, g$_i$ the degeneracy of states for the ion, ϵ_i the energy required to reach ionisation degree i starting from neutral and Λ the thermal de Broglie wavelength of the electron.

Using the definitions

$y = n_{\text{H}^\circ}/2n_{\text{H}_2}$ (the degree of dissociation of hydrogen)
$x = n_{\text{H}^+}/n_{\text{H}^\circ}$ (the degree of ionisation of hydrogen)
$z_1 = n_{\text{He}^+}/n_{\text{He}^\circ}$ (the degree of single ionisation of helium)
$z_2 = n_{\text{He}^{++}}/n_{\text{He}^+}$ (the degree of double ionisation of helium)

the mean molecular weight is given by

$$\mu_i = \mu(\rho_i, T_i) = \left[(1 + y + 2xy)\frac{X}{2} + (1 + z_1 + z_1 z_2)\frac{Y}{4}\right]^{-1}$$

and the specific internal energy can be calculated using:

$$u_{\text{H}_2} = X(1 - y)\left[\frac{3}{2} + c_i(T_i)\right]\frac{k_{\text{B}}T_i}{2m_{\text{H}}}$$

$$u_{\text{H}} = X\, y\, (1 + x)\frac{3k_{\text{B}}T_i}{2m_{\text{H}}}$$

$$u_{\mathrm{He}} = Y \left(1 + z_1 + z_1 z_2\right) \frac{3 k_{\mathrm{B}} T_i}{8 m_{\mathrm{H}}}$$

$$u_{\mathrm{H_2 DISS}} = X\, y\, \frac{\mathcal{D}_{\mathrm{H_2 DISS}}}{2\, m_{\mathrm{H}}}$$

$$u_{\mathrm{H\,ION}} = X\, x\, y\, \frac{\mathcal{I}_{\mathrm{H\,ION}}}{m_{\mathrm{H}}}$$

$$u_{\mathrm{He\,ION}} = Y\, z_1 \left(1 - z_2\right) \frac{\mathcal{I}_{\mathrm{He\,ION}}}{4\, m_{\mathrm{H}}}$$

$$u_{\mathrm{He^+ION}} = Y\, z_1\, z_2\, \frac{\mathcal{I}_{\mathrm{He^+ION}}}{4\, m_{\mathrm{H}}}$$

with $\mathcal{D}_{\mathrm{H_2 DISS}} = 4.5\,\mathrm{eV}$ the dissociation energy of H_2 and $\mathcal{I}_{\mathrm{H\,ION}} = 13.6\,\mathrm{eV}$, $\mathcal{I}_{\mathrm{He\,ION}} = 24.6\,\mathrm{eV}$ and $\mathcal{I}_{\mathrm{He^+ION}} = 54.4\,\mathrm{eV}$ the ionisation energies of H°, He° and He⁺.

The function

$$c_i(T_i) = \left(\frac{T_{\mathrm{ROT}}}{T_i}\right)^2 f(T_i) + \left(\frac{T_{\mathrm{VIB}}}{T_i}\right)^2 \frac{\exp(T_{\mathrm{VIB}}/T_i)}{\left[\exp(T_{\mathrm{VIB}}/T_i) - 1\right]^2}$$

with $T_{\mathrm{ROT}} = 85.4\,\mathrm{K}$ and $T_{\mathrm{VIB}} = 6100\,\mathrm{K}$ accounts for the rotational and vibrational degrees of freedom of H_2. The function $f(T_i)$ depends on the relative abundances of ortho- and para-H_2. The authors of Stamatellos et al. (2007) assume a fixed ortho-to-para ratio of 3:1.

For a small optical depth $\bar{\Sigma}^2\,\bar{\kappa}_{\mathrm{R}}(\rho, T) \ll \kappa_{\mathrm{P}}^{-1}(\rho, T)$ equation (2.65) reduces to the usual cooling term for the optically thin cooling regime.

$$\frac{du}{dt} \simeq -4\, \sigma_{\mathrm{SB}}\, T^4\, \kappa_{\mathrm{P}}(\rho, T)$$

For a large optical depth $\bar{\Sigma}^2\,\bar{\kappa}_{\mathrm{R}}(\rho, T) \gg \kappa_{\mathrm{P}}^{-1}(\rho, T)$ equation (2.65) reduces to the diffusion approximation.

$$\frac{du}{dt} \simeq \frac{4\, \sigma_{\mathrm{SB}}\, T^4}{\bar{\Sigma}^2\, \bar{\kappa}_{\mathrm{R}}(\rho, T)}$$

The actual implementation of the cooling into Gadget works as follows. At each simulation timestep the following steps are undertaken:

- Approximate the mean optical depth of the environment of each SPH particle by using the density and gravitational potential following the procedure as described above. In the case of non-SPH particles, exclude them from the gravitational potential calculation.

- Calculate the compressive heating rate and radiative cooling rate. In the case of T < T_0 we have radiative heating instead of cooling.

- In contrast to the original implementation of Stamatellos et al. (2007) we do not adjust the individual particle timesteps. The particle density should not change much during the particle timestep due to the stability criterion of the hydrodynamics calculations. Instead we force the particle onto the cooling curve by only allowing a certain percentage of the specific internal energy to be radiated away at a constant cooling rate. For this the particle timestep is subdivided inside the cooling routine. As soon as a certain percentage of the total internal energy is radiated away, the cooling rate will be re-calculated. This process is repeated until the particle timestep is used up. Tests have shown that the results are relatively insensitive to the actual value. We choose a value of 10 percent for our simulations (the value is a trade-off between computational cost and accuracy). Tests have been performed down to 0.1 percent.

- Update the internal energy of each SPH particle according to the total change in heating plus cooling.

Chapter 3

Paper I

3.1 Simulations of Direct Collisions of Gas Clouds with the Central Black Hole

C. Alig, A. Burkert, P.H. Johansson, M. Schartmann

We perform numerical simulations of clouds in the Galactic Centre (GC) engulfing the nuclear super-massive black hole and show that this mechanism leads to the formation of gaseous accretion discs with properties that are similar to the expected gaseous progenitor discs that fragmented into the observed stellar disc in the GC. As soon as the cloud hits the black hole, gas with opposite angular momentum relative to the black hole collides downstream. This process leads to redistribution of angular momentum and dissipation of kinetic energy, resulting in a compact gaseous accretion disc. A parameter study using thirteen high resolution simulations of homogeneous clouds falling onto the black hole and engulfing it in parts demonstrates that this mechanism is able to produce gaseous accretion discs that could potentially be the progenitor of the observed stellar disc in the GC. A comparison of simulations with different equations of state (adiabatic, isothermal and full cooling) demonstrates the importance of including a detailed thermodynamical description. However the simple isothermal approach already yields good results on the radial mass transfer and accretion rates, as well as disc eccentricities and sizes. We find that the cloud impact parameter strongly influences the accretion rate whereas the impact velocity has a small affect on the accretion rate.

3.2   Introduction

Observations reveal an interesting feature in our Galactic Centre (GC): one (Lu et al., 2009) or two (Genzel et al., 2003; Ghez et al., 2005; Paumard et al., 2006; Bartko et al., 2009) sub-parsec-scale rings of young stars near the radio source SgrA* which cannot be explained by normal means of star formation due to the hostility of the environment. Tidal forces would disrupt typical molecular clouds in the vicinity of the central black hole, preventing their normal condensation into stars due to the self-gravity induced collapse of the cloud.

Observations find around 100 young and massive stars distributed in a warped clockwise rotating disc/ring and a second inclined counter-clockwise rotating disc/ring, the existence of which is still a matter of debate (Lu et al., 2009). The observed outer edge of the system is at around 0.5 pc. This estimate is still increasing due to the addition of newly observed stars belonging to the disc structure. The inner edge is at around 0.04 pc (Genzel et al., 2003). The mean eccentricity of the clockwise rotating system is measured to be 0.34 ± 0.06 (Bartko et al., 2009).

The currently most plausible formation scenario postulates that the stellar rings formed by fragmentation of self-gravitating (in some cases eccentric) accretion discs (Poliachenko & Shukhman 1977; Kolykhalov & Syunyaev 1980; Shlosman & Begelman 1987; Rice et al. 2005; Alexander et al. 2008 and first applied to our GC in Sanders 1998; Levin & Beloborodov 2003). These studies concentrated mainly on the fragmentation of an already existing accretion disc. The question how these discs formed in the first place has only recently been discussed, e.g. by Wardle & Yusef-Zadeh (2008), Mapelli et al. (2008), Hobbs & Nayakshin (2009) and Bonnell & Rice (2008). In their models, reviving the origin of the stars from a molecular cloud, the accretion discs are built up by the rapid deposition of gas around the central black hole through the infall and tidal disruption of a gas cloud. However, here the problem arises that a gas cloud that most likely formed far from the GC where tidal forces are inefficient must be placed on an orbit with a close passage around the black hole.

Furthermore, the cloud should not be disrupted by internal star formation processes before encountering the black hole. Mapelli et al. (2008), Hobbs & Nayakshin (2009) and Bonnell & Rice (2008) studied the formation of a disc by a cloud or clouds passing the central black hole at some distance larger than the cloud radius. However, Wardle & Yusef-Zadeh (2008) showed that it is very unlikely for a cloud to be captured by the black hole without engulfing it during the encounter, as only a small set of initial parameters would lead to such an event. Thus Wardle & Yusef-Zadeh (2008) proposed a model in which the infalling cloud covers the black hole in parts during its passage. This process efficiently redistributes angular momentum through the collision of material streaming around the black hole with opposite angular momentum, finally resulting in a compact accretion disc. A related scenario for the effective cancellation of angular momentum has also been simulated by Hobbs

& Nayakshin 2009, who studied the collision of two clouds with opposite angular momentum close to the GC black hole.

In this first paper we elaborate on this scenario and study direct encounters of gas clouds with the central black hole in detail using high-resolution numerical simulations. We focus on the resulting gaseous disc properties for cloud impact parameters that match the Milky Way GC. The resulting gas disc could then be the progenitor of the observed stellar disc. Clearly, a potential caveat is the fact that the GC stellar disc is already many orbital periods old and could have undergone substantial secular dynamical evolution (see e.g. Ulubay-Siddiki et al. 2009; Löckmann et al. 2009; Madigan et al. 2009).
Arguments have however also been presented that the observed stellar disc properties are more or less set by the initial gaseous disc properties (Alexander et al. 2007; Cuadra et al. 2008). The estimated mass of the gaseous disc that formed the stars is expected to be around 10^{4-5} M$_\odot$ (Nayakshin & Cuadra, 2005; Nayakshin et al., 2006). Some fraction of the disk might have been accreted onto the central black hole. Note, that here, we are not focusing on this long term viscous evolution of the resulting accretion disc which we are in any case unable to follow and resolve with our current numerical scheme. Instead we focus on the formation of the initial gaseous disc resulting from the collision of the cloud with the black hole. In a follow-up paper we will discuss fragmentation and star formation inside the accretion disc.

This paper is structured as follows. In Section 3.3 we present a motivation for our model. In Section 3.4 the numerical method and the initial setup of the model are presented. The main results as a function of varying impact parameters, initial cloud velocities and different equations of state are presented in Section 3.5. Finally, we summarise and discuss our findings in Section 3.6. In the appendix, code tests to demonstrate the numerical stability of our results are presented.

3.3   Motivation

In order to motivate our model we consider a cloud (modelled as a homogeneous sphere of gas) on an arbitrary Keplerian orbit around the black hole. We define d_0 to be the initial distance of the cloud from the black hole, v_0 to be the initial absolute cloud velocity with respect to the stationary black hole, α to be the angle between the radial vector and the velocity vector and r_{cl} to be the cloud radius (see Figure 3.1). In addition we define the plane opened by the radial vector and the velocity vector to be the xy-plane in Cartesian coordinates. We also restrict ourselves to $\alpha = 0$ - $\frac{\pi}{2}$ due to symmetry.
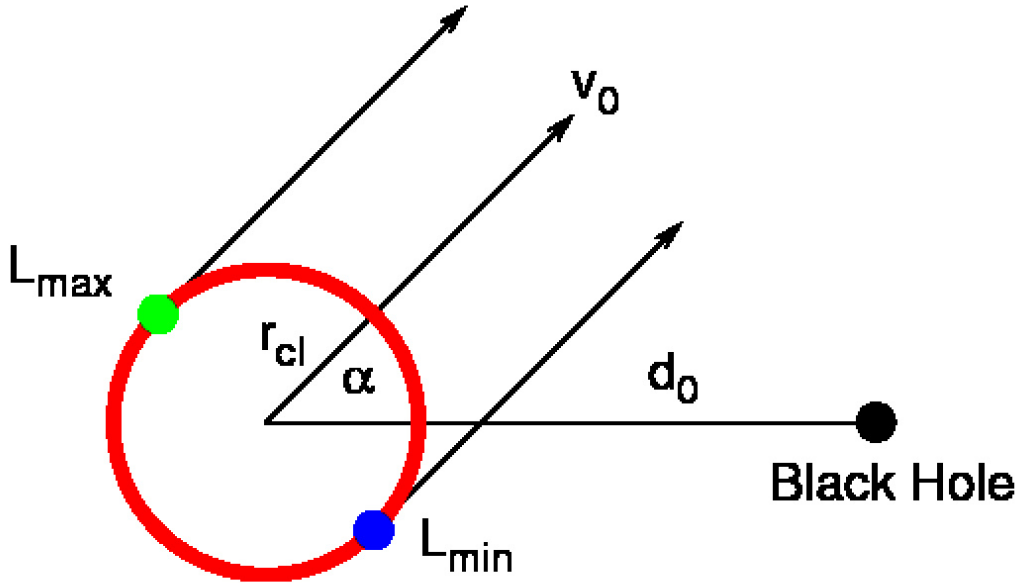

Figure 3.1: Coordinate system used to calculate the cloud angular momentum. We define d_0 to be the distance from the black hole to the cloud, v_0 to be the initial absolute cloud velocity, α to be the angle between radial vector and velocity vector and r_{cl} to be the cloud radius. L_{max} is the point with largest angular momentum and L_{min} the point with the smallest angular momentum (as long as the cloud is not engulfing the black hole).

The minimum/maximum angular momentum of the cloud is then given by the points on the cloud-surface in the xy-plane for which the velocity vector is tangential to the cloud surface ($L_{z,min}$ will only be the minimum angular momentum as long as the cloud is bypassing the black hole). The z-components of the specific angular momentum for these points are:

$$L_{z,min} = +v_0(r_{cl} - sin(\alpha)d_0) \qquad (3.1)$$

$$L_{\mathrm{z,max}} = -v_0(r_{\mathrm{cl}} + sin(\alpha)d_0) \qquad (3.2)$$

All parts of the cloud will have the same direction of rotation if the sign of $L_{\mathrm{z,min}}$ is equal to the sign of $L_{\mathrm{z,max}}$. Otherwise, a part of the cloud will rotate in the opposite direction. Since all quantities are larger than zero, the sign of $L_{\mathrm{z,min}}$ is given by the term $r_{\mathrm{cl}} - sin(\alpha)d_0$. If this term becomes negative the whole cloud will bypass the black hole, if it becomes positive parts of the cloud will engulf the black hole (and now $L_{\mathrm{z,min}}$ represents the maximum angular momentum of the counter-rotating part of the cloud). Both of these scenarios can lead to the formation of an accretion disc.

In general, a clump of gas coming from infinity can still be captured by a black hole due to dissipation of its kinetic energy induced by the gravitational interaction with the black hole. Shearing along the path of infall and tidal compression leads to colliding flows inside the clump close to the black hole. This effectively turns kinetic energy into thermal energy and thus reduces the cloud velocity. This way a previously unbound cloud can become bound to the black hole. However, angular momentum needs to be conserved. As long as the cloud stays on an eccentric orbit, tidal forces will lead to dissipation of kinetic energy during every pericentre passage until the cloud finally ends up on a circular orbit with the same angular momentum as initially. By comparing the angular momentum of a circular orbit to the initial angular momentum we can therefore calculate the radius of the final circular disc. Using $L_{\mathrm{z,max}}$ we get:

$$r_{\mathrm{disk}} = \frac{v_0^2(r_{\mathrm{cl}} + sin(\alpha)d_0)^2}{GM_{\mathrm{BH}}} \qquad (3.3)$$

In order to estimate the likelihood of a cloud bypassing or engulfing the central black hole and thus forming the observed stellar disc we restrict our parameters to values suited for the Milky-Way GC. We take d_0 to be in the range of 5 - 50 pc and uniformly distributed. Here 5 pc corresponds to the centre of the circum-nuclear disc (Vollmer et al., 2003), a reservoir of clumpy, molecular gas (around 10^5 M$_\odot$) which is the first substantial source of gas near the black hole. Following Vollmer et al. 2003 we restrict the source of our clouds to be within the central 50 pc region. We already restricted α to 0 - $\frac{\pi}{2}$ and assume a Gaussian distribution in α centred on $\frac{\pi}{4}$ since it should be very unlikely that a cloud is on a direct radial orbit towards the black hole or that it originates exactly from the apocentre of an elliptic orbit. For the cloud velocity we take fixed values of 20, 30, 50 and 80 km/s.

We restrict the cloud radius r_{cl} to be in the range between 1.8 - 10 pc, which is motivated as follows. Based on a GC region survey, Miyazaki & Tsuboi 2000 were able to derive the distribution of molecular cloud sizes to be $dN/dr_{\mathrm{cl}} \sim r_{\mathrm{cl}}^{-4}$ which spans a range between 10 pc and their resolution limit of 3.3 pc. Taking into account the total molecular gas of 10^8 M$_\odot$ in the inner 500 pc (Güsten & Philipp 2004), the observed number of clouds of 160 and a mean cloud mass of 10^5 M$_\odot$, we find that there should be roughly an additional 1000 clumps of 10^5 M$_\odot$. We note that the required mass in the gaseous disc that formed

the observed stellar disc is around 10^5 M$_\odot$ (Nayakshin & Cuadra, 2005; Nayakshin et al., 2006). Thus the smallest cloud radius, if we assume the distribution $dN/dr_{cl} \sim r_{cl}^{-4}$ to be still valid, should be around 1.8 pc.

However, this assumption will strongly overestimate the number of small clouds at the rather high mass of 10^5 M$_\odot$. Our aim is to show that it is more likely that a cloud engulfs the black hole forming the observed stellar disc than just bypassing it. Since small clouds are more likely to bypass the black hole we overestimate the amount of bypassing clouds this way. In addition, since e.g. a cloud of 10 pc radius cannot start at a distance d_0 smaller than 10 pc, we also assume the upper limit on r_{cl} to be 3.5 pc at the smallest distance $d_{0,min}$ ($d_{0,min}$ - 3.5 pc gives roughly the inner edge of the circum-nuclear disc at 1.5 pc) increasing linearly up to the maximum of 10 pc at the largest distance $d_{0,max}$. We note that we exclude a number of possible formation scenarios such as the formation of a small disc by capturing only part of a larger cloud or the possibility of a small stellar disc formed by a large accretion disc only fragmenting in the inner parts. Thus, the discussion presented in this section only gives a rough estimate for the likelihood of such an event. A detailed study including hydrodynamics and also other formation models such as the plausible cloud-cloud collision model of Hobbs & Nayakshin 2009 is beyond the scope of this paper.

We use a Monte-Carlo approach to sample values from the corresponding distributions, calculate the corresponding outer disc radius and check if the cloud would bypass or engulf the black hole. Tests have shown that convergence in the first three digits after the decimal is reached after roughly 10^8 iterations. We define N_{engulf} and N_{bypass} to be the total number of cases that lead to a small disc ($r_{disk} < 0.6$ pc) out of the total number of 10^8 values. The ratio N_{engulf}/N_{bypass} for different cloud velocities determines the likelihood of the two scenarios. The ratio $N_{engulf,bypass}/N_{total}$ gives the absolute likelihood of the individual scenarios.

v_{cloud} [km/s]	$\frac{N_{engulf}}{N_{bypass}}$	$\frac{N_{engulf}}{N_{total}}$	$\frac{N_{bypass}}{N_{total}}$
20	2.75	2.17 %	0.79 %
30	-	0.75 %	0 %
50	-	0.006 %	0 %
80	-	0 %	0 %

Table 3.1: Likelihood of the two scenarios of a cloud bypassing or engulfing the black hole during passage, calculated for values suited for the Milky-Way GC. For a low cloud velocity of 20 km/s it is around three times more probable that a small disc will be formed by a cloud engulfing the black hole than by a cloud bypassing the black hole. For higher velocities a bypassing cloud is no longer able to form a small disc at all. In the case of a high velocity cloud of 80 km/s neither of the two scenarios is able to produce a small disc.

Table 3.1 summarises the results. For cloud velocities larger than 20 km/s the bypassing scenario is not able to form a small disc at all. For the 20 km/s cloud it is still almost three times more likely that the disc was formed by a cloud engulfing the black hole instead of a bypassing cloud. At velocities of 30 km/s or higher only a cloud engulfing the black hole during passage is able to form a small disc. The most prominent observed cloud near the GC has a velocity of 50 km/s. For higher cloud velocities such as 80 km/s neither of the two scenarios can produce a small disc, which limits the velocity of the original cloud that could have formed the observed disc to below 80 km/s. The results can be explained by the fact that for the engulfing scenario we can have smaller impact parameters and thus lower maximum angular momentum compared to the bypassing scenario. Thus even a rather large cloud can lead to a small disc. With this we conclude that it is very likely that the cloud that formed the progenitor gaseous accretion disc of the observed stellar disc, engulfed the black hole during its passage through the very centre of the galaxy.

3.4   Model and Numerical Method

3.4.1   Simulation Code

The hydrodynamical evolution of the impact of the gas cloud with the central black hole is studied using simulation runs performed with the N-body Smoothed Particle Hydrodynamics (SPH) Code Gadget2 (Springel, 2005). The code solves the Euler equations for hydrodynamics which neglect friction. To enable friction, Gadget2 uses a modified version of the standard Monaghan, Gingold; Balsara (Gingold & Monaghan 1983; Balsara 1995) artificial viscosity:

$$\Pi_{ij} = -\frac{\alpha}{2} \frac{(c_i + c_j - 3w_{ij}) \, w_{ij}}{\rho_{ij}} \tag{3.4}$$

with $w_{ij} = \vec{v}_{ij} \cdot \vec{r}_{ij}/|\vec{r}_{ij}|$, c_i being the sound speed of particle i, v_{ij}, r_{ij} the relative particle velocity and separation respectively, ρ_{ij} the mean density and α the artificial viscosity strength parameter.

The modification is necessitated, as the original form weights viscous forces strongly towards particles with small separation. In the new formulation the induced pressure does not explicitly depend on the hydro-smoothing length or particle separation. Tests have shown that in simulations with dissipation this has the advantage of reducing very large viscous accelerations (Springel, 2005). Gadget2 also includes an additional viscosity-limiter to remove spurious angular momentum transport. This is implemented by using the mechanism proposed by Balsara (1995) which adds a factor $(f_i + f_j)/2$ to the viscosity tensor, where

$$f_i = \frac{|\nabla \times \vec{v}|_i}{|\nabla \cdot \vec{v}|_i + |\nabla \times \vec{v}|_i} \tag{3.5}$$

measures the shear around particle i.
It has been shown that the standard SPH artificial viscosity produces a significant shear viscosity in rotationally-supported discs, leading to spurious transport of angular momentum and that numerical dissipation is almost never negligible and can be dominant (Balsara 1995; Murray 1996; Lodato & Rice 2004; Nelson 2006). Thus we performed stability tests as shown in the Appendix to demonstrate that the above modifications are sufficient to make our results numerically stable and that we are not dominated by numerical viscosity. For our standard simulations we used a value of $\alpha = 0.75$. The tests shown in the Appendix 3.8.1 vary α in the range between 0.5 - 1.0 which is the suggested range suited for numerical simulations (Springel, 2005).

Springel 2005 conducted a number of tests to show that Gadget2 is able to resolve strong shocks. The main difference of SPH codes compared to grid based codes is that droplets of gas which form during shocks can survive rather long and do not mix as efficiently with the background material as in grid codes (see e.g. Steinmetz & Mueller 1993; Agertz et al.

2007). This is due to the fact that in SPH the forces at the edges between two phases are smoothed out since there are always contributions from both SPH particles inside the clump and from SPH particles in the surrounding medium.

In order to carefully account for the thermodynamics of disc formation, we implemented the cooling formalism of Stamatellos et al. (2007) into Gadget2. It approximates cooling processes for optically thin, as well as optically thick regions by applying a approximative radiative transfer mechanism using the diffusion approximation. The basic equation determining the cooling rate is given by:

$$\frac{du}{dt} = \frac{4\,\sigma_{\mathrm{SB}}\,(T_0^4 - T^4)}{\bar{\Sigma}^2\,\bar{\kappa}_{\mathrm{R}}(\rho, T)\,+\,\kappa_{\mathrm{P}}^{-1}(\rho, T)} \tag{3.6}$$

with T_0 the background radiation temperature, T and ρ the particle temperature and density, $\bar{\Sigma}$ the pseudo-mean surface-density, $\bar{\kappa}_{\mathrm{R}}$ the pseudo-mean opacity and κ_{P} the Planck-mean opacity. We refer to Stamatellos et al. (2007) for the definition and interpretation of the pseudo-mean surface-density and the pseudo-mean opacity, which are crucial for their method in approximating radiative transfer (see Equations 18 and 23 in Stamatellos et al., 2007).

The method uses the particle density, temperature and gravitational potential to estimate a mean optical depth for each SPH particle which then regulates its heating and cooling. For a small optical depth, Eqn. 3.6 reduces to the usual cooling term for the optically thin cooling regime.

$$\frac{du}{dt} \simeq -4\sigma_{\mathrm{SB}}T^4\kappa_{\mathrm{P}}(\rho, T) \tag{3.7}$$

For a large optical depth, Eqn. 3.6 reduces to the diffusion approximation (see Eqn. 27 and 28 in Stamatellos et al. (2007)).
At each timestep the following steps are undertaken:

- Approximate the mean optical depth of the environment of each SPH particle by using the density and gravitational potential following the procedure as described in Stamatellos et al. (2007). In the case of non-SPH particles, exclude them from the gravitational potential calculation.

- Calculate the compressive heating rate and radiative cooling rate. In the case of T < T_0 we have radiative heating instead of cooling.

- Update the internal energy and temperature of each SPH particle according to the total change in heating plus cooling.

In this cooling formalism the molecular weight is temperature dependent, taking into account the degree of dissociation and ionisation of hydrogen as well as the degree of single and double ionisation of helium. The specific internal energy of an SPH particle is the sum

of contributions from molecular, atomic and ionised hydrogen as well as the contributions from atomic, single and double ionised helium together with the associated dissociation energies. The method is suited for a wide range of temperatures (T = 10 - 10^6 K), a wide range of densities ($\rho = 10^{-19}$ g/cm^3 - 10^{-2} g/cm^3) and optical depths in the range of 0 $< \tau < 10^{11}$ as shown in tests performed by Stamatellos et al. (2007). The additional computational overhead for this method is not too high, since it can primarily be implemented through look-up tables and requires only a few real-time calculations.

3.4.2   Numerical Parameters

The simulations are run with a total number of 10^6 SPH particles. To test the resolution dependence of our results we did one very high resolution simulation with 5×10^6 SPH particles presented in the Appendix 3.8.2. The number of SPH neighbours is set to $n_{\mathrm{neigh}} = 50 \pm 5$. All simulations use a gravitational softening length of $\epsilon = 10^{-3}$ pc. In what follows we only discuss the gravitational softening length since the code only allows to change this value directly and sets the minimum hydro-smoothing length to a fraction of this value. In our case we choose the minimum hydro-smoothing length to be equal to the gravitational softening length according to Bate & Burkert 1997. We use the standard Gadget2 implementation of a fixed gravitational softening length and a variable hydro-smoothing length, thus the gravitational softening length is always $\epsilon = 10^{-3}$ pc. The softening length strongly influences the simulation runtime, with a lower value leading to a longer runtime. To test the dependence of our results on softening length we performed test simulations with a softening length of $\epsilon = 10^{-4}$ pc. The outcome of this test is presented in the Appendix 3.8.3.

In order for the simulations not to become too time-consuming as a result of very small particle time steps in the vicinity of the black hole we define an accretion radius r_{acc} within which all SPH particles are considered to be accreted by the black hole. These particles are removed from the simulation and will no longer take part in the dynamical evolution. The fixed-position sink is not associated with a particle. This mechanism does not strictly conserve linear or angular momentum, but due to the small amount of accreted gas (at most 1% of the black hole mass) the violation of angular momentum conservation is negligible.

We want the accretion radius r_{acc} to be larger than the softening length of 10^{-3} pc and smaller than the observed inner disc edge of 4×10^{-2} pc. Test simulations showed that a value of $r_{\mathrm{acc}} = 2 \times 10^{-2}$ pc allows us to simulate the encounter within a reasonable total runtime such that the whole cloud has passed the black hole and an compact accretion disc has formed.

We investigate three different types of simulations. The first type of simulations are purely adiabatic simulations with cooling only due to adiabatic expansion. The second type of simulations are isothermal simulations and finally, representing the most realistic case, we performed simulations using the full cooling prescription of Stamatellos et al. (2007) presented in section 3.4.1.

Adiabatic simulations

Using the ideal gas approximation we have an equation of state of $P = \frac{\rho k_B T}{\mu m_H}$ with ρ, T gas density and temperature respectively, k_B the Boltzmann-constant, m_H the hydrogen mass and the molecular weight $\mu = 2.35$ assuming a mixture of 70% hydrogen and 30% helium

(molecular). The initial temperature is set to $T_{cloud} = 50$ K which is a typical temperature for a cloud in the GC (Güsten & Philipp, 2004).

Isothermal simulations

The isothermal simulations represent the case for which cooling is balanced by heating. Given our assumed low temperatures, it corresponds to very efficient cooling. The isothermal simulations use an equation of state of $P = c_s^2 \rho$ with ρ the gas density and c_s the sound speed of the gas, calculated initially by using $c_s^2 = \frac{k_B T}{\mu m_H}$. Again the initial temperature is set to 50 K.

Heating and cooling processes in the disc will however play an important role when investigating the fragmentation and condensation of the disc into stars (see e.g. Bonnell & Rice 2008). Observations have shown that the stellar disc IMF is very top-heavy (Bartko et al., 2010), indicating that a large Jeans-mass is required for the forming stars, which in term implies that cooling should not be too efficient. On the other hand the temperatures have to remain low enough for the system to form. If compressional heating becomes too efficient the strong expansion of the gas prevents the formation of the accretion disc, as our purely adiabatic simulations show.

Full Cooling simulations

Our third set of simulations uses the full cooling prescription of Stamatellos et al. (2007) presented in section 3.4.1. The ideal gas approximation is used again, assuming initial cloud temperature T_{cloud} and background radiation temperature T_0 (due to the old spherical cluster of stars near the GC) to be 50 K. The molecular weight is a function of temperature and takes into account the processes described in section 3.4.1.

3.4.3   Initial Conditions

ID	$\frac{b}{r_{cl}}$	$\frac{v_0}{v_b}$	v_0 [km/s]	b [pc]	$j_{specific}$ $\left[\frac{pc^2}{Myr}\right]$
I01	0.28	0.29	50	1	50
I02	0.57	0.41	50	2	100
V01	0.85	0.3	30	3	90
V02	0.85	0.5	50	3	150
V03	0.85	0.8	80	3	240
V04	0.85	1.0	100	3	300
C01	0.57	0.98	120	2	240

Table 3.2: Summary of initial conditions for our simulations. The cloud velocity is varied for V01, V02, V03 and V04. The impact parameter is varied for I01, I02 and V02. C01 is a comparison setup with the same initial specific angular momentum ($j_{specific}$) as V03.

In this first study we start with a spherical and homogeneous cloud of radius 3.5 pc which is typical for the GC (Miyazaki & Tsuboi 2000, derived from CS(1-0) radio surveys). The H_2 gas density is 10^4 cm^{-3} (Güsten & Philipp 2004, taken from high-resolution surveys of CS and CO in the GC), leading to a cloud mass of 8.81×10^4 M$_\odot$. The SPH particle mass is then $m_{SPH} = 8.81 \times 10^{-2}$ M$_\odot$ and the corresponding minimum mass that can be resolved is $m_{min} = n_{neigh} \times m_{SPH} = 4.4$ M$_\odot$ (following Bate & Burkert, 1997).

The black hole is included as a static potential of a point mass of $M_{BH} = 3.5 \times 10^6$ M$_\odot$ (Genzel et al., 2003) placed at the origin of the coordinate system. We do not include black hole growth in order to speed up the simulations. This growth is anyhow negligible since at most only around one percent of the black hole mass was accreted at the end. Energetic feedback from the accreting black hole, (see e.g. Johansson et al., 2009) might however be important and will be investigated in a subsequent paper. The Gadget2 Code treats gravitational forces as Newtonian up to 2.8 times the gravitational softening length, which in any case is beyond our accretion radius for the softening length.

Initially, the centre of mass of the cloud is placed at a distance d_{x0}=5 pc from the origin/black hole on the x-axis (the direction of motion) and an offset b on the y-axis. Note that compared to the coordinate system used in the motivation (Sec. 3.3) where we defined the x-axis to be along the line connecting the centre of the cloud with the black hole, we now define the x-axis to be parallel to the cloud velocity vector passing through the coordinate origin/black hole position. This way the cloud to black hole distance d_0 defined in the motivation section relates to d_{x0} and b by $d_0^2 = b^2 + d_{x0}^2$.

We have chosen this relatively small distance in order to prevent the cloud from collapsing before it reaches the black hole. Additionally this is also the distance of the so called circum-nuclear disc (a reservoir of clumpy, molecular gas of around 10^5 M$_\odot$) from the GC

(Vollmer et al., 2003) for which there is evidence for infall of gas towards the GC (Montero-Castaño et al., 2009). The origin of gas with low enough angular momentum to feed the GC in general (e.g. King & Pringle 2007) is still an area of active research and beyond the scope of this paper.

The free fall time of a cloud with $n = 10^4$ cm^{-3} is only around 0.36 Myrs. For an average infall velocity of 50 km/s the cloud's centre of mass should reach the black hole after roughly 0.1 Myrs (assuming no acceleration due to the black hole). The evolution is characterised by the fraction $\frac{b}{r_{cl}}$ where r_{cl} is the cloud radius and b is the initial cloud's centre of mass offset on the y-axis. $\frac{b}{r_{cl}}$ is always smaller than one in our case of a cloud engulfing the black hole.

The initial cloud velocity v_0 in (negative) x-direction is a typical value, taken from the observations presented by Miyazaki & Tsuboi (2000). The evolution is then characterised by the ratio $\frac{v_0}{v_b}$ where v_0 is the initial cloud velocity and $v_b^2 = \frac{2GM_{bh}}{b}$ is the black hole's escape velocity at distance b. The initial conditions of our parameter studies are shown in Table 3.2.

Three setups (I01, I02, V02) use a fixed initial cloud velocity of 50 km/s and varying offsets b, set to 1, 2 and 3 pc, respectively. In addition there are four setups (V01, V02, V03, V04) with b fixed to 3 pc and varying initial cloud velocities, set to 30, 50, 80 and 100 km/s, respectively. The comparison setup C01 has the same initial specific angular momentum as V03 but a smaller impact parameter and higher velocity.

We do not include the potential of the massive stellar cusp in the GC (Genzel et al., 2003) into our simulations which would lead to precession of the orbits on a time-scale that is short compared to the infall time (Ivanov et al., 2005). In this first step we only concentrate on the dynamics due to the black hole cloud interaction and postpone investigation of the effects of including the stellar cusp to the next paper in our series.

The simulations were typically run for an evolutionary time of 0.25 Myrs which corresponds roughly to the instant when all parts of the cloud have crossed the black hole. Taking into account that disc formation is finished after roughly 0.15 Myrs, when the disc becomes almost static, we evolve the disc for a bit less than 2 full orbits at a radius of 1 pc. During this short time period, viscous evolution does not play any significant role.

Only simulation I01 was stopped already after 0.2 Myrs. At that time, due to the small impact parameter, the time step became very small making the simulation very time-consuming and too expensive to continue. Again we want to stress that in this paper we are only interested in the resulting gaseous disc properties directly after the collision with the black hole without following the viscous evolution of the accretion disc and we defer the study of fragmentation and star formation to a follow-up paper.

3.5 Results

3.5.1 The Adiabatic Case
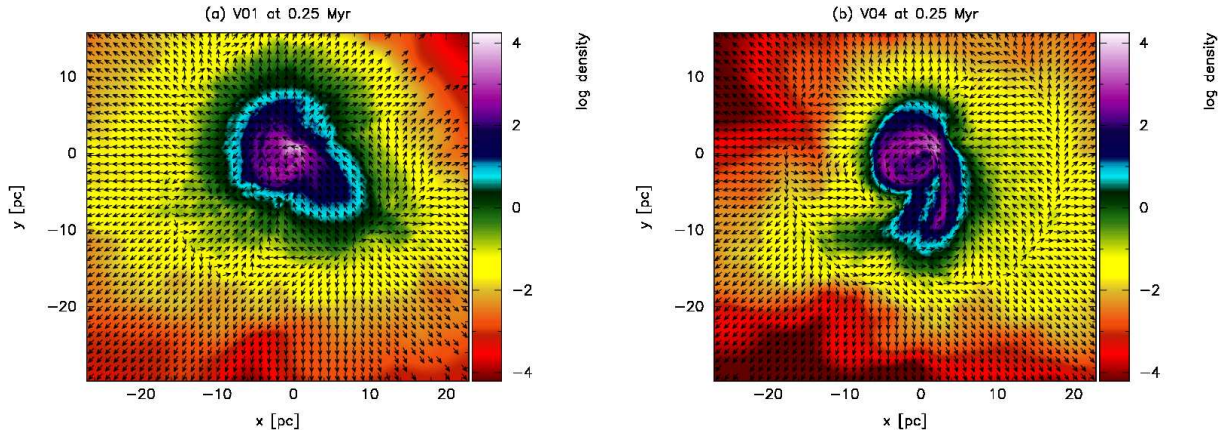
Figure 3.2: Logarithmic density in units of $\frac{M_\odot}{\text{pc}^3}$ in the xy-plane with z=0 pc for purely adiabatic simulations using initial conditions V01 (a) and V04 (b) shown at the final time step of t=0.25 Myrs. Velocity vectors are all set to the same length and only indicate the local direction. Clearly visible in (a) and (b) is the spherically expanding shell of gas due to the strong adiabatic heating. In addition, an extended ring of gas formed in the inner 5 pc around the black hole.

The first simulations we present are purely adiabatic without cooling and use initial conditions V01 and V04, which differ only in initial cloud velocity with 30 km/s for V01 and 100 km/s for V04. The resulting densities in units of $\frac{M_\odot}{\text{pc}^3}$ in the xy-plane for z=0 pc at the end of the simulations (t=0.25 Myr) are shown in Figure 3.2. All velocity vectors are set to the same length and thus only represent the corresponding local direction of the velocity field.

The gas is strongly spherically expanding as a result of the heating due to adiabatic compression during the initial impact. This mechanism basically completely prevents the formation of a disc. Only an extended ring-like structure evolves inside the inner 5 pc as seen in Figure 3.2. A huge bubble of hot gas with a radius of roughly 30 pc forms around the ring which is still expanding at the end of the simulation.

Figure 3.3 shows the increase in thermal energy over time for both simulations. The thermal energy for the 100 km/s cloud rises by a larger amount compared to the 30 km/s cloud as expected due to the stronger shocks. At a later point the expanding gas starts to cool because of adiabatic expansion. Since there is more gas initially bound to the black hole in the case of the 30 km/s cloud, more material is still in the centre and thus shocks inside the

surviving ring generate more heat compared to the faster cloud. The final energy can rise up to several times 10^{51} erg and becomes comparable with supernova energies of typically 10^{51} erg. From this we conclude that if cooling becomes too inefficient, the interaction of a cloud with the central super-massive black hole will lead to an explosion and the formation of a hot, expanding bubble with energies comparable to supernova explosions. However this is a very unlikely scenario since high gas-densities typically lead to strong cooling.
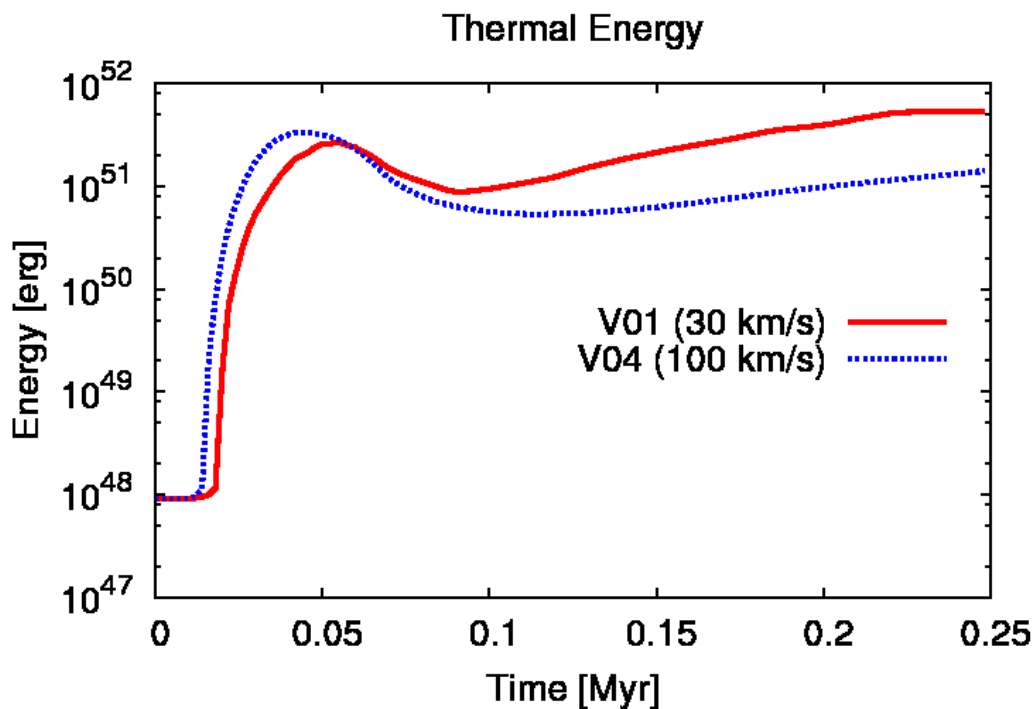
Figure 3.3: Evolution of total thermal energy as a function of time for the two adiabatic simulations, which increases nearly four orders of magnitude. This is already comparable with supernova energies of typically around 10^{51} erg. Shown are the cases for initial condition V01 (red, solid line) and V04 (blue, dotted line).

3.5.2 The Isothermal and Full Cooling Cases

We used initial conditions I02, V01, V02, V03 and C01 for the isothermal and the full cooling cases. As already mentioned, I01 is a very time-consuming setup and we have only run this setup for the computationally faster isothermal case.

The Isothermal Case

From a simulation standpoint an isothermal equation of state is easy to implement and thus a good starting point in a number of cases. Judging from our results in this case compared to the more realistic case using the full cooling prescription we can say that at least some results can already be obtained with the isothermal approximation. Still one has to keep in mind that there are problems with the isothermal approach, which we will show in the following sections and which we already mentioned in section 3.4.2.

First we note that with an isothermal equation of state fragmentation is artificially enhanced because of our extremely low temperatures. However, we do not yet include star formation and are only interested in the properties of the forming gaseous disc. Another point is that in all isothermal simulations, the SPH particles in the inner 0.1 pc reach the minimum softening length so that we are limited by numerics in this region and the physics is not resolved due to the strong softening over the forces and thus we cannot make any reliable predictions about the disc properties here.
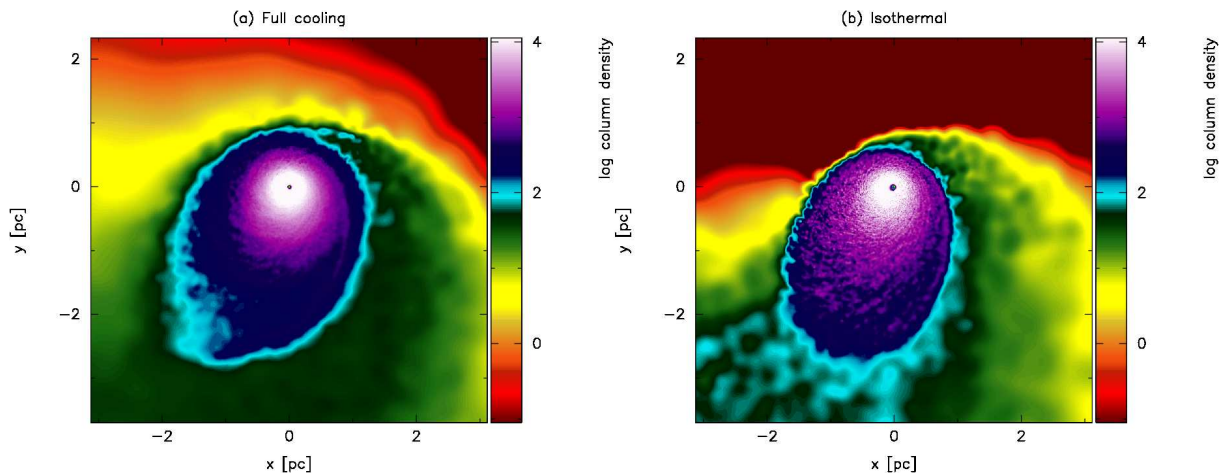

Figure 3.4: A comparison of the surface-density in units of $\frac{M_\odot}{pc^2}$ in the xy-plane for the full cooling case (a) and the isothermal case (b) at the final timestep of 0.25 Myrs using initial condition C01. Both discs are very similar in terms of size and shape. As expected the isothermal disc shows stronger signs of condensation compared to the hotter disc from the full cooling simulation.

The time evolution of surface density of the discs in the xy-plane in the isothermal case is very similar to the full cooling case (as shown for C01 in Fig. 3.4) we will present next. However the isothermal discs are very flat in the z-direction due to the low temperature in comparison to the full cooling discs. Because of this the evolution of density in the xy-plane for z=0 pc differs for the isothermal and full cooling discs, with the full cooling discs obviously showing lower densities. Still the evolution and general shape of the forming disc as presented for the full cooling case in the next section can also be taken as representative for the isothermal discs.

The Full Cooling Case

The time evolution of density in units of $\frac{M_\odot}{pc^3}$ in the xy-plane (z=0 pc) for initial condition C01 can be seen in Figure 3.5 for the cooling case. Velocity vectors are all set to the same length and only represent the local direction in the xy-plane. We have chosen to show C01 (cloud velocity of 120 km/s and impact parameter of 2 pc) since it represents an extreme case in which nearly no gas is bound to the black hole initially due to the high cloud velocity. Nonetheless, we form a gaseous accretion disc around the black hole at the end of the simulation.

After starting the simulation, the cloud approaches the black hole from the right hand side along the x-axis. Due to tidal forces the parts closest to the black hole quickly start to form a finger-like extension stretching towards the black hole located at the coordinate origin as seen in Figure 3.5a.

The gas passes the black hole on orbits corresponding to its initial angular momentum. 12000 yrs later (Figure 3.5b), this material begins to collide with gas streaming around the black hole from the opposite side. This leads to a high density region along the line of impact between the two streams. The high density region along the negative x-axis, as seen in Figures 3.5b,c and d, is created by material with a large initial distance in z-direction, concentrated into the z=0 pc plane.

Due to the larger amount of gas initially rotating counter-clockwise the overall rotation follows this direction, but the interaction with the clockwise rotating gas removes kinetic energy and lowers the angular momentum, forcing the gas on bound orbits or to fall directly into the black hole. This bound gas builds up the accretion disc as seen in Figures 3.5d,e.

The simulation was stopped after 0.25 Myrs when the cloud passed around the black hole. An inner gaseous accretion disc has formed at that time. This evolutionary state is shown in Figure 3.5f. Figure 3.6 shows a larger region around the final state shown in Figure 3.5f. Clearly visible is the escaping part of the cloud below -10 pc on the x-axis and at around -10 pc on the y-axis, as well as material still falling onto the accretion disc.
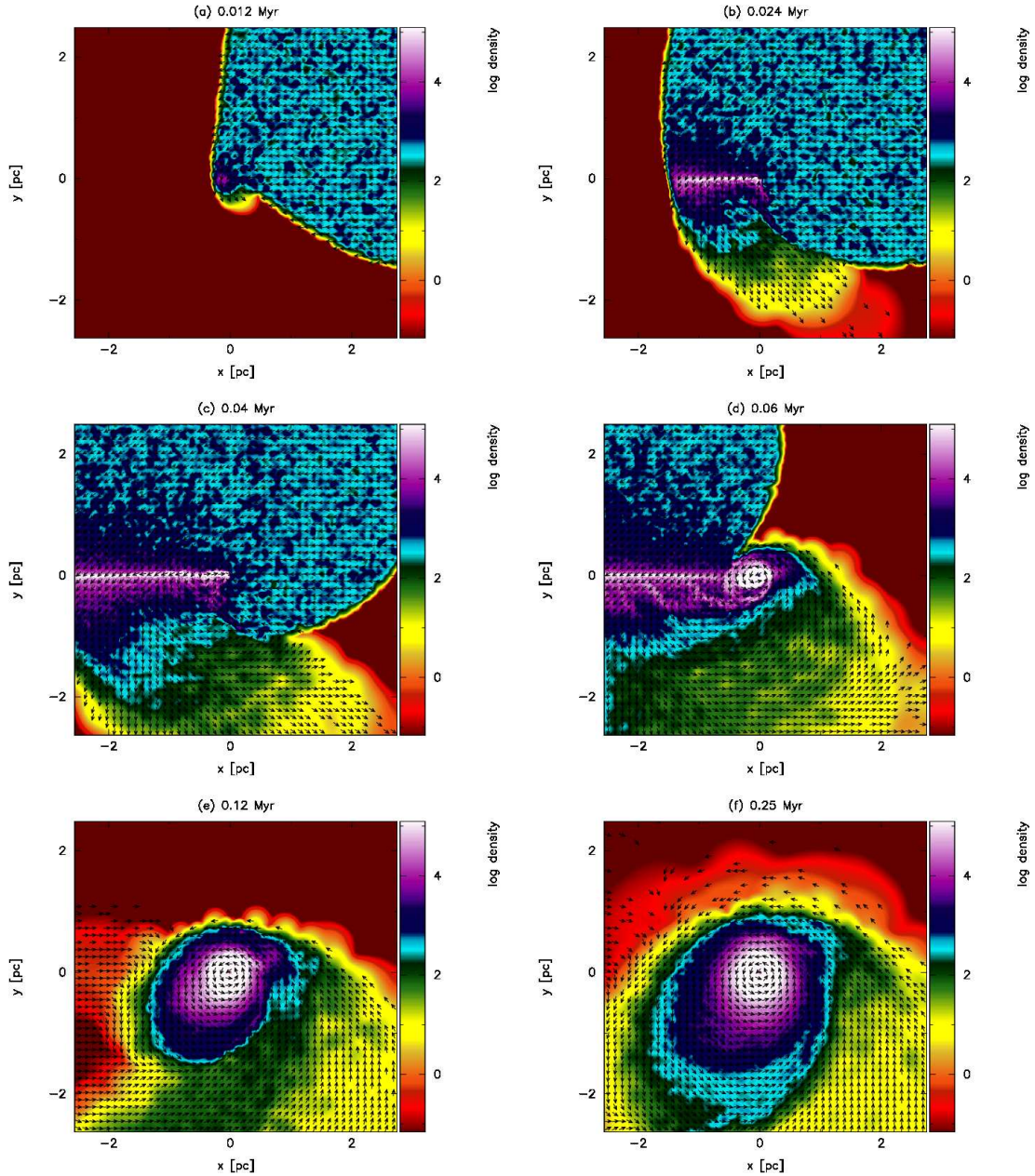
Figure 3.5: Logarithmic density in units of $\frac{M_\odot}{pc^3}$ in the xy-plane with z=0 pc at different times using initial condition C01 with cooling enabled. Velocity vectors are all the same length and only indicate local direction. Gas rotates around the black hole from opposite directions and collides, leading to a high density region along the line of impact between the two streams. The high density region seen in b,c,d along the negative x-axis is created by material with a large initial distance in z-direction, concentrated into the z=0 pc plane. Global rotation is counter-clockwise due to the initially larger amount of gas on counter-clockwise orbits, however due to the interaction at the high density region more gas becomes bound to the black hole than expected from the initial setup. C01 represents an extreme case in which there should be nearly no gas bound to the black hole at all. Thus, the formation of an accretion disc supports our proposed mechanism.
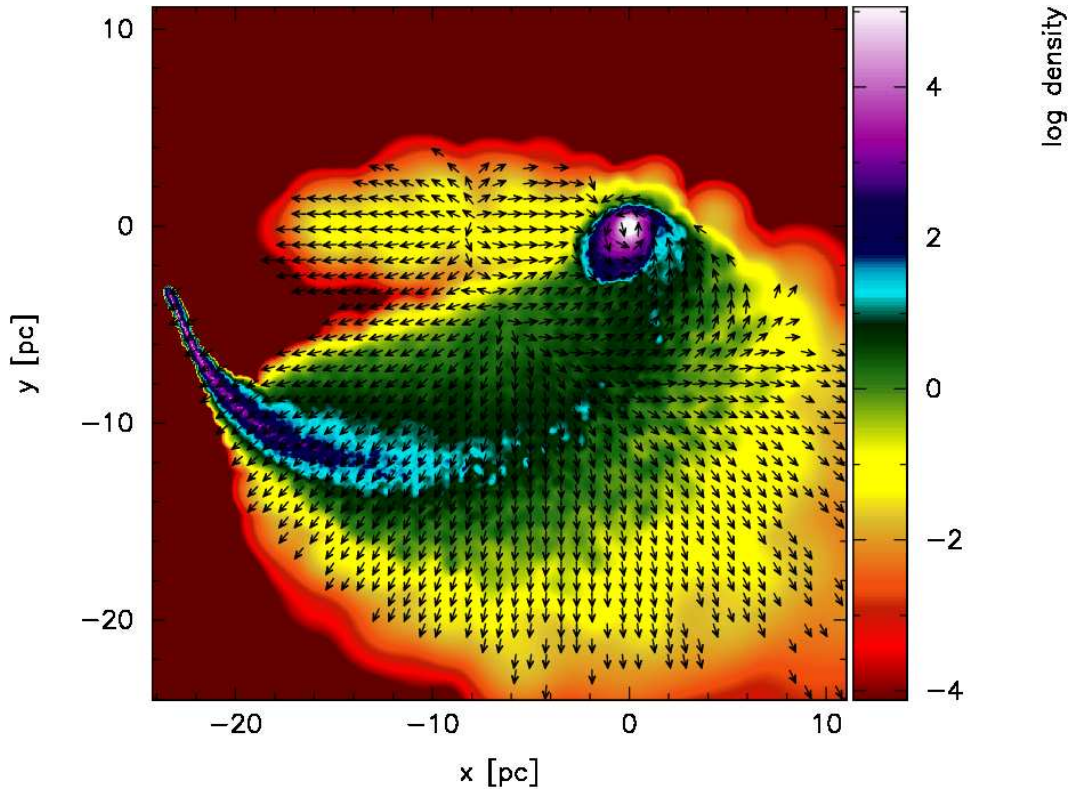
Figure 3.6: A zoom-out of the logarithmic density plot from Figure 3.5f in units of $\frac{M_\odot}{\mathrm{pc}^3}$ in the xy-plane with z=0 pc. Velocity vectors again only indicate the local direction, all vectors are set to the same length. Clearly visible is the escaping part of the cloud in the lower-left part of the plot, as well as material still falling onto the accretion disc.

In general other initial conditions show similar behaviour as described above. They differ in the amount of gas which is already bound to the black hole initially due to lower cloud velocities and thus lead to more massive discs. For larger impact parameters the amount of gas on clockwise orbits is smaller and thus the interaction inside the region where the counter-rotating streams collide is not as strong as in the cases with smaller impact parameter. This can also be seen when we discuss accretion later in section 3.5.4. Cloud velocity determines the final rotation of the resulting discs semi-major axis with respect to the x-axis in the xy-plane. For a 50 km/s cloud the semi-major axis aligns directly with the x-axis, whereas for a 80 km/s cloud it is rotated towards the negative y-axis and for a 30 km/s cloud towards the positive y-axis.

3.5.3   Eccentricity and Mass Distribution

In order to derive the mass fraction which is bound to the black hole, we calculate the orbital structure of the gas by using eccentricity

$$e^2 = 1 + \frac{2J^2 E_{\text{mech}}}{G^2 M_{\text{BH}}^2 m^3} \tag{3.8}$$

where J is the angular momentum of the SPH particle, M_{BH} the black hole mass, m the SPH particle mass and E_{mech} the total mechanical energy of the SPH particle ($E_{\text{mech}} = E_{\text{potential}} + E_{kinetic}$). Here eccentricity e = 0 corresponds to a circular orbit, 0 < e < 1 to a elliptic orbit, e = 1 to a parabolic or radial orbit and e > 1 to a hyperbolic orbit. SPH particles with e < 1 are on bound orbits, SPH particles with e > 1 are on unbound orbits and can escape the black hole potential. For SPH particles with e = 1 which are on radial orbits, the SPH particle velocity must be compared to the black hole escape velocity $v_{esc}^2 = \frac{2GM_{BH}}{r}$ at SPH particle radius r in order to determine if they are bound to the black hole or if they can escape to infinity. Table 3.3 summarises the total bound mass for all initial conditions in the full cooling and the isothermal cases.

ID	$M_{\text{bnd,ini}}$[1]	$M_{\text{bnd,iso}}$[1]	$M_{\text{bnd,cool}}$[1]
I01	88.10	48.03	-
I02	88.10	76.20	85.20
V01	88.10	83.37	82.82
V02	88.10	85.58	85.35
V03	15.50	51.53	49.78
C01	0.84	19.03	17.61

[1]All masses in units of 10^3 $M_\odot$

Table 3.3: The total initially bound (eccentricity e < 1) mass $M_{\text{bnd,ini}}$ compared to the total bound mass at the end of the simulations (0.25 Myrs) for the isothermal case $M_{\text{bnd,iso}}$ and the full cooling case $M_{\text{bnd,cool}}$. Only for initial conditions C01 and V03 not all the mass (88.1×10^3 $M_\odot$) is already bound to the black hole initially. Due to accretion the bound mass is lower than the initial value for the initial conditions that have all mass bound to the black hole initially. This represents just the difference between initial total mass and final total accreted mass. For initial conditions C01 and V03 there is a significant fraction of the initial total mass that got bound to the black hole (20% - 40%) and a part that is still unbound and escaping.

We use initial condition V03 as an example here (cloud velocity of 50 km/s and an impact parameter of 3 pc) since we used V03 for our numerical tests shown in the Appendix where we performed a simulation with numerical viscosity turned off and we need this special setup for comparison to the standard simulations in this section. In Figure 3.7a we show

the distribution of mass onto orbits of different eccentricity. The black (double-dotted) line shows what we expect from initial condition V03. The red (solid) line shows the result of the isothermal simulation using initial condition V03 with artificial viscosity turned off. In this case (isothermal and no artificial viscosity) there are no large pressure gradients during the simulation so that the change in mechanical energy and eccentricity is small. Because of this the final distribution approximately reflects the initial conditions. Running the same simulation (isothermal and initial condition V03) with artificial viscosity turned on leads to the distribution shown by the blue (dotted) curve. Here it can clearly be seen that more material is on bound (e<1), more circular orbits than expected from the initial conditions.
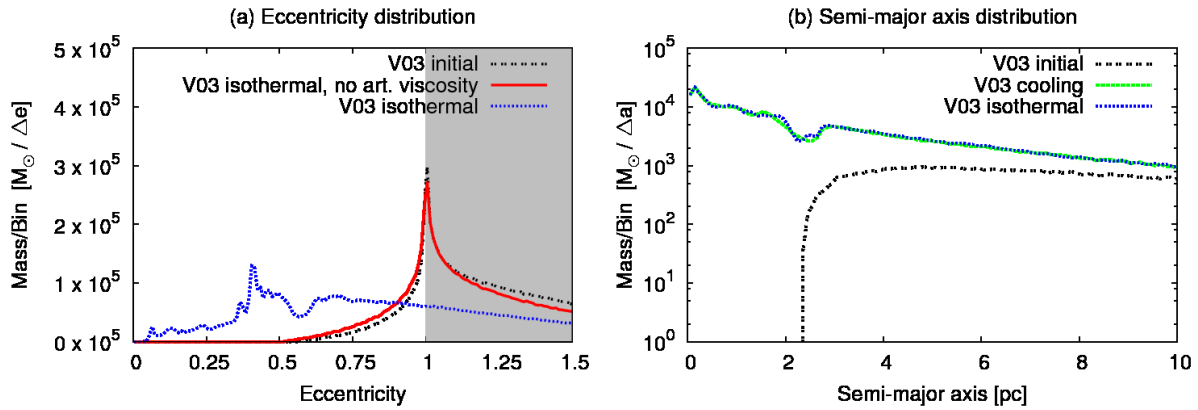

Figure 3.7: Comparison of the distribution of mass onto orbits of different eccentricity (a) and semi-major axis distribution (b). The black (dash-dotted) line in (a) shows the expected distribution from initial condition V03. Particles with e > 1 are not bound to the black hole, indicated by the grey background. The red (solid) line shows an isothermal simulation without artificial viscosity using initial condition V03 at the final time step of t=0.25 Myrs. In this run there are no large pressure gradients during the simulation so that the change in mechanical energy and eccentricity is small. The final distribution thus approximately reflects the initial conditions. The blue (dotted) curve shows the same simulation (isothermal and using initial condition V03) at t=0.25 Myrs with artificial viscosity now turned on. In this case significantly more mass settles into closed, more circular orbits than expected from the initial conditions. In (b) the black (dash-dotted) line represent the distribution of mass onto orbits with different semi-major axis for initial condition V03, compared to the isothermal (blue, dotted) and full cooling case (green, dashed) at the end of the simulations. A significant amount of gas settles into orbits very close to the black hole. Table 3.4 summarises the cancellation of angular momentum which leads to the formation of the compact (semi-major axis < 1pc) disc.

Figure 3.7b shows the distribution of (bound) mass onto orbits of different semi-major axes for initial condition V03 in the full cooling and isothermal case at the end of the

simulations. Again this plot shows that at the end of the simulations we accumulate a significant amount of mass onto orbits close to the black hole compared to the initial condition. Using the information from Figure 3.7a and 3.7b we can calculate the degree to which the cancellation of angular momentum contributes to the formation of the compact disc. We define the compact accretion disc to be all material with a semi-major axis below 1pc. First we calculate the mean change in angular momentum compared to the initial angular momentum for all particles present at the final timestep. This is done by taking the ratio of the absolute value of the final angular momentum to the absolute value of the initial angular momentum for every particle from the last snapshot and averaging over those values. We ignore all particles which have already been accreted (around 2%-15% of the total initial particle number) since they are no longer present in the final snapshot. In general the mean change in angular momentum is around 10%-30% of the initial angular momentum for all particles that have not been accreted. The mean values for the individual simulations are listed in Table 3.4. The small impact parameter simulations I01, I02 and C01 lead to a larger change in final angular momentum compared to the large impact parameter simulations V01, V02 and V03 because of the larger amount of material which can collide with a small impact parameter.

ID	Isothermal[1]	Full cooling[1]	Compact disc[1]
I01	0.58	-	0.47
I02	0.76	0.76	0.67
V01	0.89	0.90	0.87
V02	0.87	0.88	0.81
V03	0.85	0.86	0.70
C01	0.72	0.75	0.37

[1]Mean of the ratio of angular momentum $\frac{|J_{\text{final}}|}{|J_{\text{initial}}|}$

Table 3.4: Ratio of the absolute value of angular momentum at the final timestep to the absolute value of initial angular momentum, averaged over all particles for the isothermal and the full cooling case. Only particles which are present in the initial and the final snapshot are compared. This neglects already accreted particles (which make up 2-15% of the total initial particle number) since they are no longer present in the final snapshot. Also shown is the mean change in angular momentum for all particles inside the compact disc, which we define as all material with a semi-major axis smaller than 1pc. In this case the values for both the isothermal and the full cooling simulations only differ after the third decimal after the comma, hence we only show them for one case.

Cancellation of angular momentum is only strong in those parts of the cloud streaming around the black hole from opposite sides. Since the impact parameter is not zero the cancellation of angular momentum will not be 100% effective and there is always a part of the cloud which just follows its initial orbit around the black hole without encountering

material with opposite angular momentum. This material can only change its mechanical energy. Since angular momentum is conserved this gas can only move to a larger radius. The only way to transport material below the initial lower boundary of the semi-major axis (which is roughly 2pc in Figure 3.7b) is the cancellation/redistribution of angular momentum. To estimate the degree of cancellation of angular momentum needed to form the compact accretion disc we calculate the mean change in angular momentum for material which has a semi-major axis below 1pc in the final snapshot. The results for all simulations are summarised in the third column in Table 3.4. Compared to the value for all particles the cancellation needed to form the compact disc is always higher, as expected. In the extreme case of C01 more than 60% of the initial angular momentum needs to be cancelled in order to form the compact disc.

ID	$M_{\mathrm{acc,exp}}$[1]	$M_{\mathrm{acc,iso}}$[1]	$M_{\mathrm{acc,cool}}$[1]
I01	2.45	40.07	-
I02	2.10	11.90	13.03
V01	3.14	4.72	5.27
V02	1.26	2.51	2.71
V03	0.50	1.57	1.76
C01	0.37	11.32	11.85

[1]All masses in units of 10^3 $M_\odot$

Table 3.5: The accumulated mass $M_{\mathrm{acc,exp}}$ on orbits within the accretion radius as expected from the initial conditions compared with the result $M_{\mathrm{acc,iso}}$ for the isothermal simulations and $M_{\mathrm{acc,cool}}$ for the full cooling simulations after the final time step of t=0.25 Myrs. The isothermal simulation using initial condition V03 without artificial viscosity presented in Figure 3.7 accreted a mass of 0.49×10^3 $M_\odot$ at the final time step of t=0.25 Myrs compared to 0.5×10^3 $M_\odot$ expected from initial conditions. This clearly demonstrates that the large difference in expected accreted mass to actual accreted mass in the table is due to the interaction of the two streams of gas around the black hole which does not happen in the special simulation without artificial viscosity.

Figure 3.8 shows the distribution of mass onto orbits of different eccentricity for all simulations in the isothermal and cooling case compared to the expected distribution from the initial conditions. As can be seen, the simulations with cooling tend in general to have more gas mass on more circular orbits compared to the isothermal case. Since the orbits become more circular the smaller the distance from the black hole gets, this corresponds to more mass closer to the black hole. In the cooling case the discs are a lot more extended in z-direction compared to the isothermal discs (this will be discussed in detail in section 3.5.5) which basically just consist of a single sheet of SPH particles in the xy-plane. Thus, in the cooling case, material can move a lot easier in radial direction compared to the isothermal case. In addition, in the isothermal case the SPH particles get very close to the softening length already at a moderate distance from the black hole. This increases

smoothing over the forces and also prevents radial movement of particles. Still the isothermal case already yields a useful approximation of the gas mass distribution compared to the more realistic cooling case.

When calculating the initial orbits, we can also calculate the minimum distance r_{min} for every SPH particle to the black hole on its specific orbit. All SPH particles which are initially on an orbit with a distance r_{min} smaller than the accretion radius r_{acc} should be accreted. In Table 3.5 we compare the accreted mass expected from this calculation to the actual accreted mass during the whole simulation. The simulations result in values that are a factor of 3-30 larger than naively expected from the initial orbits. Again we see that radial movement is suppressed in the isothermal case, leading to lower values for the total accreted mass $M_{acc,iso}$ at the end of all simulations compared to the full cooling case. Ignoring the gas physics (taking the isothermal simulation using V03 without artificial viscosity again) we accreted almost exactly what we would expect from initial conditions when comparing the 0.49×10^3 $M_\odot$ accreted at the end of the simulation to the 0.5×10^3 $M_\odot$ expected just from the initial conditions. Thus the results in Table 3.5 support the claim of our model that we can efficiently dissipate kinetic energy and redistribute angular momentum forcing more gas onto lower, more circular orbits, often even below the accretion radius.
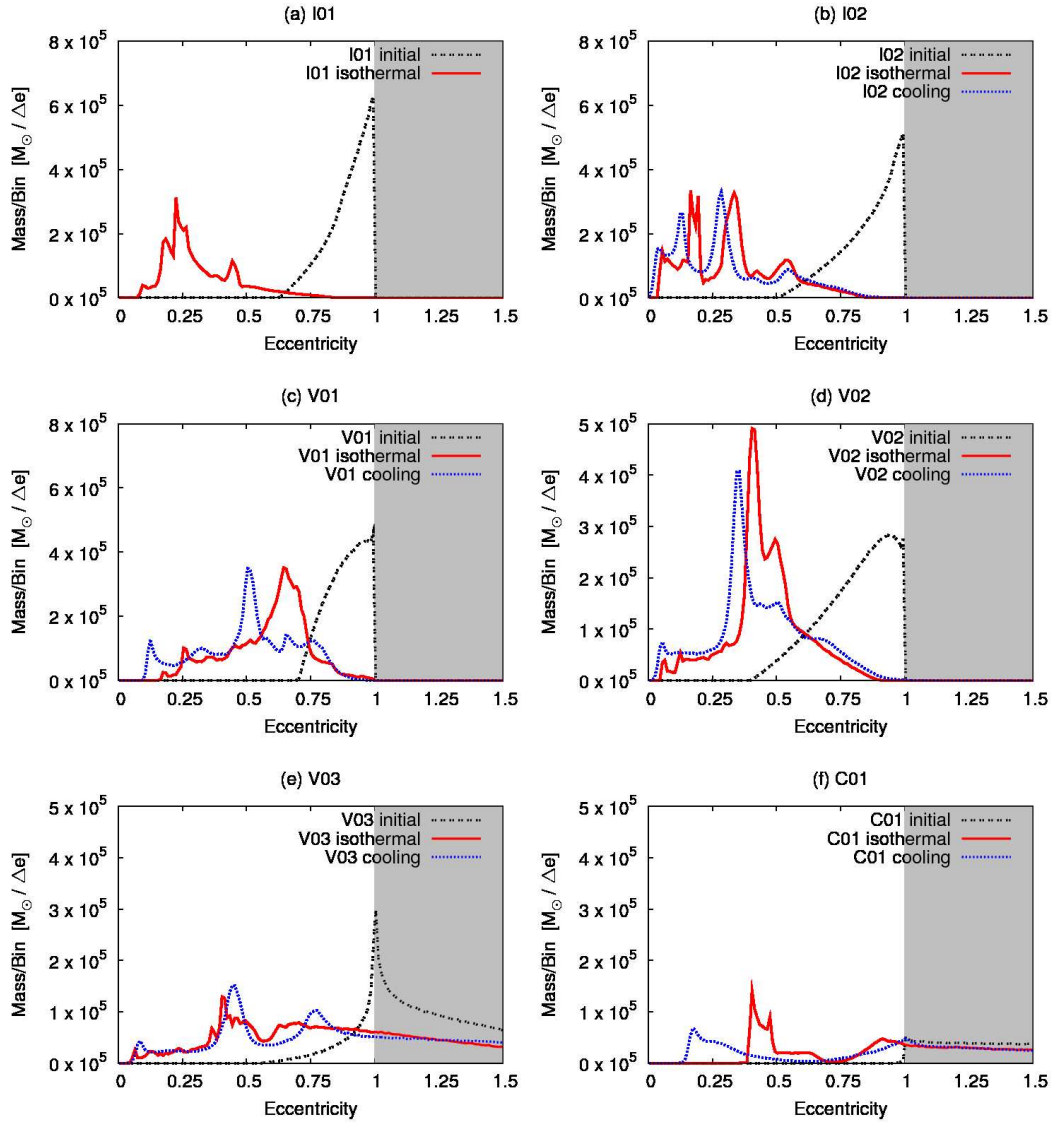
Figure 3.8: Comparison of the distribution of mass onto orbits of different eccentricity for all initial conditions using isothermal simulations and adiabatic simulations with cooling. Particles with e > 1 are not bound to the black hole, indicated by the gray background. The black line always shows the distribution resulting from the initial conditions. The red (solid) line shows the distribution for the isothermal simulations and the blue (dotted) curve the distribution for the simulations with cooling. In general, the more realistic full cooling simulations tend to form more circular discs compared to the isothermal case. Still the isothermal simulations already yield results similar to the cooling case for most initial conditions.

3.5.4 Accretion
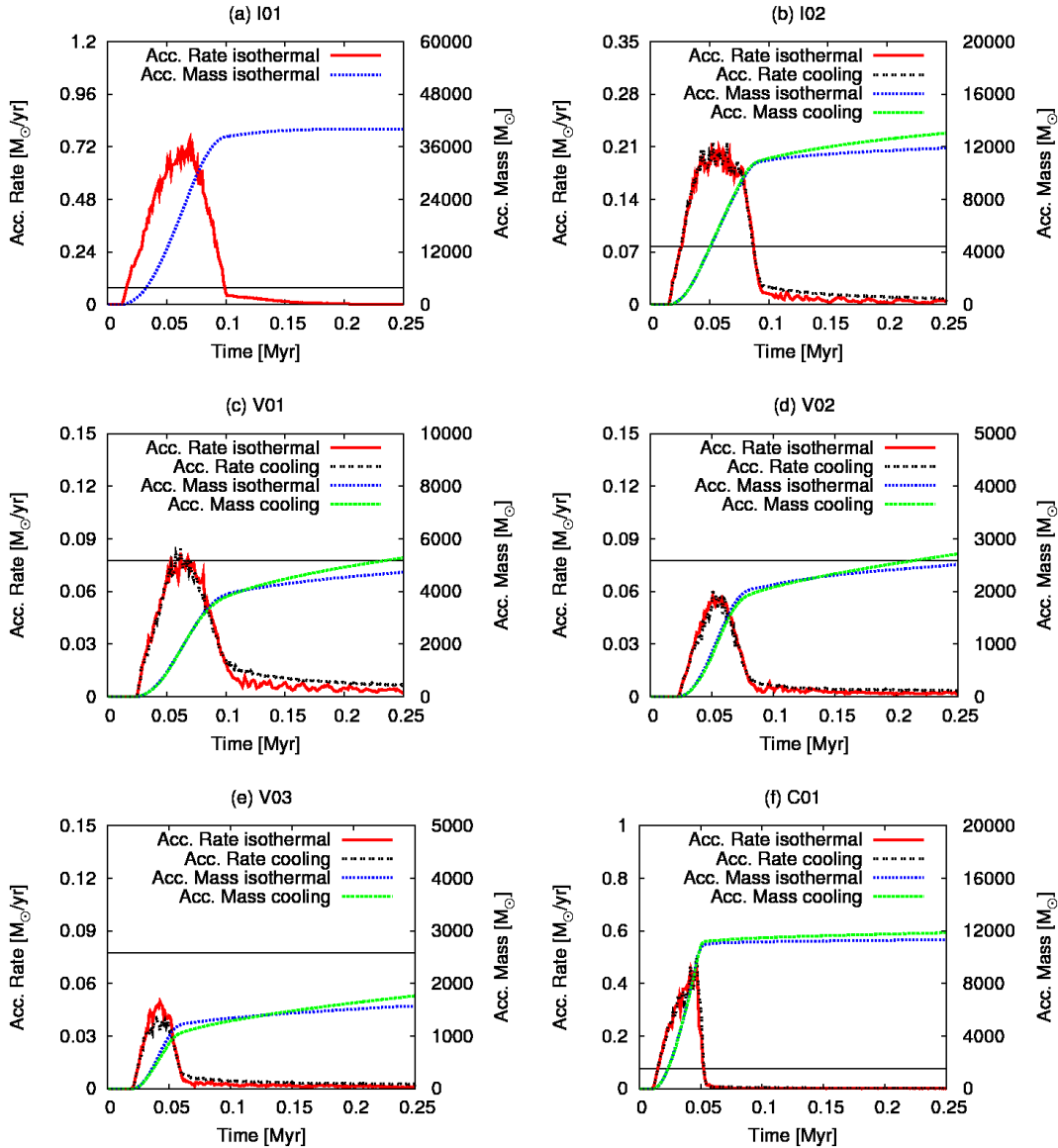
Figure 3.9: The red (solid) and green (dashed) lines show the accretion rate in $\frac{M_\odot}{yr}$ (left y-axis) for the isothermal and cooling case. The thin horizontal black line shows the Eddington limit of a 3.5×10^6 $M_\odot$ black hole at 10% accretion efficiency. Also plotted is the total accreted mass in blue (dotted) and black (dash-dotted) in $M_\odot$ (right y-axis) again for the isothermal and full cooling cases. The low impact parameter simulations can accrete at Super-Eddington rates since we do not include black hole feedback, whereas the high impact parameter simulations stay below Eddington accretion at all times. In general the isothermal and cooling simulations show a very similar accretion behaviour.

Accretion rates are calculated from material which falls below our accretion radius of $r_{\mathrm{acc}} = 2 \times 10^{-2}$ pc. We note that our simulations can lead to Super-Eddington accretion rates with the prescription we are using, since there is no black hole feedback regulating the accretion rate. However, accretion in our case does not necessarily mean black hole accretion since the formation of a small and hot black hole accretion disc evolving viscously is beyond the resolution limit and outside the scope of our current simulations. Nevertheless, it is interesting to compare our accretion rates for all simulations to the Eddington rate of the black hole which is shown in Figure 3.9.

The Eddington mass accretion rate is defined as $\dot{M}_{edd} = \frac{4\pi G M_{BH} m_p}{\epsilon \sigma_T c}$, with m_p being the proton mass, ϵ the accretion efficiency and σ_T the Thompson scattering cross-section. From this we get an Eddington rate of $\dot{M}_{edd} = 0.0775 \, \frac{M_\odot}{\mathrm{yr}}$ using an accretion efficiency of 10% and a 3.5×10^6 M$_\odot$ black hole as in the Milky Way GC.

Figure 3.9 shows that the isothermal and full cooling simulations differ only marginally in their accretion behaviour, thus we will describe accretion independent of the used equation of state. Note that the y-axis is scaled differently for different simulations due to the large range of accretion rates we get. At the end of all simulations we reach very low accretion rates indicating that we have reached a nearly stationary state. The accretion rates of the large impact parameter simulations using initial conditions V02 and V03 stay below the Eddington rate at all times.

A comparison of the simulations with initial conditions I01, I02 and V02 in Table 3.5 shows that the impact parameter plays the most important role in determining the final accreted mass while the cloud velocity has a much smaller effect (compare V01, V02 and V03). This is also confirmed by comparing the simulations using initial condition C01, which has the same initial specific angular momentum as V03, to simulations using V03. Clearly the main factor determining the final accreted mass is the impact parameter. In all simulations we still have accretion at the end of the runs, however at very low rates, thus the values shown in Table 3.5 would only slightly increase if the simulations were continued for a longer time.

3.5.5 Disc Structure
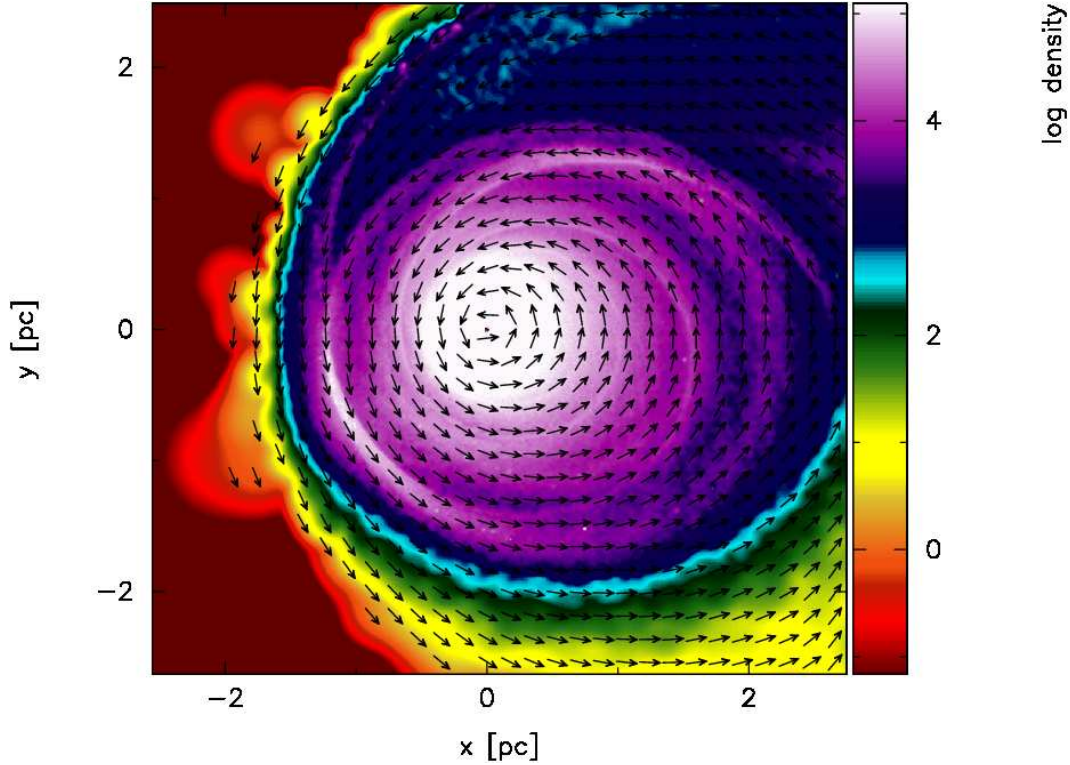
Figure 3.10: Logarithmic density in units of $\frac{M_\odot}{\text{pc}^3}$ in the xy-plane for z=0 pc at 0.25 Myrs for initial condition V02 with cooling. Velocity vectors are all the same length and only indicate local direction. The semi-major axis of the final disc aligns well with the x-axis.

Finally, we study the structure of our discs in the z-direction at the final timestep. For this we define our disc scale height to be the position where the density in z-direction drops to e^{-1} times the mid-plane density. We take the simulation using initial condition V02 as an example since in this case the disc aligns well in the xy-plane with the semi-major axis along the x-axis as can be seen in Figure 3.10.

The Isothermal Case

For a standard thin accretion disc assuming hydrostatic equilibrium in z-direction, where thermal pressure is balanced by the z-component of the central force we can calculate the disc scale height. The resulting disc scale height is $H = c_s \left(\frac{r_{xy}^3}{GM} \right)^{1/2}$ with r_{xy} the SPH particle distance to the black hole in the xy-plane and c_s the SPH particle sound speed. For our initial temperature of 50 K in the isothermal case we get a scale height of 5×10^{-5} pc at the inner boundary of 0.02 pc and a scale height of the order of the softening length at 0.5 pc. Thus the accretion disc scale height gets artificially blown up to our softening

length of $\epsilon = 10^{-3}$ pc in the inner region. The disc scale height should be resolved to at least four times the softening length according to Nelson (2006), thus we would need a softening length of around 10^{-5} pc or preferably better at the inner boundary.

This is however not feasible with respect to the simulation runtime. From this we can conclude that it is important to include the detailed thermodynamical treatment of the full cooling prescription in order to investigate the z-structure of the accretion disc, which is more extended due to the higher temperature and thus can be resolved using a realistic value for the softening length.

The Full Cooling Case

Here we resolve the disc scale height to at least four times the softening length at a radius of 0.1 pc and up to 40 times the softening length at a radius of 1 pc. A test-simulation using initial condition V03 and a softening length of $\epsilon = 10^{-4}$ (presented in the Appendix) resolving the disc scale height to one order of magnitude more in softening length shows no difference in the results compared to the larger softening length of $\epsilon = 10^{-3}$ indicating that we reached convergence.

The green line in Figure 3.11a shows the disc scale height resulting from our simulations for a y=0 pc slice along the x-axis for the disc shown in Figure 3.10 in the full cooling case. This is compared to what we would expect from assuming hydrostatic equilibrium in z-direction, shown by the blue line in Figure 3.11a. The over-plotted structure shows the absolute value of $\frac{\partial \phi}{\partial z} - \frac{1}{\rho}\frac{\partial P}{\partial z}$ with ϕ the point-mass potential of the black hole. Black indicates the minimum value (normalised to the global minimum value). The colour gradient from black to white spans two orders of magnitude in the deviation from the global minimum deviation. We see that the central part of the disc (pure-black in the plot) is close to hydrostatic equilibrium with a good fit to the expected theoretical value (blue line). The outer parts of the disc consist of fresh material that just fell onto the disc and did not yet settle into hydrostatic equilibrium.
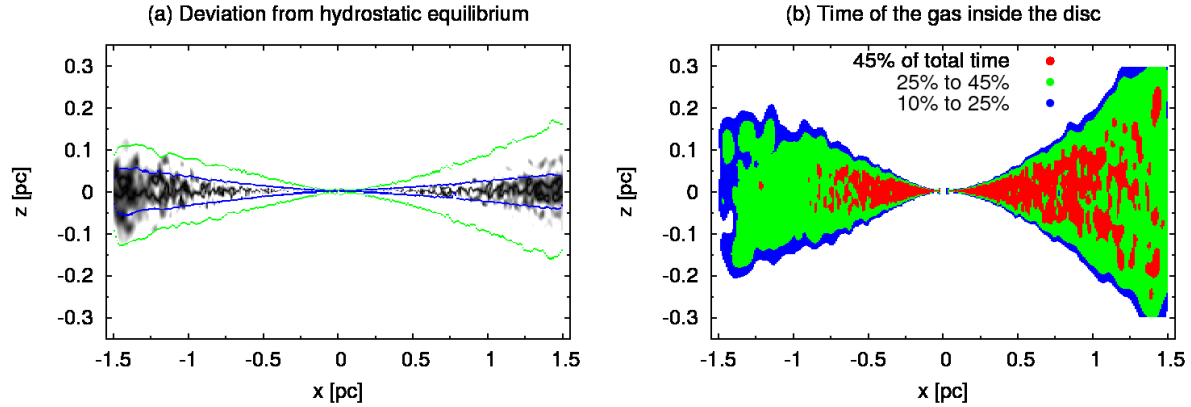
Figure 3.11: In (a) the green line shows the disc scale height resulting from our simulation for V02 in the full cooling case. The blue line in (a) shows what is expected from theory for a hydrostatic equilibrium. The over-plotted structure in (a) shows the deviation of the simulation from a hydrostatic equilibrium $(\frac{\partial \phi}{\partial z} - \frac{1}{\rho}\frac{\partial P}{\partial z})$. Black indicates the lowest deviation, normalised to the global minimum deviation. The colour gradient from black to white spans two orders of magnitude in the deviation from the global minimum deviation. The pure-black part which is close to a hydrostatic equilibrium is in good agreement with the expectation from theory (blue line). Plot (b) shows the time the gas spent inside the accretion disc. Red shows all gas which spent more than 45% of the total time inside the disc, green all gas which spent 25% to 45% of the total time inside the disc and blue shows all gas which spent 10% to 25% of the total time inside the disc. The old (red) gas settles into the disc mid-plane whereas the young (green/blue) gas builds up the atmosphere which is not yet in hydrostatic equilibrium (comparing gas at fixed radius along the z-axis). We also see that the disc is growing inside out since in general material at larger radii is younger. This hides the atmosphere described above in the very inner parts of the disc where all gas is very old and in the outer parts where all gas is very young. At around $\pm$ 0.75 pc on the x-axis the atmosphere around the older gas that already settled into the disc-midplane can be seen the best.

This can be seen in Figure 3.11b, where the age of the gas inside the disc is plotted. Red shows all gas which already spent more than 45% of the total time inside the disc, green all gas which spent 25% to 45% of the total time inside the disc and blue shows all gas which spent 10% to 25% of the total time inside the disc. Old (red) gas is concentrated more in the disc mid-plane, whereas fresh (green/blue) gas builds up the atmosphere of the disc, which is not yet in hydrostatic equilibrium (comparing gas at fixed radius along the z-axis). In addition Figure 3.11b also shows that the disc is growing inside out since in general the material at larger radii is younger. This hides the atmosphere described above in the very inner parts of the disc where all gas is very old and in the outer parts where all gas is very young. At around $\pm$ 0.75 pc on the x-axis the atmosphere around the older gas that already settled into the disc-midplane can be seen the best.

3.6   Summary and Discussion

We have performed simulations of a gas cloud colliding with a super-massive black hole, with parts of the cloud engulfing the black hole during the process. We demonstrate that even when the cloud is initially unbound to the black hole due to a high velocity, sub parsec-scale gas discs can form. Clearly, there are a lot of additional details that can be studied, which we will explore in a subsequent paper. Firstly, we did not investigate fragmentation and star formation yet which is necessary to directly compare the simulations with the observations. Secondly, the potential of the stellar cusp observed in the GC clearly influences SPH particle orbits around the black hole. Finally, black hole and stellar feedback could also play an important role in the formation process.

An adiabatic equation of state leads to an explosion of the cloud during infall with thermal energies comparable to supernova energies of 10^{51} erg. This prevents formation of a compact accretion disc and leads to a large expanding bubble of hot gas. For very inefficient cooling, this could be an alternative interpretation for a hot bubble of gas seen near a black hole like e.g. Sgr A East in our milky-way GC, which has been attributed to a supernova explosion (Herrnstein & Ho 2005).

The isothermal case produces already viable results for the accretion behaviour and distribution of mass onto orbits of different eccentricity compared to the full cooling case. However, numerical and other problems especially with resolving the disc in z-direction lead to the conclusion that a full thermodynamical treatment is necessary. In addition, the isothermal approach enhances fragmentation strongly. Due to the low Jeans-mass at a temperature of 50 K a huge number of low mass fragments forms. To study fragmentation in detail, again a full thermodynamical treatment will be necessary.

The simulations using the full cooling prescription of Stamatellos et al. (2007) represent the most realistic case. Here we are not dominated by numerics and resolve the disc scale height to multiple times the softening length due to the higher temperatures resulting in a larger scale height. In this case we do not artificially suppress radial movement, leading to more circular orbits compared to the isothermal case.

We find that the disc mid-plane consists of old (= already inside the disc for a long time) gas close to hydrostatic equilibrium, surrounded by an atmosphere of young gas that was just falling in and that did not yet settle into hydrostatic equilibrium. This explains the deviation of the disc scale height we find in our simulations compared to what we would expect from gas in hydrostatic equilibrium.

Generally we find that the impact parameter is the dominant factor in determining the accretion rates, from Sub-Eddington accretion rates for large impact parameters to Super-Eddington accretion for small impact parameters. Cloud velocity determines the final rotation of the resulting discs semi-major axis with respect to the x-axis in the xy-plane.

Fast clouds ($v_{cloud} > 50$ km/s) lead to discs that are rotated towards the negative y-axis and slow clouds ($v_{cloud} < 50$ km/s) to discs that are rotated towards the positive y-axis. Also cloud velocity strongly determines the amount of gas bound to the black hole initially. Low velocities lead to more mass inside the final disc compared to simulations with velocities such that nearly no SPH particle is bound to the black hole initially.

The goal of this paper is to provide a proof of principle of the idea of a cloud engulfing the black hole during passage. With this mechanism we are able to produce parsec to sub-parsec sized dense accretion discs even when the initial cloud is unbound to the black hole.

3.7 Acknowledgements
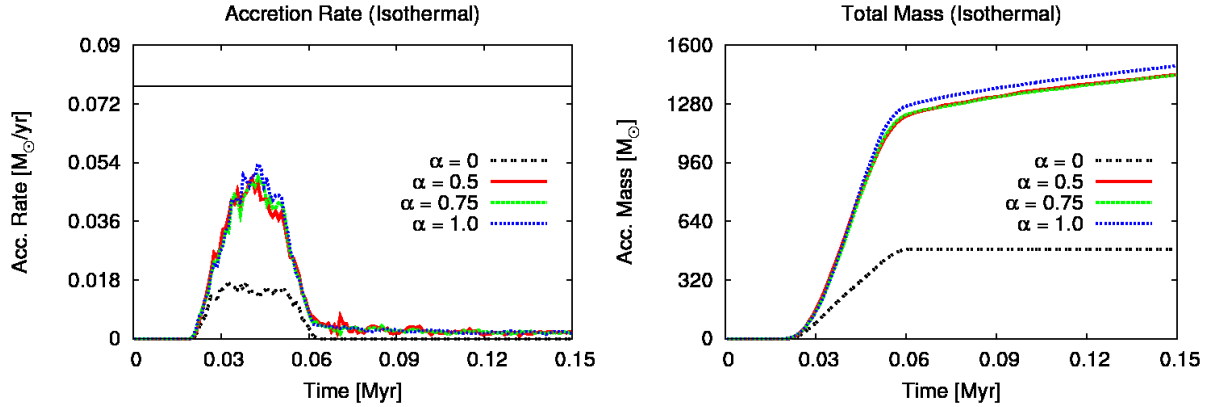
Figure 3.12: The impact on accretion rate and total accreted mass as a function of the numerical viscosity α parameter for the isothermal case. To visualise the differences better, the plots are shown only from 0 to 0.15 Myrs. Red (solid) shows the results for $\alpha = 0.5$, green (dashed) shows the results for $\alpha = 0.75$ and blue (dotted) the results for $\alpha = 1.0$. The black line (dashed-dotted) shows the special case $\alpha = 0$, which turns off the interaction of gas so that only material which initially already was on an orbit smaller than the accretion radius gets accreted. As expected with higher viscosity the gas interacts stronger and thus more material falls onto the black hole, but the results are not strongly dominated by the actual choice of the viscosity parameter. The thin black horizontal line in the accretion plot again shows the Eddington limit for the GC black hole.

3.8   APPENDIX: Numerical Stability

In this section we present results of our numerical stability test-simulations, for which we used isothermal and full cooling simulations with initial condition V03.

3.8.1   Artificial Viscosity

To study the dependence of our results on artificial viscosity we performed a parameter-study in α of the artificial viscosity presented in section 3.4 for the isothermal and the full cooling case. The range of α suited for simulations is $\alpha = 0.5$ - 1.0 (Springel, 2005). We performed test simulations with $\alpha = 0$, 0.5 and 1.0. The simulations presented throughout the paper used $\alpha = 0.75$. Figure 3.12 and 3.13 show the dependence of accretion rate and total accreted mass on the α parameter in the isothermal and cooling case. As can be seen, the results are stable as a function of α within the range suited for simulations. The special case $\alpha = 0$ leads to no transport of material at all into the accretion boundary region, only material which initially already was on an orbit smaller than the accretion radius gets accreted here. As expected, a high viscosity parameter leads to a somewhat higher transport of material, however this artificially enhanced gas transport is negligible compared to the physical processes described in this paper.
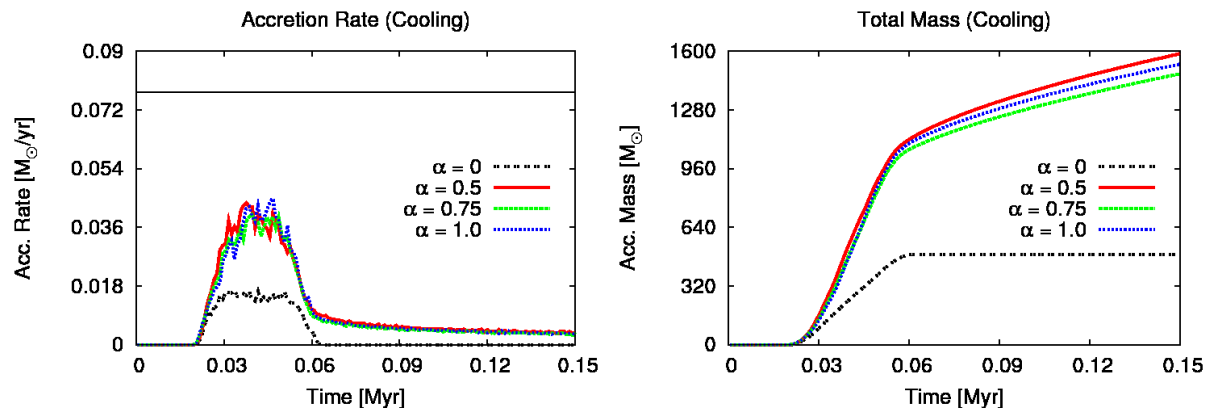
Figure 3.13: Same plot as 3.12, but for the cooling case.
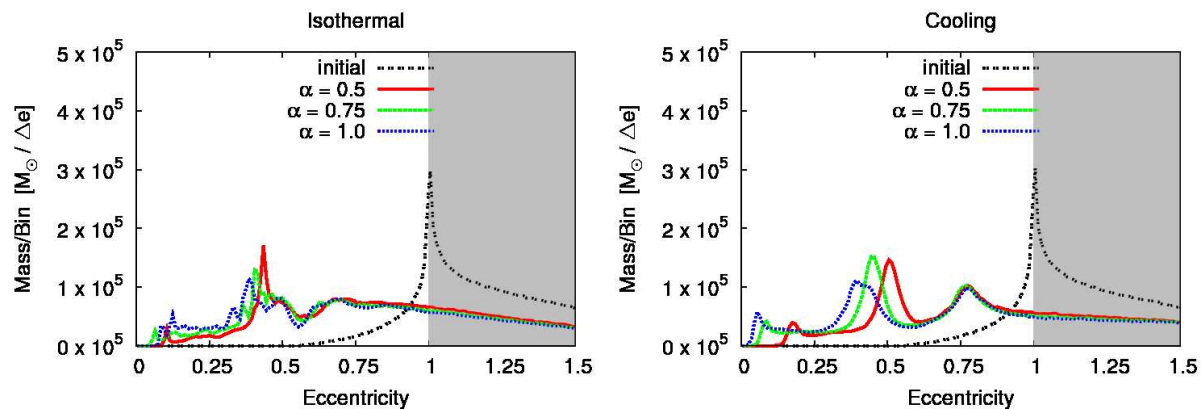
Figure 3.14: Comparison of the distribution of mass onto orbits of different eccentricity depending on numerical viscosity α for the isothermal and cooling case. SPH particles with e > 1 are not bound to the black hole, indicated by the gray background. In the isothermal case the suppression of radial movement as described in section 3.5.3 leads to a similar behaviour for all values of the α parameter. In the full cooling case we expect a larger difference in the results due to stronger interaction of the initial colliding flows of gas with a larger α parameter and the relative ease of radial movement because of the higher disc scale-height. The choice of $\alpha = 0.75$ gives a good mean between the results of the suggested range of $0.5 < \alpha < 1$.

Figure 3.14 shows the distribution of mass onto orbits of different eccentricity for different values of the numerical viscosity parameter α. As described in section 3.5.3 in the isothermal case radial movement suppression gets larger the closer we get to the black hole. This leads to the difference especially at low eccentricities between the full cooling case and the isothermal case. In the full cooling case different values for the strength of the numerical viscosity lead to a stronger effect on the final distribution compared to the isothermal case, as material can move in radial direction more easily. We do not expect the resulting distributions to be exactly the same for the cooling case since clearly a stronger viscous force should lead to more interaction of the initial colliding flows of gas, transporting more material onto lower, more circular orbits. However, we are not dominated by this effect, as the outer parts, the total amount of gas and the general shape are very similar for all cases. The choice of $\alpha = 0.75$ gives a good mean between the results of the suggested range of $0.5 < \alpha < 1$.

3.8.2 Resolution
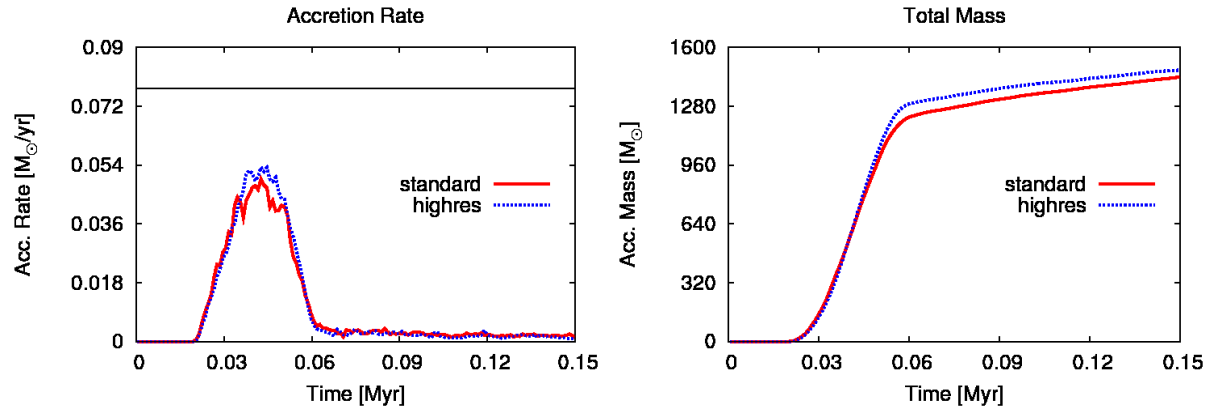
Figure 3.15: Impact on accretion rate and total accreted mass as a function of simulation resolution in the isothermal case. Red (solid) shows the results for 10^6 SPH particles, blue (dotted) the results for 5×10^6 SPH particles. To visualise the differences better, the plots are shown again only from 0 to 0.15 Myrs. The high resolution simulation shows somewhat larger accretion rates during the impact.
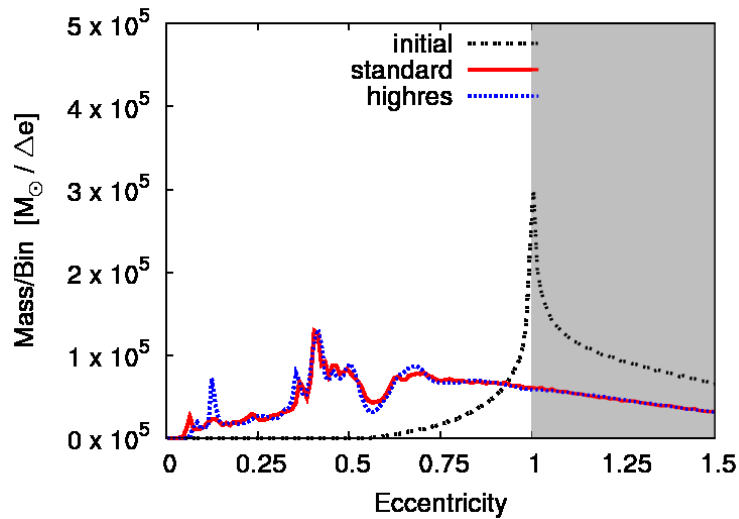

Figure 3.16: Comparison of the distribution of mass onto orbits of different eccentricity for our standard resolution and a high-resolution test. The difference is very small, with the high resolution simulation leading to a bit more circular orbits compared to the lower resolution case. SPH particles with e > 1 are not bound to the black hole, indicated by the grey background.

To study the effect of resolution on our results we repeated the isothermal simulation using V03 with SPH particle number increased to 5×10^6 SPH particles, compared to 10^6 SPH particles for the normal runs. Figure 3.15 shows the resulting accretion rates and total accreted mass. The high resolution simulation shows slightly stronger accretion at the beginning.

Figure 3.16 shows the distribution of mass onto orbits of different eccentricity for the high and standard resolution isothermal simulation. Here the difference is very small with the high resolution simulation leading to slightly more circular orbits compared to the lower resolution case.

3.8.3 Softening Length
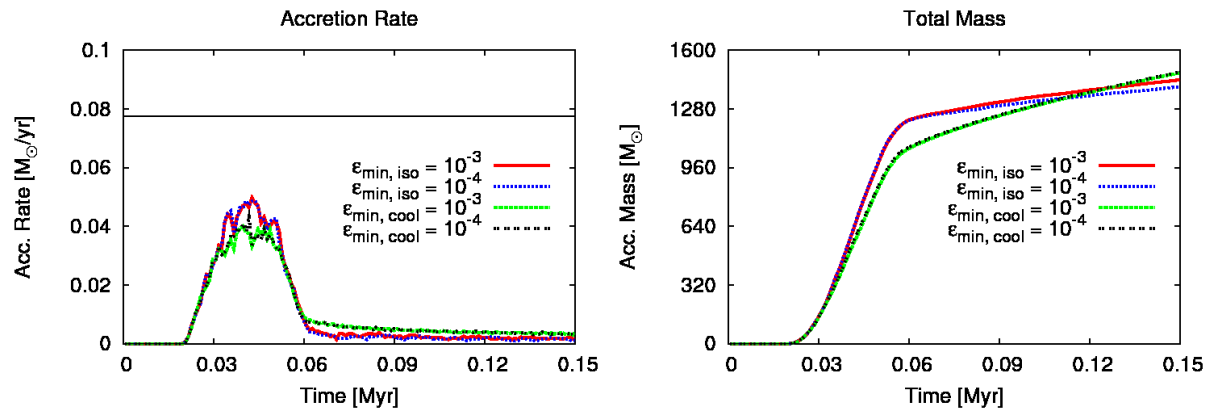
Figure 3.17: Accretion rate and total accreted mass as a function of softening length. Red (solid) shows the results for $\epsilon = 10^{-3}$ pc, blue (dotted) the results for $\epsilon = 10^{-4}$ pc. To visualise the differences better the plots are shown only from 0 to 0.15 Myrs. The difference is almost completely negligible.
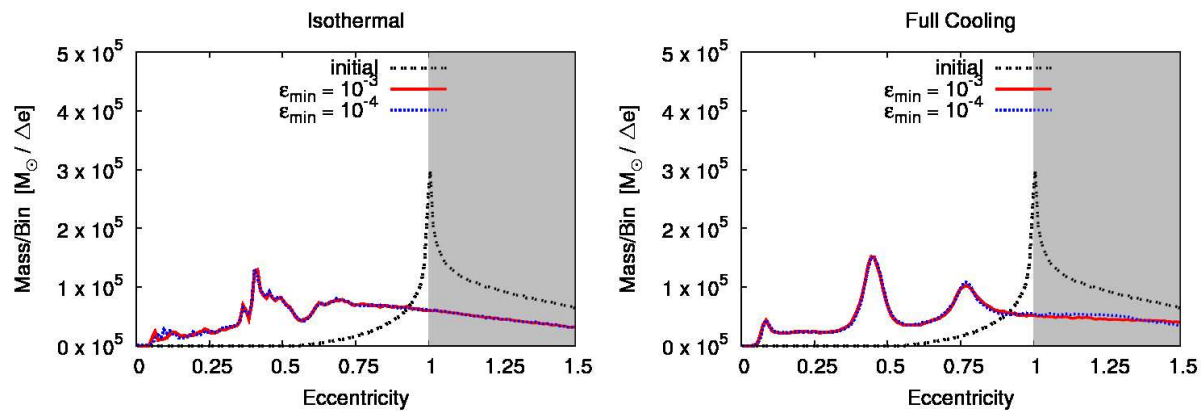

Figure 3.18: Comparison of the distribution of mass onto orbits of different eccentricity depending on softening length. Again the difference is almost completely negligible. SPH particles with e > 1 are not bound to the black hole, indicated by the grey background.

Finally, we studied the dependence of our results on the softening length. For this we repeated the full cooling and isothermal simulation using V03 with softening length $\epsilon = 10^{-4}$ pc (compared to our standard simulations with $\epsilon = 10^{-3}$ pc) making it very expensive in terms of computing time. Figure 3.17 shows the resulting accretion rates and total accreted mass and Figure 3.18 the distribution of mass onto orbits of different eccentricity.

It can be clearly seen that the difference in both cases is almost completely negligible. In the isothermal case we still do not resolve the disc scale height to even one time the softening length, so that we expect the influence of an order of magnitude smaller softening length to have no real impact. In the cooling case we already resolve the disc scale height to multiple times the softening length for our standard value of $\epsilon = 10^{-3}$, thus the stability of our results in this case indicates that we have reached convergence.

Chapter 4

Stellar Disc Formation Studies

In this chapter we present simulations of fragmenting compact accretion discs. The simulations were intended to explain the top-heavy IMF of the Galactic Centre stellar discs. However numerical problems which we present later prevent us from being able to trust the results. We also present other aspects of the infall of a cloud onto a black hole which we studied.

4.1 Fragmentation

4.1.1 Compact Accretion Discs

In this part we are assuming the same model as presented in the first paper. We investigate the model in more detail by studying the fragmentation behaviour of the accretion disc to compare the formed clumps directly to observations of the stars. To find a better fit in terms of size of the disc compared to our previous work we performed a number of low resolution simulations. Using the initial conditions from the best fit of those simulations we run a high resolution simulation which we present in the following.

Again the cloud orbit is set such that a part of the cloud will rotate clockwise around the black hole. The larger part of the cloud will rotate counter-clockwise around the black hole thus setting the rotational direction of the final accretion disc. The collision of material with opposite angular momentum leads to redistribution of angular momentum and the formation of a compact accretion disc.
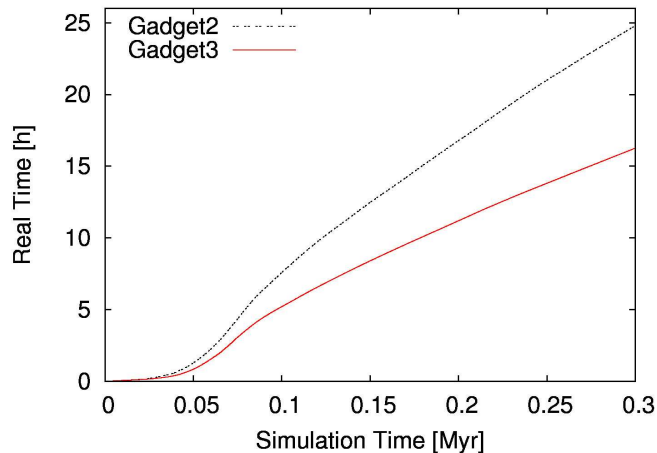
Figure 4.1:   Comparison of simulation time against total real time for a low resolution disc formation test-simulation. Gadget3 needs around 40% less time to advance to the same point in the simulation as Gadget2.

To simulate the cloud infall we are using the N-body Smoothed Particle Hydrodynamics (SPH) Code Gadget3. The physics included into Gadget3 is already described in the Gadget2 part in the first paper. Gadget3 increases the simulation speed compared to Gadget2 with a new domain decomposition scheme, which balances work and memory-load at the same time, but requires more communication. Figure 4.1 shows a comparison of the time it takes Gadget2 and Gadget3 to advance to a certain simulation time. For the type of simulation we are interested in, Gadget3 shows an improvement of up to 40% in simulation speed for an evolution time up to 0.3 Myrs.

In order to prevent artificial fragmentation we make sure that we fulfil the resolution requirement given by (2.64). We check if the density ρ of an SPH particle is above ρ_{crit} and adjust the temperature of the particle such that $\rho_{crit} = \rho$. A particle inside a collapsing core will quickly reach the critical density since we do not have infinite resolution. Those particles will be heated during the exponential collapse phase, thus reaching very high temperatures. This can lead to overheating and the sudden rapid expansion of a former collapsing region if we follow the exponential collapse over a few orders of magnitude in density. To prevent this from happening we also check if a particle is a fixed factor of 10 above the tidal density for a fluid (2.18). At 10 times the tidal density we turn off the artificial heating prescription and let the particles heat and cool due to adiabatic compression and our cooling formalism.

The simulation does not include any feedback from the black hole or the forming stars. While feedback from the black hole could be important, depending on the angle of the outflow with respect to the gaseous disc, we do not expect any feedback from the stars to be important during the short simulation time of only 0.16 Myrs. At this point, as test

simulations show, all collapsing regions have entered the exponential collapse phase and can not return below the tidal density at any point on their orbit.

We do not include sink particles to replace forming clumps during our simulation. This makes the simulation very expensive in terms of runtime when the clumps have formed. The minimum hydro-smoothing length prevents the clumps from collapsing infinitely, thus setting a lower limit on the clump size. However with this prescription we do not have to make any assumptions about accretion like in the sink particle case. The accretion here occurs "naturally". We can also study the clump structure in more detail, for example the internal rotation or stripping of a clump during pericentre passage.

We identify clumps in our simulation in a post processing step by using a clumpfinder, which searches minima in the local gravitational potential. The clumpfinder then compares kinetic, potential and thermal energy of the SPH particles. If the total energy is below zero the particle is bound to the local minimum.

The initial particle distribution for the cloud is cut from a glass in order to remove any residual forces. A glass is created by evolving a random distribution of particles with a reversed sign (repulsion instead of attraction) in gravity. Initially the cloud centre of mass has a distance of 4 pc from the coordinate-origin on the x-axis and 0.7 pc on the y-axis. The cloud velocity is set to -80 km/s. We also include the additional potential of the nuclear star cluster (1.1).

The cloud approaches the black hole from the positive x-axis, seen in the density cut through the equatorial plane in units of $\frac{M_\odot}{pc^3}$ in Figure 4.2a. Quickly a disc forms around the black hole (Figure 4.2b) which circularises (Figure 4.2c,d) due to dissipation of kinetic energy and starts to fragment (Figure 4.2e,f). In the last timestep, shown in Figure 4.2f one can still see the rest of the tail of the infalling cloud on the right side, which did not redistribute enough angular momentum or dissipate enough kinetic energy to be inside the compact disc.
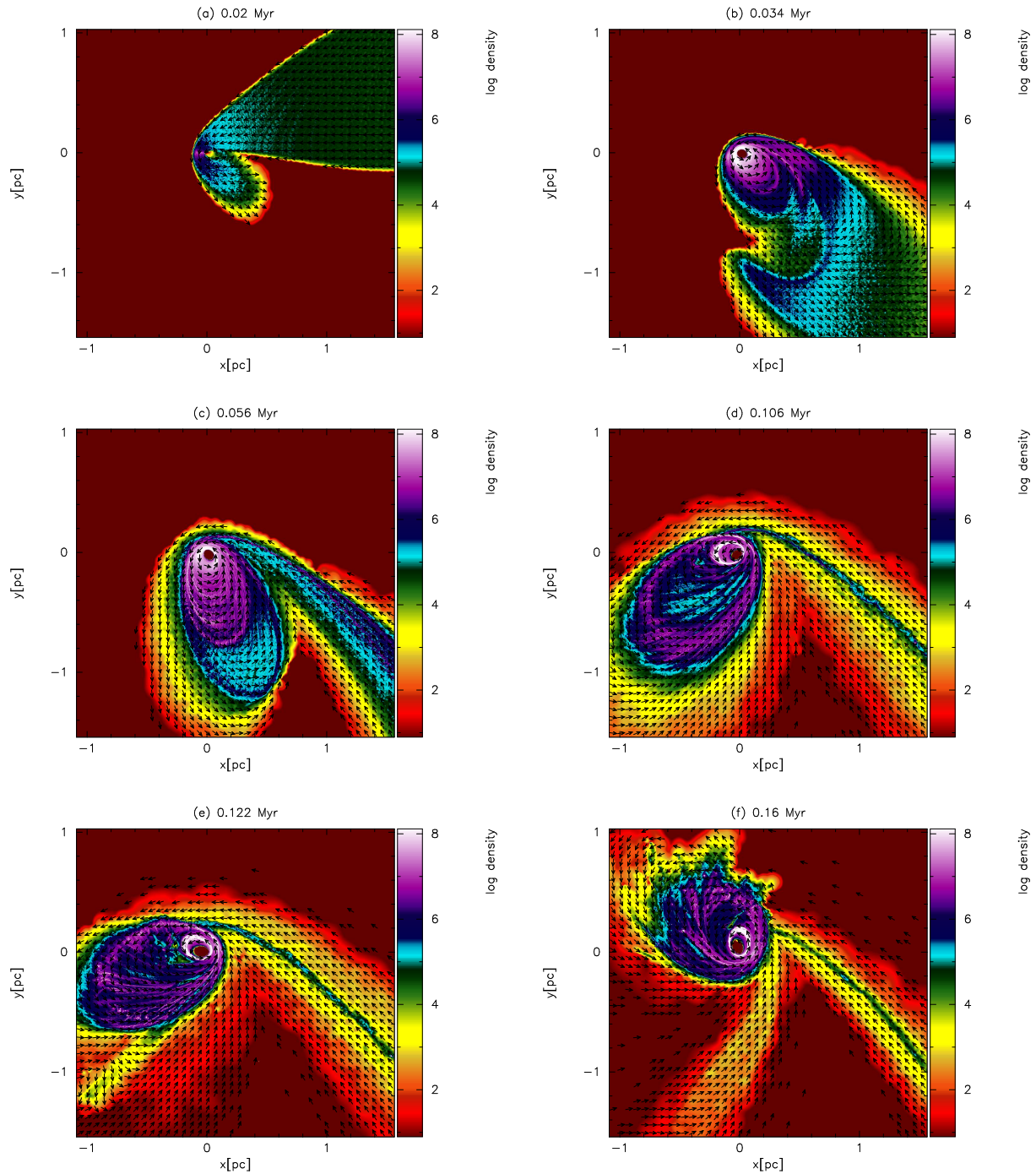
Figure 4.2: Time evolution of the logarithmic density in units of $\frac{M_\odot}{pc^3}$ in the xy-plane with z=0 pc. Velocity vectors are all the same length and only indicate local direction. The cloud approaches the black hole from the right side. The global rotation of the forming disc is counter-clockwise due to the initially larger amount of gas on counter-clockwise orbits. Quickly a compact and strongly fragmenting accretion disc forms.
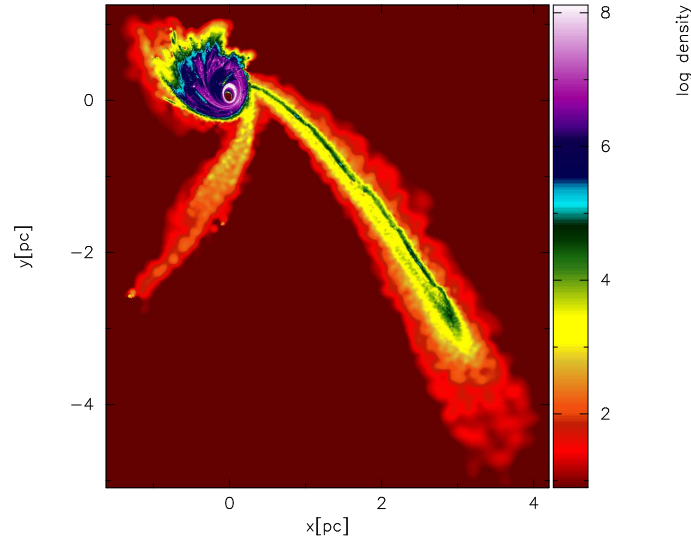
Figure 4.3: A zoom-out of the logarithmic density plot from Figure 4.2f in units of $\frac{M_\odot}{pc^3}$ in the xy-plane with z=0 pc. On the left side a stream of gas can be seen created by a clump from the cloud tail which dragged gas along its path through the disc. The stream of gas on the right side is highly eccentric gas from the cloud which did not redistribute its angular momentum.
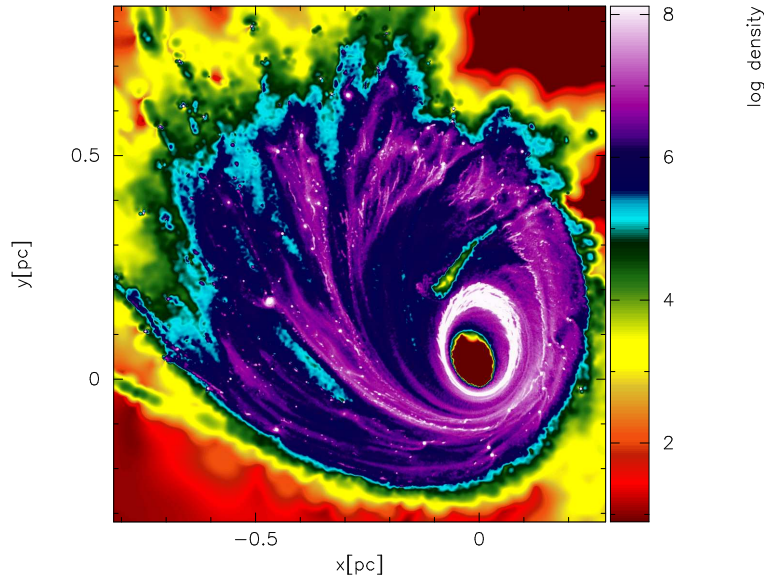

Figure 4.4: A zoom-in of the logarithmic density plot from Figure 4.2f in units of $\frac{M_\odot}{pc^3}$ in the xy-plane with z=0 pc. The compact disc shows strong signs of fragmentation. There is also a visible void created by a clump originating from the cloud tail.

There is also another stream of gas visible falling back onto the disc from the left side. The cloud tail and the stream of gas can be better seen in Figure 4.3 which shows a zoomed out plot of Figure 4.2f. The stream of gas on the left side is created by clumps that formed inside the infalling tail of the cloud, which dragged gas out of the disc while crossing through it. Figure 4.4 shows a zoom onto the compact accretion disc from Figure 4.2f. Clearly visible are the dense clumps across the disc. We will discuss the evolution of the very prominent clump seen on the left side at around -0.5 pc on the x-axis and 0.15 pc on the y-axis in detail later. There is also a gap visible around 0.2 pc above the coordinate origin, created by a clump that originates from the cloud tail which went through the disc and dragged gas along with it.

In Figure 4.5 the temperature distribution of the disc is shown in units of Kelvin for a slice at z=0 pc in the xy-plane. Compared to the initial cloud temperature of 100 K the disc is rather hot with roughly 1500 K on the average. Due to adiabatic compression the gas can heat up to 2500 K during pericentre passage.
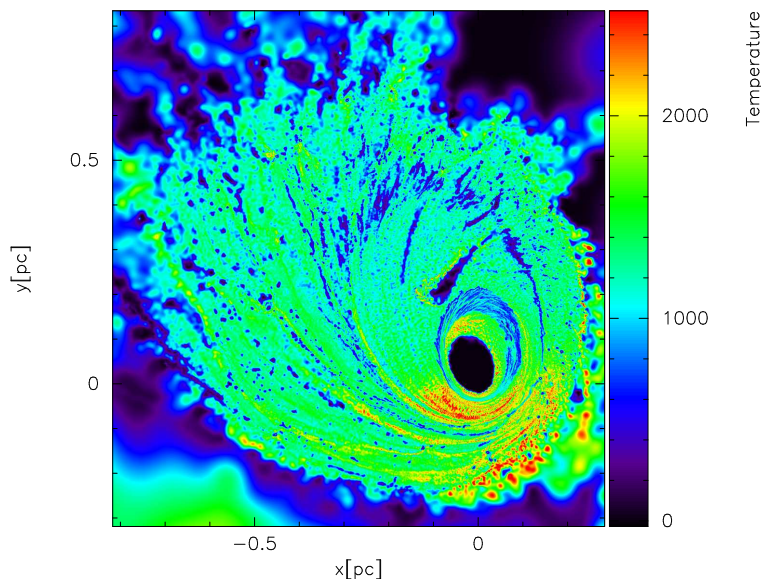

Figure 4.5: Temperature distribution in Kelvin for a slice at z=0 pc in the xy-plane. The overall disc temperature is at roughly 1500 K. During pericentre passage the gas can heat up to 2500 Kelvin due to adiabatic compression.

4.1.2   Clump Evolution

We follow the evolution of the most prominent clump seen in Figure 4.4 at around [-0.5, 0.15]. Figure 4.6 shows the density in units of $\frac{M_\odot}{pc^3}$ in the xy-plane for a slice at z=0 pc. The plots are always centred on the centre of mass of the clump and show a region of 0.1 pc around this centre. Velocities are shown relative to the velocity of the centre of mass of the clump. The length of the velocity vectors indicate speed in units of km/s. The top left corner in each plot shows which vector length corresponds to which velocity. Note that we changed the units in Figures 4.6 d,e and f so that the vectors are still visible during pericentre passage.

Figure 4.6a and b show the clump before pericentre passage. The clump is rotating and gathers material from its surrounding seen as a large red halo around the central yellow part. During pericentre passage in Figure 4.6c we can see the clump stripped of its halo but also passing a dense filament. This way the clump is able to gather a lot more material compared to the previous orbit leading to the very large halo forming around the clump in Figure 4.6d. Figure 4.6e shows the clump shortly before another pericentre passage. Compared to Figure 4.6b the halo is now multiple times larger and also denser. In Figure 4.6f the clump enters again a dense region during the pericentre passage. This time the halo is not stripped completely due to the higher density.

The clump evolution shows that the process is highly-dynamic, stripping and growth is dependant on the current environment, thus it is hard to predict the global clump mass distribution.
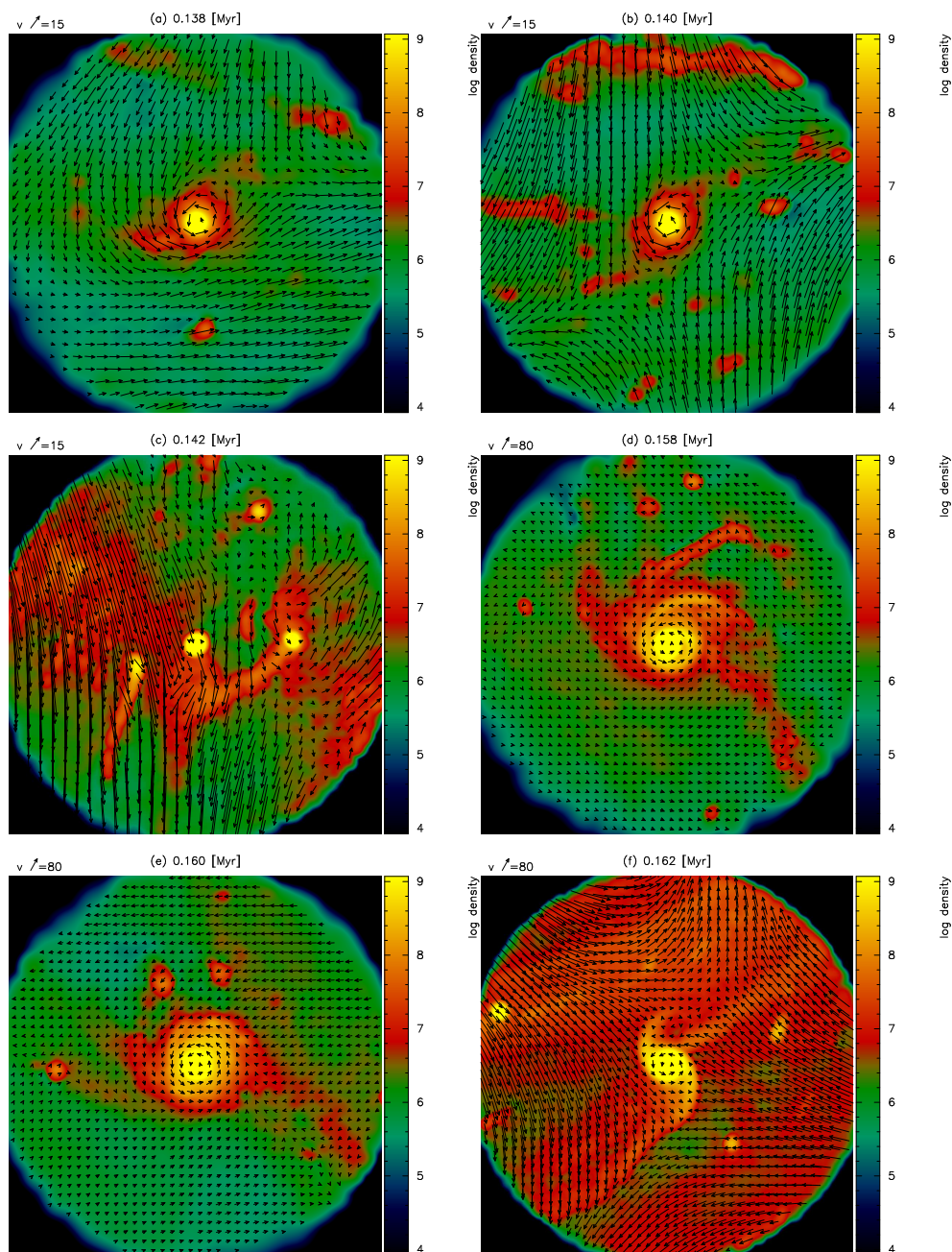
Figure 4.6: Evolution of a single clump. Density is shown in units of $\frac{M_\odot}{pc^3}$ in the xy-plane for a slice at z=0 pc. The top left corner of each plot shows which vector length corresponds to which velocity (given in units of km/s). The plot is always centred on the centre of mass of the clump and shows an area of radius 0.1 pc around the clump. Velocities are shown relative to the centre of mass. The clump is rotating and collects material from its surrounding (a,b). During pericentre passage the clump is stripped to its dense core (c) but crosses a dense filament. This way the clump can grow a lot larger compared to before (d,e). The final plot shows the clump again during pericentre passage, this time without loosing a large fraction of its accumulated mass.

4.1.3   Clump Mass Function

In order to compare our simulation to observations of the stellar disc at the Galactic Centre we will look at clump formation in more detail. Since we do not use sink particles in our simulation, it becomes very slow as soon as clumps start to form. Thus we want to end the simulation as quickly as possible. On the other hand we have to make sure that we are converged as good as possible in the number of clumps that have formed and that the mass of the clumps is not growing too much if we would run the simulation any further.
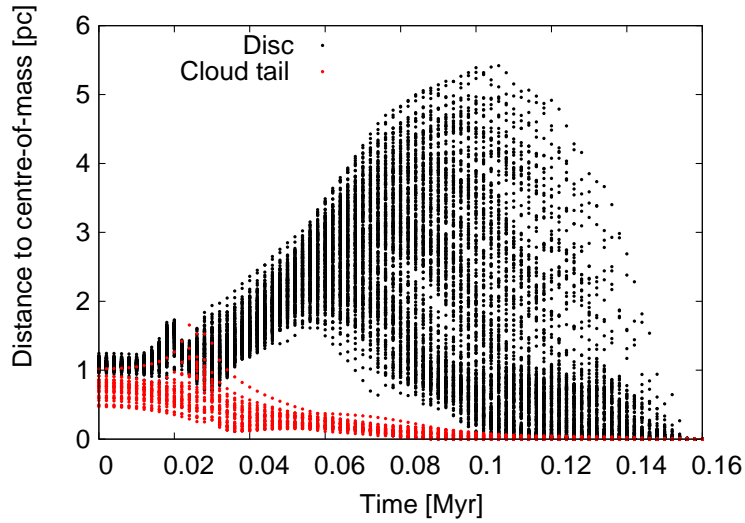

Figure 4.7: Maximum distance of all particles of a single clump from their centre of mass over time, for all clumps. In black all clumps originating in the accretion disc are shown and in red all clumps originating from the infalling cloud tail are shown.

At the final simulation time (0.16 Myrs) we count a total number of 277 clumps using the clumpfinder. The total mass in clumps is 1292.6 $M_\odot$, with a mean clump mass of 4.66 $M_\odot$ and a maximum clump mass of 29.96 $M_\odot$. Figure 4.7 shows for every clump that is identified at the final time the maximum distance to the centre of mass of all particles that will end up in a single clump, plotted over time. Thus for every timestep there are 277 data points.

The plot shows an interesting feature, the division of clumps into two distinct populations. The population shown in red forms quickly and already collapses to a tight bound clump early on. Those clumps are the ones originating inside the cloud tail and are thus little affected by the harsh environment of the black hole. The second population quickly spreads out and takes a lot longer to form a tight bound clump. The tight bound state is only reached a short time before the end of the simulation. The clumps in this population are formed inside the accretion disc.

Dividing the clump population shows for the disc clumps a total number of 246 clumps and a combined mass of 1226.4 $M_\odot$. The mean mass is 4.98 $M_\odot$ and the maximum mass 29.96 $M_\odot$. There are in total 31 clumps that formed inside the cloud tail, with a combined mass of 66.2 $M_\odot$, a mean mass of 2.13 $M_\odot$ and a maximum mass of 7.6 $M_\odot$.
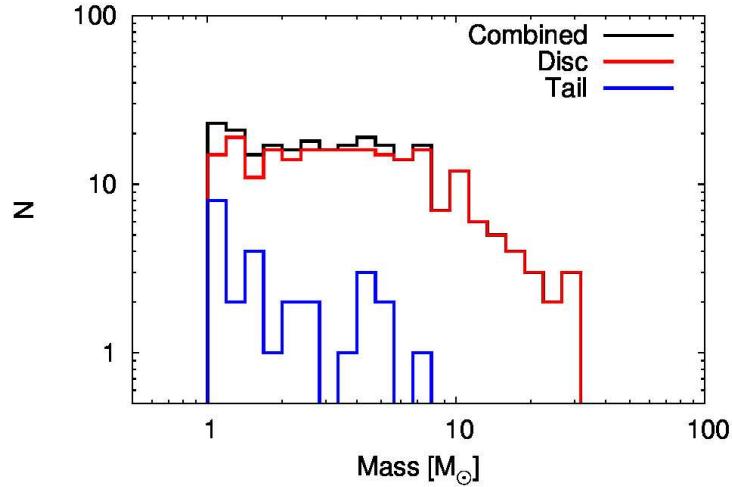

Figure 4.8: Core mass function (CMF) for the different clump populations at the final timestep. In black the combined distribution of clumps formed inside the accretion disc and inside the cloud tail are shown. In red the disc-only population is shown and in blue the clumps formed inside the cloud tail.

In Figure 4.8 we plot the clump-mass-function (CMF) for the clumps identified at the last snapshot at 0.16 Myrs. The combined population is shown in black, the disc population in red and the tail population in blue. Fitting the disc population gives a slope of -0.34, which compares well to the observed top-heavy IMF slope of -0.45 $\pm$ 0.3 (Bartko et al., 2010). Note that we compare the clump mass function to the stellar mass function since we do not want to make any assumptions on the conversion of the CMF to an IMF. A fit to the cloud tail population (although the statistics are low) gives a slope of -1.78, which is more consistent with a standard Salpeter/Kroupa IMF. The combined CMF has a slope of -0.41.

However, comparing the mean mass of the disc clumps of around 5 $M_\odot$ to the mean mass of the observed stars of around 30 $M_\odot$(Bartko et al., 2010) we are way below the mean mass observed in the Galactic Centre. One way to increase the mass would be to increase the temperature inside the disc (for example through black hole feedback). This would lead to a lower number of stars at a higher mass. But since we already reproduce the number of observed stars inside the disc (around 200) quite well, we would also have to increase

the mass of the initial cloud to get a higher number of stars, thus increasing the problem of how to stabilise the initial cloud even more. The star-formation efficiency is quite low with only around 1 percent.
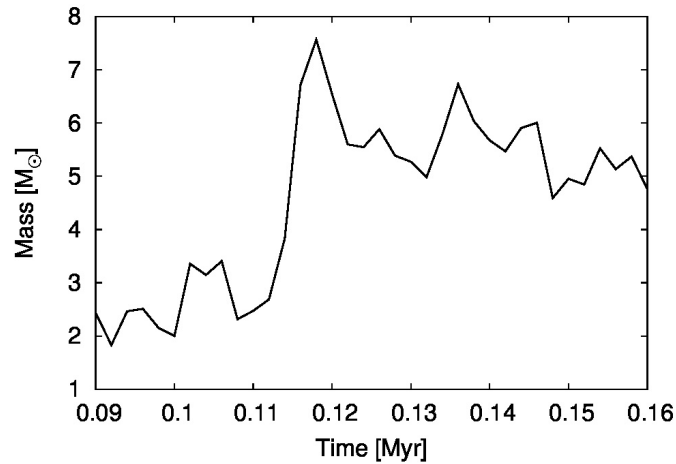
Figure 4.9: Mean clump mass in $M_\odot$ plotted against simulation time in Myrs. The distribution converges against a value of roughly 5 $M_\odot$.

In Figure 4.9 we show the mean clump mass for all 277 clumps over time. The distribution looks reasonably flat at the end indicating convergence. Figure 4.10 shows the total mass in clumps for all clumps over time. Although there are fluctuations, the distribution seems to have reached convergence at around 1300 $M_\odot$. Finally in Figure 4.11 the total number of clumps is plotted over time. Again the distribution still fluctuates but settles around a value of 250.
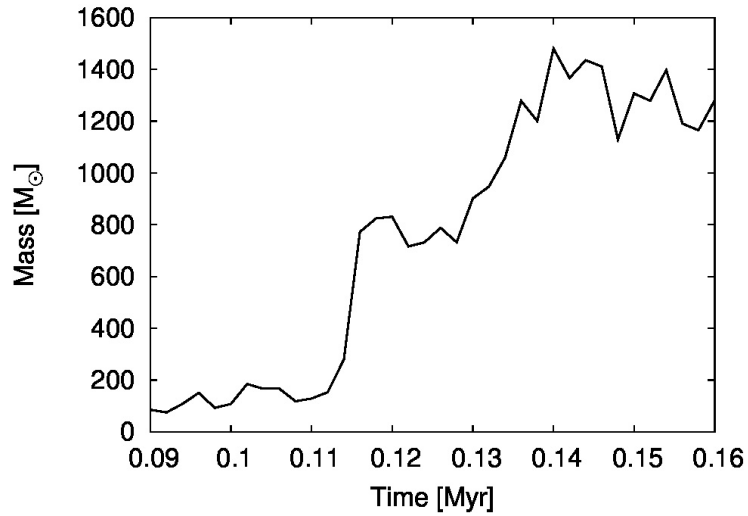
Figure 4.10: Total mass in clumps in M$_\odot$ plotted against simulation time in Myrs. The distribution is fluctuating, but reaches a mean value of roughly 1300 M$_\odot$ at the end.
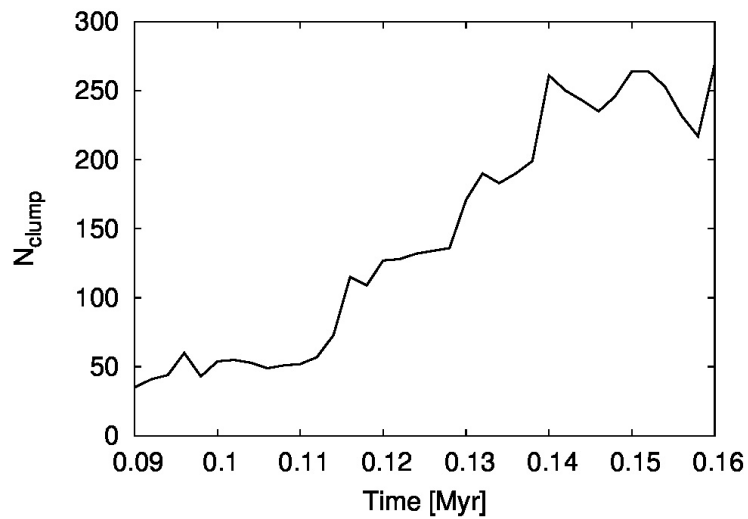

Figure 4.11: Number of clumps detected plotted against simulation time in Myrs. A mean of roughly 250 is reached at the end.

4.1.4 Stellar Disc Evolution
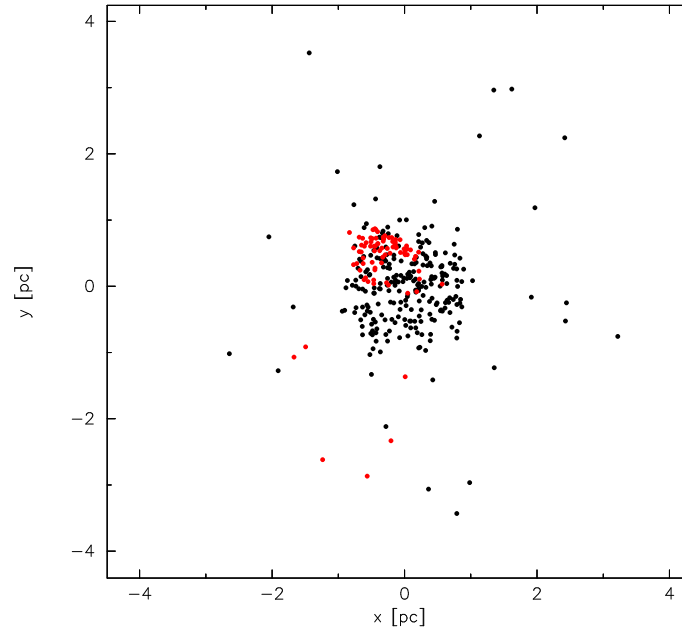
Figure 4.12: Distribution of stars at the beginning of the N-body simulation (red) and at the end of the N-body simulation (black) at 6 Myrs. Due to phase-mixing the distribution evolves from the initial eccentric disc towards a circular disc. The outer radius of the initial eccentric disc is still retained in the final state.

The Galactic Centre stellar discs are around 6 ± 2 Myrs old. We stopped our hydro-simulation already at 0.16 Myrs, keeping in mind that the number of clumps and the clump masses are reasonably well converged at this point. We took the distribution of clumps to set up a pure N-body simulation, taking the centre of mass of the individual clumps as position of a single N-body particle with the mass of the whole clump. We evolved this distribution within the same potential as the hydro-simulation, up to a time of 6 Myrs.

The initial and final distribution of stars at 6 Myrs can be seen in Figure 4.12. The stars are precessing inside the cluster-potential. Due to phase mixing, the final distribution looks circular, although the individual stars are still on eccentric orbits. The central dense disc of around 1 pc radius is formed by the clumps originating from the accretion disc. The outer disc, spread up to 4 pc in radius is formed by the clumps originating from the tail of the cloud. Those stars closely trace the original orbit of the initial cloud. Observationally they should be detectable if the cloud scenario is valid, however they follow a different IMF compared to the disc stars which are mostly O/B and WR stars.

We already see that the disc of 1 pc radius we form is still too large compared to the observed outer disc radius of 0.5 to 0.6 pc. We could decrease the cloud impact parameter so that the redistribution of angular momentum becomes stronger. But then the problem arises that an increasingly larger amount of the cloud will be accreted onto the black hole so that we would have to put more mass into the cloud to provide enough material for the accretion disc.
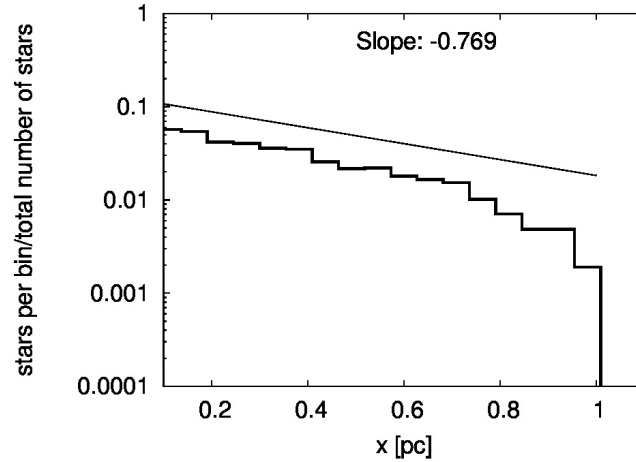
Figure 4.13: Stellar surface density of stars per bin, divided by the total number of stars against distance from the black hole in pc at the final N-body simulation timestep. The distribution is rather flat compared to the observed slope of -1.95 $\pm$ 0.25.

In Figure 4.13 we show the surface density of the disc stars only at the final timestep of the N-body simulation. With a slope of around -0.769 our distribution is too flat compared to the value of -1.95 $\pm$ 0.25 from observations (Bartko et al., 2009). If we compare the mean eccentricity of 0.62 from the central stellar disc to observations which give 0.34 $\pm$ 0.06 (Bartko et al., 2009) our disc is also too eccentric. Overall we can say that apart from the top-heavy IMF and the number of clumps our disc does not compare very well to observations. The solution to improve the correspondence is always to increase the cloud mass or to reduce the cloud size, which would make the cloud infall scenario even more unlikely as the cloud parameters become more and more extreme compared to the observations.

4.1.5 Resolving Fragmentation

In Figure 4.14 we calculate the expected scale-height of a thin accretion disc at different temperatures for different distances from the black hole. The red line represents the inner edge of our disc simulations, the green line the outer edge. The black horizontal line marks the minimum feasible smoothing length of 10^{-4} pc for the disc simulation. A value of 10^{-5} pc or lower slows down the simulations so much that they become unfeasible.
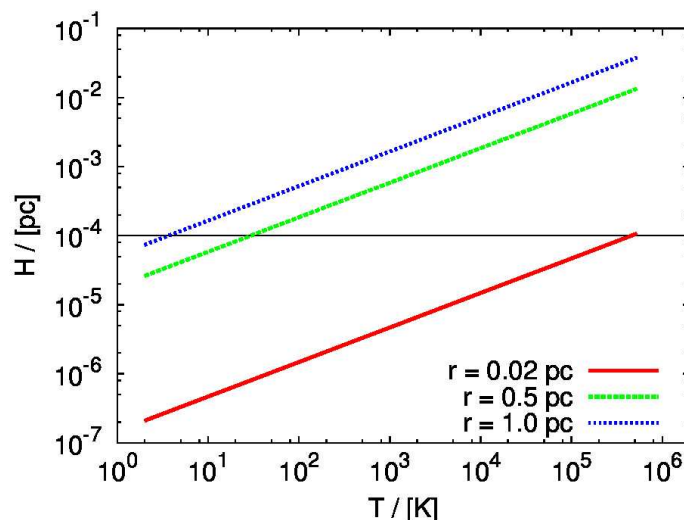

Figure 4.14: Theoretical scale-height of a thin accretion disc at different temperatures. The colours represent distance from the black hole. The red line represents the inner edge of the disc in our simulations, the green line the outer edge. The horizontal black marker shows the minimum feasible smoothing length for the simulation.

We know from the resolution requirements section 2.4.4 that we have to resolve the disc scale height to at least 4 times the minimum smoothing length. Thus in total we should resolve the disc by roughly 10 times the minimum smoothing length. At the lowest temperature in Figure 4.14 this would not be possible, even for the outer edge of the disc. The scale-height of the disc itself is already almost at 10^{-5} pc, so that we would need a minimum smoothing length of 10^{-6} pc to resolve the disc. The inner edge would even require 10^{-8} pc to be resolved.

Figure 4.5 showed that the temperatures in the disc can rise up to 2500 K. Even in that case the inner edge is not resolved well and we would need less than 10^{-6} pc to resolve the inner edge. At 10^{-4} pc minimum smoothing the outer edge is barely resolved. Thus we conclude that we can not fully trust the fragmentation simulation presented in this part. The closer we get to the inner edge of the disc, the worse the resolution constraint is fulfilled and the less we can trust fragments to be real.

Looking at the density temperature plot in Figure 4.15 for the SPH particles of the accretion disc at the final timestep, we can see several important points. In black, resolved gas is plotted. In blue, gas that has to be heated due to the resolution criterion is plotted leading to a tight correlation between temperature and density. In red collapsed regions that are resolved are plotted. Green just represents a higher density region of resolved gas.
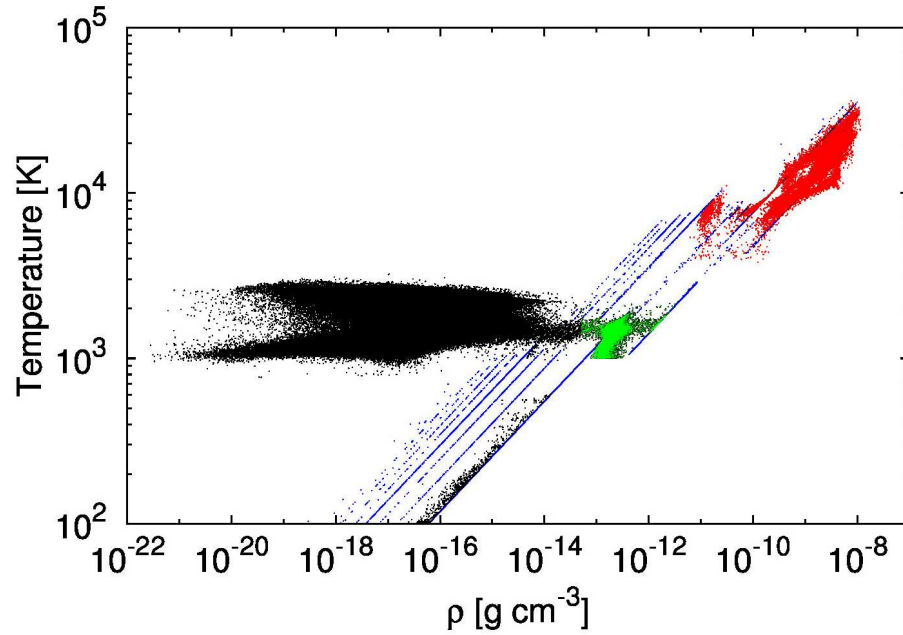
Figure 4.15: Temperature/density correlation for all SPH particles from the final timestep of our compact accretion disc simulation. In black resolved gas is plotted. In blue gas that has to be heated to fulfil the critical density criterion is plotted. Green shows a high density region of resolved gas and red shows resolved clumps.

If we now look at the structure of the disc itself in Figure 4.16 and again mark the particles in the same colours as in Figure 4.15 we see that large parts of the disc are not resolved well (blue) and have to be artificially heated. This gas makes up 50% of the total disc mass.
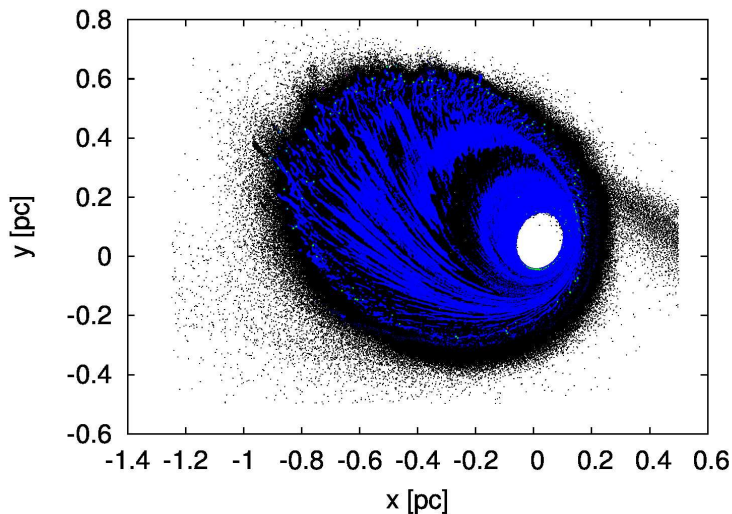
Figure 4.16:   The accretion disc plotted in the colour coding of Figure 4.15. The blue unresolved gas makes up nearly 50% of the disc.

One problem in dealing with resolution is that the structure of the final accretion disc is not clear from the beginning. In our first simulations the final accretion disc was density capped due to a high minimum smoothing length (The right side of Figure 4.15 was completely cut off). After using a smaller minimum smoothing length the background disc density was resolved but now cooling was more efficient so that lower temperatures could be reached and the critical density criterion is no longer fulfilled. To resolve the critical density at all times, judging from the above plots we would need a factor of 10 (or more) particles at the same initial cloud mass, which would require around 50 million SPH particles. Together with the scale height requirement of a minimum smoothing length of 10^{-6} pc to resolve the inner disc edge scale height, the resulting simulation would be extremely expensive.

The above considerations should also apply to other simulations of a compact fragmenting accretion disc, like the ones we presented in the introduction. Typical values used in those simulations would be around 2 million particles and a smoothing length of around 10^{-3} pc. Thus it is not yet clear if any of those simulations really has proven that an infalling cloud leads to a top-heavy IMF. Most of the simulations use sink particles instead of keeping fragments. Still the question is if such a sink would have formed in the first place if the scale height was really resolved.

Second, if sinks are not implemented correctly they can artificially enhance the resulting clump mass. A simple sink particle just acts like a little hole which leads to extreme accretion rates onto the sink inside the very dense disc. Improved sink particle formulations also introduce a pressure from the sink itself so that there is no pressure hole inside the

disc. In addition to a higher resolution and a lower minimum smoothing length it would also be desirable to use an adaptive gravitational softening length instead of a fixed value, as pointed out in Nelson (2006).

As a final remark, the disc scale height was calculated for a thin accretion disc in hydrostatic equilibrium. In our case we normally have eccentric, self-gravitating accretion discs, so that the assumptions in calculating the scale-height are not fully valid. The disc is not completely in hydrostatic equilibrium, which we showed in the first paper in Figure 3.11. A strongly self-gravitating accretion disc can make the standard thin accretion disc (also called α-disc) prescription invalid (Balbus & Papaloizou, 1999). Resolution requirement tests for self-gravitating accretion discs have been performed for a number of examples by Lodato & Clarke (2011) and the results indicate that the basic requirements we presented in section 2.4.4 still hold.

4.2 Influence of Turbulence
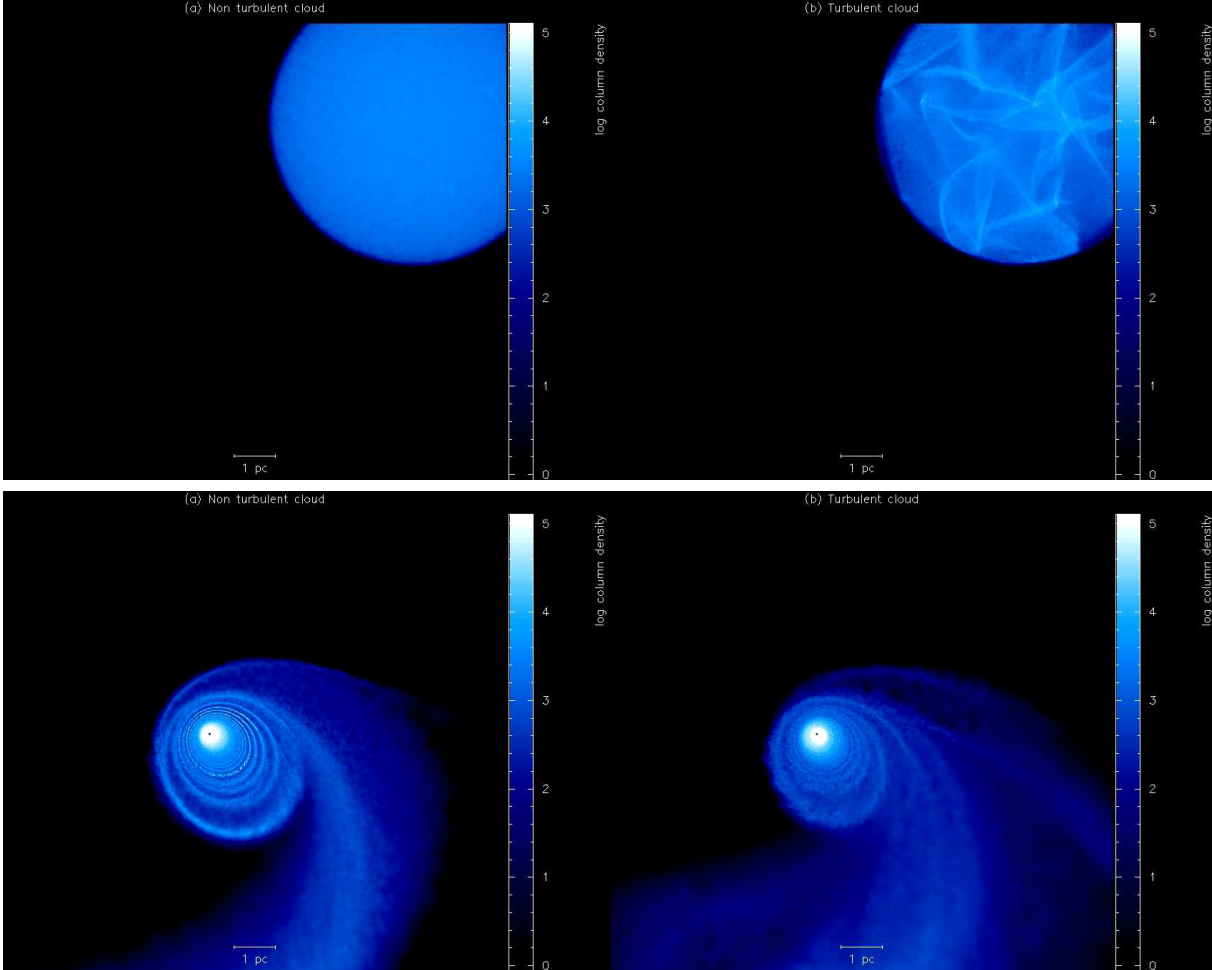
Figure 4.17: Initial and final state of a comparison simulation using a turbulent cloud on the right side and a homogeneous cloud on the left side. The upper panel shows initial conditions, the lower panel the final state.

To test the influence of the initial cloud structure on our results we performed a comparison study between an initially homogeneous cloud and a turbulent cloud. The turbulent cloud is cut out from a turbulent box. The turbulent box is created with all kinetic energy within the first three modes. We then let the box evolve so that the turbulent energy cascade can form. Since we are not actively driving the turbulence, the mean mach number drops. At a mach number of around 20 we stopped the simulation (verifying the Kolmogorov spectrum) and cut out the cloud.

Figure 4.17 shows the comparison between the homogeneous and the turbulent cloud simulation. In the upper panel, the initial condition is shown, with the cloud approaching

from the right. The lower panel shows the resulting accretion discs at the final simulation timestep. Both discs are very similar. In the turbulent case the disc is a bit more diffuse. Still, the simulations confirm that the influence of the initial cloud structure is not strong, which reflects the fact that the black hole orbital velocities are so large that they dominate over the internal velocity structure of the cloud.

4.3   Clump Merging
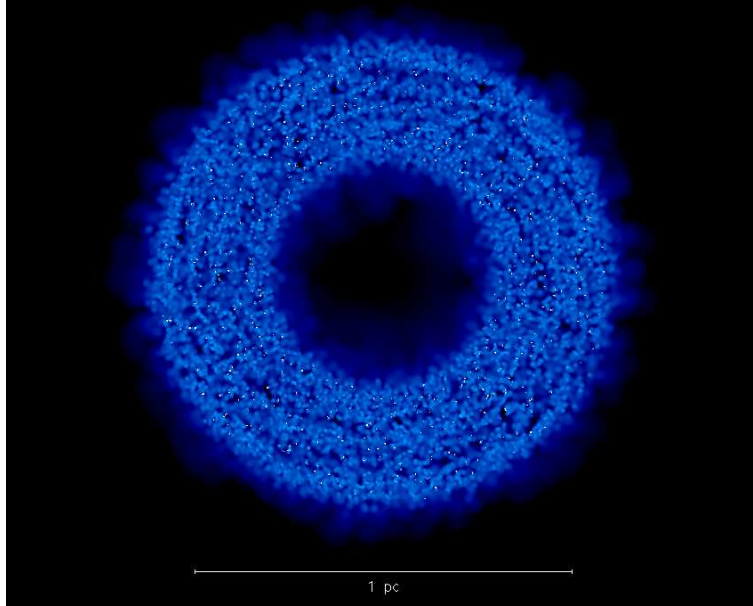
Figure 4.18:   Idealised simulation of a circular compact accretion disc to test the clump merger prescription.

In our second paper, we are not interested in fragmentation since we can not resolve the accretion disc scale height anyways. To speed up our simulations we merge SPH particles within a clump. This is a trade off between a sink particle formalism and calculating the full clump. We still have a pressure acting from the clump, but the clump itself does not slow down the simulation as much as before. To test the clump merging formalism we performed idealised simulations of a compact accretion disc, shown in Figure 4.18. The disc is set up completely circular.

The merging works as follows. Only two SPH particles of the same mass are allowed to merge and only if they are both at the minimum softening length. The resulting replacement particle is placed at the centre of mass of the initial particles with the combined particle masses and centre of mass velocity. This conserves linear momentum, but not angular momentum. The tests show however that the error is negligible. To take care that a certain number of SPH particles remains within a clump an option can be used to allow merging only if a certain number of initial merger particles is within a potential merger region.

Figure 4.19 shows the resulting CMF (clump mass function) if we allow particles to merge two times (top left), three times (top right) and three times together with enforcing that

a certain number of particles stays within the clump (lower left). In black the CMF if we do not merge particles is shown. The impact of particle merging is not big, especially in the case when we enforce that a certain number of particles stays within a clump.
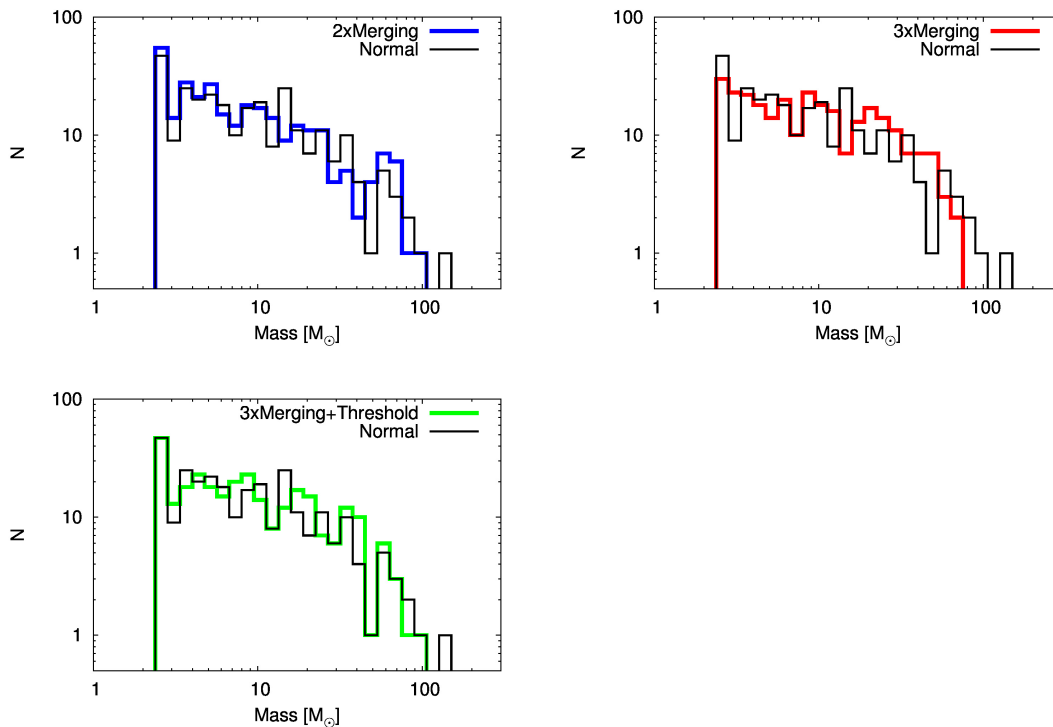
Figure 4.19:   CMF for different allowed merging numbers. Black always represents the CMF without any merging. In blue, two mergers are shown, in red three and in green three together with the requirement that a certain number of particles stays within a clump.

Simulation runtimes, resulting from the merging prescription are shown in Figure 4.20. Especially in simulations with three allowed mergers (SPH particles can have up to 8 times their initial mass) the total runtime can be reduced to nearly one third of the runtime without merging.
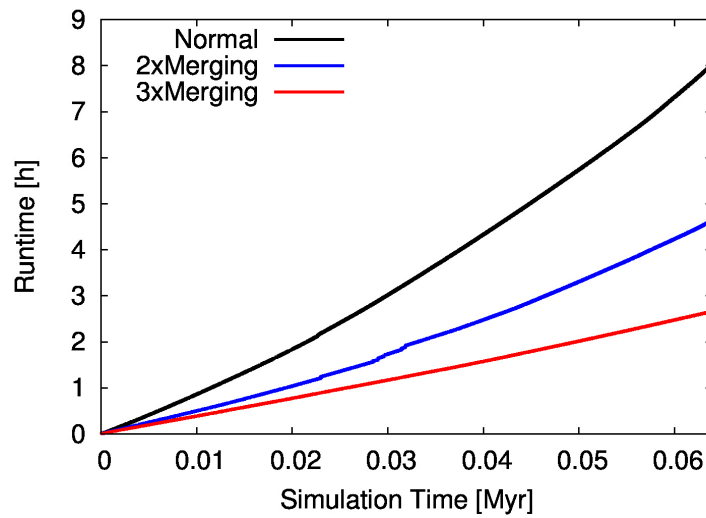
Figure 4.20: Simulation evolution time against real time. The black line shows the run without merging, blue with two allowed mergers and red with three mergers. The runtime can be reduced drastically with three mergers.

Chapter 5

Paper II

5.1 Numerical simulations of the possible origin of the two sub-parsec scale and counter-rotating stellar disks around SgrA*

C. Alig, M. Schartmann, A. Burkert, K. Dolag

We present a high resolution simulation of an idealized model to explain the origin of the two young, counter-rotating, sub-parsec scale stellar disks around the supermassive black hole SgrA* at the Center of the Milky Way. In our model, the collision of a single molecular cloud with a circum-nuclear gas disk (similar to the one observed presently) leads to multiple streams of gas flowing towards the black hole and creating accretion disks with angular momentum depending on the ratio of cloud and circum-nuclear disk material. The infalling gas creates two inclined, counter-rotating sub-parsec scale accretion disks around the supermassive black hole with the first disk forming roughly 1 Myr earlier, allowing it to fragment into stars and get dispersed before the second, counter-rotating disk forms. Fragmentation of the second disk would lead to the two inclined, counter-rotating stellar disks which are observed at the Galactic Center. A similar event might be happening again right now at the Milky Way Galactic Center. Our model predicts that the collision event generates spiral-like filaments of gas, feeding the Galactic Center prior to disk formation with a geometry and inflow pattern that is in agreement with the structure of the so called mini-spiral that has been detected in the Galactic Center.

5.2   Introduction

Recently the Milky Way Galactic Center (GC) region has again sparked a lot of interest. A number of remarkable discoveries were made, including the detection of two large gamma-ray bubbles (Su et al., 2010). The bubbles are perpendicular to the galactic plane, extending 50° above and below the GC and could be linked to the GC star formation event described in this paper, as pointed out by Zubovas et al. (2011). The model we describe in this work leads to the infall of multiple times 10^4 M$_\odot$ onto the black hole within a short time. This could be the origin of the accretion event that created the gamma-ray bubbles. The age of the stars observed at the GC which, according to our model formed as a result of this accretion event, tells us that this event happened more than 6 ± 2 Myr ago (taking into account that it takes a while for the stars to form) which coincides roughly with the age of the lobes of 10 Myr.

A new feature has also been detected in the GC region which previously was only identified partially and thought of as separate components: the 100 pc elliptical and twisted ring of cold and dense molecular clouds (Molinari et al., 2011). This structure fits nicely into the 'stuff within stuff' scenario described by Hopkins & Quataert (2010) to explain the radial transport of material through the galactic disk. According to this scenario, gravitational instabilities generate a series of rings, bars and spirals within each others from galactic scales down to the central few parsec region. On a smaller scale compared to the 100 pc ring we find the circum-nuclear disk (CND) which is again a ring of gas (Becklin et al., 1982) extending roughly from 1.5 pc to around 7 pc.

Inside the central evacuated region of the CND the so-called mini-spiral can be found (Ekers et al., 1983; Lo & Claussen, 1983), a spiral-like structure of hot gas with a total mass of around 10^2 to 10^3 M$_\odot$ on its way towards the black hole. At even smaller distances we find two inclined and counter-rotating disks of young stars, extending from 0.05 pc to around 0.5 pc (Lu et al., 2009; Genzel et al., 2003; Ghez et al., 2005; Paumard et al., 2006; Bartko et al., 2009) which are the main focus of the work presented here.

All the central gas is embedded into a nuclear star cluster of about 10^7 M$_\odot$. The cluster follows a density profile that has a core of roughly 0.5 pc size (the stellar disks) and decreases in density up to around 30 pc (Genzel et al., 2003).

Finally, very recently a small gas and dust cloud has been found, called G2. The cloud will reach its pericenter distance of only 9×10^{-4} pc on its orbit around the black hole as soon as in mid 2013 (Gillessen et al., 2012, 2013a). This will provide the unique opportunity for numerical simulations to make predictions of the future evolution of G2 and its interaction with the environment that will be tested directly by observations within the next years. One prediction that was already made is that the cloud might originate from the inner edge of one of the two stellar disks (Burkert et al., 2012; Schartmann et al., 2012; Murray-Clay & Loeb, 2012).

In this work we will focus on the formation of the two stellar disks, which are an important ingredient in understanding the GC region. In Alig et al. (2011) (denoted as AL1 from here on) we tested a model that was suggested by Wardle & Yusef-Zadeh (2008) to explain the formation of the progenitor accretion disk (which then should fragment into a stellar disk) by a cloud which crosses over the black hole in parts during infall. This way parts of the cloud pass the black hole in the clockwise direction, while the other parts move around the black hole counter-clockwise, leading to efficient redistribution of angular momentum at the focal point of collision, downstream. This model is able to explain the formation of a compact accretion disk. In AL1 we used parameters for the initial cloud that are common in the GC region (Miyazaki & Tsuboi, 2000; Güsten & Philipp, 2004), which leads to a disk that is somewhat larger than the one observed in the GC.

The IMF of the disk-stars is quite unique, Bartko et al. (2010) argue that it is extremely top-heavy whereas Lu et al. (2013) more recently find that it is not as extreme as suggested by Bartko et al. (2010) but still top-heavy compared to a standard Salpeter-slope. This provides a hint to the origin of the stellar disks from an eccentric hot accretion disk. A hot accretion disk would imply a larger Jeans length and thus a small number of high mass clumps compared to a large number of small clumps for a cold disk. The mean eccentricity of the disk stars is measured to be around 0.34 ± 0.06 (Bartko et al., 2009). It has already been shown that in an eccentric accretion disk, the formation of low mass clumps can be suppressed due to tidal disruption during pericenter passage (Alexander et al., 2008). In addition an eccentric disk will be heated quite efficiently during pericenter passage of the gas. These mechanisms as well as the feedback from the already formed stars which could again disrupt low mass clumps, will lead to a strong suppression of the low mass end of the IMF and could explain the observed top-heavy IMF.

The papers of Bonnell & Rice (2008) and very recently Mapelli et al. (2012) also explain the formation of a progenitor accretion disk by infall of a cloud with very low angular momentum into the GC. They studied the subsequent fragmentation and star formation inside the accretion disk and found that clouds with masses of the order 10^5 M$_\odot$ can lead to a top-heavy clump mass function.

The one disadvantage of those models is that they can only explain the formation of a single disk. Since the stars in both disks are almost equal in age (6 ± 2 Myr, Paumard et al. (2006)) they must have formed almost at the same time. The two stellar disks are sharing the same region, which is not possible for two gaseous counter-rotating accretion disks. They therefore must have formed at least shortly one after another. The basic idea here is that the first accretion disk has enough time to fragment, before the formation of the second accretion disk. The fragments and stars are then frozen into their orbits and can share the volume of the second accretion disk, which later on also fragments thus forming the second stellar disk.

The infall of a cloud with a mass larger than 10^4 M$_\odot$ with a sub-parsec impact parameter is already very unlikely. For the two disk scenario a second cloud has to fall into the central region very shortly after the first cloud, with a similar small impact parameter but inclined with respect to the first clouds orbital plane and with opposite angular momentum.

In the model of Hobbs & Nayakshin (2009) this problem is addressed by assuming the collision of two clouds further away from the black hole. This way two streams of gas can make their way into the central region, leading to the formation of an inner compact accretion disk surrounded by a ring of gas. The paper of Lucas et al. (2013) tries to explain the formation of two disks by the infall of a turbulent cloud.

In this paper we present a new model in which a single event, the interaction of a cloud with a gaseous disk around the central black hole, naturally leads to the subsequent formation of multiple inclined and counter rotating accretion disks around the central black hole. We present a high resolution simulation which uses initial parameters taken from a low resolution parameter study to reproduce the observed stellar disk parameters as good as possible. This model is inspired by observational evidence which shows that a similar event to what presumably happened more than 6 Myr ago might be happening again right now in the GC. The paper of Montero-Castaño et al. (2009) shows evidence for the so called GC 20 $\frac{\text{km}}{\text{s}}$ cloud crashing into the CND, leading to the inflow of gas into the central parsec region. This event has already been discussed before and was presented first in the paper of Jackson et al. (1993). Recent follow-up observations of Montero-Castaño et al. (2009) are shown in Liu et al. (2012) and Liu et al. (2013). The gaseous disk in our model has similar parameters compared to the currently observed CND.

The extreme parameters of the two disks are quite challenging to reproduce. First they are almost equal in size, largely inclined and counter-rotating. Second the total mass in stars is quite high with 10^4 M$_\odot$ for the clockwise rotating disk and 0.5×10^4 M$_\odot$ for the counter-clockwise disk (Genzel et al., 2010).

In section 5.3 we present our formation model in detail, as well as a description of the algorithms we are using for our simulation and the parts we added to the standard version of the code. We also summarize the initial parameters for the simulations. The simulations are shown in section 5.4. Finally in section 5.5 we discuss the results and give a summary of our work.

5.3   Model and Numerical Method

First we describe the basic physical ingredients of our model in section 5.3.1. In section 5.3.2 we present the hydrodynamics code we employed for running our simulations and the numerical parameters used for the simulations. The parameters used to model the Galactic Center environment are summarized in section 5.3.2.

5.3.1   Model

Inspired by observations of Montero-Castaño et al. (2009) we simulate the collision of a cloud with a gaseous disk (GD) around the central black hole. The angular momentum direction of the cloud is chosen to be opposite to the GD angular momentum. A similar model has been tested by Vollmer & Duschl (2001, 2002) in their work of prograde and retrograde encounters of clouds with the observed CND to investigate the mass infall into the central region, but they do not relate this process to the formation of the two stellar disks.

Since the simulated GD is destroyed in the process, the parameters do not necessarily have to be the same as the currently observed CND. However, the general idea for the creation of the CND is that a number of clouds with similar angular momentum are captured within the central region forming a gaseous ring within the galactic plane. Hydrodynamical simulations of this model have been carried out by Coker et al. (2003). This simple process could also have happened before, thus we assume the parameters of our GD to be similar to the CND currently observed. Even if this is not true, it makes sense that a progenitor disk co-rotates with and lies within the galactic plane, since the overall source for the gas is the galactic disk.

In our first low resolution parameter study we have chosen a number of different inclinations between the GD orbital plane and the cloud orbital plane. These studies have shown that the best choice, if we want to create a small compact accretion disk, is always to choose those planes to be equal. This choice also makes sense given the fact that the CND (and thus also our GD) is aligned with the galactic plane (Paumard et al., 2006) and that the GC clouds are mostly confined to the galactic plane (Miyazaki & Tsuboi, 2000). Thus the probability for a cloud to approach the CND/GD within the same orbital plane is high.

As long as clouds with the same angular momentum direction as the galactic disk and thus also the GD fall in, the GD will grow in mass. Once in a while (a crude estimate from the two data points we have would be roughly every 10 Myr) a cloud with opposite angular momentum direction enters the region. This leads to the destruction of the GD, resulting in the formation of spiral-like accretion filaments that feed the Galactic Center and subsequently form a single or multiple stellar disk(s).

There is a high degree of freedom in the choice of our initial parameters. The basic sim-

plifications we assume are as follows. The cloud is always assumed to be spherical and homogeneous. The GD is also assumed to be homogeneous with an inner cavity. Observations show that the observed CND is a rather clumpy structure with a volume filling factor of a few percent (Launhardt et al., 2002). However, it turns out to be hard to model the clumpy structure of the CND without any additional stabilizing mechanism besides self-gravity. The clumps are quickly tidally torn apart, reverting the disk into a homogeneous state. Since we do not want to deal with the question of clump stability, we use a homogeneous disk as a first approximation. This point will be discussed further in section 5.4.4 and 5.5.

Another simplification is the assumption that the cloud and the GD always have the same mass. This is a strong restriction and could very well be different but in order to reduce the degree of freedom we need a starting point. In a subsequent paper we plan to study the effect of different masses and non-homogeneous density distributions. Our current simulations do not include any feedback from the black hole or stellar feedback. Again we discuss possible implications of this simplification in section 5.5.

In our second low resolution parameter study we always started with the GD aligned with the xy-plane, rotating counter-clockwise. For the infalling clockwise rotating cloud, we vary the radius, mass, impact parameter and offset in z-direction. As already explained we now assume no inclination between the cloud's orbital plane and the GD orbital plane. For the GD we vary the outer and inner radius and always set the mass equal to the cloud mass. We present the numerical values of the final set of parameters used for the high resolution simulation in section 5.3.3.

5.3.2 Numerical Setup

We carry out our hydrodynamical simulations using the N-Body Smoothed Particle Hydrodynamics (SPH) Code Gadget3 (Springel et al., 2001; Springel, 2005), which makes use of the entropy-conserving formulation of SPH. Gadget3 improves the parallel performance of the previous version by adding a new domain decomposition scheme, which balances work and memory-load at the same time by a more fine grained distribution of the particles among the CPUs, requiring slightly more communication between tasks. For our setup, where the time-steps of particles in the vicinity of the black hole are much smaller than in the outer parts, this already significantly improves the efficiency of the code compared to previous versions. Additionally, we are using some modifications of the code as described in the following paragraphs.

The extremely high velocity in the vicinity of the black hole puts great stress on the domain decomposition. After only a few iterations, particle properties need to be communicated to other domains, which could reside on non-local CPUs. This strongly increased need for communication slows down the overall performance. Usage of the new hybrid OpenMP-MPI implementation in Gadget3 helps to overcome this problem. Here we reduce the number of MPI tasks to the number of physical CPUs on each node and for every MPI task we spawn additional OpenMP tasks corresponding to the number of cores on each of the CPUs. With this approach a larger number of particles can be processed locally without the need of MPI communication. Tests have shown that with our simulation setup we can expect a factor of 3-4 in performance over the standard MPI only approach.

Our low resolution parameter studies have shown that after crashing into the GD, the cloud is compressed into a flat pancake like shape. This leads to strong fragmentation right from the beginning of the simulation. In order to prevent the time step from becoming too small due to the high density fragments we allow SPH particles to merge during the simulation. This is similar to using sink particles although we do not replace a large number of SPH particles by a single non-SPH particle, we only replace two SPH particles by a single SPH particle of higher mass. Since we only allow equal mass particles to merge and also only allow them to merge up to 3 times, the maximum mass of a high mass SPH particle can only be 8 times higher compared to the common SPH particle mass.

Merging is only allowed for particles which are exactly at the minimum hydro smoothing length (see the end of this section). All of these particles are in a totally collapsed region, artificially prevented from further collapse by the choice of the minimum hydro smoothing length. The minimum hydro smoothing length sets an upper limit on density which should always be higher than any normal region of interest inside the simulation. Only Jeans unstable fragments which are infinitely collapsing then reach the minimum hydro smoothing length.

With this prescription we reduce the number of particles within a fragment. To make sure

that we still resolve the fragment with a certain number of SPH particles, we only allow merging to start if the number of possible candidates within the hydro smoothing length of a starting particle (a candidate being a particle at the minimum hydro smoothing length) is at least equal to the number of SPH neighbors which is 50 in our case.

Two particles are merged by using the center of mass position and velocity of the two particle system for creating the replacement particle. This way linear momentum is conserved but not angular momentum. However, due to the fact that only particles within a minimum hydro smoothing length are able to merge, the error is extremely small and tests have shown that this does not influence the results at all. The particle merging approach is a trade off between the sink particle formalism and a brute force calculation of the fragments. Tests have shown that we can expect a factor of 4 or better in simulation speed compared to a brute force calculation.

To account for the thermodynamics of disk formation, we use the same cooling formalism as in AL1, namely that of Stamatellos et al. (2007). It approximates cooling processes for optically thin, as well as optically thick regions by applying an approximative radiative transfer mechanism using the diffusion approximation. The method is suited for a wide range of temperatures (T = 10 - 10^6 K), a wide range of densities ($\rho = 10^{-19}$ g/cm^3 (and lower) - 10^{-2} g/cm^3) and optical depths in the range of $0 < \tau < 10^{11}$ as shown in tests performed by Stamatellos et al. (2007).

In order to prevent small particle time steps in the vicinity of the black hole we define an accretion radius r_{acc} (given in section 5.3.3) within which all SPH particles are considered to be accreted by the black hole. Those particles are removed from the simulation and will no longer take part in the dynamical evolution. The fixed-position sink is not associated with a particle.

The number of SPH neighbors is set to $n_{\mathrm{neigh}} = 50 \pm 5$ and the fixed gravitational softening length is set to $\epsilon = 10^{-3}$ pc. The hydro-smoothing length is adaptive, with the minimum allowed length set to be equal to the gravitational softening length to prevent suppression or amplification of artificial fragmentation according to Bate & Burkert (1997). Gadget3 treats gravitational forces as Newtonian up to 2.8 times the gravitational softening length.

We assume a cloud (and thus also GD) mass of 6×10^4 M$_\odot$. The number of particles in the cloud is 10^6, so that the mass of a single SPH particle is $m_{\mathrm{SPH}} = 0.06$ M$_\odot$. Since the GD contains the same number of particles as the cloud, the SPH particle masses are also the same. Our choice for the particle mass leads to a minimum resolvable mass (Bate & Burkert, 1997) of $m_{\mathrm{min}} = n_{\mathrm{neigh}} \times m_{\mathrm{SPH}} = 3$ M$_\odot$.

### 5.3.3   Modeling the Galactic Center Environment
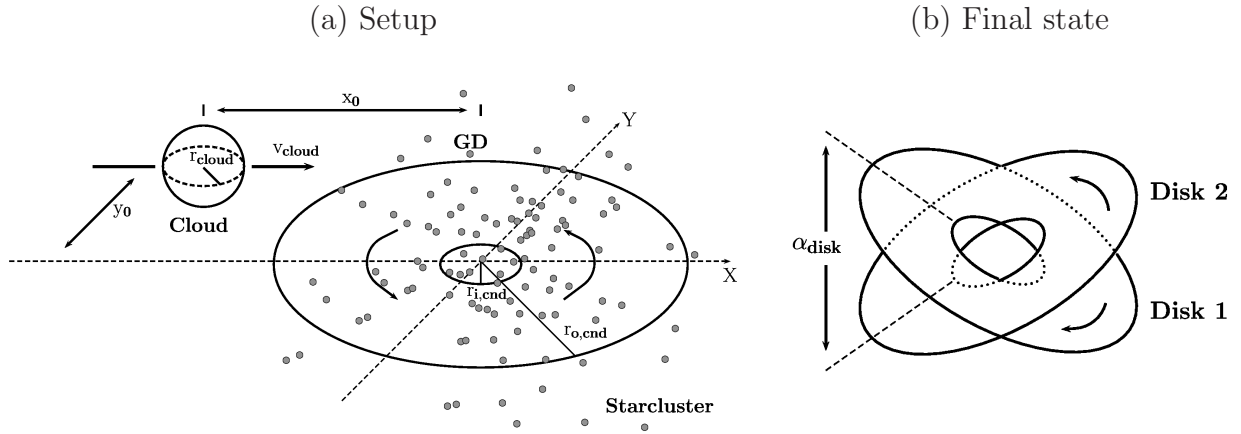
Figure 5.1:   The initial setup is shown in (a) together with the simulation parameters. In (b) the two resulting accretion disks are shown at the same time.

Like in our previous work (AL1) the black hole is included as a static point mass potential, located at the origin of a Cartesian coordinate system. However, to account for newer data from observations we increased the mass of the black hole to 4.4×10^6 $M_\odot$ (Genzel et al., 2010) compared to 3.5×10^6 $M_\odot$ in AL1.
For the black hole accretion radius we chose a value of $r_{\mathrm{acc}} = 0.1$ pc.

In addition to the black hole potential we also include the potential of the old cluster of stars at the GC. The density distribution is taken from observations by Genzel et al. (2003) and has the form

$$\rho_\star(R) = 1.2 \times 10^6 \left(\frac{R}{0.4pc} \right)^{-\alpha} [M_\odot pc^{-3}]$$

with $\alpha = 2.0$ for R $\geq$ 0.4 pc and $\alpha = 1.4$ for R < 0.4 pc.

The initial cloud has constant density and a radius of $r_{\mathrm{cloud}} = 2$ pc. For the mass given in section 5.3.2 (6×10^4 $M_\odot$) this corresponds to a density of around 10^{-19} $\frac{g}{cm^3}$.

We assume an ideal gas with an adiabatic equation of state, with the cooling mechanism included as described in section 5.3.2. The initial cloud and GD temperature is 100 K. The global minimum allowed temperature is also set to 100 K to account for the background UV field from the old cluster of stars at the GC.

The cloud's center of mass is initially placed at an offset of x_0 = -10 pc on the x-axis and an offset of y_0 = 5.2 pc on the y-axis. There is no offset in z-direction, however due to the random particle distribution there is a slight (0.1 percent) abundance of mass above the xy-plane which effectively acts like a small z-offset. The cloud velocity is initially set to v_{cloud} = 145 $\frac{km}{s}$ in the x-direction, thus the cloud's orbit is clockwise around the black hole.

The GD is modeled as a flat disk with an inner edge of $r_{i,cnd}$ = 1.8 pc and an outer edge of $r_{o,cnd}$ = 7.5 pc. It is placed within the xy-plane and rotates counter-clockwise. Fig. 5.1 depicts the simulation parameters for the initial setup and the final state.

5.4   Results

In this section we present the results from our high resolution simulation. First we describe the evolution of the infall of the cloud and the interaction with the GD in 5.4.1. The amount of mass concentrated around the black hole over time is shown in 5.4.2. In 5.4.3 we present the angular momentum distribution of the compact accretion disks and in 5.4.4 we investigate their Toomre parameter. Finally in 5.4.5 we shortly present results on the similarity between the inflow pattern of gas during the cloud-GD interaction and the observed mini-spiral.

5.4.1   Evolution of the cloud-GD interaction

Fig. 5.2 shows a large scale view of the evolution of the cloud-GD interaction. The surface density is given in units of $\frac{M_\odot}{\text{pc}^2}$ and the length units are given in pc. A closer view of the inner region can be seen in Fig. 5.3 using the same units and time slices as Fig. 5.2.

Figures 5.2 (a) and 5.3 (a) show the initial setup with the cloud approaching the counter-clockwise rotating GD from the left side. In Fig. 5.2 (b) the cloud just crashed into the GD and reached the opposite side. The cloud is strongly compressed and fragments are forming inside its high density region. The formerly evacuated central region of the CND is filling up with low angular momentum gas, better seen in Fig. 5.3 (b).

Following its highly eccentric orbit, the cloud moves outside the central 5 pc region (Fig. 5.2 (c)) and thus will no longer be visible on the next plots. The cloud is tidally torn apart and a stream of gas forms that slowly falls back towards the black hole, seen on the lower right in Fig. 5.2 (c). Fig. 5.3 (c) shows the first sub-parsec scale accretion disk that has formed around the black hole at its peak mass. The disk has very low mass (6.5×10^2 M$_\odot$), is short lived (roughly 0.1 Myr) and highly eccentric. There is still a lot of material inside the GD, which is now spiraling towards the center.

The tight stream of gas entering from the bottom of Fig. 5.2 (d) still originates from the cloud. This stream mixes with the ambient gas from the GD (Fig. 5.3 (d)), by this loosing angular momentum, and winds up around the black hole. This leads to the formation of the second accretion disk shown in Fig. 5.2 (e) and Fig. 5.3 (e).

The disk has a high mass (1.35×10^4 M$_\odot$) and exists for a long time (roughly 0.5 Myr). Besides forming the first high mass accretion disk the stream also collides with material inside the GD, thus slowly reducing the angular momentum (due to the collision with material of opposite angular momentum) of the GD material, moving it further towards the center.

The high mass accretion disk is now slowly eroded by GD gas with opposite angular momentum falling in at the outer edges. This destroys the disk from the outside in. A
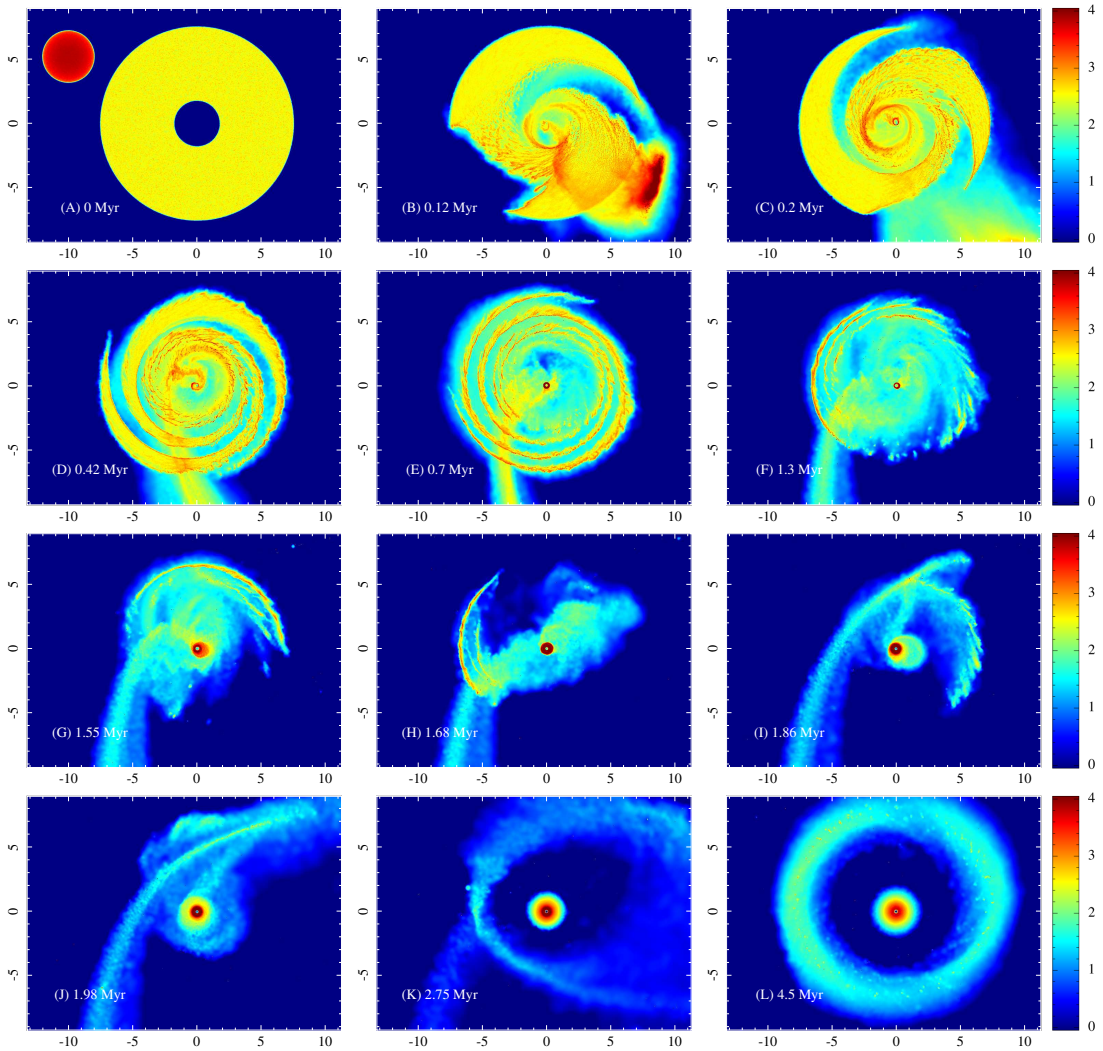
Figure 5.2:   Large scale view of the cloud-GD interaction evolution. Shown is the log-arithmic surface-density in units of $\frac{M_\odot}{\text{pc}^2}$ and the length units are given in pc. In (a) the initial setup with the cloud approaching from the left is shown. The cloud crashes into the GD and gets strongly compressed (b). Next the cloud reaches the opposite side of the GD and the first low mass accretion disk forms (c). A stream of cloud material flows backward into the inner region of the GD and starts winding up around the black hole (d). Plot (e) shows the first high mass accretion disk at peak mass. After the high mass accretion disk is destroyed by gas of opposite angular momentum eating it up from the outside in, another low mass, high eccentricity and short lived accretion disk forms, shown in (f). A small amount of material left from the original GD starts its last orbit (g), crossing the stream of gas from the cloud in (h). After the GD is completely destroyed, forming the second high mass accretion disk (i), the stream of gas from the cloud can overshoot the GD region in (j). This leads to the formation of a large eccentric ring of gas around the central accretion disk (k). This ring slowly circularizes, leading to the final steady state shown in (l).
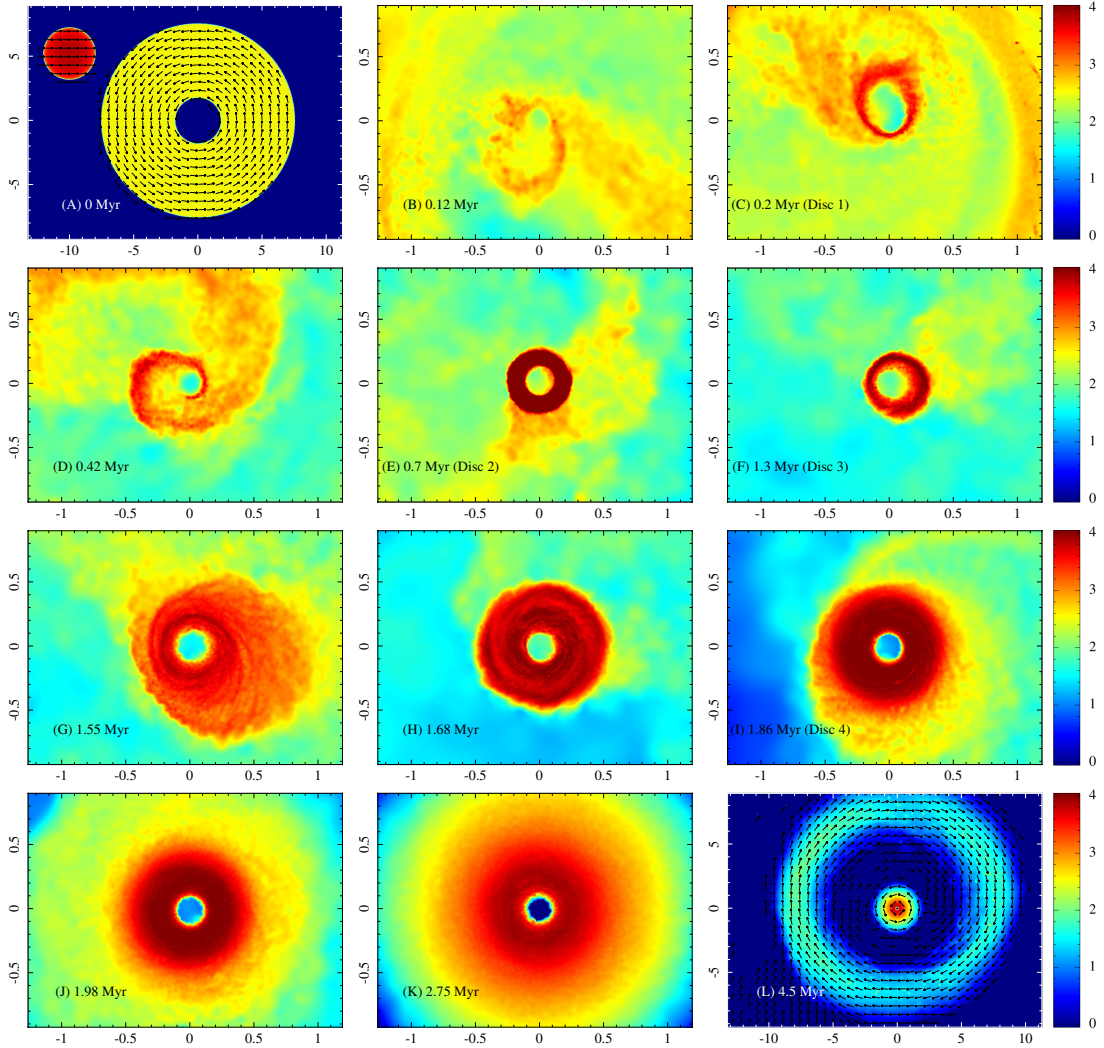
Figure 5.3: Shown is the logarithmic surface-density in units of $\frac{M_\odot}{\text{pc}^2}$ and the length units are given in pc. In (a) the initial setup with the cloud approaching from the left is shown. Velocity vectors are all the same length and only indicate direction. Panels (b) to (k) give a close view of the inner region of the cloud-GD interaction evolution. The cloud crashes into the GD and the inner cavity of the GD starts to fill up with material (b). Formation of the first low mass accretion disk is shown in (c). The stream of cloud material which flows backward into the inner region of the GD winds up around the black hole (d). Plot (e) shows a close view of the first high mass accretion disk at maximum mass. In (f) the second low mass accretion disk can be seen. The remaining GD material is moving into the central area leading to the formation of the second high mass accretion disk (g, h, i). The configuration now remains fairly steady for a long time and the disk circularizes (j, k). At the final step (l), the outer ring of gas is almost completely circular and replaces the original CND at lower density and with opposite angular momentum.

detailed study of the evolution of nested accretion disks with opposite angular momentum close to supermassive black holes has been carried out by Nixon et al. (2012)). They find that accretion rates can increase more than 100 times above the accretion rate of a single planar viscously evolving accretion disk. This provides a very efficient way to feed SMBHs.

After the disk has vanished another short lived (roughly 0.1 Myr), low mass (9.5×10^2 M$_\odot$) and high eccentricity accretion disk forms (Fig. 5.2 (f) and Fig. 5.3 (f)). The GD is now almost completely destroyed by the stream of gas flowing back in from the cloud.

Transition into the final steady state is shown in the series of plots (g-l) in Fig. 5.2 and Fig. 5.3. In Fig. 5.2 (g) the last material remaining in the GD starts its last orbit, crossing the stream of backwards flowing gas from the cloud in Fig. 5.2 (h). All this material now winds up around the central black hole and forms the second high mass accretion disk (5.65×10^3 M$_\odot$), presented in Fig. 5.2 (i) and Fig. 5.3 (i) at peak mass.

When most of the GD gas has fallen inwards the gas from the clockwise rotating stream, resulting from the disrupted gas cloud cannot lose angular momentum anymore and feeding of the central accretion disk stops. Fig. 5.2 (j) shows the stream of gas from the cloud overshooting the GD region since there is no more material from the GD left to collide with.

Finally in Fig. 5.2 (k) the stream of gas from the cloud forms a large, eccentric ring of gas around the inner compact accretion disk. The ring slowly dissipates kinetic energy and circularizes, leading to the final steady state at 4.5 Myr shown in Fig. 5.2 (l). An interesting feature of this ring is that it almost replaces the original GD (concerning location and width, although with a much lower density) but now rotates clockwise (compare velocity vectors in Fig. 5.3 (a) and (l)), as it is comprised almost completely of cloud material. The subsequent infall of additional clouds with the same angular momentum as the initial cloud could now add to the mass of this new GD eventually building up the currently observed CND. The infall of a cloud with opposite angular momentum could trigger the next accretion phase onto the supermassive black hole, which we might be witnessing currently (Montero-Castaño et al., 2009). The inner accretion disk is no longer affected by the infall of gas and remains more or less steady (Fig. 5.3 (j, k)).

A comparison of the density of the two high mass accretion disks in the z=0 pc plane is shown in Fig. 5.4. Several points which we investigate in more detail later are already visible from these plots. First the disks are clearly counter-rotating, the first accretion disk rotates clockwise, the second accretion disk counter-clockwise. Second the disks are inclined with respect to the xy-plane. They are rotated along the connection of the high density parts in Fig. 5.4, almost horizontal for (a) and almost vertical for (b). The disks can not be inclined in the same way, since the axes of rotation are nearly perpendicular to each other.
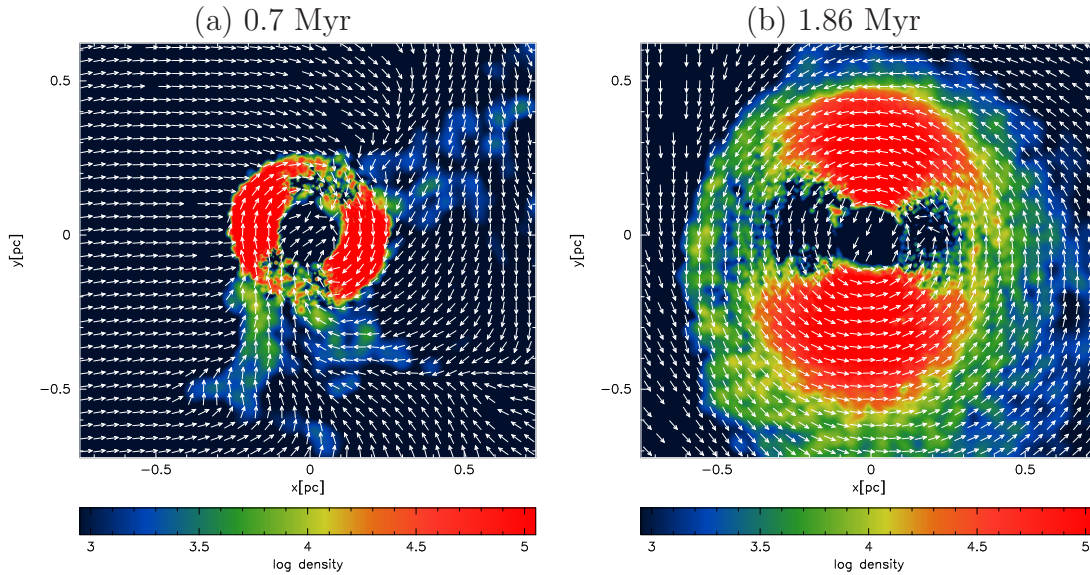
Figure 5.4: Density cut in the z=0 pc plane in units of $\frac{M_\odot}{pc^3}$. We compare the density in the z=0 plane of the two high mass accretion disks forming at 0.7 Myr (a) and 1.86 Myr (b). Velocity vectors are all the same length and only indicate direction. The disks are counter-rotating, inclined with respect to the xy-plane and with respect to each other.

5.4.2 Amount of mass within the central region

We now look at the amount of mass within the central 0.6 pc around the black hole against time. This radius is taken simply because it is a bit further out than the radius of the largest accretion disk that formed. We distinguish between contributions from the cloud and the GD. This provides a good first hint for the formation of the various disks around the black hole and about their sense of rotation. A peak in the mass distribution represents a compact accretion disk. If the contribution to the mass of the disk is dominated by the cloud we expect the disk to be rotating clockwise, if the GD dominates we expect the disk to be rotating counter-clockwise. In our low resolution parameter study this provided a quick way to identify good models.

The arrows in Fig. 5.5 indicate the points at which we plotted the disks in section 5.4.1. First we can see that the two low mass disks at 0.2 Myr and 1.3 Myr are indeed very short lived and contain almost no mass above the ambient level, thus they are completely negligible. On the other hand the first high mass disk contains around 11 percent (1.35×10^4 $M_\odot$) and the second high mass disk around 4 percent (5.65×10^3 $M_\odot$) of the total initially available mass (1.2×10^5 $M_\odot$). The lifetime of the first disk of around 0.5 Myr should be long enough for the disk to fragment if it was unstable. A typical value for the fragmentation time of such a disk is 0.2 to 0.3 Myr as found in the simulations of Bonnell & Rice (2008), Mapelli et al. (2012) and our own accretion disk fragmentation studies.
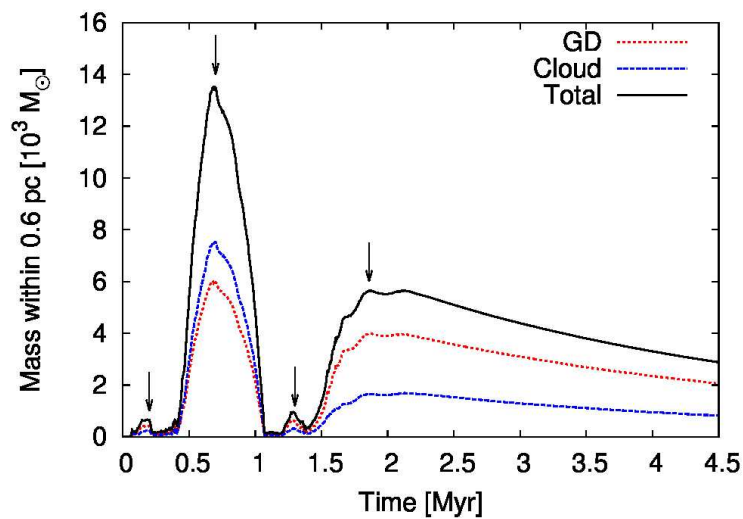
Figure 5.5: Amount of mass within the central 0.6 pc versus simulation time. The black (solid) line shows the total mass, the blue (dashed) line the contribution from the cloud and the red (dotted) line the contribution from the GD to the total mass. The arrows indicate the points at which we plotted the disks in Fig. 5.3.
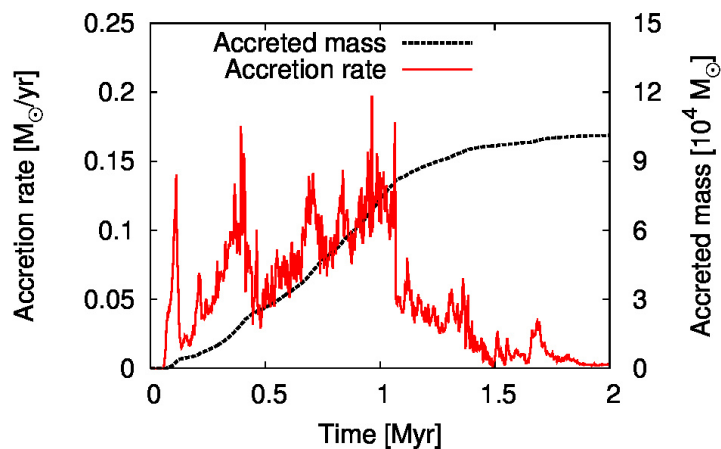
Figure 5.6: Accretion rate (red, solid line) and total accreted mass (black, dashed line) over time. The plot is cut beyond 2 Myr since the accretion rate stays near zero until the end of the simulation at 4.5 Myr.

The main contribution to the mass of the first disk comes from the cloud, thus the disk is rotating clockwise. Although the disk is smaller compared to the second high mass disk, it contains more mass and thus is closer to being able to fragment as we will show in 5.4.4. For the second disk, the contribution to the mass is higher from the GD leading to a counter-clockwise rotating disk.

The mass in our disks is opposite to what is seen in observations. The observed larger disk has double the mass (10^4 $M_\odot$) in stars compared to the smaller disk (0.5×10^4 $M_\odot$). In our simulation the smaller disk contains roughly three times the mass of the larger disk (Note that we compare the observed stellar disks to the simulated gaseous accretion disks). However, we regard this as a matter of fine tuning, like a more fine grained search over the initial cloud radius or GD size, which is beyond this first approach.

Fig. 5.6 shows the accretion rate and total accreted mass over time. In total around 10^5 $M_\odot$ are accreted over 2 Myr and the mean accretion rate is roughly 0.05 $M_\odot$/yr. Accretion in our case represents the flow of material below the accretion radius r_{acc} and is not connected to a black hole accretion rate. The material could settle into an actual black hole accretion disk at much smaller radii. The Lense-Thirring effect aligns the disk angular momentum with the black hole angular momentum, thus removing the accretion rate amplifying effect of counter-rotating gas falling in at later times. The accretion disk then could evolve viscously, thus feeding the black hole at lower rates compared to Fig. 5.6.

### 5.4.3   Angular momentum distribution and disk orientation
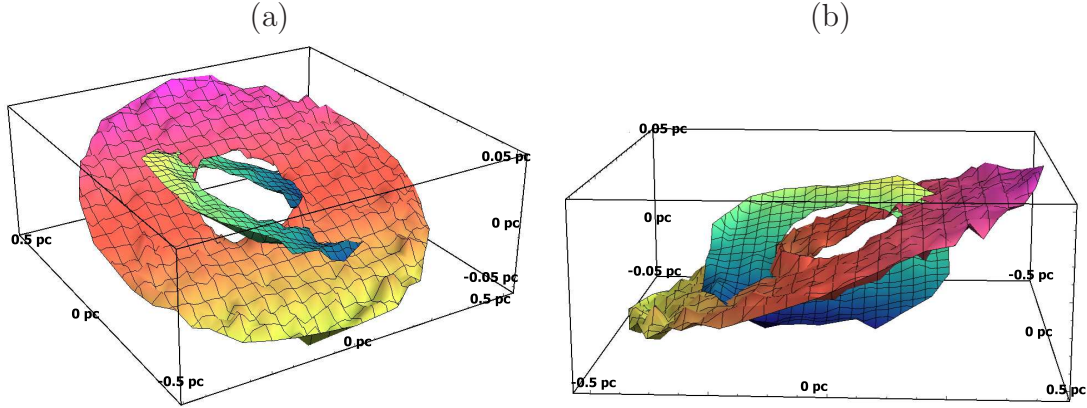
Figure 5.7:   The two high mass accretion disks combined in a single plot, fitted at midplane at the times shown in Fig. 5.3 (e) at 0.7 Myr and Fig. 5.3 (i) at 1.86 Myr from different viewing angles.

To visualize the disk configuration better, we fitted each of the high mass accretion disks with a thin sheet at the times shown in Fig. 5.3 (e) and Fig. 5.3 (i), positioned at the midplane of the disks. Then we combined the results into a single plot, shown in Fig. 5.7 (a) and (b) for different viewing angles. Clearly the disks are inclined with respect to each other and share the same volume. The smallest angle between the disks (see Fig. 5.1 (b)) is roughly $\alpha_{\mathrm{disk}} = 15°$ in our case, compared to 70° inferred from observations (Bartko et al., 2009). For comparison, the best fit of the observational data can be seen in Fig. 20 in Bartko et al. (2009). Although the second high mass disk is weakly warped in our case, the warp is not as strong as the observed one. However, there are also cases in the low resolution runs in which a highly warped disk was produced.

In Fig. 5.8 we show a histogram of the binned cosine of the angular momentum vector with respect to the x,y and z-axis for all the gas particles within the central 0.6 pc from the black hole. The first disk, shown in Fig. 5.8 (a) has a strong peak in the z-component near -1, thus the z-component of angular momentum is anti-parallel to the z-axis for all the gas inside the disk. On the other hand the second high mass disk peaks near 1, thus the z-component of angular momentum is parallel to the z-axis.
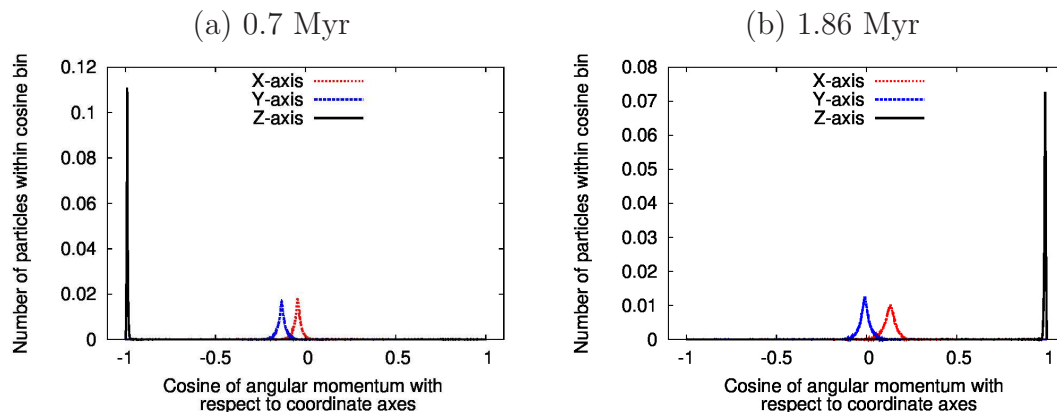
Figure 5.8: Histogram of the cosine of angular momentum with respect to the x,y and z-axis. The black (solid) line shows the cosine of angular momentum with respect to the z-axis, the blue (dashed) line with respect to the y-axis and the red (dotted) line with respect to the x-axis. The two peaks near -1 and 1 for the first (a) and second (b) high mass accretion disks show that the z-component of angular momentum is opposite for the two disks.

On the plane of sky, the GD is seen almost edge on from earth. One of the observed stellar disks is seen almost completely face on in the plane of sky. The second stellar disk is again seen almost edge on, but perpendicular to the GD. This configuration is not too far from what our simulation shows. None of our simulated disks lies within the plane of the GD, both of them are inclined with respect to the GD and with respect to each other, making our model an attractive formation mechanism for the stellar disks.

To show that the disk angular momentum distribution is determined by the mixture of cloud and GD material we now look only at the first high mass accretion disk. We isolate all the particles within the disk at 0.7 Myr and trace them back to the initial setup. For every snapshot we then plot the mean of the cosine of angular momentum with respect to the x,y and z-axis of those isolated particles.

To measure how strongly the material is mixed, we determine for every snapshot the mean number of particles from the GD within the hydro-smoothing length of every cloud particle, as well as the other way around. If a particle is within the hydro-smoothing length of another particle it contributes to its density, which by definition means that the two particles are interacting (or more sloppy formulated "mixed").
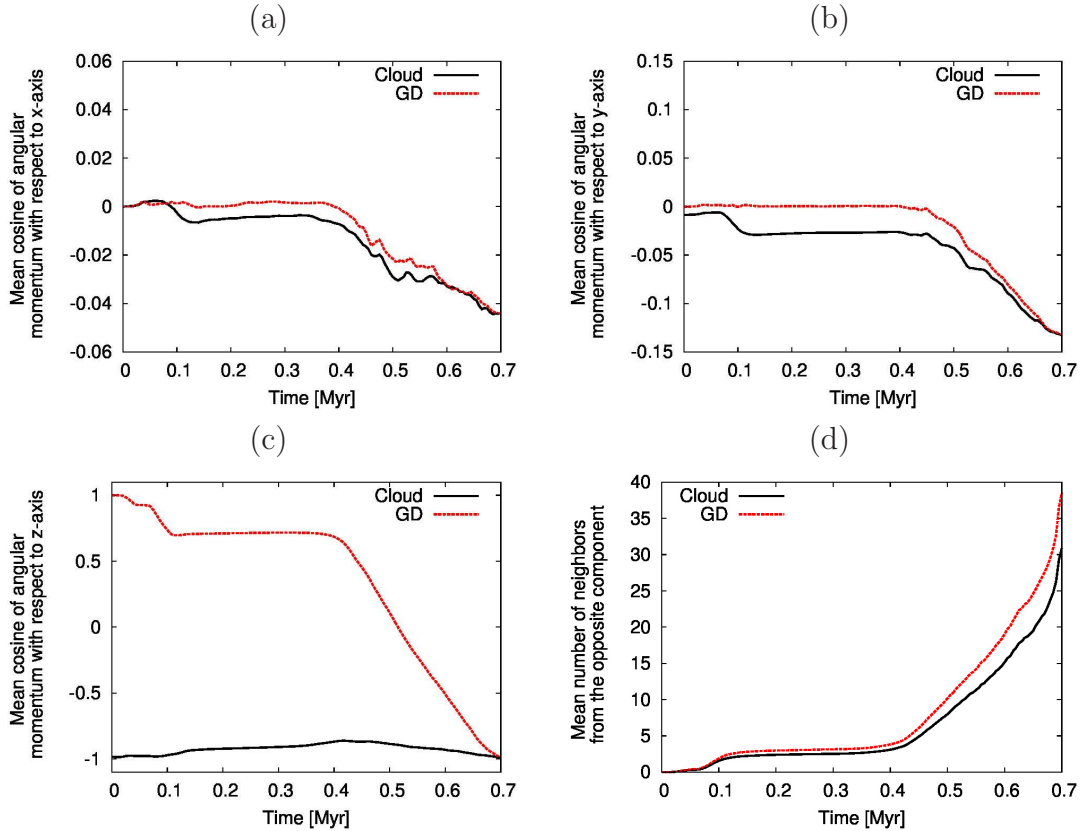
Figure 5.9: Shown in (a), (b) and (c) is the mean cosine of angular momentum with respect to x,y and z-axis of the subset of particles from the first high mass accretion disk over time. The black (solid) line shows the angular momentum orientation for the cloud particles and the red (dashed) line for the GD particles. In (d) we show the mean number of neighbors within the hydro-smoothing length from the opposite component for each of the components (GD and cloud). Again only the subset of particles inside the first high mass accretion disk at 0.7 Myr is shown. This provides a way to see how well "mixed" the two components are. The mean number of neighbors from the GD for the cloud material is shown as black (solid) line and the mean number of neighbors from the cloud for the GD material is shown as red (dashed). There is a clear correlation between mixing and angular momentum distribution.

The distribution of the mean cosine of angular momentum over time obtained this way is shown in Fig. 5.9 (a), (b) and (c). For comparison the mean number of neighbors from the opposite component can be seen in Fig. 5.9 (d). In the beginning, cloud and GD are well separated, with no particle from the opposite component nearby and with the angular momentum only aligned parallel and anti-parallel to the z-axis. At around 0.12 Myr the cloud reaches the opposite side after crashing into the GD. The interaction of cloud and GD leads to mixing of the particles and now each of the components has

a small number of neighbors from the opposite component. This is also reflected in the mean cosine distribution, taking the z-component (Fig. 5.9 (c)), one can clearly see that a fraction of the GD material is affected and now co-rotates with the cloud material.

At around 0.4 Myr formation of the accretion disk starts. Now the number of neighbors from the opposite component steeply rises for both the GD and the cloud. This is mirrored in the angular momentum distribution, again best seen in the z-component (Fig. 5.9 (c)). The plots show that there is a strong correlation between mixing of the two components and the angular momentum distribution. The contribution of GD material to the cloud material reduces its angular momentum, so that it can settle into a tight orbit around the black hole. Fig. 5.9 (b) shows that the particles from the cloud which end up inside the accretion disk already have a small y-component in their angular momentum, which leads to the inclination of the accretion disk with respect to the xy-plane. This asymmetric distribution originates from the small imbalance of mass above and below the xy-plane due to the random particle setup, which effectively acts like a small cloud offset in z-direction. A higher mass imbalance or a non zero cloud offset in z-direction would increase the inclination, which we confirmed in test-simulations.

### 5.4.4   Toomre parameter and disk fragmentation
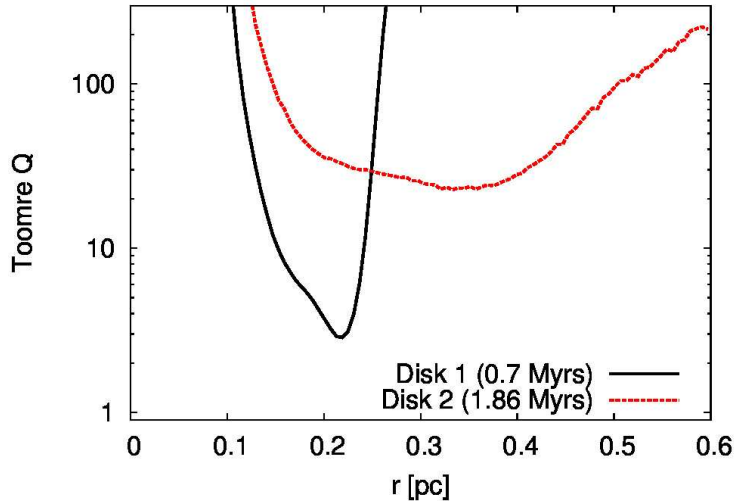
Figure 5.10: Toomre Q at peak mass for both compact accretion disks. Plotted is the Toomre parameter in radial bins against distance from the black hole. The black (solid) line shows the first high mass accretion disk which formed around 0.7 Myr, the red (dashed) line the second high mass accretion disk which formed around 1.86 Myr.

After we have formed gaseous accretion disks, the next important step is disk instability. Our scenario assumes that the first high mass accretion disk fragments into cores before the gaseous component gets destroyed and the second high mass accretion disk forms, leaving a collisionless disk of star forming cores from the first accretion disk. After that the second accretion disk fragments, leaving two inclined disks of cores which turn into stars and probably undergo further evolution (e.g. change of inclination, warping) leading eventually to the stellar disks observed today.

To investigate the fragmentation behavior we look at the Toomre instability parameter for our two high mass accretion disks, shown in Fig. 5.10. For this we rotate each of the disks into the xy-plane and calculate Q for different radial bins. The Toomre parameter for the first high mass accretion disk, plotted in black (solid), drops to Q=2.8 at around 0.22 pc distance from the black hole, which is still in the stable regime. An even higher value is seen for the second high mass accretion disk shown in red (dashed) in Fig. 5.10. Here Q=23 represents the lowest value reached at around 0.36 pc. Thus both our disks are stable against fragmentation.

This is not unexpected since we set up our initial conditions with a rather low total mass. As already pointed out in the introduction, simulations which use a cloud of low angular momentum captured by the black hole need up to 10^5 $M_\odot$ of mass in the cloud to explain

the top-heavy IMF in a single disk. In our case we have a starting mass of 1.2×10^5 M$_\odot$ that is potentially available for a total of two disks.

The low initial mass comes from considerations about cloud and GD stability. We already discussed the problem of stabilizing clumps within the GD/CND in section 5.3.1. At high masses corresponding to several times 10^5 M$_\odot$ the disk and the GD quickly become unstable and start fragmenting.

Observations indicate that there are around 10^4 to 10^5 M$_\odot$ of gas inside the currently observed CND and that the CND is a transient structure ($t_{\text{life}} < 10^5$ yrs) (Guesten et al., 1987). However there are also models which assume the CND to be a rather stable structure ($t_{\text{life}} > 10^7$ yrs) (Vollmer et al., 2003). Our simulations start with a progenitor of the current CND, so the mass does not necessarily have to be the same as the current CND mass, leaving us some freedom in the choice. The issue of how to stabilize the GD or a cloud goes beyond the scope of our work. Hence, our choice of parameters is a trade-off between a GD and cloud stable enough to survive the first encounter given our limited physics and a preferably high initial mass. Turbulent, rotating clumps inside the GD together with a magnetic field could be ingredients needed to stabilize such a system.

(a) Overview at 1.3 Myr   (b) Accretion disk at 1.3 Myr
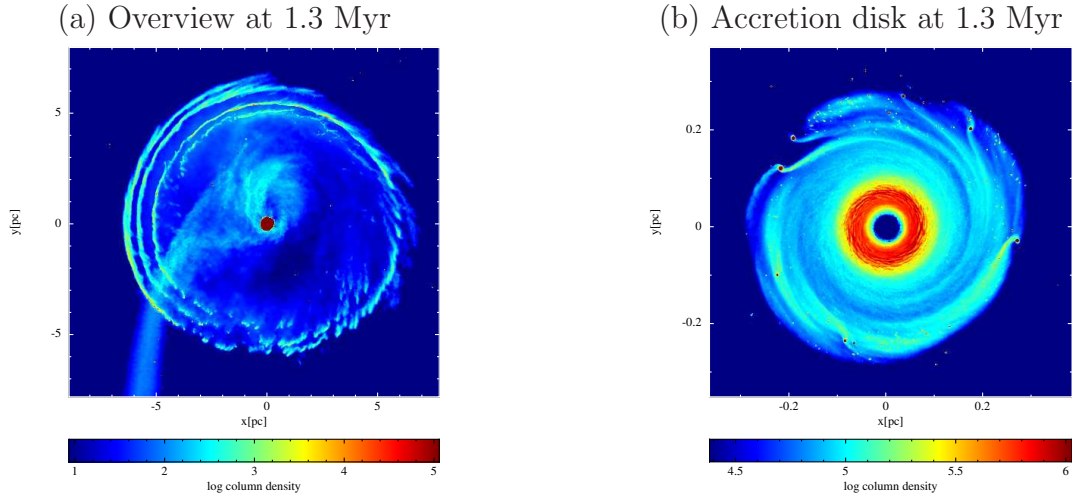
Figure 5.11: Logarithmic surface-density in units of $\frac{M_\odot}{\text{pc}^2}$. A test case with different initial conditions from the simulation presented throughout the paper leads to a high mass accretion disk that breaks up into fragments.

However, even at our current initial mass we were able to find initial conditions which lead to enough mass inside the first high mass accretion disk so that it becomes unstable. Fig. 5.11 shows such a simulation in which the first high mass accretion disk that forms quickly becomes unstable and breaks up into cores. Unfortunately this simulation evolves

very slowly and we are not yet far beyond the point at which the simulation is shown. The results of this improved model will be shown in a subsequent paper.

A number of clumps, originating from the cloud after crashing into the GD and fragmenting, are spread out over a large area (up to 40 pc) around the central black hole. Those clumps might represent the population of young massive stars at radii larger than 0.5 pc that were recently found by Nishiyama & Schödel (2013).

5.4.5   Formation of the mini-spiral
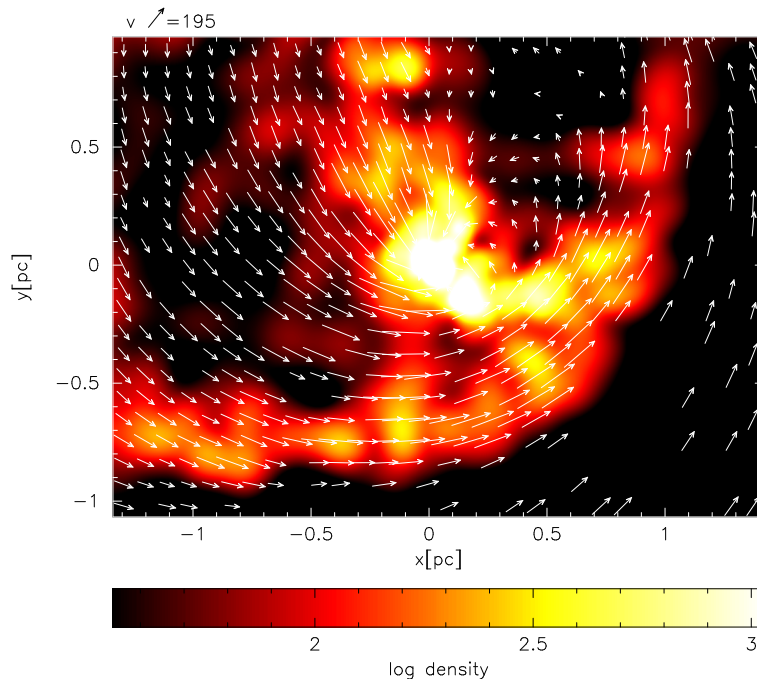
Figure 5.12: Density cut in the z=0 pc plane in units of $\frac{M_\odot}{pc^3}$ through the inflow pattern of gas from a low-resolution test simulation that resembles the mini-spiral. The 2D velocity field agrees with observations presented in Zhao et al. (2009), but a detailed 3D comparison still has to be undertaken.

The inflow pattern of gas especially at the beginning of our simulations always consists of multiple streams of gas flowing into the central region from different points of the inner edge of the GD. In one particular case of a low-resolution test simulation, the inflow pattern resembles the mini spiral surprisingly good. We present this case in Fig. 5.12. The mini spiral has already been credited as source for the black hole SgrA* in its bright state (Czerny et al., 2013).

A comparison to observations, e.g. Fig. 2 in Zhao et al. (2009) shows that the 2D velocity field matches observations quite well, especially the small loop forming at the upper right half of the plot. In our picture the eastern-arm (stream of gas on the left side of the plot) crosses the black hole from below and also forms the so called bar below the black hole. From the north we have the northern-arm flowing past the black hole on the left side, colliding with the bar at the crossing point of the streams.

A detailed comparison of the 3D structure of the inflow pattern to the fit from observations by Zhao et al. (2009) is still necessary and will be postponed to a future publication. The

formation of a structure similar to the mini-spiral seems to be a natural feature of our model for the formation of the two counter-rotating sub-parsec scale accretion disks, suggesting that we observe a similar event today at the GC which happened 10 Myr ago and lead to the formation of the disks.

5.5   Discussion and Summary

We presented a simple, plausible model for the formation of two counter-rotating accretion disks. This model is for the first time able to explain the formation of the puzzling configuration of the two stellar disks which are observed at the Galactic Center (GC) without relying on long chains of individual events.

So far it was assumed that a single cloud with a very small (sub-parsec) impact parameter gets captured and disrupted by the black hole to form a single accretion disk. To form a second disk, one would need within a short time a second, counter-rotating cloud with equally small impact parameter. Already the existence of a single cloud with a sub-parsec impact parameter is highly unlikely. It would have to be created very close to the black hole from the beginning. However, the only real source of gas close to the black hole is the circum-nuclear disk (CND) (for the current event) or our simulated gaseous disk (GD) (for the previous event), so it is likely that the gas which formed the accretion disks originates there.

The CND/GD is placed far enough from the black hole so that collisions with clouds become possible. Observations even confirm that there is currently a cloud colliding with the CND. Test simulations have shown that it is easy to create multiple accretion disks using this model. There are cases with up to four compact accretion disks forming. Sometimes all the disks have the same rotational direction, sometimes only a single disk forms. But in all cases the formation of an accretion disk due to low angular momentum gas winding up around the black hole is possible. The inflow patterns of the streams of gas can even resemble the mini-spiral which is currently observed at the GC.

Due to the high degree of freedom in our initial conditions we don't expect to get a perfect match to observations. For our high resolution simulation we took the parameters from a low resolution simulation that produced two prominent, counter-rotating disks of roughly the correct size compared to observations, in order to show the basic mechanism of our proposed model.

The stellar disks themselves had a long time to evolve since their formation and there is a number of papers (Ulubay-Siddiki et al., 2009; Kocsis & Tremaine, 2011; Madigan et al., 2009; Ulubay-Siddiki et al., 2013) that deal with how the disks could become warped with time or increase their inclination. In this work we concentrate on the initial formation of the progenitor accretion disks and hence a perfect fit to all observed characteristics of the stellar disks is not intended. Test simulations have shown that increasing the mass imbalance above and below the xy-plane, as well as allowing a small cloud offset in z-direction also leads to a larger inclination, thus an improved simulation later on could also be able to explain the high inclination directly.

We have made a number of simplifications which could impact our results, which will be

briefly presented here. First we always assume the cloud and the GD to have equal mass. A naive improvement judging from Fig. 5.10 would be to increase the mass in the GD so that the second high mass accretion disk becomes more massive, since the main contribution to mass in this disk comes from the GD. This could also push the first high mass accretion disk over the fragmentation point. In addition this would bring the disks closer to the observed mass ratio of 1:2 (10^4 $M_\odot$ in the clockwise disk and 0.5×10^4 $M_\odot$ in the counter-clockwise disk).

Feedback from the black hole would depend on the orientation of the black hole spin axis with respect to the accretion disks. A real first hint on the spin axis orientation might be given by the recent possible detection of a jet-like outflow from SgrA* (Yusef-Zadeh et al., 2012). Such a jet could prevent the formation of a second disk after material from the first disk feeds the black hole.

Another important point to keep in mind is the possible impact of stellar feedback. We do not include stellar feedback in our simulations. If there are stars forming in the first accretion disk, they could possibly influence the formation of the second accretion disk, given enough time between the two events. Thus it is desirable that the disks form as short after one another as possible.

On the other hand, the disks must have enough time to fragment at all. This last point does not seem to be overall problematic judging from our test simulations. Simulations of fragmenting high mass (10^5 $M_\odot$) accretion disks close (< 0.5 pc) to SgrA* typically only need around 0.2 to 0.3 Myr to form clumps and protostellar cores, as already pointed out in section 5.4.2. Even in cases where we had four high mass accretion disks forming, each single accretion disk existed for around 0.2 Myr and thus would have had enough time to fragment.

More problematic is the time between the formation of the two disks. In our case it takes roughly 1 Myr between formation of the two disks, during which feedback from the stars forming in the first disk could become already important. However, taking the stellar models of Ekström et al. (2012) into account this should be short enough, so that stellar feedback even from high mass stars (> 60 $M_\odot$) should not play a role.

Compared to observations we are well within the uncertainty of age determinations of the stars of 2 Myr. The stellar and black hole feedback problem also applies to the low angular momentum cloud capture model and is not a special property of our particular formation model.

Overall, seeing how easy it is to create multiple disks, we are still confident that our results will hold when including additional physics. This first study already produced a reasonable fit when compared to observations and future refinements will surely increase the agreement. For the first time we are able to create two massive, sub-parsec scale

counter-rotating accretion disks which are inclined with respect to each other and with respect to the CND.

5.6 Acknowledgments

Chapter 6

The G2 Cloud

In this chapter we present SPH simulations of the G2 cloud together with the numerical problems that arise.

6.1 SPH Simulations of G2

An overview of the physics of G2 will be given in the third paper of this thesis. Here we present SPH simulations of the compact cloud scenario as described in the third paper. The cloud parameters can be found in Table 7.1. Instead of using the density and temperature model for the Galactic Centre atmosphere 7.2, we first start with a constant density atmosphere taking the value of the atmosphere at the distance of the cloud from the black hole given in Table 7.1.

The first studies with a constant density atmosphere were aimed at determining the influence of hydrodynamics effects on the evolution of the cloud. For this we simulated the G2 cloud orbiting around the black hole using SPH particles in one simulation and N-body particles in another simulation. The resulting particle distributions are plotted over each other in Figure 6.1. On the left side, the cloud is approaching the pericentre (we plot the cloud in the centre of mass frame). The white dots represent the N-body particles. The distribution is similar, thus hydrodynamics effects do not seem to play a large role. After pericentre passage the distributions start to deviate strongly, as can be seen on the right side of Figure 6.1.
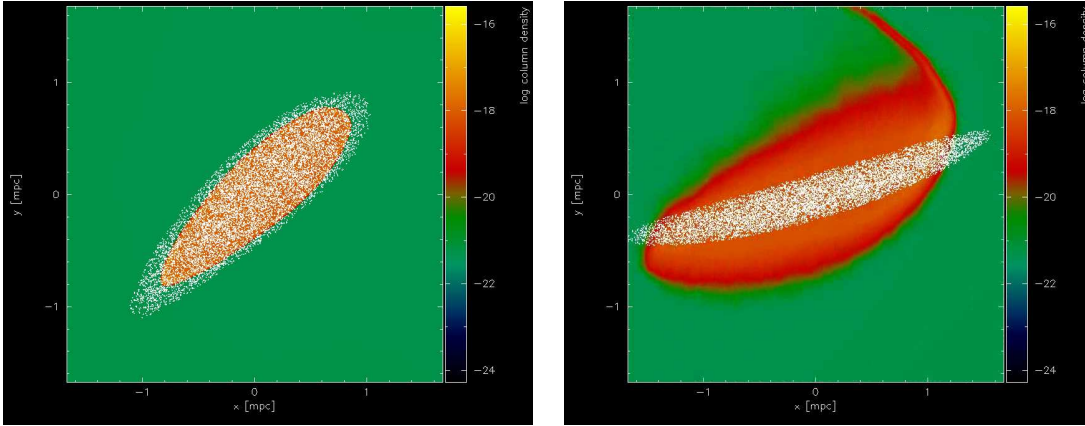
Figure 6.1:   SPH and N-body simulations of G2 within a constant density atmosphere. The left panel shows the cloud before pericentre passage, the right panel after pericentre passage. Before pericentre passage hydrodynamical effects do not seem to play a large role and the cloud evolution seems to be well described by the N-body simulation.

Other simulations using over and under-pressured clouds showed that the density and temperature gradient in the atmosphere has to be taken into account to really see how the cloud evolves. If the infall time is short enough so that the cloud can not react to the change in atmosphere pressure, the influence of hydrodynamics effects during the infall should be small enough so that the N-body prescription gives a good first approximation of the cloud evolution.

We model the atmosphere at the Galactic Centre using equations 7.2. Since the $\frac{1}{r}$ atmosphere is extremely unstable in the inner part, we have to treat this region differently. The particles here are held at fixed positions, ignoring all forces. The outer parts of the atmosphere can then "rest" on this central pressure support.

Figure 6.2 shows the resulting initial setup on the left side with G2 starting at apocentre. After a short time, shown in Figure 6.2 on the right side, the atmosphere already becomes unstable, despite the treatment of the inner parts. Also around the cloud a void forms, which can be better seen in the zoom in Figure 6.3.
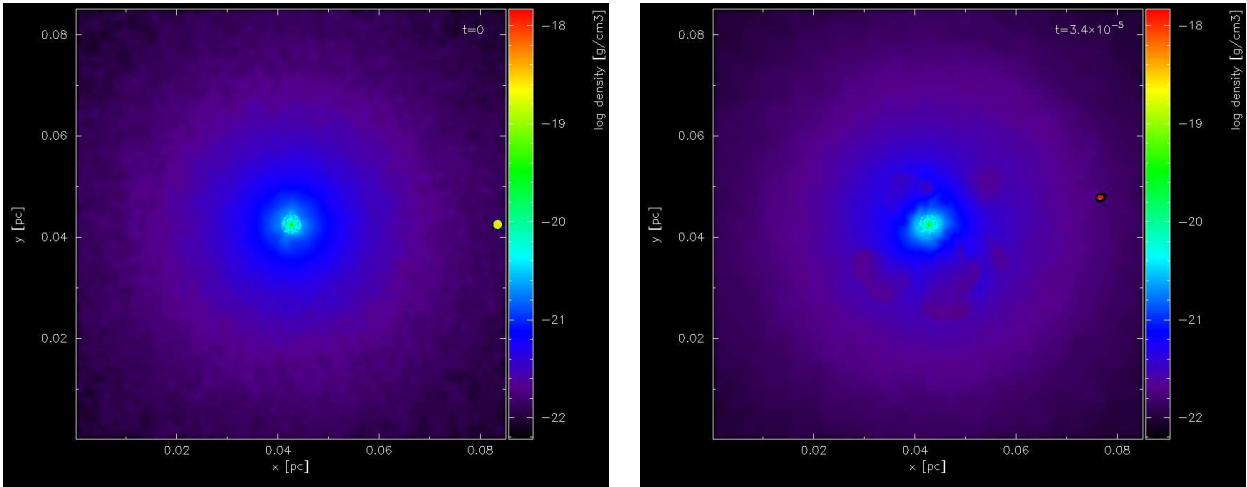
Figure 6.2:   Simulation of G2 using the density and temperature gradient of the atmosphere given by equations 7.2. The left panel shows the initial setup with G2 starting at apocentre. The right panel shows the same simulation a short time later.
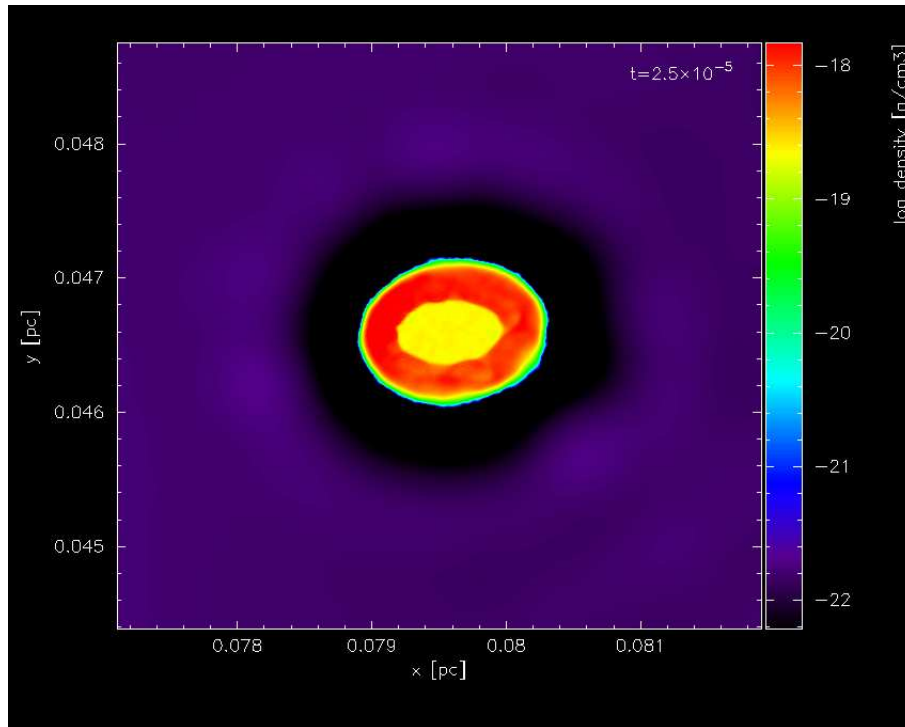
Figure 6.3:   A zoom onto the G2 cloud from the right panel of Figure 6.2. A thick void region around the cloud forms.

6.2 Numerical Problems

The effect that creates the void around G2 is one of the problems of standard SPH which neglects thermal conduction. We can imagine two fluids next to each other which are in pressure equilibrium ($P = c_s^2 \rho$). One of the fluids is very hot (high c_s) and has a low density (low ρ). The other fluid is cold (low c_s) and has a high density (high ρ) such that the pressure of both fluids is the same.

We now look at particles within the low density fluid. Even with a sharp boundary between the fluids, the smoothing length of a particle inside the low density fluid close to the boundary can contain particles from the high density fluid. Thus the density estimate for this particle is higher compared to the common density within the low density fluid. The same effect is true for particles close to the boundary within the high density fluid, for those particles the density is underestimated.

The effect of this over- and underestimation close to the boundary is a density transition in which density gradually increases from the low density region into the high density region. However the thermal energy due to c_s does not show such a gradient, there is only the sharp jump which was initially set up. Since the distributions of c_s and ρ now differ, due to the SPH density estimate at the interface, the resulting pressure is no longer balanced.

Particles inside the low density fluid which are close to the fluid boundary have a higher density compared to normal low density particles but still the same high c_s as the rest of the low density fluid particles, which results in a higher pressure. On the high density fluid side, the density is underestimated at the boundary, so that the particles have a lower pressure in total. This gradient in pressure pushes the two fluid phases apart leading to the void zone between them, which is exactly the effect we see in the simulations of G2.

Figure 6.4 shows the pressure if we start from the atmosphere and go into the G2 cloud. At the boundary between atmosphere (left) and cloud (right), marked by the black vertical line, we can see the pressure rising in the atmosphere part and then dropping inside the cloud. In total the pressure difference is nearly two orders of magnitude.
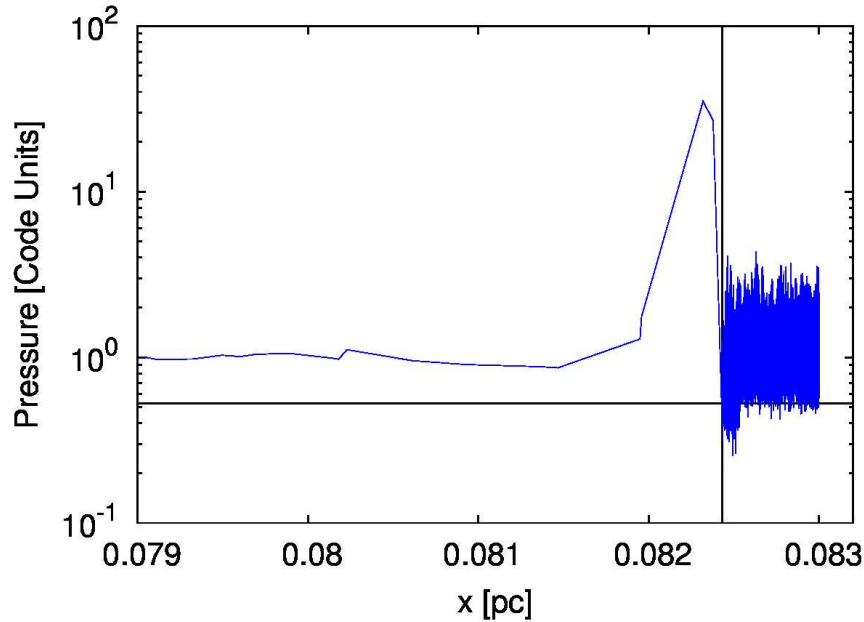
Figure 6.4: Pressure during the transition from the atmosphere into the G2 cloud. The pressure difference at the edge leads to the void zone, seen around G2 inside the simulation.

To fix this problem one could introduce a smoothing also in the thermal energy, which is exactly what thermal conduction will do. In the case of G2 however there is an additional problem. The density contrast between the cloud and the medium is extremely high, with a ratio of nearly 1:3000. Thus for particles within the cloud it is highly likely that they will not find any particles of the atmosphere within their smoothing length, basically decoupling the cloud from the atmosphere. Particles within the atmosphere on the other hand, if they are close to the cloud, will find enough particles of the cloud within their smoothing length, so that the density estimate will be extremely wrong. Following the density evolution of the G2 simulation one can see individual particles from within the atmosphere basically decoupling from the rest of the atmosphere, hitting the cloud and then bouncing off.

The above considerations assume that all SPH particles have the same mass. One could also imagine that the particles within the atmosphere get a lower mass, such that the amount of particles at the boundary is roughly the same for the cloud and the atmosphere. However the number of particles inside the atmosphere would be enormous, rendering this approach useless. Due to the very low mass, the contribution from particles within the atmosphere would also be negligible and only cloud particles would contribute, dominating the density sum for atmosphere particles close to the boundary. A solution to all the problems SPH has with G2 could be to use a gradient in particle mass close to the boundary, together with thermal conduction and a few other modifications to SPH. The upcoming paper of

Zintl et al. will discuss this solution in more detail. Better suited for this type of problem are grid codes, which have no problem with the density contrast between the atmosphere and the cloud. M. Schartmann simulated the G2 scenario using the grid code PLUTO (Mignone et al., 2007, 2012). The results are presented in the third paper.

Paper III

7.1 Simulations of the origin and fate of the Galactic Center cloud G2

M. Schartmann, A. Burkert, C. Alig, S. Gillessen, R. Genzel, F. Eisenhauer
and T.K. Fritz

We investigate the origin and fate of the recently discovered gas cloud G2 close to the Galactic Center. Our hydrodynamical simulations focussing on the dynamical evolution of the cloud in combination with currently available observations favor two scenarios: a *Compact Cloud* which started around the year 1995 and a *Spherical Shell* of gas, with an apocenter distance within the disk(s) of young stars and a radius of a few times the size of the *Compact Cloud*. The former is able to explain the detected signal of G2 in the position-velocity diagram of the Brγ emission of the year 2008.5 and 2011.5 data. The latter can account for both, G2's signal as well as the fainter extended tail-like structure G2t seen at larger distances from the black hole and smaller velocities. In contrast, gas stripped from a compact cloud by hydrodynamical interactions is not able to explain the location of the detected G2t emission in the observed position-velocity diagrams. This favors the *Spherical Shell Scenario* and might be a severe problem for the *Compact Cloud* as well as the so-called *Compact Source Scenario*. From these first idealized simulations we expect a roughly constant feeding of the supermassive black hole through a nozzle-like structure over a long period, starting shortly after the closest approach in 2013.51 for the *Compact Cloud*. If the matter accretes in the hot accretion mode, we do not expect a significant boost of the current activity of Sgr A* for the *Compact Cloud* model, but a boost of the average infrared and X-ray luminosity by roughly a factor of 80 for the *Spherical Shell* scenario with order of magnitude variations on a timescale of a few months. Assuming that a part of the gas is accreted in cold disk mode, even higher boost factors can be reached. The near-future evolution of the cloud will be a sensitive probe of the conditions

of the gas distribution in the milli-parsec environment of the massive black hole in the Galactic Center.
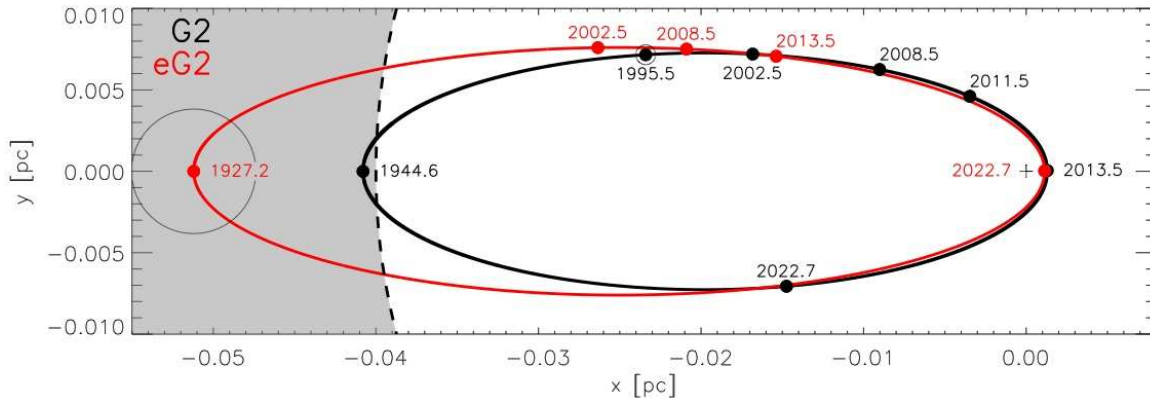
Figure 7.1: Orbits of our two scenarios: The black line represents the orbit of G2, as determined in Gillessen et al. (2012), representative for the *Compact Cloud Scenario* and the red line denotes the orbit of eG2 as determined in this work, representative for the *Spherical Shell Scenario*. The location of the central black hole is denoted by the plus sign and the dashed line denotes the inner rim of the disk(s) of young stars. The sizes of the shell and the cloud are shown by the thin black lines.

7.2 Introduction

The Galactic Center harbors a nuclear supermassive black hole (SMBH). Due to its proximity, its mass of $4.31 \times 10^6 \, M_\odot$ (Gillessen et al., 2009b; Ghez et al., 2008; Genzel et al., 2010) has been derived from direct long-term (≈ 20 years) monitoring of stellar orbits in the sub-parsec-scale vicinity of the central compact nonthermal radio source Sgr A* – thought to be the radiative counterpart of the central SMBH. The uncertainties in the mass-estimate of the order of 10% are mostly due to the distance measurement. The parsec-scale environment of the center is comprised of seven main constituents (e. g. Melia & Falcke, 2001; Genzel et al., 2010): an atmosphere of diffuse hot gas (e. g. Baganoff et al., 2003, Yuan et al., 2003, see also Sect. 7.4.1), a cluster of evolved stars (Genzel et al., 2003), one or two warped disks of young stars ranging between 0.04 pc and 0.5 pc (Genzel et al., 2003; Levin & Beloborodov, 2003; Bartko et al., 2010; Lu et al., 2009; Alig et al., 2011), the B-stars in the central half-parsec (Gillessen et al., 2009b), spiral shaped thermal gas streams in the inner 2 pc, which reaches down to 0.17 pc (called Sgr A West, (Ekers & Lynden-Bell, 1971; Downes & Martin, 1971; Ekers et al., 1983; Yusef-Zadeh & Wardle, 1993; Zhao et al., 2009)), a molecular dusty ring ranging from 2 pc to 5 pc (Genzel et al., 1985; Montero-Castaño et al., 2009) and a shell-like, elliptical non-thermal structure with a size of roughly 6×8 pc (called Sgr A East, Ekers & Lynden-Bell, 1971; Downes & Martin, 1971; Ekers et al., 1975; Maeda et al., 2002). For a more detailed review of the Galactic Center environment we refer to Genzel et al. (2010).

Recently, a gas cloud has been detected on its way towards the Galactic Center (Gillessen et al., 2012). It consists of a two-component system: (i) the high surface brightness compact component G2 and (ii) a lower surface brightness cone-like structure, which we will refer to

as G2t from now on, as it was originally described as the *tail* of G2 (Gillessen et al., 2012). The whole complex (G2 plus G2t) will be called eG2, the *extended G2* cloud complex, in order to avoid confusion. Traced back on archival data, Gillessen et al. (2012) were able to determine an accurate orbit for G2 (Fig. 7.1), which has a very high eccentricity ($e = 0.9384$). It will reach its closest approach of only 4×10^{15} cm to the SMBH in 2013.51 (corresponding to 3100 Schwarzschild radii). Clear evidence for ongoing tidal velocity shearing and stretching of G2 within the last couple of years has been detected, confirming its extended nature. This provides an interesting challenge for hydrodynamical simulations that aim at reproducing the currently visible tidal shearing and that can be used to predict the future tidal evolution over the next couple of years. G2 comprises of a multi-phase medium with the bulk of its mass being ionized gas ($M_{G2} \approx 1.7 \times 10^{28} f_V$ g, with f_V being G2's volume filling factor, which we assume to be unity throughout this paper). Ionization equilibrium with the radiation field of the nearby massive stars is expected to keep the temperature of this component at around 10^4 K. Additionally, it contains a small amount of warm dust with a temperature of ≈ 550 K. Only very little is known about G2t, but its mass could be substantially larger than the mass estimate for G2 itself.
Several questions are of immediate theoretical interest:

- Which physical process formed the cloud?

- What determines the physical cloud properties (mass, size, thermodynamic state) and the dynamics?

- Can it be used to probe the direct vicinity of Sgr A*?

- What is the fate of the cloud in the next years?

- How does it influence the activity of Sgr A*?

In Burkert et al. (2012) (paper I) we mainly tackled the first three of these questions mostly with the help of analytical considerations. We especially concentrated on possible formation scenarios and evolutionary paths of G2. Two basic models proved to be the most successful:

- **The Compact Cloud Scenario (CC)**
  A cloud with uniform density structure can explain the evolution of the observed position-velocity (PV) diagrams of G2.

- **The Spherical Shell Scenario (SS)**
  A tidally disrupted, initially spherical shell of gas with a much larger radius and mass than G2 can account for both, the G2 and G2t component in the position-velocity diagram.

In paper I we also found that the cloud is a sensitive probe of the hot accretion zone of the SMBH and the currently available observations of G2 are in good agreement with models of captured, shock-heated stellar winds. We were able to derive constraints on the

mass of G2, which is above the critical mass below which clouds would evaporate before reaching the presently observed radius, and which is small enough for the sound crossing timescale at apocenter to be of order its orbital period. Analytical estimates of various other time scales showed that many physical processes might contribute to the evolution of the cloud. Therefore, detailed numerical simulations are needed, which is the topic of this publication. The wealth of available observational data (now and in future) as well as its proximity make this event an ideal tool to study gas accretion physics in the vicinity of SMBHs. It will also give us very valuable insight into the evolution and the activation of galactic nuclei in general.

An alternative model to our *Compact or Spherical Cloud Scenario* – called the *Compact Source Scenario* in paper I – was proposed by Murray-Clay & Loeb (2012) (see also Miralda-Escudé, 2012): a dense, proto-planetary disk, which is bound to its parent low-mass star. The star is assumed to be scattered roughly 100 years ago from the observed disk(s) of young stars. Far away from Sgr A*, the protostellar gas disk remains bound to the star and resists tidal stretching. When approaching the SMBH, it looses mass through photo-evaporation due to the extreme flux of ionizing and FUV photons in the Galactic Center and due to tidal stretching. Murray-Clay & Loeb (2012) analytically estimate that this results in a cloud with similar properties as observed.

The main idea of this paper is to present a first set of idealized hydrodynamical simulations and to test the influence of the hot atmosphere on the late-time evolution of such a cloud for our two best-fit cloud infall models as already described in paper I, namely the *Compact Cloud Scenario* and the *Spherical Shell Scenario*. We discuss simple test particle simulations in Sect. 7.3 before we describe the model we employ for the Galactic Center environment in Sect. 7.4 and review some of the complicated physical processes in Sect. 7.5. The results of our hydrodynamical simulations are presented in Sect. 7.6, followed by a discussion (Sect. 7.7) and finally the conclusions (Sect. 7.8). We assume a Galactic Center distance of 8.33 kpc, where $1'' = 40\,\text{mpc} = 1.25 \times 10^{17}\,\text{cm}$ (Gillessen et al., 2009b).

7.3   Test particle simulations

In order to find initial conditions for our hydrodynamical studies, which are able to reproduce current observations, we calculate a grid of test particle simulations in two dimensions, varying a large number of the parameters, as described below. This is done for both models of origin as discussed in Sect. 7.3.1 and 7.3.2. Such kind of simulations are very fast and hence a large number of test calculations can be done on a short timescale (approximately 16 000 simulations for this paper), allowing for a huge scan of the involved parameters. The test particle simulations are run with the N-body code REBOUND (Rein & Liu, 2012) and 100 test particles are distributed along the boundary of the cloud or ring, restricted to the orbital plane. The particles are then evolved in the gravitational potential of the black hole and describe the evolution of the shape of the cloud when tidal forces completely dominate. The best fit model is found by comparing the simulated to the observed position velocity diagrams. We use these N-body simulations to roughly constrain the formation time and initial conditions of G2 and eG2, respectively. The best fitting initial conditions are then used to study the detailed hydrodynamical evolution (Sect. 7.6).

7.3.1   Compact Cloud Scenario
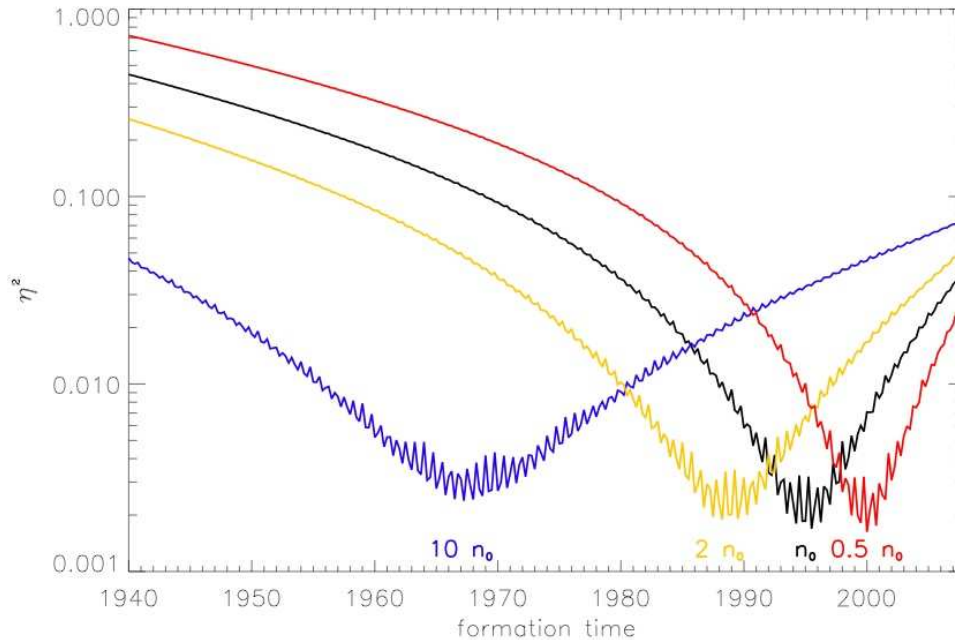
Figure 7.2: Possible formation times of the compact cloud models as inferred from test particle simulations for various densities of the atmosphere. The black line corresponds to our standard atmosphere, whereas the colored lines refer to multiples of the density as indicated in the plot. The η^2 value quantifies the goodness of fit with the observed position-velocity diagrams in 2008.5 and 2011.5 (see Sect. 7.3.1).

For the compact cloud scenario, we assume that the cloud started *in situ* in pressure equilibrium with the surrounding hot atmosphere on the observed orbit of G2 and that G2's mass is known[1]. Then, the initial radius and density of the cloud are fixed along the orbit and we only vary the date of birth of the cloud. As estimated in paper I, hydrodynamical effects – especially ram pressure – play a minor role in the early evolution of the cloud in the compact cloud scenario. This means that we can directly compare the resulting distribution in the position-velocity diagram of the year 2008.5 and 2011.5 with the observations and can expect to get a reasonably well determined initial condition. The goodness of fit is judged from the position and spread of the test particles in the PV diagram. We compare the minimum and maximum values of the projected distance ($d_{\mathrm{min,max}}^{\mathrm{sim}}$) as well as the line of sight velocity ($v_{\mathrm{min,max}}^{\mathrm{sim}}$) of the simulated distribution with the respective extrema of the observed PV diagram ($v_{\mathrm{min,max}}^{\mathrm{obs}}, d_{\mathrm{min,max}}^{\mathrm{obs}}$). For the latter we chose a representative contour line (0.8 times the maximum value of the observed PV diagram, shown by the two plus signs in the left two panels of Fig. 7.10). The quadratic sum of these relative deviations of the 2008.5 and 2011.5 observations with the respective simulated snapshots are summarized in an η^2-value, used to judge the goodness of the fit:

$$\eta^2 = \sum_{2008.5, 2011.5} \left(\frac{v_{\mathrm{min,max}}^{\mathrm{sim}} - v_{\mathrm{min,max}}^{\mathrm{obs}}}{v_{\mathrm{min,max}}^{\mathrm{obs}}} \right)^2 + \left(\frac{d_{\mathrm{min,max}}^{\mathrm{sim}} - d_{\mathrm{min,max}}^{\mathrm{obs}}}{d_{\mathrm{min,max}}^{\mathrm{obs}}} \right)^2 \tag{7.1}$$

Fig. 7.2 displays the result of this study for our assumed standard atmosphere (see Sect. 7.4.1). It shows a clear η^2 minimum around the year 1995.5. A study of different density normalizations of the atmosphere (Fig. 7.2) shows that the preferred origin of the cloud depends sensitively on the density distribution of the atmosphere. Increasing the atmospheric density by a factor of two shifts the starting time to the year 1988, whereas a factor of ten would necessitate a starting time of 1967 and a decrease of the density distribution by a factor of two yields a starting date of roughly 2000. This can be understood as the cloud sizes depend on the atmospheric pressure, when we assume pressure equilibrium between the cloud and the atmosphere. However, the values also depend on the choice of the limiting contour for the fitting procedure. Therefore, these studies only serve as rough estimates for possible origin dates of the cloud. To determine and describe the future hydrodynamical evolution, we will start the cloud in 1995.5 (Sect. 7.6.1).

---

[1]The observationally determined mass actually depends on the unknown volume filling factor, which we assume to be one here.

7.3.2   Spherical Shell Scenario
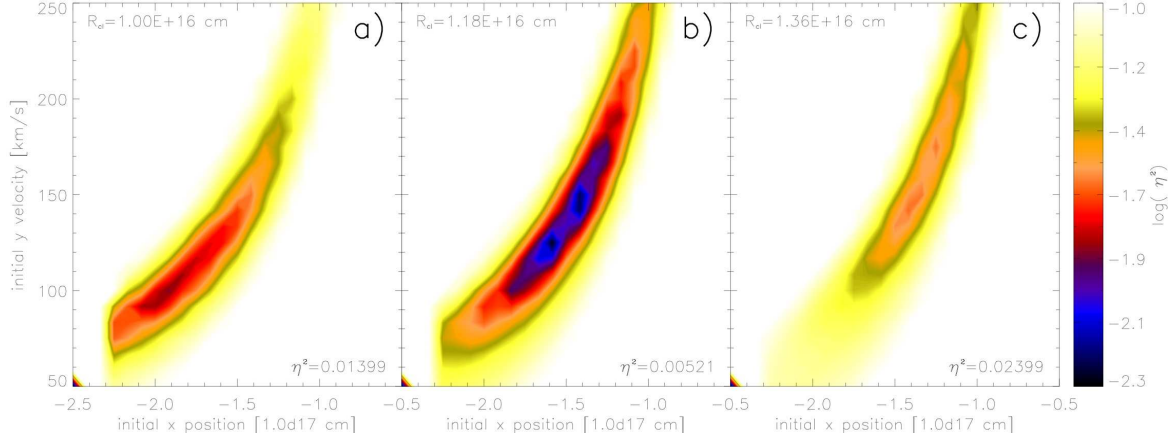
Figure 7.3: Distribution of η^2-values (see Sect. 7.3.1) of the spherical shell scenario as inferred from test particle simulations in the initial x-position vs. initial y-velocity plane. We assume the ring starts at arbitrary time at the apocenter, which is located on the negative y-axis. The three different panels refer to three exemplary initial ring radii: 1.00×10^{16} cm (a), 1.18×10^{16} cm (b) and 1.36×10^{16} cm (c). The η^2 value quantifies the proximity of the match with the observed position-velocity diagrams in 2008.5 and 2011.5 (see text for details of the fitting procedure).

As shown in paper I, the observations can also be interpreted in such a way that G2 and G2t are parts of a larger cloud complex (eG2), which is already partly disrupted by tidal forces in the 2008.5 and 2011.5 observations. As these shells are typically a factor of five to ten larger than the compact clouds mentioned above, ram pressure effects cannot be neglected anymore. In order to find reasonable starting parameters for this model as well, we take the ram pressure effects roughly into account by offsetting the comparison values from the observed contour (compare to blue plus signs in panels c,d of Fig. 7.10). This offset is determined by comparing a number of hydrodynamical simulations with test particle simulations. Thought to be the result of emission of stellar material, we assume that this shell started close to the apocenter of its elliptical orbit, which lies well within the disk(s) of young stars (see Fig. 7.1), making it the most likely origin of the cloud. For this model, the total mass of the cloud is not fixed, as the mass of G2t cannot be constrained observationally very well at present. In the subsequent hydrodynamical modelling we then choose the density of the shell to reach approximate pressure equilibrium with the surrounding atmosphere. Again, we are only interested in a rough match of the hydrodynamical realization with the observed PV-diagram in order to investigate the basic evolution of such a model. In this case, every time step is compared to the 2008.5 PV diagram and the stage three years later with the 2011.5 observation in order to find the best matching timestep, as the date of birth is not fixed in this model. The result of this fitting procedure with a grid of 25^3 test particle simulations is summarized in Fig. 7.3.

Shown is the distribution of η^2 values determined as described in Sect. 7.3.1 and equation 7.1 in a plane spun by the initial position on the negative x-axis and the initial velocity in y-direction. The panels display the distribution for three examples of the initial outer ring radius: 1.00×10^{16}cm (panel a), 1.36×10^{16}cm (panel c) and our best fit value of 1.18×10^{16}cm (panel b). The minimum η^2 valley is quite shallow and we take the global minimum of our simulated grid, which is a model starting at apocenter in the year 1927.2 at a distance from the black hole of 1.58×10^{17} cm and an initial orbital velocity of $125 \, \mathrm{km \, s^{-1}}$.

7.4 Modelling the Galactic Center environment

7.4.1 The hot atmosphere

X-ray observations of hot gas emission near Sgr A* (Baganoff et al., 2003) are attributed to the atmosphere close to the SMBH, which can be explained as gas being shock-heated by the interaction of strong stellar winds of the surrounding massive stars (e. g. Krabbe et al., 1991; Melia, 1992; Baganoff et al., 2003; Muno et al., 2004). The observed very low bolometric luminosity of the order of $3 \times 10^{-9}\, L_{\mathrm{Edd}}$ together with a Bondi accretion rate of $10^{-5}\, M_\odot \mathrm{yr}^{-1}$ (Yuan et al., 2003) disfavor standard accretion disk theory (Shakura & Sunyaev, 1973). They are rather consistent with so-called *Radiatively Inefficient Accretion Flows* (RIAFs), in which only a small fraction of the gravitational energy is radiated. Following Gillessen et al. (2012), we adopt the ADAF (*Advection-Dominated Accretion Flow*, e. g. Ichimaru, 1977; Abramowicz et al., 1995; Narayan & Yi, 1994) model of Yuan et al. (2003), which is an analytical approximation for such a RIAF solution, in concordance with available Chandra observations (Baganoff et al., 2003) and rotation measure data derived from radio observations (Bower et al., 2003). In the idealized simulations presented in this paper, we neglect the rotation and the actual dynamics of the accretion flow and rescale the normalization of the temperature distribution accordingly, in order to yield hydrostatic equilibrium. This yields the following number density distribution n_{at} and temperature distribution T_{at} of the hot atmosphere:

$$n_{\mathrm{at}} = 930\,\mathrm{cm}^{-3}\, f_{\mathrm{hot}}\, \left(\frac{1.4 \times 10^4 R_{\mathrm{S}}}{r} \right)^{\alpha} \tag{7.2}$$

$$T_{\mathrm{at}} = 1.2 \times 10^8\,\mathrm{K}\, \left(\frac{1.4 \times 10^4 R_{\mathrm{S}}}{r} \right)^{\beta} \tag{7.3}$$

where r is the distance to the black hole, R_{S} is its Schwarzschild radius, $\alpha \approx \beta \approx 1$ and $f_{\mathrm{hot}} \approx 1$ is a factor taking the uncertainty of the model into account. A mean molecular weight of $\mu = 0.6139$ has been assumed, typical for a gas with solar metallicity.

However, as the entropy $S = T/\rho^{2/3}$ decreases outwards, this is not a stable equilibrium, but unstable to convection (see discussion in paper I), which we confirmed with the help of test simulations: small perturbations start growing at the inner boundary surrounding the black hole, which quickly leads to the formation of unphysically high pressure bubbles. Due to the unstable nature of the atmosphere we do expect an inhomogeneous density distribution. However, setting up a realistic RIAF solution is a complicated task in itself (e. g. Stone et al., 1999, Stone & Pringle, 2001 and Igumenshchev et al., 2003) and beyond the scope of this first idealized study presented in this article as it would require the inclusion of many more physical processes, like e. g. magnetic fields (see Sect. 7.7.3 for a discussion of possible effects), thermal conduction, etc. Some of these effects are already taken into account (not completely self-consistently) in the models of Yuan et al. (2003). We are rather interested in the interaction of the cloud with a smooth atmosphere, representing an average distribution in concordance with available observations. To this end, we artificially stabilize it and keep

the atmosphere's density and temperature distribution fixed with time. This is done by additionally evolving a passive tracer field ($0 \leq tr \leq 1$), which allows us to distinguish between those parts of the atmosphere which have interacted with the cloud ($tr \geq 10^{-4}$, see Sect. 7.7.2) from those which changed due to the atmosphere's inherent instability ($tr < 10^{-4}$). Those cells fulfilling the latter criterion are reset to the values expected in hydrostatic equilibrium. We discuss numerical issues and proof that this is a sensible assumption in Sect. 7.7.2 below.

7.4.2 The initial conditions of the cloud models and the numerical treatment

We use the two best-fit models presented in Sect. 7.3 as basis for our hydrodynamical exploration of the origin and fate of the cloud complex eG2. In these first simulations, we generally set the adiabatic index $\Gamma = 1$, but also present the comparison to a purely adiabatic simulation. This seems to be a reasonable assumption, as the temperature structure of the atmosphere is supposed to be given by adiabatic heating of the accretion flow itself and stellar processes (see Sect. 7.4.1) and the temperature of the cloud material is expected to be set by photoionization equilibrium in the radiation field of the surrounding stars (Gillessen et al., 2012) during the early evolution of the cloud. In order to explain the observed position-velocity diagram, two basic scenarios have been identified in paper I. Both are based on the simple assumption that the cloud started with spherical shape and in pressure equilibrium with the atmosphere on an orbit compatible with the observed positions on the sky. In the first set of models we follow the interpretation of Gillessen et al. (2012), who discern the observations into *cloud head* and *tail* emission. Our second set of models interprets the observations as being the result of the disruption of a larger cloud, which – for concordance with observations – necessitates the cloud to be a spherical shell.

Our two-dimensional simulations are done within the orbital plane of the cloud, with the major axis parallel to the x-axis and the apocenter of the orbit on the negative x-axis of our fixed Cartesian coordinate system with a spatial resolution of 7×10^{13}cm. The computational grid of our standard model ranges from -1.3×10^{17}cm to 1.2×10^{16}cm in x-direction and -6.2×10^{16}cm to 2.5×10^{16}cm in y-direction. The cloud is on a clockwise orbit with the major axis parallel to the x-axis and the pericenter of the orbit on the positive x-axis. The black hole is located at the origin of our coordinate system. As discussed above we use a passive tracer field in order to trace the evolution of the cloud (and to stabilize the atmosphere) and initially assign the cloud a value of 1 and the atmosphere 0 and let it evolve.

The hydrodynamical equations are integrated with PLUTO, version 3.1.1 (Mignone et al., 2007). For all simulations shown in this article, we use the two-shock Riemann solver, do a parabolic interpolation and employ the third order Runge-Kutta time integration scheme. A cartesian two-dimensional grid is used and the boundary conditions in all directions are set to the values expected for hydrostatic equilibrium of the hot atmosphere, enabling

outflow but no inflow. We introduce an additional spherical boundary surrounding the central black hole. All gas flowing into this part of the integration domain is removed and counted as being accreted. All values inside this boundary are set to the atmospherical values, in order to mimic the pressure exerted by this region, which is necessitated by the steep pressure gradient.

We neglect thermal conduction, magnetic fields as well as feedback from the central source for the sake of simplicity. A summary of the used and varied parameters is given in Table 7.1 and Table 7.3, respectively.

Table 7.1: Observed and calculated parameters of the cloud G2 and the Galactic Center region.

Parameter		Value
mass of the SMBH	M_{BH}	$4.31 \times 10^6\,M_\odot$
Galactic Center distance	R_0	$8.33\,\mathrm{kpc}$
mass of the cloud G2 a	m_{cloud}	$1.7 \times 10^{28}\,\mathrm{g}$
pericenter distance	r_{peri}	$4 \times 10^{15}\,\mathrm{cm}$
time of closest approach	t_{peri}	2013.51
orbit eccentricity	ϵ	0.9384
semi-major axis	a_{semi}	$6.49 \times 10^{16}\,\mathrm{cm}$
orbital period	T_{orbit}	137.77
inclination of ascending node	i	106.55
position angle of ascending node	Ω	101.5
longitude of pericenter	ω	109.59

Table 7.2: Parameters of G2 and the Galactic Center obtained or derived from observations in Gillessen et al. (2012). (a) Throughout the paper we assume a volume filling factor of one.

Table 7.3: Parameters of the (hydrodynamical) simulations.

	τ_0 a yr AD	ρ_{cloud} b $10^{-19}\,\text{g cm}^{-3}$	R_{cloud} c $10^{15}\,\text{cm}$	x_{ini} d $10^{16}\,\text{cm}$	y_{ini} e $10^{16}\,\text{cm}$	v_{ini}^x f km s^{-1}	v_{ini}^y g km s^{-1}	Γ h	f_{hot} i	Δx j $10^{13}\,\text{cm}$	tr k
CC01	1995.5	6.21	1.87	−7.22	2.21	794.59	48.45	1	1	7.0	10^{-4}
CC02	1944.6	2.24	2.63	−12.59	0.0	0.0	167.29	1	1	7.0	10^{-4}
CC03	1944.6	223.64	0.57	−12.59	0.0	0.0	167.29	1	1	7.0	10^{-4}
CC04	1995.5	6.21	1.87	−7.22	2.21	794.59	48.45	5/3	1	7.0	10^{-4}
CC05	2000.0	4.33	2.11	−5.99	2.24	953.00	−5.41	1	0.5	7.0	10^{-4}
CC06	1988.0	8.57	1.68	−8.87	2.03	605.85	98.85	1	2.0	7.0	10^{-4}
CC07	1995.5	6.21	1.87	−7.22	2.21	794.59	48.45	1	1	14.0	10^{-4}
CC08	1995.5	6.21	1.87	−7.22	2.21	794.59	48.45	1	1	3.5	10^{-4}
CC09	1995.5	6.21	1.87	−7.22	2.21	794.59	48.45	1	1	7.0	10^{-6}
CC10	1995.5	6.21	1.87	−7.22	2.21	794.59	48.45	1	1	7.0	10^{-2}
SS01	1927.2	1.42	11.80 l	−15.80	0.0	0.0	125.00	1	1	7.0	10^{-4}

Table 7.4: CC refers to simulations of the Compact Cloud scenario and SS to those of the Spherical Shell scenario. Simulations CC02 and CC03 are only discussed in paper I. (a) Start time of the simulation, (b) initial density of the cloud, (c) initial radius of the cloud, (d) initial x-position of the cloud, (e) initial y-position of the cloud, (f) initial x-velocity of the cloud, (g) initial y-velocity of the cloud, (h) adiabatic index, (i) uncertainty factor of the density distribution of the hot atmosphere, (j) cell size in x- and y-direction, (k) tracer threshold value, (l) the shell has a thickness of 25% of this outer radius.

7.5   Cloud physics

The components of the Galactic Center environment which have the largest impact on the gas cloud are the gravity of the central SMBH and the hydrodynamical interaction with the hot atmosphere. Therefore, we restrict our discussion to the physical effects related to these two components. The relevant physical processes of the cloud/atmosphere system are discussed in great detail in paper I. Here, we only briefly summarize those important for the interpretation of our hydrodynamical simulations and estimate the timescales of the various processes for different phases of the evolution of the cloud.

7.5.1   Tidal deformation

Tidal forces lead to a stretching in direction of the black hole and a squeezing perpendicular to it. As G2's orbit has a very high eccentricity, the cloud gets distributed along the orbital path. The acceleration of this stretching is given by

$$|a_{\mathrm{tf}}| = 2\,\Delta r\, G\,\frac{M_{\mathrm{BH}}}{r^3}, \tag{7.4}$$

where Δr refers to the width of the cloud in direction of the black hole, G is the gravitational constant, M_{BH} is the mass and r the distance to the SMBH. Therefore, a change of the cloud elongation of the order the width of the cloud by tidal forces is expected on a timescale of:

$$\tau_{\mathrm{tf}} \approx \sqrt{\frac{2\,\Delta r}{|a_{\mathrm{tf}}|}} \approx \frac{r^{3/2}}{\sqrt{G\,M_{\mathrm{BH}}}} = 10.60\,\mathrm{yr}\,\left(\frac{r}{10^{16}\,\mathrm{cm}}\right)^{3/2}, \tag{7.5}$$

which varies between 27.6 yr at the 1995.5 position of the cloud and 0.5 yr at the pericenter.

7.5.2   Ram pressure compression and deceleration

Ram pressure of the surrounding medium has two effects: (i) Locally, it changes the cloud structure by compressing the upstream part of the cloud and (ii) globally it decelerates the cloud, leads to angular momentum exchange with the atmosphere and finally accretion of matter towards the center. In paper I we analytically estimate the loss of kinetic energy for our compact cloud model to be of the order of a few percent under the assumption of a cloud evolving in pressure equilibrium. In realistic hydrodynamical simulations, the situation is much more complex as we will show in detail in Sect. 7.6.

7.5.3   Thermal conduction and evaporation

Thermal conduction leads to the evaporation of parts of the cloud. Following Cowie & McKee (1977) we find an evaporation time scale of

$$\tau_{\text{evap}} = 81 \, \text{yr} \left(\frac{r}{10 \, r_{\text{peri}}} \right)^{15/8} \left(\frac{R_{\text{c}}}{10^{15} \, \text{cm}} \right)^{13/8} \frac{M_{\text{c}}}{1.7 \times 10^{28} \, \text{g}} \tag{7.6}$$

in the so-called saturated limit for a spherical cold gas cloud immersed in the hot atmosphere described in equation 7.2 and 7.3. Assuming that the cloud stays spherical and in pressure equilibrium along the whole orbit, the evaporation time scale changes between 97 yr for the cloud at its initial distance in the year 1995.5 and 10 yr when the cloud reaches the pericenter. However, this neglects tidal effects and hydrodynamical instabilities, which finally lead to the disruption of the cloud. Thereby, the cloud increases in size and the evaporation time scale might decrease. Hence, evaporation effects get important mostly during the late evolution of the cloud.

As was shown in paper I and briefly discussed here, all of the mentioned physical processes are acting on similar timescales close to the orbital timescale of the cloud. This is especially the case for the late-time evolution and necessitates the use of numerical hydrodynamical simulations to determine the fate of the cloud.

7.6   Results of the hydrodynamical simulations

7.6.1   The evolution of the density distribution in the Compact Cloud Scenario (CC01)
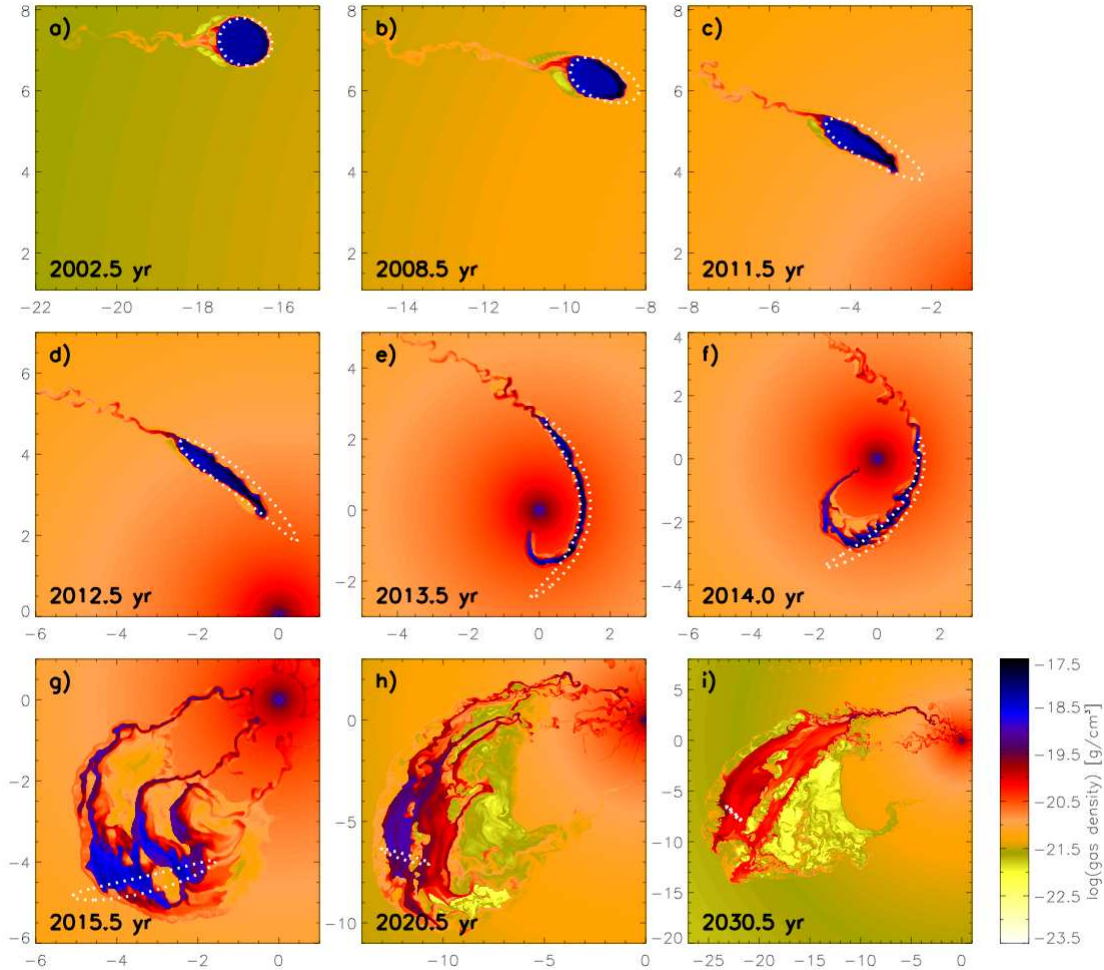

Figure 7.4: Density evolution of the compact cloud model CC01. Overlayed as dotted white lines are the positions of test particles initially located at the cloud boundary. The axis labels are given in mpc (milli-parsec). Mind the different scalings of the panels.

The temporal evolution of the two-dimensional gas density distribution of model CC01 is shown in Fig. 7.4. Overlayed are the results of a simulation in which we placed test particles at the boundary of the initial cloud setup and let them evolve under the influence of the gravitational potential alone. They serve as an indicator for the differences in the evolution due to hydrodynamical effects. We start with a phenomenological description of the cloud

evolution and back our findings in the course of the paper with several analysis tools. The initially spherical cloud begins its journey at the year 1995.5 position on G2's observed best-fit orbit. The early phase towards the pericenter which is reached in 2013.5 is dominated by tidal forces (panels a to e). Due to the highly eccentric orbit, the cloud gets stretched along the orbital direction. At the same time, the surrounding density and the increase in orbital velocity lead to an increase of ram pressure forces, resulting in a compression of the cloud head which can be inferred from the deviation of the density distribution from the test particle model (panel d). The shear flow at the boundary of the cloud leads to stripping of gas and the formation of a long turbulent wake, which develops typical rolls of the Kelvin-Helmholtz instability (KHI, panel e). At the time of the pericenter passage, the cloud has developed into a long spaghetti-like filament more or less aligned with the test particle orbit of the cloud. This elongation of the cloud in combination with the large velocity and density difference (along G2's orbit) between the cloud and the atmosphere causes a rapid growth of the KHI, well visible by the meandering shape of the cloud (panel f). In the subsequent evolutionary phase, a number of effects lead to the buckling of the cloud in direction of orbital motion (panel g): First, the pure gravitational effect, leading to a deceleration of the front while the back still has a high velocity. This is the dominant effect, as the horizontal width of the test particle distribution almost coincides with the horizontal width of the gas cloud. Second, this is the region of the orbit, where the atmosphere is the densest. Hence, strong ram pressure forces shape the head of the cloud and lead to additional compression along the orbit and elongation perpendicular to the orbital motion. Increasing the cross section, ram pressure forces get more and more important. A boundary layer builds up at the front of the cloud, which looses angular momentum and cloud material is able to accrete towards the center, forming a number of filaments pointing towards Sgr A* (panel g). Their number and location is dictated by the earlier growth of the Kelvin-Helmholtz instability mainly during the pericenter passage. In the course of the following evolution, the rear filaments – being in the *shadow* of the leading one – merge with the one in front and form a nozzle-like structure of matter streaming towards Sgr A* and causing an increased accretion rate (Sect. 7.6.3, panel h). The later evolution of the cloud is dominated by hydrodynamical effects in our simulations: The large effective area of the cloud makes it susceptible to hydrodynamical instabilities and ram pressure. The phase during and shortly after the pericenter passage is also the time when for the first time, the cloud is able to mix with the atmosphere. Due to the large temperature difference between cloud and atmosphere and the moderate density contrast in this region, this mixing is able to increase the cloud temperature to approximately $10^5 - 10^6$ K. At the end of this mixing process, about 1% of the cloud is made up of atmospheric gas.

Whereas hydrodynamical instabilities shape the outer region of the cloud, ram pressure interaction with the atmosphere enables further deceleration and accretion of gas from the boundary layer. However, it is very difficult to make detailed predictions of the late evolution of the gas with the help of our idealized simulations, as by then, several other effects become important. Thermal conduction will be able to act on the much increased surface area of the cloud and will evaporate it outside-in and the detailed thermodynamical

treatment might as well significantly change the morphology and accretion behavior in this evolutionary phase (see discussion in 7.6.5).
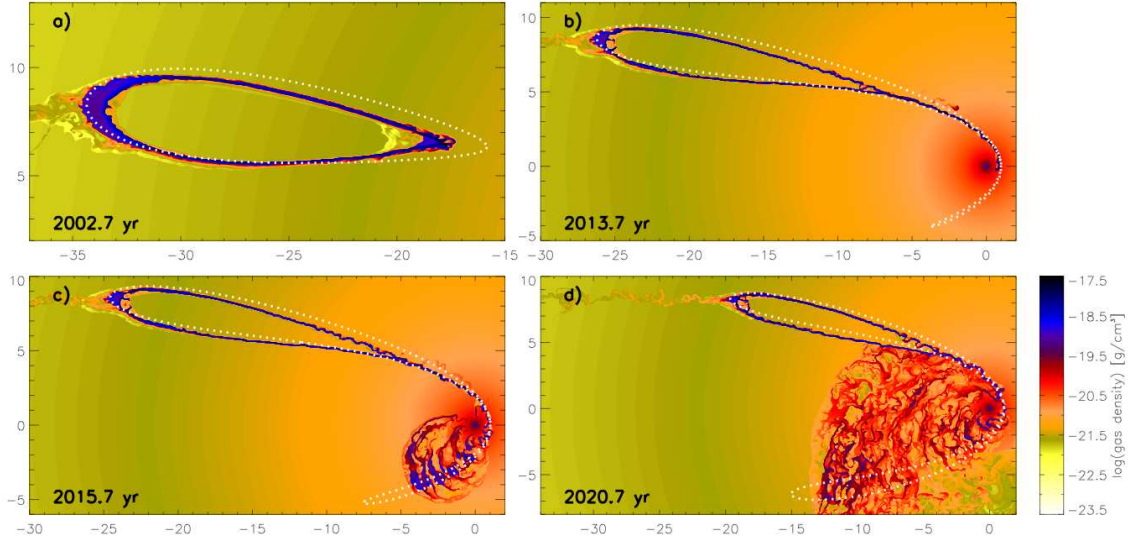

Figure 7.5: Density evolution of the spherical shell model SS01. Overlayed as dotted white lines are the positions of test particles initially located at the outer ring boundary. The axis labels are given in mpc (milli-parsec). Mind the different scalings of the panels.

7.6.2 The evolution of the density distribution in the Spherical Shell Scenario (SS01)

Density snapshots showing the evolution of the spherical shell scenario (simulation SS01) are displayed in Fig. 7.5. The basic physical processes acting on the orbit until the pericenter passage are very similar to the evolution of the compact cloud. Firstly, the ring squeezes into a drop-shaped morphology due to the interaction in the gravitational potential of the black hole (panel a). Secondly, the hydrodynamical interaction with the hot atmosphere leads to the formation of a turbulent wake behind the shell and at the ring border, KHI start to grow (panel b). In a three-dimensional simulation, the structure would correspond to a hollow conical morphology, with one major focal point at the very front of the cloud. This is in good agreement with what is seen in observations: The focal point then corresponds to the actual cloud G2 and the conical structure is the diffuse tail G2t, which indeed shows signs of a conical shape. In reality, the conical appearance is irregular and not continuous as the spherical shell is expected to have an inhomogeneous density distribution initially. At pericenter, the front part of the ring – which we interpret as the cloud G2 – has already collapsed into a thin, spaghetti-like shape. In contrast to our compact cloud model (see Sect. 7.6.1), the thin filament shows already the typical disturbances expected for the KHI and hence a larger effective cross section compared to the compact cloud (panel b). Being very close to the center of the hot atmosphere, the steep density gradient causes a rapid

increase of the ram pressure, decelerating the front part of the ring. The KHI disturbances already present before pericenter passage grow on short timescale and finally lead to a fast disruption of the ring (panel c). It efficiently exchanges angular momentum with the dense inner atmosphere and a filamentary disk-like structure is able to form (panel d). This leads to a much higher mass accretion rate through the inner boundary (see Sect. 7.6.3). We refer to Sect. 7.7 for a critical discussion of the influence of numerical effects as well as our idealized treatment of the atmosphere.

### 7.6.3 Angular momentum redistribution and mass accretion towards the center
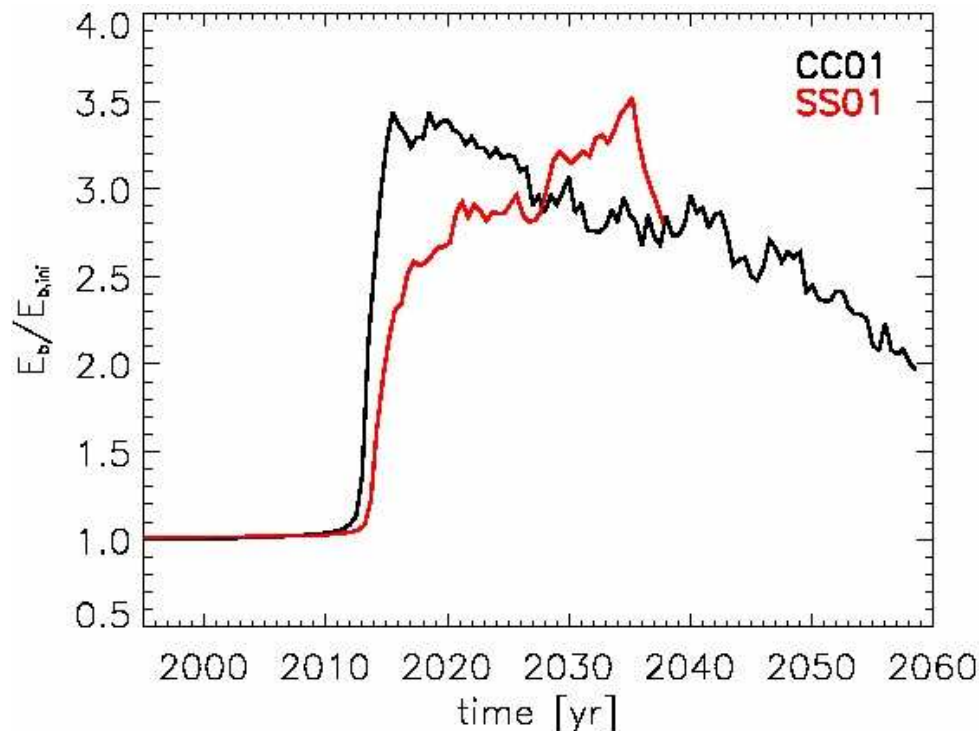
Figure 7.6: Binding energy of the cloud/ring in units of the initial binding energy.

The temporal evolution of the binding energy of the cloud (selected with the usual tracer threshold limit) is shown in Fig. 7.6 for the two models CC01 and SS01. As already discussed in paper I, the loss of kinetic energy due to ram-pressure in the early evolutionary phase is minor and the binding energy stays more or less constant until the first part of the cloud reaches the dense inner part of the hot atmosphere around the year 2012/2013, where we see a strong increase of ram pressure deceleration. As a consequence, the cloud gets bound more strongly to the SMBH. Ram pressure forces increase with the effective cross section of the cloud, they rise sharply shortly after the pericenter passage of the CC model, when the cloud compresses in direction of motion and expands perpendicular to

the orbital direction. A small fraction of the gas in the mixing zone of the cloud and atmosphere then carries angular momentum outwards, enabling part of the cloud to be accreted towards the center. When this outward moving gas has become very diluted and mixed with the atmosphere, the angular momentum is removed from the simulation due to our treatment to stabilize the unstable atmosphere. After the pericenter passage a dilute high pressure bubble forms (see Fig. 7.4, panel i), which rises buoyantly, thereby pushing some of the gas outward and the remaining gas gets less bound to the SMBH (Fig. 7.6). Model SS01 forms a disk-like structure, with a large amount of mass remaining in the high density inner region of the atmosphere.
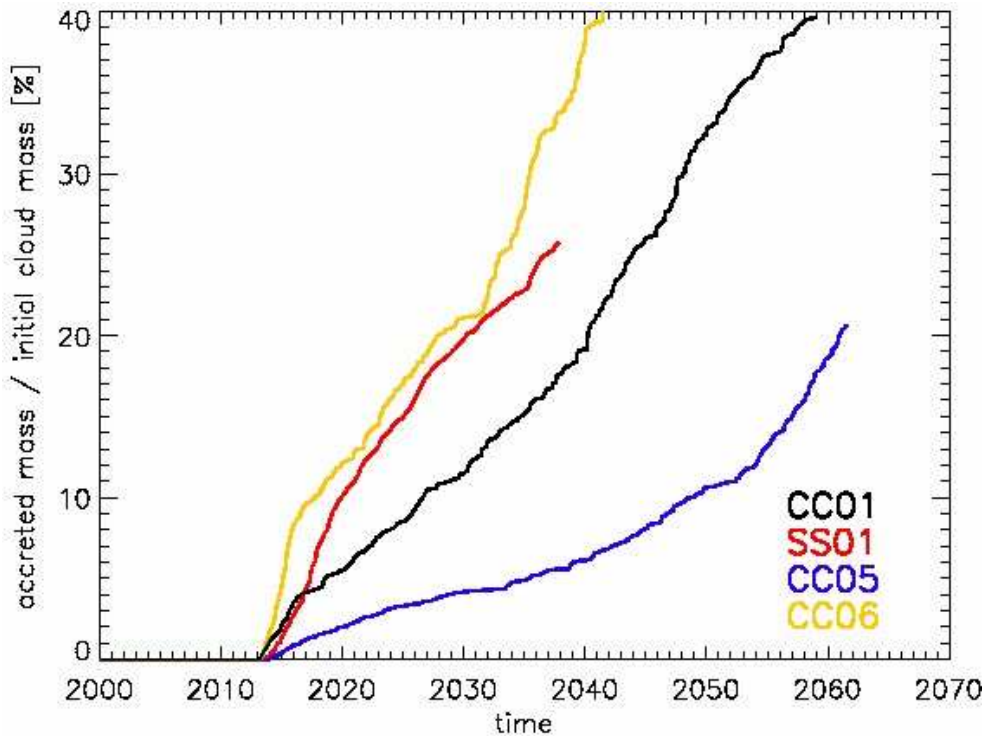

Figure 7.7: Accreted cloud mass of the models discussed in this paper relative to their initial cloud masses. See Table 7.3 for more details on the simulations.

During the simulations, we trace the mass inflow through the inner boundary and the resulting total accreted mass is plotted against time in Fig. 7.7 as a fraction of the initial total cloud mass. Only the accreted mass originally in the cloud is taken into account. Shortly before G2's pericenter passage in 2013.5, material moves through the inner boundary for the first time, but it takes roughly until 2060 to swallow 40% of the cloud material in model CC01. This corresponds to an additional average accretion rate of $6 \times 10^{-8}\, M_\odot\, \mathrm{yr}^{-1}$ until the year 2025. The time resolved accretion rate is shown in Fig. 7.8 for our standard cloud and ring model. During the whole simulation, the time averaged accretion rate remains approximately constant. However, hydrodynamical instabilities break up the nozzle-like stream of gas leading to clumpy accretion. Hence we observe deviations from the mean of

up to a factor of ten with a typical time scale of the order a few months. Concerning the ring model SS01, the accretion through the inner boundary starts approximately half a year later and we estimate the average accretion rate of cloud material to $4 \times 10^{-6}\,M_\odot\,\mathrm{yr}^{-1}$ (until the year 2025), roughly 67 times higher compared to model CC01, again remaining roughly constant on average, but highly variable. However, these numbers have to be interpreted with great care: Firstly, they only concern cloud material and secondly, in these idealized simulations, we do not take the back reaction of the cloud onto the ambient atmosphere into account. The latter could cause either enhanced accretion due to a fractional destabilization or a lower accretion rate due to the creation of an even hotter inner bubble or feedback from the central source. What actually happens depends crucially on the detailed thermodynamics and the state of the hot atmosphere in this region, which is both not very well understood and not easily accessible via observations.
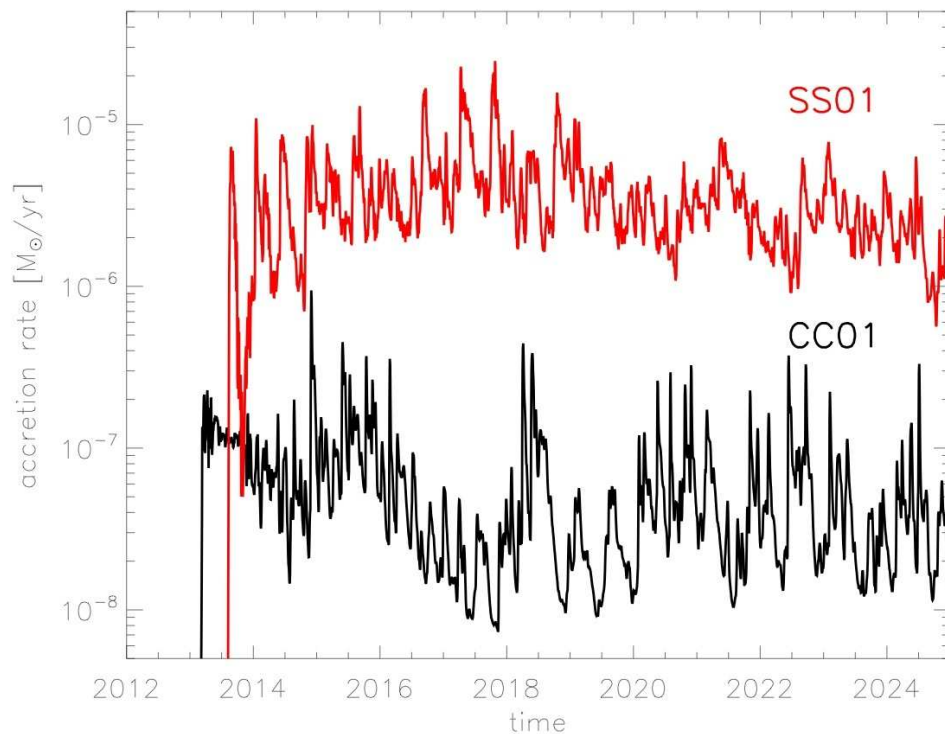

Figure 7.8: Measured mass accretion rate through the inner boundary of our standard model CC01 (black line) and the spherical ring model SS01 (red line).

### 7.6.4 Connection to observations and predictions for future observations
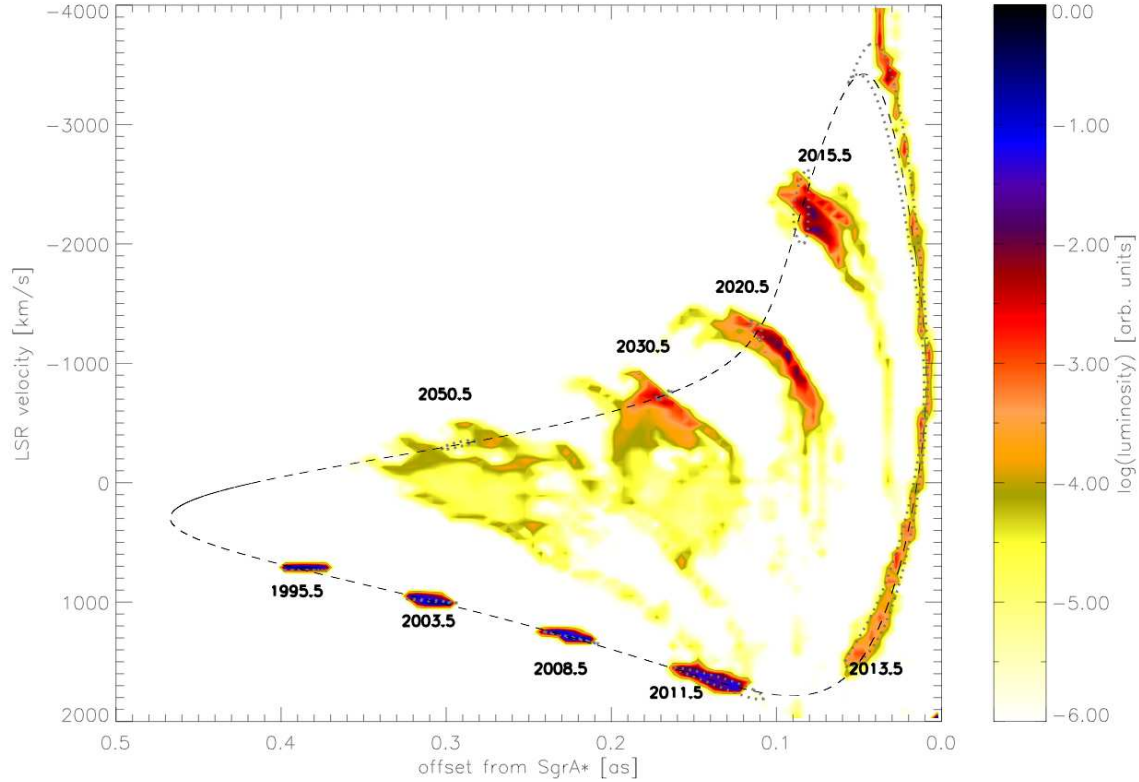
Figure 7.9: Position-velocity diagram for the simulation CC01. The distance to Sgr A* – projected on the sky – is plotted against the line-of-sight velocity. The colored contours display the square of a mass histogram, relative to the total initial mass of the cloud, representative for the Br γ emission. The dashed line represents the evolutionary path of a test particle in the center of the cloud on the orbit of G2 with the parameters given in Table 7.1 for a full orbital revolution. The dotted lines show the result of the test particle simulation.

Fig. 7.9 displays the position-velocity (PV) diagram of the whole orbit of G2. It shows the projected distance of the cloud material to the black hole on sky and the line-of-sight velocity of the cloud, taking the orbital angles as inferred from observations into account (Tab. 7.1). Overlayed as filled contours are the data of the hydrodynamical simulation CC01 at various stages of its evolution, as indicated in the plot. It represents the square of a mass histogram of the 2D gas distribution, representative for the Br γ emission of the cloud gas. The cloud starts with overall constant velocity. When moving towards the SMBH, it develops a velocity shear, which is the largest during pericenter passage. After being disrupted shortly after the closest approach, the shear decreases when the cloud gets compressed again, but never reaches the values expected from test particle simulations, as

in these stages, hydrodynamical effects dominate the evolution of the cloud. Nonetheless, the maximum signal is in this model always expected to arise from close to the test particle orbit of the cloud for the whole evolutionary time probed with our simulations.
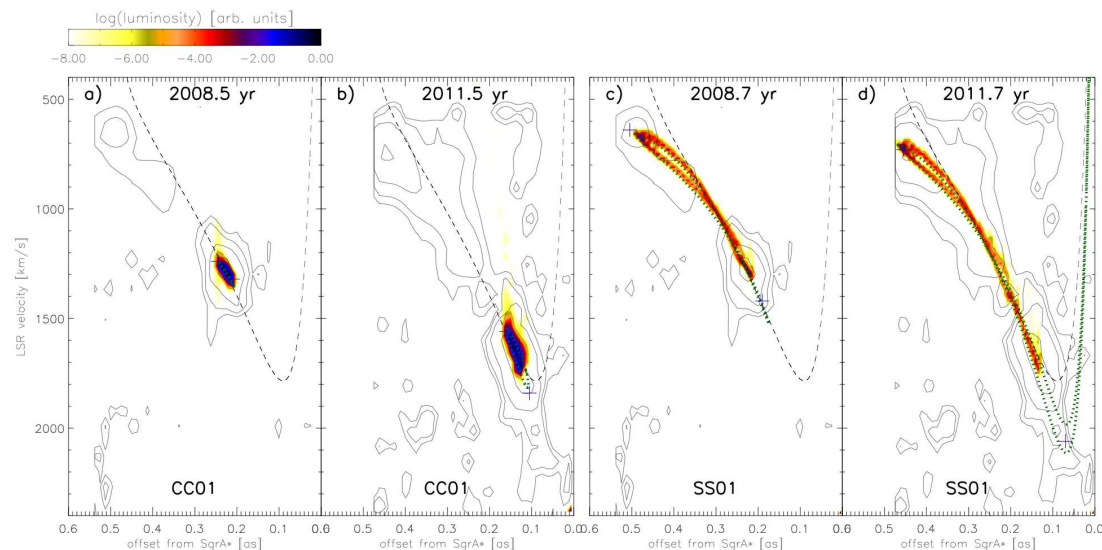

Figure 7.10: Comparison of the position-velocity diagrams for the simulations CC01 (panels a,b) and SS01 (panels c,d) with observations (background contours). The distance to Sgr A* – projected on the sky – is plotted against the line-of-sight velocity. The colored contours display the square of a mass histogram, relative to the total initial mass of the respective cloud model. The dashed line represents the evolutionary path of a test particle in the center of the cloud on the orbit of G2 with the parameters given in Table 7.1 for a full orbital revolution. The green dotted lines show the result of the test particle simulation.

We zoom into the lower part of the diagram in Fig. 7.10 for the CC model (panels a,b) and the SS model (panels c,d) in order to compare to available observations and make predictions for the near-future evolution. The compact cloud model was designed in order to give a good match with the observed head emission in the 2008.5 and 2011.5 data, which is very well fulfilled. In contrast to this, we interpret the observations for the case of the spherical shell model such that the *head* (G2) and *tail* (G2t) emission are the focal points of an already disrupted large cloud complex (eG2). In order to get a reasonable match with the observed PV diagram, this requires a spherical shell of gas, realized as a ring in our two-dimensional simulations. As the ring starts at its apocenter distance of 0.05 pc at the inner edge of the disk(s) of young stars, it seems obvious to interpret it as being the result of stellar evolutionary processes. As can be seen in Fig.7.10 (panels c,d), it is in reasonable agreement with the combined observations of the *head* and *tail emission* of the cloud and can well explain the offset of the *tail* from the inferred test particle orbit of G2. Fig. 7.11 show our predictions for observations in 2013. Distinct and observable differences are visible: Whereas our compact cloud simulation (panels a,b)

produces emission spread around the expected location of the test particle orbit of the cloud, the spherical shell simulation differs significantly by extending to higher velocities up to $+2000\,\mathrm{km\,s^{-1}}$ (panels c,d).
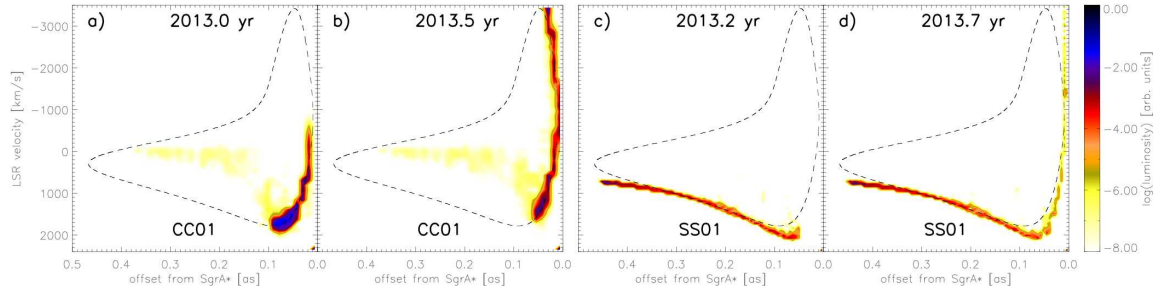

Figure 7.11: Predictions for the distribution of the compact cloud model CC01 (panels a,b) and the spherical shell model SS01 (panels c,d) in the position-velocity diagram for the year 2013. The distance to Sgr A* – projected on the sky – is plotted against the line-of-sight velocity. The colored contours display the square of a mass histogram, relative to the total initial mass of the respective cloud model. The dashed line represents the evolutionary path of a test particle in the center of the cloud on the orbit of G2 with the parameters given in Table 7.1 for a full orbital revolution.

In Fig. 7.12 we restrict the PV-diagram to the expected emission from the hydrodynamically formed tail of the cloud in the *Compact Cloud Scenario*. As expected, the stripped-off gas fills the interior of the test particle curve centered on G2 (thick black dashed line). The earlier the gas was removed from the compact cloud, the lower its present velocity due to the ram-pressure interaction and mixing with the ambient hot medium. The turbulent motions of this low-density material can be seen in the large width of the distribution in velocity direction, which even extends to velocities with the opposite sign. The contours vertically offset from the actual location of G2 could be related to the stripped-off gas from the front part of the cloud. Fig. 7.12 shows that what was often referred to as the *tail* of G2 in the observed PV diagram, cannot be explained by stripped material from the compact cloud, causing problems for the Compact Cloud model or any model where the cloud is the result of a compact invisible source of gas (*Compact Source Scenario*, see Section 7.2 and Murray-Clay & Loeb (2012)). Instead, the so far undiscussed contours at low distances to Sgr A* and low velocities could be related to a hydrodynamically stripped tail of gas. In contrast, our *Spherical Shell Scenario* is qualitatively able to explain the whole structure of the observed PV-diagram.
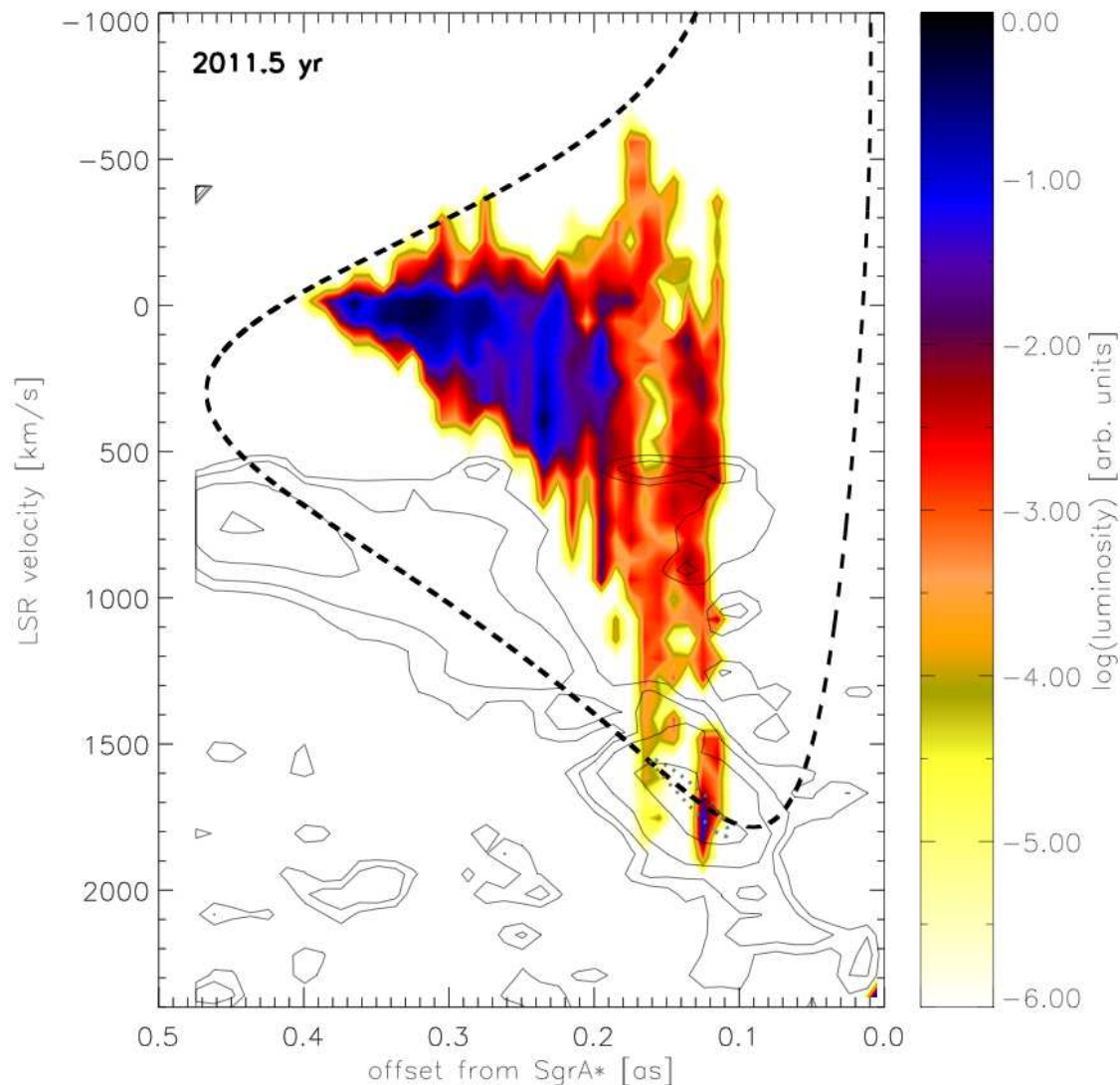
Figure 7.12: Position-velocity diagram for the simulation CC01, where we only show the emission of the tail of the cloud, selected by tracer values between the threshold value and 0.5. The distance to Sgr A* – projected on the sky – is plotted against the line-of-sight velocity. The colored contours display the square of a mass histogram, relative to the total initial mass of the cloud. The thick dashed line represents the evolutionary path of a test particle in the center of the cloud on the orbit of G2 with the parameters given in Table 7.1 for a full orbital revolution.

A second promising possibility to distinguish between different model predictions is via X-ray and IR-observations. In Sect. 7.6.3, we discussed the mass accretion rate through the inner boundary of our domain. Baganoff et al. (2003) observationally determine an accretion rate of $10^{-6} \, M_\odot \, \mathrm{yr}^{-1}$ at the Bondi radius, located at 10^5 Schwarzschild radii (Genzel et al., 2010). We use the scaling relation

$$\dot{M}_{\text{in}} = \dot{M}_{\text{Bondi}} \left(\frac{r_{\text{in}}}{r_{\text{Bondi}}} \right)^s , \tag{7.7}$$

where $r_{\text{in,Bondi}}$ is the inner radius or the Bondi radius and $\dot{M}_{\text{in,Bondi}}$ is the mass accretion rate at the inner boundary of our domain or the Bondi radius, respectively (e. g. Blandford & Begelman, 1999; Igumenshchev et al., 2003) and $s = 0.27$ (Yuan et al., 2003) to calculate the accretion rate expected at the inner boundary of our domain, which is located at roughly 1500 Schwarzschild radii distance from the SMBH. It results in a value of $3 \times 10^{-7} \, M_\odot \, \text{yr}^{-1}$. As discussed in Sect. 7.6.3, the matter streams through our inner boundary in form of small droplets or filaments. Given the proximity of the SMBH, the evaporation timescale is very short (see equation 7.6). Hence our first assumption is that the cloud material will evaporate on its further way in and join the hot accretion flow. To estimate the effect on the observable luminosity of Sgr A*, we use the spectral energy distributions derived for the ADAF models of Yuan et al. (2004). We interpolate their SEDs for various mass accretion rates shown in their Fig. 5 to match the average mass accretion rates of the flow through the inner radii of our models and compute the IR $(0.8 - 2.5$) and X-ray (2-8 keV) luminosity. If the mass accretion proceeds in this mode, we do not expect a significant boost of the X-ray or IR luminosity for the CC01 model, as even the spikes ten times above the average accretion rate would only lead to a factor of 1-2 increase of the IR and X-ray signal. In contrast to this, model SS01 would result in an X-ray luminosity of $4 \times 10^{34} \, \text{erg s}^{-1}$, corresponding to a boost of a factor of roughly 80 compared to the quiescent X-ray luminosity of Sgr A* ($4 \times 10^{32} \, \text{erg s}^{-1}$ derived from Yuan et al., 2004, Fig. 5). The expected IR luminosity amounts to $5 \times 10^{35} \, \text{erg s}^{-1}$, roughly the same factor above the assumed quiescent value ($7 \times 10^{33} \, \text{erg s}^{-1}$). Concerning the spikes of the accretion rate distribution (roughly a factor of ten above the average accretion rate), we calculate boost factors of roughly 3×10^4 in the X-ray and 6×10^3 in the IR. These high boost factors would enable us to test the validity of our spherical shell scenario in the coming years. However, another possibility (we are unable to test with our current models) is that the cold, disrupted cloud significantly affects the thermodynamic structure of the hot accretion flow close to the GC. This might then prevent the complete thermal evaporation of the cloud fragments and enable the formation of a thin and relatively cold accretion disk. To get a first rough estimate of the expected signal, we use the average mass transfer rate through the inner boundary of our domain (Fig. 7.8) and assume it is representative for the steady-state mass accretion rate through such an inner accretion disk, which we assume forms instantly. Given this assumption, the bolometric luminosity of the disk can be estimated to be (Krolik, 1999):

$$L_{\text{bol}} = \frac{1}{12} \, \dot{M} \, c^2 \tag{7.8}$$

This results in an average bolometric luminosity of $8 \times 10^4 \, L_\odot$ and $5 \times 10^6 \, L_\odot$ for the cloud model and the ring model respectively (averaged over a time period from the start of the

accretion until the year 2025). In order to derive the observable X-ray luminosity, we use the accretion disk spectral energy distribution constructed in Schartmann et al. (2005) from a combination of observations and simulations. This results in averaged values of $L_{2-8\mathrm{keV}} = 4 \times 10^{33}\mathrm{erg\,s^{-1}}$ and $L_{2-8\mathrm{keV}} = 3 \times 10^{35}\mathrm{erg\,s^{-1}}$ for the cloud and ring model in the energy range between two and eight keV and $3 \times 10^{37}\mathrm{erg\,s^{-1}}$ and $10^{39}\,\mathrm{erg\,s^{-1}}$ for the two models in the IR, the latter being orders of magnitude above the current quiescent luminosity. Which fraction of the cloud material will accrete in this mode is currently unclear and the detailed prediction of the resulting SED is clearly beyond the scope of this publication, but might influence these values significantly. However, a similar increase of the luminosity compared to the current state might in turn influence the RIAF solution itself (Yuan et al., 2004) as well as the dynamical evolution of the cloud via its radiation pressure interaction, as has for example been investigated by Schartmann et al. (2011). More detailed modelling of the physical processes at work as well as the hot atmosphere is necessary to determine the expected light curve, triggered by the future evolution of the cloud. Thermal conduction might be one of the key players here as the cloud evaporation timescale becomes very short in this phase.

### 7.6.5   Influence of the equation of state
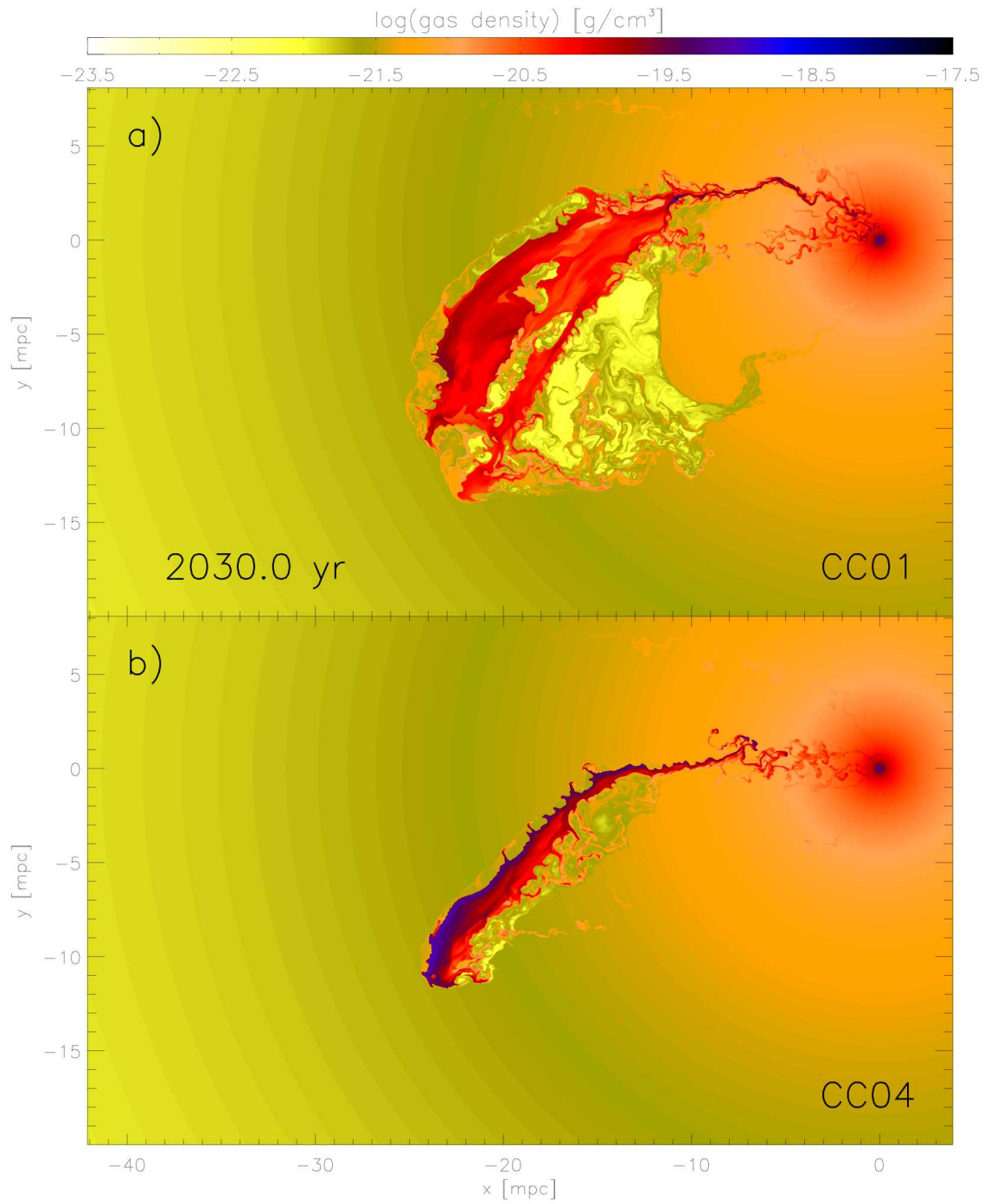
Figure 7.13: Comparison of the density of the cloud in 2030 for our standard model (panel a, CC01) and the adiabatic test simulation (panel b, CC04).
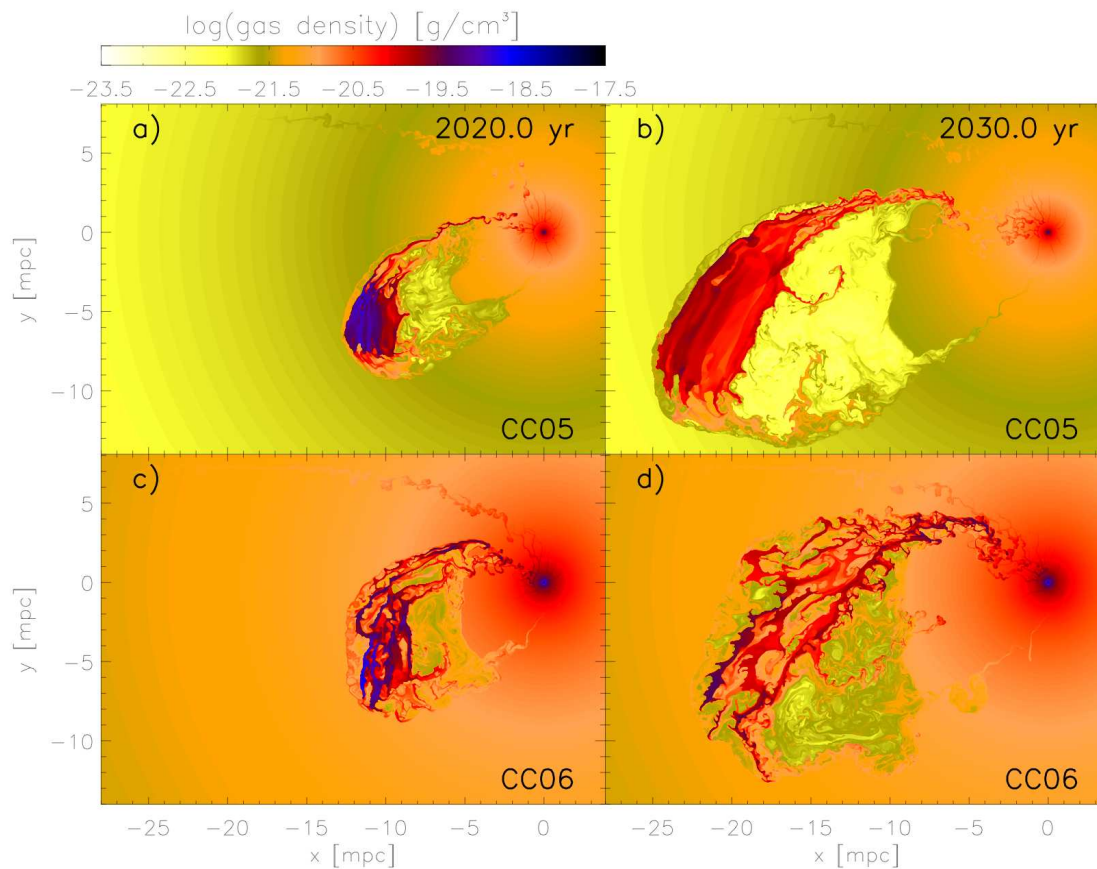
Figure 7.14: Comparison of two compact cloud models with a factor of two decreased density of the atmosphere (panel a,b, CC05) and a factor of two increased density of the atmosphere (panel c,d, CC06) with respect to our standard model.

A test simulation has been run with an adiabatic equation of state (simulation CC04). This represents inefficient external cooling and heating sources, but takes adiabatic cooling and heating via expansion and contraction into account. The early evolution of the density distribution is very similar in both cases. Major differences only arise after the pericenter passage. A comparison of the state in the year 2030 is presented in Fig. 7.13. We find that in simulation CC01, the pressure inside the remaining cloud gas is larger compared to the adiabatic case CC04. The reason is that the gas in the adiabatic simulation is able to cool when the cloud expands and gets disrupted after the pericenter passage. This effect is also visible in the formation of a low density but high pressure region in downstream direction of the cloud, which is less pronounced in the adiabatic simulation. The lower temperature and pressure in the adiabatic case lead to a more filamentary cloud with a stronger density enhancement, whereas in the other case, the larger pressure support leads to a more uniform density distribution, spreading over a larger area. This example shows again that the early evolution of the cloud can easily be understood with simple hydrodynamical simulations and we can trust the predictions for the near-future

observations. However, the late-time evolution – after tidal disruption has severely affected the cloud structure – significantly depends on the detailed physical processes and the structure of the surrounding atmosphere. For an in-depth understanding of the long-term fate of the cloud, more sophisticated (magneto)-hydrodynamical simulations are required.

7.6.6   Influence of the atmospheric density distribution

Our knowledge of the temperature and density distribution of the hot atmosphere in the Galactic Center region is based on theoretical models, which are consistent with the small number of data points observed with the Chandra satellite and the rotation measures (see above). Hence, it is interesting to ask whether the current and future evolution of the cloud will enable us to probe the hot atmosphere. A first impression of the effect of the density distribution of the ambient atmosphere on the cloud evolution was given in Sect. 7.3.2. As was shown there under the assumption of initial pressure equilibrium, the starting date would be changed by five to ten years if the atmospheric density distribution would be changed by a factor $f_{\rm hot}$ of 0.5 (CC05) or 2.0 (CC06). However, the absolute values of the preferred origin date of the cloud depend on the not very well known total mass of the cloud and hence our results should be taken with care. Here, we briefly discuss the hydrodynamical realizations of these two best-fit models from the test particle simulations for the *Compact Cloud Scenario*. As expected, both clouds are in good agreement with the observed PV diagrams in 2008.5 and 2011.5, but the late-time evolution of the density distribution changes significantly, as can be seen in Fig. 7.14. The growth of hydrodynamical instabilities scales with the density contrast of the cloud/atmosphere system and the importance of ram pressure effects increases with the density of the environment (see Sect. 7.5). The earlier onset of KHI in the high-density case – already during the pericenter passage – leads to a more filamentary cloud boundary. The interior is affected as well due to the partly disruption and the later buckling of the cloud. Gas transfer through the inner boundary starts roughly at the same time in both cases. However, the reduced ram pressure for the case of simulation CC05 leads to a smaller accretion rate (blue graph in Fig. 7.7) compared to the high density atmosphere (CC06), which displays a steeper increase of the accretion rate with time (yellow curve in Fig. 7.7). Concerning the evolution in the PV-diagram, model CC06 spreads over a larger region during the late evolution due to the faster disruption of the cloud in the high density case.

7.7 Discussion

Numerically, the most critical point of the simulations is the treatment of the atmosphere. As already discussed in Sect. 7.4, the ADAF solution which fits the Chandra observations of the hot atmosphere best is unstable to convection and cannot be modeled in a simple way. In order to enable a first investigation of the origin and further evolution of the cloud, we artificially stabilize the atmosphere and make several simplifying assumptions: (i) We neglect the accretion flow of the diffuse atmosphere towards the center and set up the central hot gas distribution in hydrostatic equilibrium. (ii) We suppress the growth of disturbances in the atmosphere by re-setting those cells within the atmosphere, which have not interacted with the cloud yet. This is necessary in particular close to the central boundary condition, where disturbances due to the Cartesian grid start to increase due to the entropy gradient. To avoid these complications, we use a passive tracer field. Cloud material is lost in those regions of the computational grid where the fraction of cloud gas relative to atmospheric gas is below a threshold of 10^{-4}. This leads to a roughly linear increase of the mass loss starting around the time of the pericenter passage in the standard model CC01. At the end of the simulation in the year 2060, roughly 1.3% of the initial cloud mass is removed from the simulation. This also means that the angular momentum and kinetic energy, which the cloud transfers to the atmosphere is finally taken out of the simulation. A critical discussion of the influence of the threshold value for the tracer is given in Sect. 7.7.2. Further limitations of our simulations are the negligence of thermal conduction, which will be important at least in the late phase of the evolution of the cloud (Sect. 7.5.3) and the restriction of the simulations to two dimensions. Perpendicular to the modelled orbital plane, we expect the cloud to collapse under the influence of the gravitational force of the black hole, forming a thin disk and later a thin filament close to pericenter. After passing the black hole, the cloud is expected to expand again in vertical direction due to the overpressure with respect to the surrounding medium. Given the larger contact surface with the hot ambient medium in rest, enhanced stripping due to KHI is expected, which is most important for the late time shredding of the cloud after pericenter passage. In contrast to this, we expect less ram pressure interaction in the 3D case, which might affect the angular momentum exchange with the atmosphere and hence slightly alter the mass transfer towards the center.

7.7.1   Resolution effects
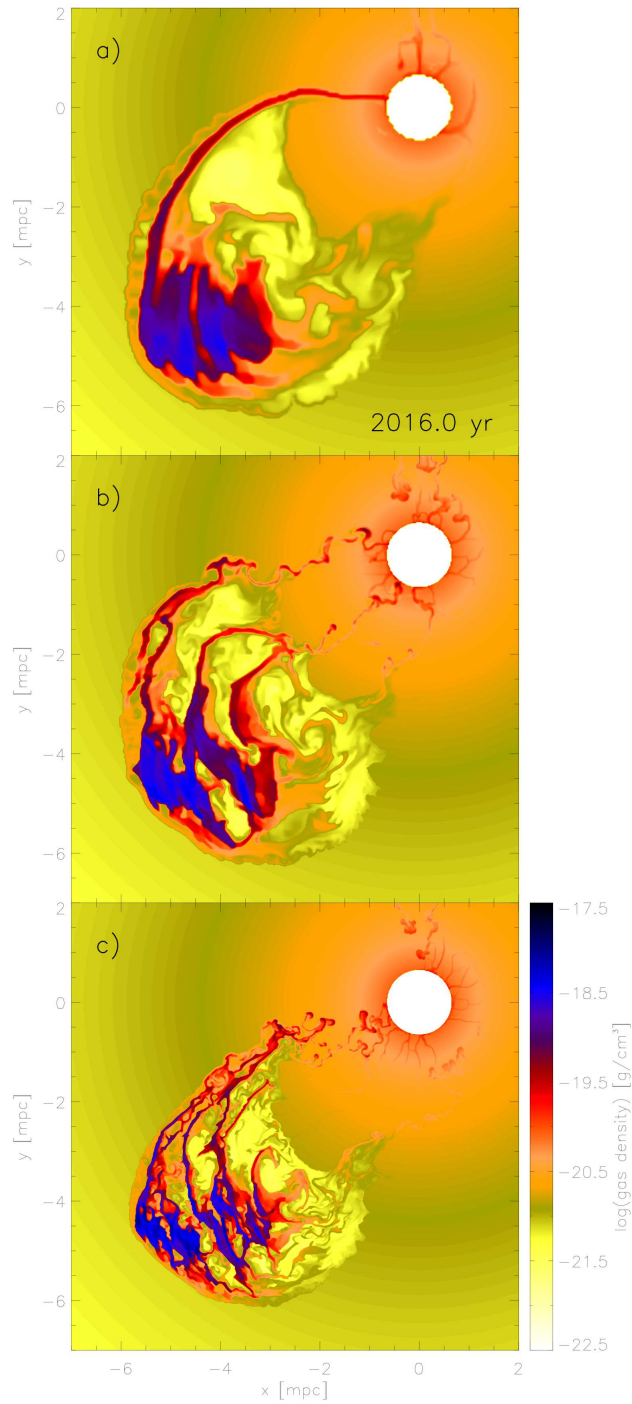
Figure 7.15: Resolution study of our standard model. Displayed is our standard resolution (panel b, CC01), half the resolution (panel a, CC07) and twice the resolution (panel c, CC08).

The effects of resolution on the density evolution of our simulations are displayed in Fig. 7.15. The snapshots are taken from the compact cloud simulation starting on G2's orbit in the year 1995.5. Panel b displays our standard resolution, whereas we decreased the resolution in both axis-directions by a factor of two in panel a and increased the resolution by a factor of two for the simulation displayed in panel c. The snapshots correspond to the year 2016, shortly after the pericenter passage. The basic dynamical evolution as well as the disruption due to tidal forces is very comparable. However, the expected resolution effects are visible in the detailed evolution of the hydrodynamical instabilities. This leads to a stronger disruption of the nozzle-shaped inflow of gas towards Sgr A* with increased resolution. In the highest resolution simulation, the stream has broken up already and the mass-flux through the inner boundary is clumpy, compared to the smooth accretion of gas through the nozzle in our low resolution run. Our standard resolution run already shows some clumpy accretion, which also increases at later stages of the evolution (Fig. 7.4, lower row). The mentioned accretion rates through the inner boundary differ by about 10% between the highest and the lowest resolution in our study.

7.7.2   Influence of the choice of the tracer threshold value

Fig. 7.16 displays the influence of the tracer threshold value. This is done for our simulation starting on G2's orbit in the year 1995.5 (model CC01) and we analyse the state of the simulation in the year 2025.5, as only the late-time evolution shows significant differences. From panel a to c, the tracer threshold value increases from 10^{-6} (panel a) to 10^{-4} (panel b) and 10^{-2} (panel c). Again, as in the resolution study, the basic dynamical evolution is unaffected by the choice of the threshold value. However, in this series, two systematic effects are visible: (i) For too high threshold values (Fig. 7.16c), the shape of the outer boundary in upstream direction changes slightly. As soon as the cloud mixes with the surrounding medium, gas is removed from the simulation. This artificially suppresses instabilities. (ii) For too low threshold values, the disturbed atmosphere in downstream direction of the cloud gets susceptible to the growth of convectively unstable regions. Bubbles are formed behind the cloud as well as in the disturbed atmosphere along the traversed orbit of the cloud. Quantifying the effects of the de-stabilization of a realistic atmosphere and its back-reaction onto the further evolution of the cloud is beyond the scope of these idealized simulations. Given the considerations briefly discussed here, we decided to use a tracer threshold value of 10^{-4}.
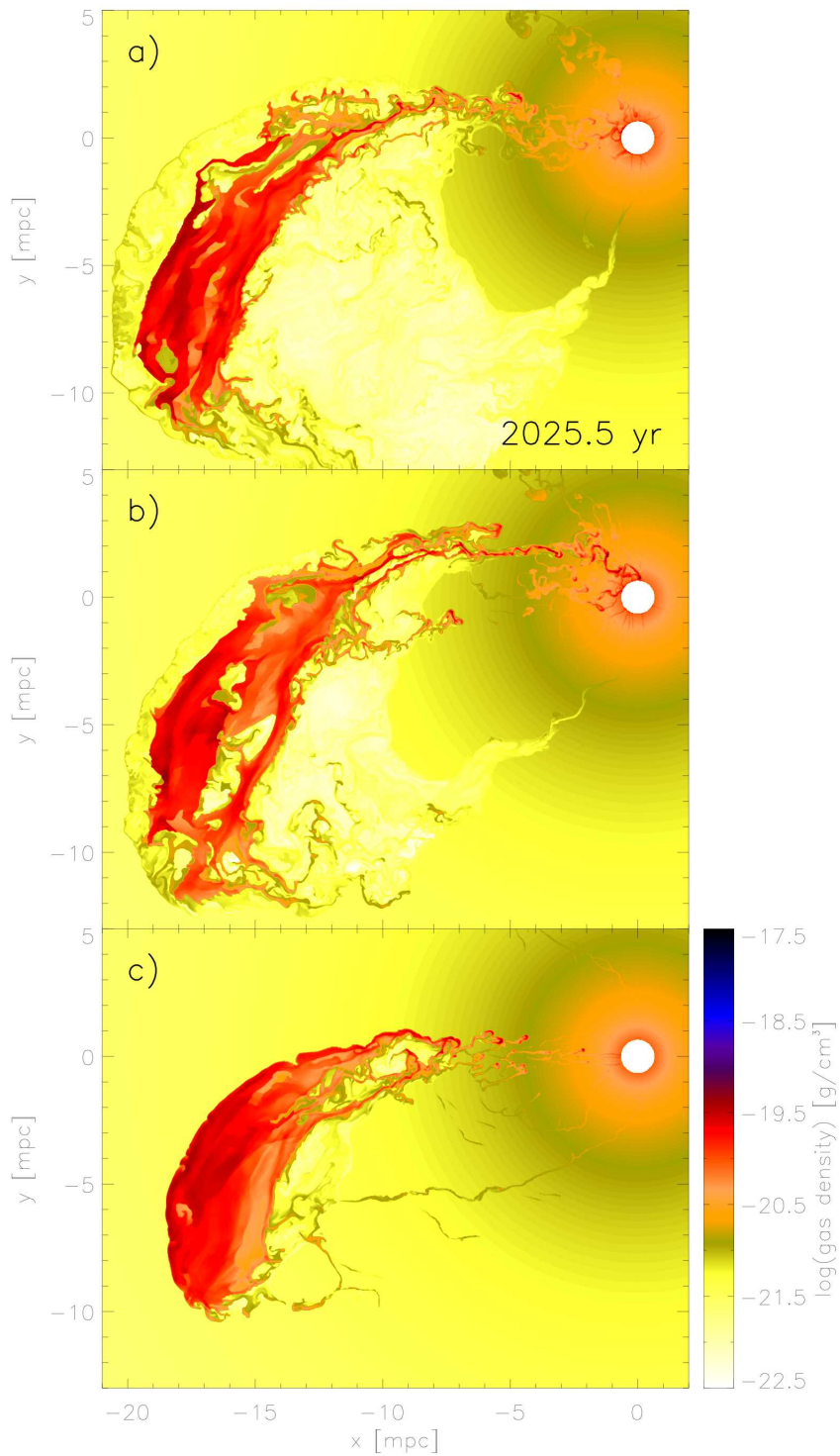
Figure 7.16: Studying the influence of the threshold value of the tracer field for artificially stabilizing the atmosphere. Displayed is a value of 10^{-6} (panel a), 10^{-4} (panel b, our standard model) and 10^{-2} (panel c).

7.7.3 Possible influence of magnetic fields on the evolution of the cloud

Strong magnetic fields of the order of $100\,\mu$G (with a lower limit of $50\,\mu$G on $400\,$pc scales) have been observationally inferred near the Galactic Center (Yusef-Zadeh & Morris, 1987; Morris & Yusef-Zadeh, 1989; Crocker et al., 2010). Field strengths of this magnitude might significantly influence the dynamics and physical interactions occuring in the interaction region of the cloud. Several effects might change the dynamics and appearance of the cloud: (i) magnetic pressure inside the cloud and of the hot atmosphere changes the total pressure balance and hence the size along the cloud's orbit, (ii) magnetic tension forces can lead to a confinement of the cloud (e. g. Krause et al., 2012), thereby alleviating the problem of the too fast tidal disruption, (iii) depending on field morphology, the Kelvin-Helmholtz-Instability can be significantly suppressed, again leading to a longer survival of the cloud and significant changes in the late time evolution and (iv) magnetic fields lead to anisotropic thermal conduction, altering the cloud evaporation time scale. Hence it will be necessary to consider magnetic fields in future simulations determining the fate of the observed cloud. The problem is that this adds additional degrees of freedom as neither the strength of the fields nor its morphology is currently known in the sub-parsec surrounding of Sgr A*.

7.8   Conclusions

In this paper, we present a set of idealized hydrodynamical simulations to study the origin and the fate of the recently discovered cloud complex in the Galactic Center. Building up on analytical estimates in paper I, we concentrate on two possible scenarios: (i) the **Compact Cloud Scenario**, where the cloud is assumed to have formed in the recent past on the orbital path of the G2 component of the cloud and (ii) the **Spherical Shell Scenario**, in which the observations are interpreted as an already disrupted spherical shell (or ring, respectively in two dimensions). The early evolution until close to the pericenter is dominated by tidal interaction in both cases. Shortly after pericenter passage, when the cloud is already tidally disrupted, secondary hydrodynamical instabilities as well as ram pressure become important, leading to some angular momentum redistribution and accretion towards the center. Nonetheless, the cloud keeps a large fraction of its initial angular momentum, which efficiently hinders direct accretion onto Sgr A*. Accretion is expected to occur via a thin nozzle-like feature connecting the cloud with the SMBH, as a result of continuous ram-pressure interaction of the upstream boundary of the cloud with the dense inner part of the atmosphere. Hence – depending on the destabilization of this stream (e. g. by thermal conduction) – there might be enhanced cold gas accretion within the next years, which might boost the luminosity of Sgr A* in an observable way. However, according to our simulations, a large fraction of the cloud will remain on a similar orbit compared to the test particle orbit and lead to a steady inflow of gas towards the Galactic Center. In contrast to the early evolution of the cloud, the post-pericenter stage depends sensitively on the detailed modelling of physical processes as well as the atmospheric density distribution, necessitating more detailed hydrodynamical simulations to predict the (far) future evolution of the cloud complex. A more realistic treatment of the unstable nature of the atmosphere might influence our derived accretion rates substantially, when taking the back-reaction of the cloud into account.

In summary, we currently favor the **Spherical Shell Scenario** for the following reasons: (i) It allows the cloud to be started within the range of the disk(s) of young stars. (ii) Being a spherical shell of gas further strengthens the notion of it being the result of stellar evolutionary processes. (iii) The model is able to explain the major part of the structure (eG2) seen in the observed position-velocity diagram, whereas the *Compact Cloud Scenario* only captures the dominant part of it (G2). (iv) Tidally stripped gas cannot account for the G2t component of the observed PV-diagram, which disfavors the *Compact Cloud Scenario* and any *Compact Source Scenario*, but a so far undiscussed component of the PV-diagram could be directly related to it.

7.9   Acknowledgements

Chapter 8

Outlook

We developed a formation model for the two stellar discs that can reproduce the unusual configuration observed around the Galactic Centre black hole. This model assumes the collision of a cloud with a ring of gas at some distance from the black hole. The latter is a much more likely scenario for the Milky Way Galactic Centre compared to the capture of a single molecular cloud by the black hole. Still simulations show that disc formation is possible assuming the direct collision of a cloud with a supermassive black hole.

One could try to apply this model to other objects. One example would be the stellar disc observed in the Andromeda Galaxy (M31). At the centre of M31 one can find a single disc of old stars close to the central black hole (Bender et al., 2005). The disc is eccentric (Tremaine, 1995) with a mass of roughly 10^7 $M_\odot$. The semi-major axis is roughly 2 pc. In the case of M31 the black hole mass is a factor of 100 higher compared to the Milky Way black hole, so that it becomes much easier for a cloud to be captured by the black hole.

Interestingly the centre of M31 does not contain a nuclear star cluster. Simulations of an infalling single cloud which do not include a star cluster potential lead to the creation of a prominent, eccentric disc. The disc retains this shape without the cluster potential. In Figure 4.12 we presented such an eccentric disc, which later on becomes circular due to phase mixing (precession inside the cluster potential). Figure 8.1 shows a comparison study of how different the above stellar disc evolves without including the cluster potential.

Test-simulations show that it is quite easy to create an eccentric disc that is similar to the M31 disc in size and shape. However there is again the drawback of the high mass requirement. If we assume a star formation efficiency of 10% the initial cloud must have a mass of around 10^8 $M_\odot$ with a radius < 10 pc, which is plain unrealistic. On the other hand, assuming an infall of multiple lower mass clouds raises the question how the eccentricity of the disc was retained.
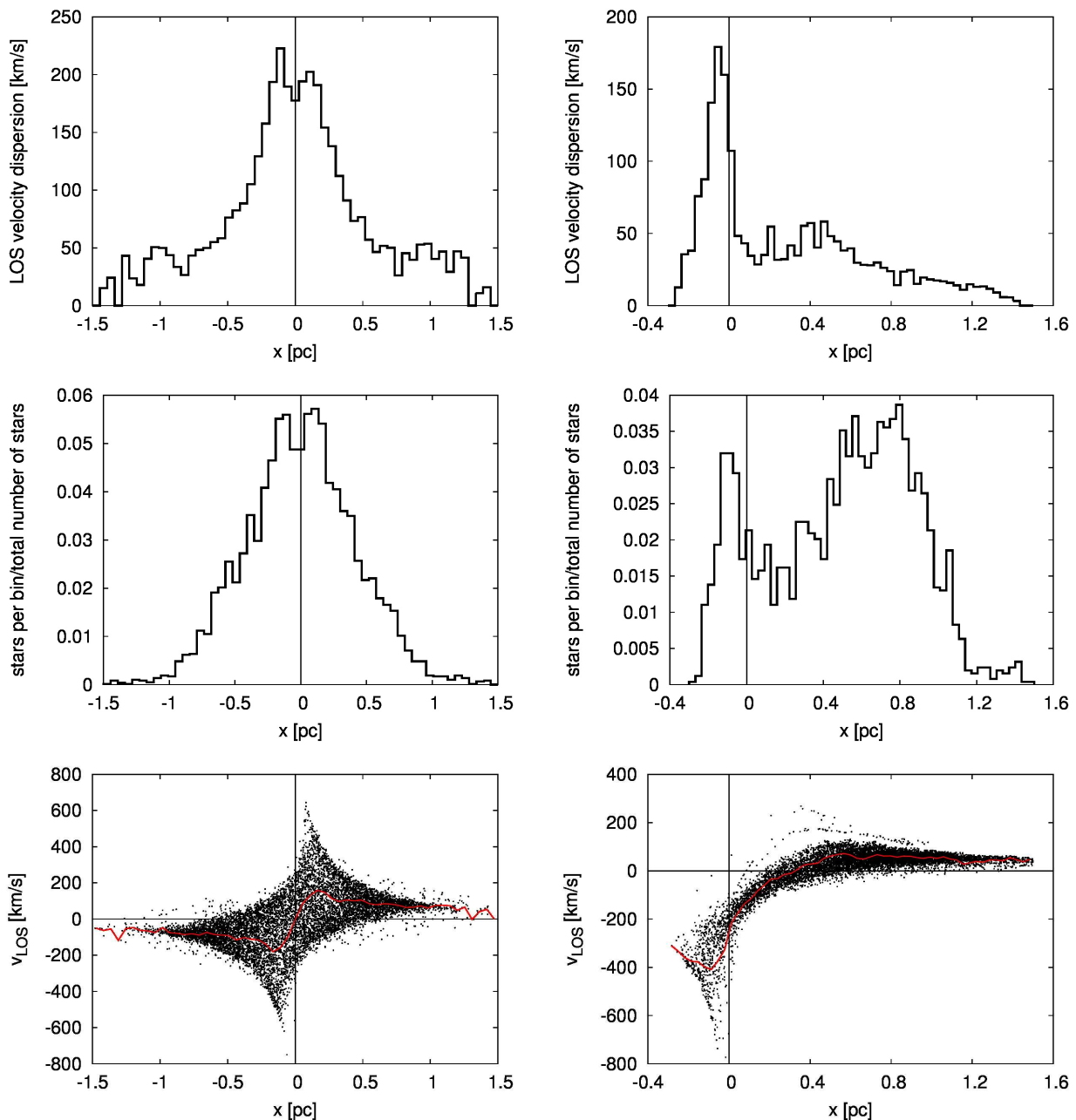
Figure 8.1:   Line of sight velocity dispersion (top row), stellar surface density (middle row) and line of sight velocity (bottom row) of a Nbody simulation that evolves the fragments which formed inside an eccentric accretion disc. The left side shows the evolution at the final timestep (6 Myrs) with the star cluster potential included, the right side without the potential. Although the individual stars stay on eccentric orbits, the disc shape becomes symmetric in the case with cluster potential included. Without the cluster, the disc retains its asymmetric shape.

In both cases (Milky Way and M31) the cloud mass had to be rather high compared to the black hole mass and one must consider if the gravitational influence of the cloud on the black hole can still be neglected.

Due to numerical constraints one important test, the comparison of the mass function, is not possible yet. Newer developments in SPH will help reducing numerical problems in simulations of fragmenting accretion discs. Adaptive gravitational softening is currently being implemented into Gadget3 as well as an adaptive viscosity strength parameter (Cullen & Dehnen, 2010). Also the possibilities offered by new hydro-codes like AREPO (Springel, 2011) which combines parts from the particle and grid approach, could proof to be very helpful in simulations like the G2 scenario and the formation of the Galactic Centre stellar discs. Finally there is always the constant increase in computational power (new technologies like GPU-computing already boost simulation speeds) and simulations which are currently too expensive will become feasible at some point.

Bibliography

Abramowicz M. A., Chen X., Kato S., Lasota J.-P., Regev O., 1995, ApJL, 438, L37

Agertz O., Moore B., Stadel J., Potter D., Miniati F., Read J., Mayer L., Gawryszczak A., Kravtsov A., Nordlund Å., Pearce F., Quilis V., Rudd D., Springel V., Stone J., Tasker E., Teyssier R., Wadsley J., Walder R., 2007, MNRAS, 380, 963

Alexander R. D., Armitage P. J., Cuadra J., Begelman M. C., 2008, ApJ, 674, 927

Alexander R. D., Begelman M. C., Armitage P. J., 2007, ApJ, 654, 907

Alig C., Burkert A., Johansson P. H., Schartmann M., 2011, MNRAS, 412, 469

Alig C., Drees M., Oda K.-y., 2006, Journal of High Energy Physics, 12, 49

Alig C., Schartmann M., Burkert A., Dolag K., 2013, ApJ, 771, 119

Almgren A. S., Beckner V. E., Bell J. B., Day M. S., Howell L. H., Joggerst C. C., Lijewski M. J., Nonaka A., Singer M., Zingale M., 2010, ApJ, 715, 1221

Anninos P., Fragile P. C., Wilson J., Murray S. D., 2012, ApJ, 759, 132

Aschenbach B., 2006, Chinese Journal of Astronomy and Astrophysics Supplement, 6, 010000

Baganoff F. K., Maeda Y., Morris M., Bautz M. W., Brandt W. N., Cui W., Doty J. P., Feigelson E. D., Garmire G. P., Pravdo S. H., Ricker G. R., Townsley L. K., 2003, ApJ, 591, 891

Balbus S. A., Papaloizou J. C. B., 1999, ApJ, 521, 650

Ballone A., Schartmann M., Burkert A., Gillessen S., Genzel R., Fritz T. K., Eisenhauer F., Pfuhl O., Ott T., 2013, ApJ, 776, 13

Balsara D. S., 1995, Journal of Computational Physics, 121, 357

Bartko H., Martins F., Fritz T. K., Genzel R., Levin Y., Perets H. B., Paumard T., Nayakshin S., Gerhard O., Alexander T., Dodds-Eden K., Eisenhauer F., Gillessen S., Mascetti L., Ott T., Perrin G., Pfuhl O., Reid M. J., Rouan D., Sternberg A., Trippe S., 2009, ApJ, 697, 1741

Bartko H., Martins F., Trippe S., Fritz T. K., Genzel R., Ott T., Eisenhauer F., Gillessen S., Paumard T., Alexander T., Dodds-Eden K., Gerhard O., Levin Y., Mascetti L., Nayakshin S., Perets H. B., Perrin G., Pfuhl O., Reid M. J., Rouan D., Zilka M., Sternberg A., 2010, ApJ, 708, 834

Bate M. R., Burkert A., 1997, MNRAS, 288, 1060

Becklin E. E., Gatley I., Werner M. W., 1982, ApJ, 258, 135

Bell K. R., Lin D. N. C., 1994, ApJ, 427, 987

Bender R., Kormendy J., Bower G., Green R., Thomas J., Danks A. C., Gull T., Hutchings J. B., Joseph C. L., Kaiser M. E., Lauer T. R., Nelson C. H., Richstone D., Weistrop D., Woodgate B., 2005, ApJ, 631, 280

Beringer J., et al., 2012, Phys.Rev., D86, 010001

Binney J., Gerhard O. E., Stark A. A., Bally J., Uchida K. I., 1991, MNRAS, 252, 210

Blandford R. D., Begelman M. C., 1999, MNRAS, 303, L1

Bonnell I. A., Rice W. K. M., 2008, Science, 321, 1060

Børve S., Omang M., Trulsen J., 2004, ApJS, 153, 447

Bower G. C., Wright M. C. H., Falcke H., Backer D. C., 2003, ApJ, 588, 331

Broderick A. E., Fish V. L., Doeleman S. S., Loeb A., 2011, ApJ, 735, 110

Broderick A. E., Loeb A., Narayan R., 2009, ApJ, 701, 1357

Buchholz R. M., Schodel R., Eckart A., 2009

Burkert A., Schartmann M., Alig C., Gillessen S., Genzel R., Fritz T. K., Eisenhauer F., 2012, ApJ, 750, 58

Carretti E., Crocker R. M., Staveley-Smith L., Haverkorn M., Purcell C., Gaensler B. M., Bernardi G., Kesteven M. J., Poppi S., 2013, Nature, 493, 66

Coker R. F., Christopher M. H., Stolovy S. R., Scoville N. Z., 2003, Astronomische Nachrichten Supplement, 324, 629

Cowie L. L., McKee C. F., 1977, ApJ, 211, 135

Crocker R. M., Jones D. I., Melia F., Ott J., Protheroe R. J., 2010, Nature, 463, 65

Crutcher R. M., 1999, ApJ, 520, 706

Cuadra J., Armitage P. J., Alexander R. D., 2008, MNRAS, 388, L64

Cullen L., Dehnen W., 2010, MNRAS, 408, 669

Czerny B., Karas V., Kunneriath D., Das T. K., 2013, in IAU Symposium, Vol. 290, IAU Symposium, Zhang C. M., Belloni T., Méndez M., Zhang S. N., eds., pp. 199–200

Davies B., Origlia L., Kudritzki R.-P., Figer D. F., Rich R. M., Najarro F., 2009, ApJ, 694, 46

Downes D., Martin A. H. M., 1971, Nature, 233, 112

Eisenhauer F., Perrin G., Brandner W., Straubmeier C., Perraut K., Amorim A., Schöller M., Gillessen S., Kervella P., Benisty M., Araujo-Hauck C., Jocou L., Lima J., Jakob G., Haug M., Clénet Y., Henning T., Eckart A., Berger J.-P., Garcia P., Abuter R., Kellner S., Paumard T., Hippler S., Fischer S., Moulin T., Villate J., Avila G., Gräter A., Lacour S., Huber A., Wiest M., Nolot A., Carvas P., Dorn R., Pfuhl O., Gendron E., Kendrew S., Yazici S., Anton S., Jung Y., Thiel M., Choquet É., Klein R., Teixeira P., Gitton P., Moch D., Vincent F., Kudryavtseva N., Ströbele S., Sturm S., Fédou P., Lenzen R., Jolley P., Kister C., Lapeyrère V., Naranjo V., Lucuix C., Hofmann R., Chapron F., Neumann U., Mehrgan L., Hans O., Rousset G., Ramos J., Suarez M., Lederer R., Reess J.-M., Rohloff R.-R., Haguenauer P., Bartko H., Sevin A., Wagner K., Lizon J.-L., Rabien S., Collin C., Finger G., Davies R., Rouan D., Wittkowski M., Dodds-Eden K., Ziegler D., Cassaing F., Bonnet H., Casali M., Genzel R., Lena P., 2011, The Messenger, 143, 16

Eisenhauer F., Perrin G., Brandner W., Straubmeier C., Richichi A., Gillessen S., Berger J. P., Hippler S., Eckart A., Schöller M., Rabien S., Cassaing F., Lenzen R., Thiel M., Clénet Y., Ramos J. R., Kellner S., Fédou P., Baumeister H., Hofmann R., Gendron E., Boehm A., Bartko H., Haubois X., Klein R., Dodds-Eden K., Houairi K., Hormuth F., Gräter A., Jocou L., Naranjo V., Genzel R., Kervella P., Henning T., Hamaus N., Lacour S., Neumann U., Haug M., Malbet F., Laun W., Kolmeder J., Paumard T., Rohloff R.-R., Pfuhl O., Perraut K., Ziegleder J., Rouan D., Rousset G., 2008, in Society of Photo-Optical Instrumentation Engineers (SPIE) Conference Series, Vol. 7013, Society of Photo-Optical Instrumentation Engineers (SPIE) Conference Series

Ekers R. D., Goss W. M., Schwarz U. J., Downes D., Rogstad D. H., 1975, A&A, 43, 159

Ekers R. D., Lynden-Bell D., 1971, ApJL, 9, 189

Ekers R. D., van Gorkom J. H., Schwarz U. J., Goss W. M., 1983, A&A, 122, 143

Ekström S., Georgy C., Eggenberger P., Meynet G., Mowlavi N., Wyttenbach A., Granada A., Decressin T., Hirschi R., Frischknecht U., Charbonnel C., Maeder A., 2012, A&A, 537, A146

Garmire G., 2001, in Astronomical Society of the Pacific Conference Series, Vol. 234, X-ray Astronomy 2000, Giacconi R., Serio S., Stella L., eds., p. 15

Geballe T. R., Najarro F., Rigaut F., Roy J.-R., 2006, ApJ, 652, 370

Genzel R., Crawford M. K., Townes C. H., Watson D. M., 1985, ApJ, 297, 766

Genzel R., Eisenhauer F., Gillessen S., 2010, Reviews of Modern Physics, 82, 3121

Genzel R., Schödel R., Ott T., Eisenhauer F., Hofmann R., Lehnert M., Eckart A., Alexander T., Sternberg A., Lenzen R., Clénet Y., Lacombe F., Rouan D., Renzini A., Tacconi-Garman L. E., 2003, ApJ, 594, 812

Gerhard O., 2001, ApJL, 546, L39

Ghez A. M., Salim S., Hornstein S. D., Tanner A., Lu J. R., Morris M., Becklin E. E., Duchêne G., 2005, ApJ, 620, 744

Ghez A. M., Salim S., Weinberg N. N., Lu J. R., Do T., Dunn J. K., Matthews K., Morris M. R., Yelda S., Becklin E. E., Kremenek T., Milosavljevic M., Naiman J., 2008, ApJ, 689, 1044

Gillessen S., Eisenhauer F., Fritz T. K., Bartko H., Dodds-Eden K., Pfuhl O., Ott T., Genzel R., 2009a, ApJL, 707, L114

Gillessen S., Eisenhauer F., Trippe S., Alexander T., Genzel R., Martins F., Ott T., 2009b, ApJ, 692, 1075

Gillessen S., Genzel R., Fritz T. K., Eisenhauer F., Pfuhl O., Ott T., Cuadra J., Schartmann M., Burkert A., 2013a, ApJ, 763, 78

Gillessen S., Genzel R., Fritz T. K., Eisenhauer F., Pfuhl O., Ott T., Schartmann M., Ballone A., Burkert A., 2013b, ApJ, 774, 44

Gillessen S., Genzel R., Fritz T. K., Quataert E., Alig C., Burkert A., Cuadra J., Eisenhauer F., Pfuhl O., Dodds-Eden K., Gammie C. F., Ott T., 2012, Nature, 481, 51

Gingold R. A., Monaghan J. J., 1977, MNRAS, 181, 375

—, 1983, MNRAS, 204, 715

Greiner W., Stock H., 1991, Verlag Harri Deutsch, Hydrodynamik 2A

Guesten R., Genzel R., Wright M. C. H., Jaffe D. T., Stutzki J., Harris A. I., 1987, ApJ, 318, 124

Güsten R., Philipp S. D., 2004, in The Dense Interstellar Medium in Galaxies, Pfalzner S., Kramer C., Staubmeier C., Heithausen A., eds., p. 253

Herrnstein R. M., Ho P. T. P., 2005, ApJ, 620, 287

Hobbs A., Nayakshin S., 2009, MNRAS, 394, 191

Hopkins P. F., Quataert E., 2010, MNRAS, 407, 1529

Hunter C., Toomre A., 1969, ApJ, 155, 747

Ichimaru S., 1977, ApJ, 214, 840

Igumenshchev I. V., Narayan R., Abramowicz M. A., 2003, ApJ, 592, 1042

Ivanov P. B., Polnarev A. G., Saha P., 2005, MNRAS, 358, 1361

Jackson J. M., Geis N., Genzel R., Harris A. I., Madden S., Poglitsch A., Stacey G. J., Townes C. H., 1993, ApJ, 402, 173

Jansky K. G., 1933, Nature, 132, 66

Johansson P. H., Naab T., Burkert A., 2009, ApJ, 690, 802

Kim S. S., Morris M., 2003, ApJ, 597, 312

King A. R., Pringle J. E., 2007, MNRAS, 377, L25

Kocsis B., Tremaine S., 2011, MNRAS, 412, 187

Kolykhalov P. I., Syunyaev R. A., 1980, Soviet Astronomy Letters, 6, 357

Krabbe A., Genzel R., Drapatz S., Rotaciuc V., 1991, ApJL, 382, L19

Kraus J. D., Ko H. C., Matt S., 1954, ApJ, 59, 439

Krause M., Schartmann M., Burkert A., 2012, MNRAS, 425, 3172

Krolik J. H., 1999, Active galactic nuclei : from the central black hole to the galactic environment. Princeton University Press, Princeton, New Jersey

LaRosa T. N., Kassim N. E., Lazio T. J. W., Hyman S. D., 2000, ApJ, 119, 3145

Lau R. M., Herter T. L., Morris M. R., Becklin E. E., Adams J. D., 2013, ArXiv e-prints

Launhardt R., Zylka R., Mezger P. G., 2002, A&A, 384, 112

Levin Y., Beloborodov A. M., 2003, ApJL, 590, L33

Lin D. N. C., Pringle J. E., 1987, MNRAS, 225, 607

Liu H. B., Ho P. T. P., Wright M. C. H., Su Y.-N., Hsieh P.-Y., Sun A.-L., Kim S. S., Minh Y. C., 2013, ApJ, 770, 44

Liu H. B., Hsieh P.-Y., Ho P. T. P., Su Y.-N., Wright M., Sun A.-L., Minh Y. C., 2012, ApJ, 756, 195

Lo K. Y., Claussen M. J., 1983, Nature, 306, 647

Löckmann U., Baumgardt H., 2009, MNRAS, 394, 1841

Löckmann U., Baumgardt H., Kroupa P., 2008, ApJL, 683, L151

—, 2009, MNRAS, 398, 429

Lodato G., Clarke C. J., 2011, MNRAS, 413, 2735

Lodato G., Rice W. K. M., 2004, MNRAS, 351, 630

Lu J. R., Do T., Ghez A. M., Morris M. R., Yelda S., Matthews K., 2013, ApJ, 764, 155

Lu J. R., Ghez A. M., Hornstein S. D., Morris M. R., Becklin E. E., Matthews K., 2009, ApJ, 690, 1463

Lucas W. E., Bonnell I. A., Davies M. B., Rice W. K. M., 2013, MNRAS, 433, 353

Lucy L. B., 1977, ApJ, 82, 1013

Lynden-Bell D., 1969, Nature, 223, 690

Lynden-Bell D., Rees M. J., 1971, MNRAS, 152, 461

Madigan A.-M., Levin Y., Hopman C., 2009, ApJL, 697, L44

Maeda Y., Baganoff F. K., Feigelson E. D., Morris M., Bautz M. W., Brandt W. N., Burrows D. N., Doty J. P., Garmire G. P., Pravdo S. H., Ricker G. R., Townsley L. K., 2002, ApJ, 570, 671

Maillard J. P., Paumard T., Stolovy S. R., Rigaut F., 2004, A&A, 423, 155

Mapelli M., Hayfield T., Mayer L., Wadsley J., 2008, ArXiv e-prints, arXiv:0805.0185

—, 2012, ApJ, 749, 168

McGary R. S., Coil A. L., Ho P. T. P., 2001, ApJ, 559, 326

McMillan S. L. W., Portegies Zwart S. F., 2003, ApJ, 596, 314

Melia F., 1992, ApJL, 387, L25

Melia F., Falcke H., 2001, Araa, 39, 309

Meyer L., Ghez A. M., Schödel R., Yelda S., Boehle A., Lu J. R., Do T., Morris M. R., Becklin E. E., Matthews K., 2012, Science, 338, 84

Mignone A., Bodo G., Massaglia S., Matsakos T., Tesileanu O., Zanni C., Ferrari A., 2007, ApJS, 170, 228

Mignone A., Flock M., Stute M., Kolb S. M., Muscianisi G., 2012, A&A, 545, A152

Miralda-Escudé J., 2012, ApJ, 756, 86

Miyazaki A., Tsuboi M., 2000, ApJ, 536, 357

Miyoshi M., Moran J., Herrnstein J., Greenhill L., Nakai N., Diamond P., Inoue M., 1995, Nature, 373, 127

Molinari S., Bally J., Noriega-Crespo A., Compiègne M., Bernard J. P., Paradis D., Martin P., Testi L., Barlow M., Moore T., Plume R., Swinyard B., Zavagno A., Calzoletti L., Di Giorgio A. M., Elia D., Faustini F., Natoli P., Pestalozzi M., Pezzuto S., Piacentini F., Polenta G., Polychroni D., Schisano E., Traficante A., Veneziani M., Battersby C., Burton M., Carey S., Fukui Y., Li J. Z., Lord S. D., Morgan L., Motte F., Schuller F., Stringfellow G. S., Tan J. C., Thompson M. A., Ward-Thompson D., White G., Umana G., 2011, ApJL, 735, L33

Monaghan J. J., 1992, Araa, 30, 543

Monaghan J. J., Gingold R. A., 1977, in Bulletin of the American Astronomical Society, Vol. 9, Bulletin of the American Astronomical Society, p. 567

Montero-Castaño M., Herrnstein R. M., Ho P. T. P., 2009, ApJ, 695, 1477

Morris M., Serabyn E., 1996, Araa, 34, 645

Morris M., Yusef-Zadeh F., 1989, ApJ, 343, 703

Müller A., Camenzind M., 2004, A&A, 413, 861

Muno M. P., Baganoff F. K., Bautz M. W., Feigelson E. D., Garmire G. P., Morris M. R., Park S., Ricker G. R., Townsley L. K., 2004, ApJ, 613, 326

Murray J. R., 1996, MNRAS, 279, 402

Murray-Clay R. A., Loeb A., 2012, Nature Communications, 3

Narayan R., Yi I., 1994, ApJL, 428, L13

Nayakshin S., 2005, MNRAS, 359, 545

Nayakshin S., Cuadra J., 2005, A&A, 437, 437

Nayakshin S., Dehnen W., Cuadra J., Genzel R., 2006, MNRAS, 366, 1410

Nelson A. F., 2006, MNRAS, 373, 1039

Nelson R. W., Tremaine S. D., 1996, in Gravitational dynamics, Lahav O., Terlevich E., Terlevich R. J., eds., p. 73

Nishiyama S., Hatano H., Tamura M., Matsunaga N., Yoshikawa T., Suenaga T., Hough J. H., Sugitani K., Nagayama T., Kato D., Nagata T., 2010, ApJL, 722, L23

Nishiyama S., Schödel R., 2013, A&A, 549, A57

Nixon C. J., King A. R., Price D. J., 2012, MNRAS, 422, 2547

Oort J. H., 1927a, BAIN, 4, 79

—, 1927b, BAIN, 3, 275

Paumard T., Genzel R., Martins F., Nayakshin S., Beloborodov A. M., Levin Y., Trippe S., Eisenhauer F., Ott T., Gillessen S., Abuter R., Cuadra J., Alexander T., Sternberg A., 2006, ApJ, 643, 1011

Paumard T., Maillard J.-P., Morris M., 2004, A&A, 426, 81

Perets H. B., Gualandris A., Kupi G., Merritt D., Alexander T., 2009, ApJ, 702, 884

Piddington J. H., Minnett H. C., 1951, Australian Journal of Scientific Research A Physical Sciences, 4, 459

Poliachenko V. L., Shukhman I. G., 1977, Soviet Astronomy Letters, 3, 134

Price D. J., 2007, Publications of the Astronomical Society of Australia, 24, 159

—, 2012, Journal of Computational Physics, 231, 759

Rappaport S., Sanchis-Ojeda R., Rogers L. A., Levine A., Winn J. N., 2013, ApJL, 773, L15

Reid M. J., 1993, Araa, 31, 345

Rein H., Liu S.-F., 2012, A&A, 537, A128

Rice W. K. M., Lodato G., Armitage P. J., 2005, MNRAS, 364, L56

Russell H. N., Shapley H., 1914, ApJ, 40, 417

Sanders R. H., 1998, MNRAS, 294, 35

Schartmann M., Burkert A., Alig C., Gillessen S., Genzel R., Eisenhauer F., Fritz T. K., 2012, ApJ, 755, 155

Schartmann M., Krause M., Burkert A., 2011, MNRAS, 415, 741

Schartmann M., Meisenheimer K., Camenzind M., Wolf S., Henning T., 2005, A&A, 437, 861

Schödel R., Eckart A., Alexander T., Merritt D., Genzel R., Sternberg A., Meyer L., Kul F., Moultaka J., Ott T., Straubmeier C., 2007, A&A, 469, 125

Schödel R., Genzel R., Ott T., Eckart A., 2003, Astronomische Nachrichten Supplement, 324, 535

Schödel R., Merritt D., Eckart A., 2008, Journal of Physics Conference Series, 131, 012044

Schödel R., Ott T., Genzel R., Hofmann R., Lehnert M., Eckart A., Mouawad N., Alexander T., Reid M. J., Lenzen R., Hartung M., Lacombe F., Rouan D., Gendron E., Rousset G., Lagrange A.-M., Brandner W., Ageorges N., Lidman C., Moorwood A. F. M., Spyromilio J., Hubin N., Menten K. M., 2002, Nature, 419, 694

Scoville N., Burkert A., 2013, ApJ, 768, 108

Shakura N. I., Sunyaev R. A., 1973, A&A, 24, 337

Shapley H., 1918, PASP, 30, 42

Shlosman I., Begelman M. C., 1987, Nature, 329, 810

Springel V., 2005, MNRAS, 364, 1105

—, 2010, MNRAS, 401, 791

—, 2011, in IAU Symposium, Vol. 270, Computational Star Formation, Alves J., Elmegreen B. G., Girart J. M., Trimble V., eds., pp. 203–206

Springel V., White M., Hernquist L., 2001, ApJ, 549, 681

Stamatellos D., Whitworth A. P., Bisbas T., Goodwin S., 2007, A&A, 475, 37

Steinmetz M., Mueller E., 1993, A&A, 268, 391

Stone J. M., Pringle J. E., 2001, MNRAS, 322, 461

Stone J. M., Pringle J. E., Begelman M. C., 1999, MNRAS, 310, 1002

Su M., Slatyer T. R., Finkbeiner D. P., 2010, ApJ, 724, 1044

Tartaglia A., 2000, Classical and Quantum Gravity, 17, 783

Török G., 2005, Astronomische Nachrichten, 326, 856

Tremaine S., 1995, ApJ, 110, 628

Tremaine S. D., Ostriker J. P., Spitzer Jr. L., 1975, ApJ, 196, 407

Ulubay-Siddiki A., Bartko H., Gerhard O., 2013, MNRAS, 428, 1986

Ulubay-Siddiki A., Gerhard O., Arnaboldi M., 2009, MNRAS, 398, 535

Vollmer B., Duschl W. J., 2001, A&A, 377, 1016

—, 2002, A&A, 388, 128

Vollmer B., Duschl W. J., Zylka R., 2003, Astronomische Nachrichten Supplement, 324, 613

Wardle M., Yusef-Zadeh F., 2008, ApJL, 683, L37

Weinberg D. H., 2003

Widrow L. M., 2002, Reviews of Modern Physics, 74, 775

Yuan F., Quataert E., Narayan R., 2003, ApJ, 598, 301

—, 2004, ApJ, 606, 894

Yusef-Zadeh F., Arendt R., Bushouse H., Cotton W., Haggard D., Pound M. W., Roberts D. A., Royster M., Wardle M., 2012, ApJL, 758, L11

Yusef-Zadeh F., Morris M., 1987, ApJ, 94, 1178

Yusef-Zadeh F., Morris M., Chance D., 1984a, Nature, 310, 557

—, 1984b, News Letter of the Astronomical Society of New York, 2, 11

Yusef-Zadeh F., Royster M., Wardle M., Arendt R., Bushouse H., Lis D. C., Pound M. W., Roberts D. A., Whitney B., Wootten A., 2013, ApJL, 767, L32

Yusef-Zadeh F., Wardle M., 1993, ApJ, 405, 584

Zhao J.-H., Morris M. R., Goss W. M., An T., 2009, ApJ, 699, 186

Zubovas K., King A. R., Nayakshin S., 2011, MNRAS, 415, L21